



universität  
wien

# DISSERTATION

Titel der Dissertation

„Particle Sources for Molecular Matter-Wave  
Interferometry with Nanoparticles“

Verfasser

Mag. Philipp Schmid

angestrebter akademischer Grad

Doktor der Naturwissenschaften (Dr. rer. nat.)

Wien, 2014

Studienkennzahl lt. Studienblatt: A 091 411

Dissertationsgebiet lt. Studienblatt: Physik

Betreuer: Univ.-Prof. Dr. Markus Arndt



# Contents

<b>Abstract</b>	<b>6</b>
<b>Zusammenfassung</b>	<b>8</b>
<b>I Introduction</b>	<b>10</b>
<b>1 Cold molecular beam sources for quantum coherence experiments</b>	<b>11</b>
1.1 Nanoparticle coherence experiments: matter-wave interferometry and OTIMA . . . . .	13
1.1.1 How the OTIMA interferometer works . . . . .	15
1.1.2 Molecular matter-wave experiments with nanoparticles . . . . .	17
1.2 Conclusion . . . . .	19
<b>II Laser desorption and photoionization of functionalized organic molecules</b>	<b>21</b>
<b>2 Motivation</b>	<b>22</b>
<b>3 Introduction to laser desorption and photoionization of molecules</b>	<b>25</b>
3.1 Laser desorption and MALDI . . . . .	25
3.2 Photoionization . . . . .	30
3.2.1 Single-photon ionization . . . . .	32
3.2.2 Multi-photon ionization . . . . .	33
3.2.3 Photoionization of the porphyrin system . . . . .	34
<b>4 Laser desorption &amp; photoionization of complex porphyrin derivatives</b>	<b>36</b>
4.1 Fluorinated porphyrins . . . . .	36
4.2 Experimental setup . . . . .	39

4.3	Experimental results . . . . .	41
4.3.1	Mass spectra of perfluoroalkyl-functionalized porphyrin derivatives . . . . .	41
4.3.2	Velocity distributions of laser-desorbed perfluoroalkyl - functionalized TPP libraries . . . . .	44
4.3.3	Ionization cross sections . . . . .	47
<b>5</b>	<b>Conclusion and discussion</b>	<b>52</b>
<b>III</b>	<b>Ion traps for molecular studies</b>	<b>55</b>
<b>6</b>	<b>Linear quadrupole ion traps</b>	<b>56</b>
6.1	Overview over the fundamental ion trap parameters . . . . .	57
6.1.1	The linear quadrupole trap . . . . .	58
6.1.2	Pseudopotential approximation and trapping depth . . . . .	66
6.1.3	Trap capacity and space charge . . . . .	67
6.1.4	Cooling of an ion cloud . . . . .	69
6.2	Laser induced fluorescence . . . . .	72
6.2.1	Properties of the absorption process . . . . .	75
6.2.2	Properties of fluorescence emission . . . . .	76
6.2.3	Laser induced fluorescence of cations in the gas-phase . . . . .	77
6.3	Design considerations for a linear ion trap . . . . .	78
6.4	The linear quadrupole ion trap - design . . . . .	81
6.5	Detection of the ion cloud by laser induced fluorescence . . . . .	90
6.6	Design of electric circuits and timing sequences . . . . .	96
6.6.1	The RF power supplies . . . . .	98
6.6.2	Endcap potentials . . . . .	104
6.6.3	TTL control and timing sequences . . . . .	106
6.7	Experimental setup . . . . .	107
6.7.1	Choice of particles . . . . .	112
6.7.2	Sample preparation techniques . . . . .	116
6.7.3	Trapping and detection of ion clouds . . . . .	117
6.7.4	Loading efficiency . . . . .	118
6.7.5	Ion signal dependencies on the buffer gas pressure . . . . .	121
6.7.6	LIF dependence on the excitation power . . . . .	126
6.7.7	Bleaching of the ion cloud . . . . .	127

6.7.8	Variation of the endcap potentials . . . . .	128
6.7.9	Radial ion cloud dimension . . . . .	130
6.7.10	Variation of the RF amplitude . . . . .	131
6.7.11	Mass selection . . . . .	133
6.7.12	Trapping of nanospheres . . . . .	141
6.7.13	Fluorescence of the polystyrene nanospheres . . . . .	142
<b>7</b>	<b>Two-tone quadrupole trap</b>	<b>144</b>
7.1	Cooling of molecular ions . . . . .	144
7.2	Simultaneous trapping of two ion species with large mass difference in a single-frequency RF trap . . . . .	145
7.3	Two-tone trapping . . . . .	147
7.4	SIMION simulations investigating trapping in a two-frequency ion trap . . . . .	149
7.4.1	SIMION simulation results . . . . .	151
7.4.2	Spectral analysis of the ion motion in a double RF potential .	157
7.5	Experimental tests of a two-tone trap . . . . .	161
7.5.1	Experimental setup . . . . .	163
7.5.2	Experimental results . . . . .	164
7.6	Conclusions and outlook of the two-tone trapping experiment . . . .	174
<b>8</b>	<b>Conclusions and future prospects on the ion trap experiment</b>	<b>175</b>
<b>9</b>	<b>Appendix</b>	<b>179</b>
9.1	Derivation of the Mathieu parameter $a, q$ . . . . .	179
9.2	Description of the ion trap design . . . . .	180
<b>10</b>	<b>Acknowledgments</b>	<b>183</b>

# Nomenclature

$\lambda_{dB}$ .....	de Broglie wavelength
$\mathbf{a}, \mathbf{q}$ .....	Mathieu parameter $a, q$
$\omega_r, \omega_z$ .....	radial/axial secular frequency
$\Phi_{LIF}$ .....	fluorescence quantum yield
$N_A$ .....	Avogadro constant
$r_0, r$ .....	ion trap inscribed radius, electrode radius
$V_{RF}$ .....	radio-frequency amplitude, zero-peak
$z_0$ .....	distance center/edge of central trapping electrode
CI .....	chemical ionization
Da .....	Dalton
DC .....	direct-current potential
EI .....	electron impact ionization
ESI .....	electrospray ionization
eV .....	electron volt
FFT .....	fast Fourier transform
IR .....	infrared radiation
K .....	Kelvin
KDTLI .....	Kapitza-Dirac Talbot-Lau interferometer
LD .....	laser desorption
LIF .....	laser induced fluorescence
MALDI .....	Matrix assisted laser desorption ionization
MCP .....	microchannel plate detector
NALDI .....	Nano-assisted laser desorption-ionization

OPO .....	optical parametric oscillator
OTIMA .....	optical time-domain ionizing matter-wave interferometer
PI .....	photoionization
PSD .....	power spectral density
SEM .....	scanning electron microscope
SPI .....	single-photon ionization
SSPD .....	Superconducting Single Photon Detector
TOF-MS .....	time of flight mass spectrometer
TPP .....	tetraphenylporphyrin
UV .....	ultraviolet radiation
VUV .....	vacuum-ultraviolet radiation
W .....	Watt
z .....	axial distance from the center of the trap

# Abstract

Nearly a century ago, Louis de Broglie predicted in his theory the wave properties of massive particles [1]. The experimental demonstration of this superposition principle of particles continues up to this date.

New experimental techniques in molecular matter wave interferometry [2] aim at increasing the accessible mass ranges up to  $10^6$  Dalton or even beyond. Independently on the type of interferometer used, an important question for all these experiments is the way of generating the particle beam. In contrast to atom interferometry, the creation of well-defined beams of neutral and cold large molecules or nanoparticles in the gas phase still remains a big challenge.

In this thesis the investigation of two different molecular source concepts for molecular matter wave interferometers are described, which have the potential to further extend the mass range in current matter wave interferometry experiments.

The first concept investigated, is laser desorption of neutral, functionalized organic molecules in the lower  $10^4$  Dalton mass range combined with VUV photoionization. Molecules were released intact from a sample surface upon the laser desorption process and were subsequently ionized in the gas-phase. The resulting velocity distributions and ionization curves show that this experimental technique can be suitable for matter wave interferometry in an already existing experimental setup.

For matter wave interferometry with particles of masses larger than  $10^6$  Dalton a different source concept is required. Here the suitability of coupling a linear radio-frequency (RF) ion trap to an interferometer was investigated. As a first step a linear quadrupole ion trap combined with a non-destructive detection method was developed. The molecular ions are created by matrix-assisted laser desorption/ionization and detected optically by laser induced fluorescence. In our experiments we could show the effective loading and manipulation of ion clouds with different masses ranging from  $10^2$  to  $10^6$  Da.

Finally, a novel ion trapping scheme was studied with respect to the possibility of sympathetic cooling of large molecular ions by laser cooled atomic ions, independent on the mass to charge ratio of the molecule. Suitable operational conditions were first identified by extended ion optics simulations and by exploring the feasibility of trapping high-mass and low-mass ions under two-tone trapping conditions.

# Zusammenfassung

Die Welleneigenschaften von massiven Teilchen wurden 1923 von Louis de Broglie theoretisch vorhergesagt [1]. Die experimentelle Untersuchung dieses Superpositions-Prinzips an komplexen Teilchen ist weiterhin ein aktives Forschungsgebiet.

Neue Techniken in molekularer Materiewelleninterferometrie [2] sind darauf ausgerichtet den Massenbereich von  $10^6$  Dalton oder noch größer zu untersuchen. Unabhängig vom Aufbau des Interferometers ist ein wichtiger Punkt die Herstellung von neutralen Teilchenstrahlen. Im Gegensatz zur Atominterferometrie ist die Produktion von wohldefinierten Teilchenstrahlen aus kalten, neutralen Molekülen in der Gasphase weiterhin eine große Herausforderung.

In dieser Dissertation werden zwei unterschiedliche Konzepte von Quellen für molekulare Materiewelleninterferometrie beschrieben, die das Potential haben den Massenbereich von bisherigen Experimenten zu vergrößern.

Für die erste Molekularstrahlquelle wurde Laserdesorption von neutralen, funktionalisierten organischen Molekülen im unteren  $10^4$  Dalton Massenbereich untersucht, kombiniert mit VUV Photoionisation. Die Moleküle wurden intakt von einer Probenoberfläche mittels Laserdesorption heruntergelöst und in der Gasphase ionisiert. Die gemessenen Geschwindigkeitsverteilungen sowie Ionisationskurven zeigen, dass diese Technik schon in derzeit aufgebauten Materiewelleninterferometern eingesetzt werden kann.

Für Materiewelleninterferometrie mit Teilchen schwerer als  $10^6$  Dalton ist ein anderes Quellenkonzept notwendig. Hierfür wurde die Kopplung einer linearen Radiofrequenz (RF) Ionenfalle an ein Interferometer untersucht. Als erster Schritt wurde eine lineare Quadrupol Ionenfalle mit zerstörungsfreier Detektion entwickelt. Die Molekülionen werden mittels Matrix-unterstützter Laser-Desorption/Ionisation produziert und durch laserinduzierte Fluoreszenz detektiert. In unseren Experimenten konnten wir ein effektives Laden sowie Manipulation von Ionenwolken im Massenbereich von  $10^2$  bis  $10^6$  Dalton zeigen.

Ausserdem wurde in dieser Arbeit ein neuartiges Konzept zur sympathetischen Kühlung von molekularen Ionen unabhängig ihres Masse-zu-Ladung Verhältnis untersucht. Geeignete Konditionen für die Speicherung der Ionen wurden zuerst in ausführlichen Simulationen gesucht. Weiters wurden in Experimenten die Möglichkeit der Speicherung von schweren und leichten Ionen in einer Zwei-Frequenzfalle untersucht.

# Part I

## Introduction

## Chapter 1

# Cold molecular beam sources for quantum coherence experiments

Since the advent of quantum theory a wide range of experimental techniques have been developed which allow us to investigate and understand better the fundamentals of quantum mechanics. Such methods in atomic and molecular physics include for instance the cooling and trapping of neutral atoms [3], Bose-Einstein condensates (BEC) [4], ultracold gases in regular structures [5], quantum simulations with photons [6] but also matter-wave interferometry [7].

Experimental demonstrations of the validity of the superposition principle are of importance for our understanding of the foundations of quantum physics and they are of practical interest with regard to future emerging technologies, taking advantage of non-classical states in highly sensitive sensors for external forces or internal particle properties [8].

Matter wave physics started with first theoretical considerations by Louis de Broglie in 1923 [1] and soon after it was demonstrated experimentally for electrons [9, 10], atoms and molecules [11] as well as neutrons [12]. In modern science and technology, the delocalized quantum nature of electrons and neutrons is routinely exploited in surface science applications [13] and the investigation of bulk crystal structures [14] or the analysis of single molecules in free flight [15].

Recently experimental developments in the manipulation of atoms [16], molecules [8] and cold nanoparticles [17–19] as well as theoretical proposals [20–26] suggest that

the quantum superposition principle could be tested also with large molecules or small particles in the mass range greater than  $10^5$  Da.

Matter wave interferometry with massive quantum objects is expected to permit tests of non-standard quantum theories, such as in the form of continuous spontaneous localization models [27–29], in the mass range of  $10^5 - 10^8$  Da [24, 25].

A straightforward combination of quantum mechanics with general relativity leads to the Newton Schrödinger equation (NSE), for which is still not known whether it describes reality and to what degree it is formally consistent. However, the NSE predicts a dynamical collapse of otherwise freely spreading quantum wave packets at masses about  $10^{10}$  Da on time scales of minutes to hours [30].

Based on fundamental considerations one may also question the coupling of quantum matter and space-time as was done by Roger Penrose: if massive matter is allowed to delocalize and if it couples to space-time as a term in its curvature, the meaning of the Schrödinger equation itself becomes finally unclear. The time derivative of the quantum wave function hinges on the well-defined notion of time itself - which may no longer be given in a superposition of space-times. Rules-of-thumb estimate [31] suggest that non-standard quantum effects may occur on the time scale of seconds if particles in the mass range of  $10^{10}$  Da are brought into a superposition of position states that are separated by more than the size of the particle itself, i.e. about 100 nm or more.

It is further expected that nanoparticle interferometry can, in the long run, contribute to many of the tests proposed of fundamental physics with atoms in space - be it for instance tests of the equivalence principle [32–34], the search for gravitational waves or dark matter [35] - in a similar yet complementary way to atom interferometry.

In contrast to atoms, macromolecules and nanoparticles offer a much richer internal structure which is both an asset and a drawback. Most atom interferometers these days are applicable for just one type of atoms, requiring a change of lasers, optics and trapping tools for any new species. For molecules, in contrast to atoms, the experimental parameters can be reconfigured more easily, if the matter interferometer is designed and adapted for such a purpose [2].

At present, nanoparticle interferometry, however, cannot yet compete with atom interferometry when it comes to high-precision measurements, mostly because nanopar-

ticle sources are orders of magnitude weaker and hotter, limiting the molecular de Broglie wavelength  $\lambda_{dB}$ . This is similar to the situation about 30 years ago, when electron diffraction was already commercialized and atoms still uncooled.

As of today, cold atom physics and atom interferometry have been studied by hundreds of scientific groups around the globe for about three decades, but nanoparticle interferometry so far has only been successfully demonstrated by the Vienna Quantum Nanophysics group. Although, several new groups in the world have recently started investigating complementary experimental approaches, too. The optical manipulation of levitating particles in the mass range of  $10^7 - 10^{12}$  Da [36–38] has only been revived throughout the last years [17–19] and good progress is made towards using these techniques as a source for new matter-wave interferometers.

## 1.1 Nanoparticle coherence experiments: matter-wave interferometry and OTIMA

Future experiments in the Vienna group will focus on quantum superposition experiments with molecules and nanoparticles in the mass range between  $10^5$  to  $10^9$  Da. This could become accessible in a newly developed optical time-domain ionizing matter wave interferometer with optical depletion gratings [2, 39, 40].

Earlier and on-going experiments in macromolecule and cluster interferometry have relied on three different concepts: far-field diffraction [41, 42], near-field Talbot-Lau interferometry [43] and Kapitza-Dirac-Talbot-Lau interferometry [44]. Far-field diffraction provides probably the most visual and intuitive example of quantum delocalization of massive matter. Richard Feynman once baptized it the "heart of quantum mechanics" [45] and in the laboratories of the Vienna Quantum Nanophysics group far-field diffraction with complex organic molecules has been realized [42]. This experimental concept has a strong benefit in teaching quantum superposition. At the same time it allows to test new grating structures visually [46].

All experiments of this type rely on the availability of coherent sources, nanosized diffraction elements and a position resolving detector of high efficiency. None of that can be taken for granted for large molecules or nanoparticles in the mass range between  $10^5 - 10^{10}$  Da.

This is why, inspired by an idea by John Clauser [47, 48], the concept of near-field Talbot-Lau interferometry (TLI) for large particles was experimentally verified, first with fullerenes [43] and biological dyes [49]. The TLI concept solves the problems of source coherence and detector resolution that was originally encountered in far-field diffraction, by adding two periodic nanomasks - one in front and one behind the diffraction grating. The first grating solves the coherence problem, while the last grating is used only for detection. Thereby the first mask represents an array of slit 'sources' of thousand fold multiplexed nanoemitters for the transmitted molecules. Since the transverse coherence increases with decreasing source size, each slit source now serves as a spatially coherent emitter - even though none of them is phase correlated with their next-neighbor emitters.

Talbot-Lau interferometry leads to the emergence of quantum fringes in the Talbot distance  $L_T = d^2/\lambda_{dB}$  with a period equal to that of the first nanomask. It is well conceivable to implement a surface deposition combined with scanning tunneling microscopy [50] or fluorescence imaging [51]. In many cases signal accumulation is enhanced by adding a third grating with again the same period, which is then used as a scanning position resolving detector [8].

Nevertheless, using large particles in coherence experiments the TL-concept still suffers from the coupling of the internal and external molecular degrees of freedom. Every nanoparticle exhibits quantum fluctuations of their charge cloud, resulting in the spontaneous formation of temporary dipole moments and van der Waals (vdW) interactions with their surroundings. Such vdW forces, for example, can already be detected in the far-field diffraction of fullerenes behind a diffraction grating with a slit period of 100 nm [52]. Since polarizability increases roughly in proportion to volume and mass, quantum objects with masses in the MDa or GDa range will be influenced by these interactions to the point that they dramatically become de-phased. This is why it proved to be useful to replace the central material grating by an optical phase mask, very similar to an early proposal by Kapitza and Dirac to demonstrate diffraction of electrons at a standing light wave [53]. The concept of Kapitza-Dirac-Talbot-Lau interferometry (KDTLI) turned out to be extremely successful [44, 54–58] and currently holds a mass record in quantum interferometry with nanoparticles [59].

For quantum interference experiments with large molecules or nanoparticles in the

mass range greater than  $10^6$  Da, however at a certain point, the ever increasing polarizability will even prevent the 'semiclassical balls' from being transmitted through any mechanical grating. Extending the grating slits to some extent is no option, because this would also reduce the grating stability or it would require stretching of the entire interferometer in proportion to the square of the increase in the grating period. This is the reason why recently the concept of an optical time domain ionizing matter wave interferometer (OTIMA) [2, 39, 40] has been introduced, which adds photo-depletion gratings [39] to the concept of Talbot-Lau interferometry in the time domain [60–63].

### 1.1.1 How the OTIMA interferometer works

An OTIMA interferometer [2] has recently been realized by the Vienna Quantum Nanophysics group. It is based on the original TLI proposal (see above) as well as [39], but realizes all selection and diffraction masks as ionizing or neutralizing optical gratings (see figure 1.1): A first laser pulse imposes spatial coherence, a second one is responsible for coherent re-phasing of the spreading wave packets and a third one probes the particle density pattern that forms because of quantum interference.

In combination with a weak and homogeneous electric field, optical ionization gratings are dominantly absorptive since they separate the charged from the neutral particles and keep the neutral fraction in all sequences of the experiment. In addition to removing particles from the beam they also add a phase to the matter wave which depends on the light intensity as well as on the particle's polarizability [40]. Currently these optical gratings are created by a fluorine excimer (F2) laser, which emits at  $\lambda \approx 157$  nm and generates a period of  $d \approx 79$  nm [2].

While matter wave interferometers usually require both spatial and spectral coherence of the incident particle beam, the advantage of OTIMA interferometry consists in the fact that it can renounce on either one and thus adapt to a much wider range of particle sources.

Transverse coherence is intrinsically correlated with the extension of the particle source: the smaller the source emission area, the wider the transverse coherence further downstream since the coherence functions are determined by the Fourier transform of the spatial source properties [64]. The nodes of the optical gratings act

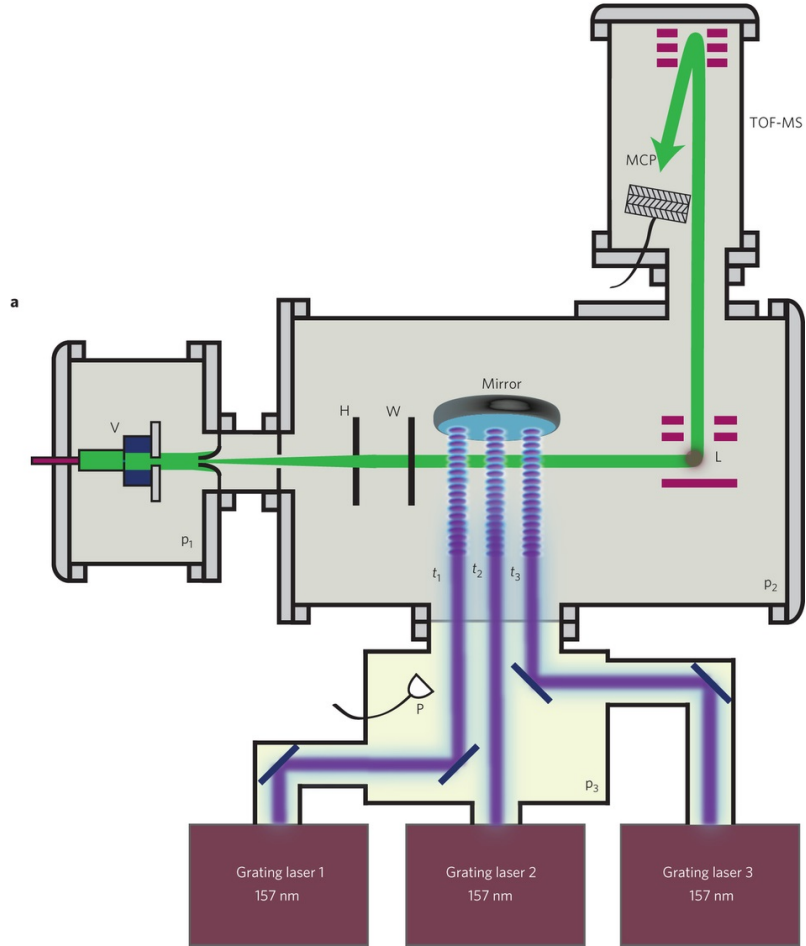


Figure 1.1: The experimental realization of the OTIMA interferometer with three short-pulse optical ionization gratings is shown. A short pulse of neutral molecules is delimited horizontally and vertically before it enters the region of the interferometer. VUV laser pulses at  $t_1 = 0$ ,  $t_2 = T$  and  $t_3 = 2T$  ( $T$  being the Talbot time) produce three standing light waves, where the coherence preparation, diffraction and its detection takes place. Finally the neutral particles are photoionized and detected in a TOF-MS. Image taken from [2].

as many parallel (yet uncorrelated) emitters for nanoparticles and they can reach a width as small as a few nanometers. Moreover, to first order, the need for longitudinal coherence is eliminated in a non-dispersive interferometer which is operated with the grating pulses separated in time rather than in space.

### 1.1.2 Molecular matter-wave experiments with nanoparticles

The current implementation of the OTIMA interferometer [2] is in principle compatible with particles up to  $10^6$  Da, provided that a suitable probe source can be realized, producing a beam of internally as well as externally cold ( $T < 100$  K) and neutral molecules. In principle, also singly charged anions could be used in the OTIMA, in which the first interference grating would photo-neutralize the ions and act at the same time as the coherence preparation stage. An important aspect of any such source is a high flux of probe molecules.

Under these preconditions (i.e. source) given, the probing of an important parameter range of continuous spontaneous localization models and new bounds on quantum macroscopicity should become possible [24].

The boundary conditions for OTIMA interferometry can be estimated by the characteristic dimensions for an optical time domain interferometer: The characteristic dimension of matter-wave near-field interferometry is the Talbot length, at which the grating structure shows self-imaging

$$L_T = \frac{d^2}{\lambda_{dB}} \quad (1.1)$$

In the specific case of pulsed gratings, with a fixed distance in time rather than in space, the re-phasing of the quantum waves occurs in time intervals close to multiples of the Talbot time,

$$T_T = \frac{m \cdot d^2}{h} \quad (1.2)$$

For the tabulated values (table 1.1) the thermal velocity and the resulting most

mass	$10^4$ Da	$10^5$ Da	$10^6$ Da	$10^7$ Da
$v_{\text{mp}} @ 10 \text{ K}$	4 m/s	1.3 m/s	0.41 m/s	0.13 m/s
$\lambda_{\text{dB,mp}} @ 10 \text{ K}$	9.8 pm	3.1 pm	1 pm	310 fm
$L_T$	630 $\mu\text{m}$	2 mm	6.3 mm	2 cm
$T_T$	0.15 ms	1.5 ms	15.5 ms	155 ms
free fall drop	1.2 $\mu\text{m}$	120 $\mu\text{m}$	1.2 cm	1.2 m
thermal expansion	1.3 mm	4 mm	1.3 cm	4 cm

Table 1.1: Range of boundary conditions and parameters in OTIMA interferometry for molecules of different mass with a temperature of 10 K.

probable de Broglie wavelength at this temperature is calculated with

$$v = \sqrt{\frac{2k_B T}{m}} \quad (1.3)$$

$$\lambda_{\text{dB}} = \frac{h}{\sqrt{2mk_B T}} \quad (1.4)$$

Finally, the thermal expansion at 10 K can be estimated by

$$D = 2vT_T = \frac{2d^2}{h} \cdot \sqrt{2mk_B T} \quad (1.5)$$

For an OTIMA interferometer with a grating constant of about  $d=78.5 \text{ nm}$  ( $\lambda_{\text{Laser}} = 157 \text{ nm}$ ) we compute the following interferometer and source parameters, as shown in table 1.1. Thereby the possibility of cooling large nanoparticles to cryogenic temperatures, at 10 K, is assumed, which clearly demonstrates the need for such a cryogenic source, if one ever wants to see high-mass interference.

From the calculations presented it is observable that for heavy particles the thermal expansion of the molecular cloud is rather large and the laser gratings have to be wide enough to still allow a large particle flux through the interferometer. Since commercial fluorine lasers have a limited coherence length of  $l_c < 1 \text{ cm}$  a new interferometer will either need new VUV laser techniques or solid state laser technology. In particular the use of a seeded and frequency-quintupled Nd-YAG laser, operating at 213 nm ( $d=106.5 \text{ nm}$ ) could be an optimal choice. Such lasers are commercially available, show stable operation conditions and have a narrow linewidth.

The internal temperature of the particles plays an essential role as it is related with the particle's capability to emit thermal radiation. Since any type of spontaneous photon emission is accompanied by some momentum recoil, this process has to be

minimized and/or shifted to the emission of long-wavelength photons which carry less 'which-path' information from the delocalized nanoparticle into the environment. This requires not only cooling of the transversal degrees of freedom, but also the internal degrees of freedom of the particles before they enter the interferometer. For the same reason the experiment has also to be conducted under condition of very low pressure, because any colliding residual gas molecules would immediately destroy the quantum interferogram [65].

Figure 1.2 shows the temperature and pressure conditions for OTIMA interferometry with high masses. It clearly indicates that cryogenic temperatures are required, internally and within the experiment. This will eliminate the exchange of blackbody radiation and ensures that molecular vibrational modes cannot further relax since they are already in their ground state.

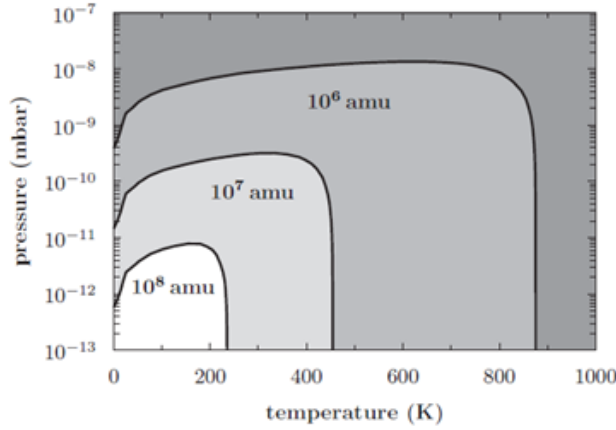


Figure 1.2: Boundary conditions on temperature and residual pressure to eliminate thermal or collisional decoherence [40]. At high temperatures, thermal blackbody scattering and the emission of thermal radiation destroy quantum coherence since the exchanged photons provide which-path information and a recoil to the delocalized particle. At low temperatures collisions represent the dominant cause of decoherence. A good vacuum, as naturally established in a low-temperature environment, is therefore imperative for such experiments.

## 1.2 Conclusion

Particles in the mass range of 100 kDa or higher would provide an interesting experimental tool for testing different theoretical models in quantum theory. To allow

experiments in this mass range, improvements not only in the current interferometers but especially in particle sources are needed. For such quantum interferometry experiments particle beams with a high flux and low internal temperature and transversal beam velocities are essential, with the final consequence of a cooling of particles to cryogenic temperatures.

One major scope of this thesis was therefore the investigation of new particle sources for future matter-wave interferometers. Two different, but complementary techniques are tested with regard to their suitability: laser desorption of tailored molecules combined with photoionization and ion trapping of fluorophores as well as polystyrene nanospheres.

In the first part of this thesis laser desorption with specially designed molecular libraries of perfluoroalkyl-functionalized tetra-phenyl porphyrin molecules are studied. After an introduction on the experimental setup it will be shown that this type of source is capable of producing slow molecular beams with molecular masses up to 20 kDa.

In the second part of this work a linear quadrupole ion trap is presented and aspects of its future use for interferometry experiments are investigated. First 'proof of principle' measurements show the readiness of this technology. Regarding the discussion above a further scope of this thesis was to investigate the prospect of sympathetically cooling heavy molecular ions trapped in a two-tone ion trap.

## PartII

# Laser desorption and photoionization of functionalized organic molecules

## Chapter 2

# Motivation

Since the 1980's, the increasing control over atomic ensembles in the gas-phase and the advent of cooling techniques down to ultra-cold temperatures ( $T < \text{mK}$ ) has led to a renaissance of atomic physics. Such cold atomic samples can be used for testing quantum physics using Bose-Einstein-Condensates (BEC) up to time-reversal symmetry or even new time standards. This great success of atom experiments led to an increased research on the possible the control and cooling of neutral molecular beams. If cold, dense samples of neutral molecules in the gas-phase can be produced, chemical reactions at very low temperatures will be accessible in experiments. Due to the large de Broglie wavelength the chemical reactivity between two collision partners could show a new behavior [66]. For small molecular systems it is already possible to produce cold and ultra-cold samples. One pathway is by using a sample of ultracold atoms as a starting point. Thereby diatomic molecules are formed by photoassociation from an ultra-cold atomic gas [67, 68]. A different approach, especially for molecules not accessible by photoassociation, is by cooling molecules being already in the gas-phase. Such molecular systems, like OH, NO or  $\text{NH}_3$ , are cooled and internally state selected either by deceleration in electrical fields (Stark decelerator) [69, 70] or strong optical fields [71].

While these techniques allow the cooling and trapping of neutral molecules, they are all limited to masses smaller than about 100 Da. An extension of these techniques to heavier systems would certainly be of interest for molecular physics. Especially in beam deflection [72–78] or in matter-wave interferometry translational

cold molecules are necessary. Matter-wave interferometry is governed by the de Broglie wavelength,  $\lambda_{\text{dB}} = h/mv$ . With increasing molecular mass the velocity must decrease proportionally such that  $\lambda_{\text{dB}}$  stays within the current experimentally required minimal length in the range of about 200 to 300 fm [2, 8]. This requires cryogenic translational beam temperatures for heavy masses in the order of  $10^5$  to  $10^7$  Da.

Cooling and manipulation of molecules is not the only problem in molecular beam studies, there is also the need of directed particle beams with high flux. Although the transversal cooling increases the longitudinal directionality of the beam, an even increased flux is favorable in most experiments. While small molecules, similar to the ones, for example used in Stark decelerators, can be brought into the gas-phase quite easily, increased molecular mass leads to a decrease of the vapor pressure at room temperature. High vapor pressures for molecules in the mass range of several hundred Dalton can be achieved by heating to temperatures below 700 K. For greater masses this method is limited, especially for most biological relevant molecules such as for proteins, which decompose already at temperatures below a sufficiently high vapor pressure is reached.

Two other techniques exist in mass spectrometry for volatilizing molecules even up to the mega-Dalton range. These are electrospray ionization (ESI) [79] and matrix-assisted laser desorption ionization (MALDI) [80]. Both methods are 'soft ionization' techniques, meaning that decomposition of molecules during the de-solvation process is small. Although both techniques are commonly used in ion formation, they are known to produce a large fraction of neutral particles of different size and mass as well [81, 82].

For molecular beam experiments in high vacuum, electrospray ionization has the disadvantage that it starts from atmospheric pressure conditions. To reduce this background pressure downstream from the source differential pumping with large pumping capacity is required. Contrary, MALDI ionization can easily be operated under vacuum conditions. A further advantage of MALDI can be the pulsed nature of this source type, because in the desorption process a pulsed laser in the nanosecond range is required. This makes it an ideal match for a pulsed detection scheme further downstream (like an TOF-MS).

In matter-wave interferometry experiments with molecular masses greater than  $10^5$

Da pulsed light gratings [2] in combination with a MALDI type source seems to be an ideal choice for such an experiment. Since this thesis aims at exploring a functional particle source for matter-wave interferometry, laser desorption was investigated in detail. The pulsed nature of this source and the high content of released neutral particles motivated this choice. Additionally, for self-seeded MALD(I) beams, at high mass the expected molecular velocities are slow enough to allow a direct coupling to an interferometer. In the following the experimental realization of a laser desorption post-ionization set-up will be described and the measured results will be discussed in detail. In the beginning a short overview over the theory of laser desorption and photoionization will be given.

## Chapter 3

# Introduction to laser desorption and photoionization of molecules

### 3.1 Laser desorption and MALDI

The transfer of complex (organic) molecules with a mass above several thousand Daltons into the gas-phase by simply heating the molecules proves not to be an efficient process. A different approach is the use of MALDI which transfers molecules into the gas-phase through short pulsed laser radiation, (nearly) independent of the molecular structure. In this way even particle masses greater than 1 MDa can be volatilized from the surface [83].

Laser desorption and its variation MALDI can be described as a two-step process. In the first step a pulsed laser beam (commonly in the UV) is guided onto a sample to begin the laser desorption process. The irradiated molecules on the sample surface, preferentially the matrix molecules, will be excited by the laser light. This leads to the removal of the upper layers of molecules on the sample and their lifting into the gas-phase. Thereby a plume is created, consisting of a mixture of charged and neutral matrix and analyte molecules. During the expansion phase of the plume further analyte molecules can be charged.

Recently a set of fundamental reviews appeared [84,85] describing the current state of the art of the MALDI process in detail. Although laser desorption and MALDI processes have been discussed already early in literature [80,86–89], the actual phys-

ical mechanism behind the desorption and the ionization processes are still not fully resolved today. A recent publication indicates that the influence of the matrix properties on the desorption process is greater than previously estimated [90], since releasing of ions from the MALDI sample surface can also be done without the influence of laser light. Several different models describing different parts of the processes involved are accepted, but still, no complete theory for MALDI is available.

Ion formation in the MALDI process is reviewed by Karas et al. [91], while Knochenmuss et al. present the influence of the MALDI plume in the desorption process and the subsequent ion formation [92]. The mechanism and the dependencies of the desorption process in MALDI is reviewed by Dreisewerd [93].

In the following the main aspects of laser desorption and its ionization will be discussed, following closely the review of Dreisewerd [93]. The main aspect here is the formation of volatile neutral molecules and their molecular properties, since they are of interest in further experiments.

In thermodynamics, desorption describes the phase transition of individual molecules in the outermost layers of a solid sample into the gas-phase. Thus, desorption is viewed as the reverse process of adsorption. In the context of MALDI this is not a valid description, since different physical mechanisms are involved. By the absorption of laser light the desorption process is initiated with a subsequent excitation of the molecules, followed by a phase transition from solid or liquid to the gas-phase.

A short laser pulse is guided onto the analyte molecules atop a sample surface. Upon light absorption mainly matrix molecules are electronically excited, which also triggers the lifting of non-matrix molecules from the surface into the gas-phase. Since a large number of molecules are released with every laser pulse, a so-called MALDI (plasma) plume is formed. During this expansion of the particles they undergo a number of collisions with other molecules which can ionize the particles by charge exchange or ionization by collisions with electrons. If high laser fluences are used for desorption, leading to dense plumes, this results in a high number of collisions, reducing the transversal plume as well as the internal molecular temperature [94]. Eventually, a fraction of the molecules carrying charges will leave the interaction region. In most of the cases the average number of charges on the molecules is between one to three, with the most abundant fraction carrying one single net-charge [95].

While a part of the molecules emerging from the plume are ions, experiments showed

that a major fraction remains neutral. The assessment of this ratio is difficult, but several groups showed that the most probable ion to neutral fraction is between  $10^{-3} - 10^{-5}$  [82,96]. The exact percentages in any given experiment are determined not only by the physic-chemical properties of the molecules and the preparation technique for the target used (e.g. ratio between matrix and analyte) but also by the laser parameters [97].

Since the desorption process is initiated by the laser, it is reasonable to argue that the properties of the laser beam will have a great influence on the desorption results. For most MALD(I) experiments lasers operating either in the UV or the mid-IR are used. The choice of the laser wavelength is mostly dependent on the absorption properties of the chosen matrix. These molecules should have a high absorption for the laser wavelength while analyte molecules should exhibit low photoexcitation at the laser wavelength. This prevents the negative influence of the laser radiation on the (mostly) labile molecules. Mostly, the analyte molecules have low photoabsorption in the near UV which makes UV MALDI the most commonly used volatilization technique for producing gas-phase ions by desorption.

Typically either nitrogen lasers ( $N_2$  lasers) at 337 nm or frequency-tripled Nd:YAG lasers operating at 355 nm with pulse durations around 3 to 10 ns are used. These short UV light pulses will eventually lead to the electronic excitation of the molecules. In IR-MALDI a different desorption pathway of the matrix molecules will take place: At around 3  $\mu m$  molecular vibrations of O-H and N-H bonds and at about 10  $\mu m$  O-H and C-H bonds are mainly excited, which subsequently leads to the molecule ejection from the surface.

Apart from the laser wavelength the pulse energy and the spot diameter irradiating the sample surface have an influence on the creation of the plasma plume and the resulting mass spectra. While a minimum laser fluence is required to lift particles from the sample surface, enhanced laser intensities lead to sharply increased ion signals. For very high fluences, the measured signal eventually saturates due to fragmentation of matrix and analyte molecules. The best signals can be observed around a threshold fluence [98]. Otherwise, at higher laser energies (and identical beam spot) the shot-to-shot signal fluctuations are leading to larger fluctuations of the recorded ion signal.

Another important parameter strongly influencing the results of LD/MALDI mea-

surements is the choice of the type of matrix molecule. The main function of matrix molecules is the absorption of the laser energy and its transfer to the sample molecule(s). Furthermore the matrix molecules are required for the ionization of neutral analytes inside the MALDI plume [92].

The quality of the resulting mass spectra depends strongly on the choice of matrix as well as on the sample preparation protocol. Even though MALDI has become a commonly used technique today, preparation procedures are still mostly empirical. Practically, for matrices a good vacuum stability and high absorption characteristics at the laser wavelength are required while at the same time they should show a high ionization ability of the analytes. Also, the matrix should not be chemical reactive and should be similar soluble as the analyte(s), displaying good crystallization characteristics when mixed with the analyte(s).

In an ideal sample preparation protocol a homogenous layer of matrix crystals containing a fraction of the analyte will provide optimal results. A matrix/analyte ratio of greater than  $10^2$  should be targeted in the preparation steps. Especially when molecules with high mass are considered for a MALDI experiment, the ratio should be increased to  $10^4$  and higher, since the high number of matrix molecules reduces a clustering of the analyte molecules on the sample surface.

For application of the matrix/analyte mixture onto the target sample surface different techniques are described, with an incomplete overview of different sample preparation techniques given in [84, 85, 99–101].

The choice of chemicals for dissolution of analyte and matrix is of importance in the preparation step of a MALDI sample, as both should be either soluble in an identical solvent or, when different chemicals are used, no precipitation of the molecules should take place in the final solution. Also, the solvent affects the matrix/analyte mixture composition during drying, whereby the crystallization properties of the crystals can change. Especially in the case of polymers in MALDI TOF-MS experiments such a behavior has been observed [102]. Large amounts of additives or salts in the preparation step of a MALDI sample can lead to a reduction of the spectrum quality or loss of ion signal altogether [103, 104]. In a recent work [105] the solvent effect could be eliminated by omitting the solvent completely, instead the matrix and analytes were mixed as powder and pressed onto the sample target surface. The solvent effect emphasizes again that a well-defined sample preparation

in a MALDI/LD experiment is required, which might take some 'trial-and-error' experimenting in finding out the best sample preparation technique with new analyte molecules. Generally, it can be stated that no universally applicable sample preparation exists [106].

While it is not easy to predict which matrix is suited best for a specific analyte, a list of common matrix molecules has been established over the years [85, 107]. Most experiments require the addition of a matrix to lift and ionize analyte(s), but several research groups also demonstrated self-seeding LD, omitting the use of chemical matrices in sample preparation or using nano-structures for the desorption of the analytes (NALDI) [108]. In the former, the (analyte) molecules show good absorption properties at the laser wavelength without experiencing too much fragmentation [109, 110]. For IR-MALDI of proteins, water-ice was found to be a suitable sample background since the O-H binding of H<sub>2</sub>O absorbs strongly around 3  $\mu\text{m}$  [111].

As a final point in this overview on LD/MALDI the molecular velocities in the gas-phase are mentioned. While the velocities of the initial ions can be determined in MALDI TOF-MS measurements (e.g. by delayed extraction method [112]), for recording the velocities of the neutral molecules an additional post-ionization step of the molecules is required. For that purpose the time delay between the desorption laser and the post-ionization laser is varied and the velocity distribution can be determined from the time variation of the signal intensity. Such measurements revealed that in MALDI ions expand into the vacuum with velocities in the order of several hundred to thousand meters/second [113, 114]. While these values represent the axial velocities of the matrix ions, similar speeds are recorded for the analyte ions as well. The data in literature is not always consistent, some show that the mass of the desorbed molecule is negligible for the recorded velocity distributions [114–116], while in a recent publication a mass dependent velocity slip could be measured [117]. A different picture is observed for the initially neutral molecules in the MALDI process where the recorded velocity distributions show a lower mean velocity. The width of the velocity distributions is typically broader compared to ions. Apart from the lower axial velocities the recorded radial velocity distributions show a shift towards lower values as well. While such velocities have been typically recorded for pure analyte samples, the addition of matrix to the sample has the consequence in shorter

flight times and also in a sharpening of the resulting velocity distribution [93]. This indicates that the addition of a matrix leads to an increase of the resulting forward velocity.

## 3.2 Photoionization

When considering molecular matter-wave interference experiments, the molecular beam must have a well-defined velocity and flux. To reduce the influence of charge-assisted decoherence, the molecules inside the interferometer should be neutral, which requires new methods for the handling of neutral particles in the gas-phase. For example, with the help of radiation pressure dielectric micro- and nanoparticles can be trapped in the focal points of laser beams [38] or possibly in the standing light wave of an optical cavity [118,119]. Such methods could serve as a starting point for slow, neutral molecules in a beam experiment. Another experimental approach is the slowing and cooling of molecules inside a particle beam by using the Stark effect by interaction of the molecules with an external electric field, which was recently demonstrated for small molecules [71,120,121]. Especially the cavity assisted cooling is not only interesting for cooling massive, neutral particles in the gas-phase to sub-cryogenic temperatures [17,19,122,123], but it opens the access to perform tests on quantum theory with particles of high molecular weight [22,23,26] or experiments in opto-mechanics [124].

While the experimental techniques for handling neutral particles in the gas-phase are getting more advanced, charged molecules can be handled more easily by electric or magnetic fields, independent from the internal structure and the size of the molecules. Another advantage is the possibility of mass analysis and their simplified detection by detectors like Faraday cups or electron multipliers [125].

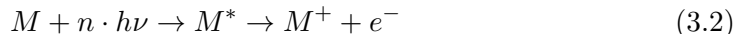
The above mentioned criteria show that the manipulation of a molecular beam is best achieved through an ionization process. For ionization of molecules in the gas phase several experimental methods exist. For thermal stable molecules (e.g. like the fullerene  $C_{60}$ ) heating by intense laser radiation leads to the ejection of one or several electrons from the molecule by thermionic emission [126,127]. A different approach is the use of hyper thermal-surface ionization [128,129], where neutral molecules are guided onto a specially prepared surface [130,131]. The kinetic en-

ergy of the molecules bridges the gap between the ionization potential and the work function of the surface. Chemical ionization (CI) can be used, based on a reaction between analyte molecules and ions from a reactant gas [132]. Since the ionization is reached by collision between the two particles, the involved kinetic energies are small, which reduces the possibility of fragmentation of the neutral molecule. This is why chemical ionization is called a 'soft ionization' mechanism, routinely used in analytical mass spectrometry [132, 133]. To enhance the ion production rate in a CI process, a high (gas) density of reactant ions is required as well as a strong beam flux of neutrals. In a matter-wave interferometer, the required gas pressures in the order of 100 Pa [134] would lead to a pressure gradient and gas drift towards the grating structure. Such a gas flow would eventually enhance the probability of collision decoherence, not compatible with a planned interferometry experiment. The other two prominent ionization mechanisms used in molecular beam experiments are electron impact ionization (EI) and photoionization (PI). In electron impact ionization the neutral molecules are bombarded by an electron beam, ejecting electrons from the neutrals in the collisions. Such a process involving the ejection of a single electron is represented by



with M being the analyte molecule in the process. This process is universal for molecular masses up to  $10^3$  Da and a wide range of molecules can be ionized this way, as long as they are in the gas-phase. Since the ionization efficiency curve has a maximum at about 70 eV electron kinetic energy, EI is typically operated with a kinetic energy in the range of 60-80 eV [135]. Since EI leads to many precursor fragments, this technique is a disadvantage when intact molecules are required.

In photoionization one or several photons of sufficient energy are used for the ejection of an electron from the neutral molecule. The process can be described by the following equation



where  $M^*$  denotes the excited analyte and  $M^+$  describes the charged content after photoionization (intact molecule or charged fragments). The absorbed energy from the photons must be at least as high as the ionization potential of the neutral molecule to allow the electron to escape into the continuum. This can be either in

a single step, the single-photon ionization process, or in multiple steps, the multi-photon ionization process. A schematic view of the different possible processes is shown in figure 3.1. Photoionization is known to be a soft-ionization process, especially in case of single-photon ionization.

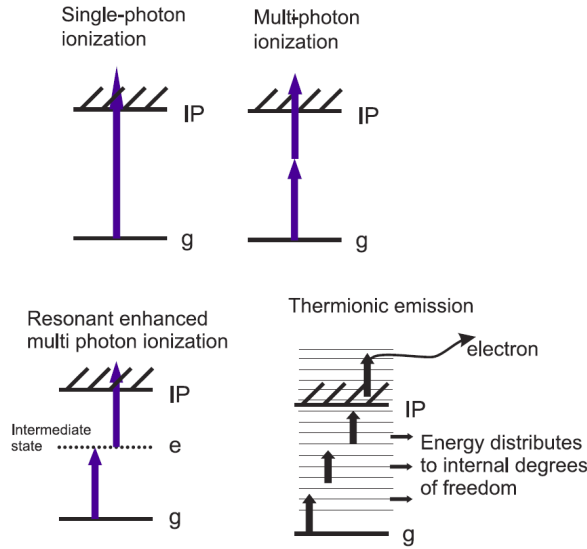


Figure 3.1: The different photoionization processes of a neutral molecule upon the absorption of a photon are shown. While in the single-photon ionization (SPI) a single photon is sufficient for the ejection of an electron, in multi-photon ionization the ionization threshold energy is achieved by the subsequent absorption of several photons. In resonant enhanced multi-photon ionization an intermediate state of the molecule is used to transfer the electron to the continuum (image from [136]).

### 3.2.1 Single-photon ionization

The single-photon ionization process is shown in the upper left corner of figure 3.1. In a compilation of ionization energies a large number of atoms and molecules show a ionization potential of the order of about 9 eV [137], which is especially the case for bio-molecules with typical ionization potentials greater than 8 eV [138–141] and saturation energies at about 20 eV [142]. For such a single-photon ionization process photons in the deep vacuum-ultraviolet (VUV) are required. Commercial available light sources in the VUV are  $F_2$  excimer lasers, emitting at a wavelength of 157 nm which corresponds to a photon energy of 7.89 eV. While this is not sufficient for many molecules, several organic molecules of interest for matter-wave interferometry like ZnTPP [143] or tryptophan [144] can still be photoionized by such energies.

For molecules requiring an ionization energy greater than the above mentioned 7.89 eV, chemical tags like anthracene or tryptophan can lower the overall ionization potential by the tagged molecule complex [145,146], which allows also SPI measurements with photons at a wavelength of 157 nm.

For ionization with even shorter wavelengths different types of light sources are available including VUV excimer lamps [147] which emit only incoherent light compared to an excimer laser but, on the other hand, have a broad emission spectrum between 100-200 nm. Other coherent, pulsed VUV light sources include laser light at 118 nm (10.5 eV) created by guiding 355 nm laser light (3<sup>rd</sup> harmonics of a Nd:YAG) through a cell filled with noble gases [148,149] which results typically in very low intensities in the order of  $\mu\text{W}$ . A different approach is the use of synchrotron radiation [138], soft x-rays [150,151] or the VUV light emission by free electron lasers [152,153].

The SPI yield of post-ionized molecules can be calculated by [154]

$$Y_{\text{SPI}}^+ = \sigma_{\text{PI}} I N \quad (3.3)$$

where  $\sigma_{\text{PI}}$  denotes the photoionization cross section and  $I$  is the intensity of the VUV light and  $N$  gives the density of desorbed molecules within the laser ionization volume. Equation 3.3 is valid as long as the ion signal does not reach saturation, which is typically not the case [154]. For more information on SPI a review on VUV single-photon ionization can be found in [155].

### 3.2.2 Multi-photon ionization

In case the ionization potential of the molecule is greater than the photon energy of the available light source, the absorption of more than one photon is required to push a bound electron into the continuum. Thereby, in multi-photon ionization, the sum of the photon energies must be greater than the ionization potential of the neutral molecule. This is depicted in the upper right corner of figure 3.1 as well as for the special case of resonant absorption, which is shown in the lower left corner. The absorption of multiple photons leads to the ejection of the electron by virtual internal energy levels of the molecule. Since absorption cross sections are low in this case, a high photon intensity is required. A different approach is the ionization of

the molecules by the resonance enhanced multi-photon ionization (REMPI) process, where the absorption of the first photon leads to the excitation of the molecule into an intermediate state and the absorption of a subsequent photon brings the electron into the continuum (in case of 1+1 REMPI). A precondition for REMPI is a stable intermediate state with sufficiently long lifetime to allow for the subsequent ionization. Since this is a resonant process lower laser intensities can be used compared to off-resonant multi-photon ionization.

For a number of small molecules the ionization process after the absorption of more than one photon was shown to be efficient [141]. With perfluorinated polyethers, a 2-photon resonance enhanced ionization was demonstrated also for molecules with a molecular weight up to 7 kDa [156]. Often wavelength tunable lasers are required, such as dye lasers, OPO or Ti:Sapph lasers.

In a multi-photon ionization process the absorption cross sections for the individual photons are independent and in most cases different from each other, determining the ionization probability of the neutral molecule. The resulting ion yield for a resonant two-photon process is given by [154]

$$Y^+ = \sigma_1 \sigma_2 I^2 N \quad (3.4)$$

$\sigma_{1,2}$  denote the two absorption cross sections of the two photons,  $I$  the laser intensity and  $N$  the density of the desorbed molecules within the ionization volume. The quadratic order of the laser intensity is a characteristic feature of two-photon ionization.

### 3.2.3 Photoionization of the porphyrin system

Porphyrin and especially tetraphenylporphyrin are interesting molecular systems for molecular matter-wave interferometry. While they are basic building blocks in chemical synthesis, they also fluoresce [157], which is an important molecular property for the detection in far-field diffraction experiments [42]. Furthermore it has good thermal properties which allow their thermal evaporation for creating a molecular beam, enabling matter-wave interference with these molecules [158]. Laser desorption as well as MALDI measurements were already performed on the basic

tetraphenylporphyrin (TPP) molecule and its derivatives [159], also electron impact ionization in the gas-phase [160] has been performed. In a recent work [59] it was demonstrated that perfluoroalkyl-functionalized tetra-phenyl porphyrin molecules with masses greater 10 kDa still showed a high contrast quantum interference pattern. As a consequence further experiments at an even higher mass range will be of interest for matter-wave interferometry.

In particular, OTIMA interferometry [2], operates with grating structures made by light pulses. This requires suitable photoionization properties of the molecular systems. The ionization energy of porphyrins in the ground state was found to be smaller than 7 eV [161], which allow the use of commercially available laser systems. Ion formation by multi-photon ionization in the UV [162] as well as SPI in the VUV range [143] have been demonstrated.

A functionalization of the stable TPP core by perfluoroalkylated sidechains increases the mass of the molecule while the photo-ionization properties (should) stay intact. If this last statement holds true, this molecular system would be a suitable candidate for interferometry. By increasing the number of sidechains and possibly adding TPP structures to the core, heavier molecules could be built with suitable optical properties for matter-wave interferometry with increased molecular weight. This motivated the current study, described in the following.

## Chapter 4

# An experiment investigating laser desorption and photoionization properties of complex porphyrin derivatives

The following chapter describes an experimental study of the UV laser desorption and VUV photoionization of functionalized TPP molecules. The main attention in the present work has been on the production of neutral molecular beams. The molecules were desorbed in a laser desorption source and afterwards photoionized by VUV light at 157 nm. Finally, the ions were detected in time-of-flight mass spectrometry (TOF-MS).

### 4.1 Fluorinated porphyrins

An overview over the structure of the different molecules studied is shown in figure 4.1. These molecules were TPPF<sub>84</sub> (1), TPPF<sub>120</sub> (2) TPPF<sub>(20-x+17x)</sub> (3), TPPF<sub>(20-x+26x)</sub> (4) as well as ZnTPP<sub>4</sub>F<sub>(60-x+17x)</sub> (5) and TPP<sub>4</sub>(TPP)F<sub>(60-x+17x)</sub> (6), where x denotes the number of C-F polymer sidechains in the molecule. While the first two compounds are monodisperse, all other molecules (e.g. (3)-(6)) are li-

braries, meaning that the compounds are mixtures with an identical molecular core but different numbers of side chains attached. The main reaction step in the synthesis process, done by J. Tüxen, L. Felix and M. Mayor (all University of Basel), is a nucleophilic aromatic substitution reaction on the tetrakis-pentafluorophenylporphyrin (TPPF<sub>20</sub>) by which the fluorine building blocks were introduced. Thereby carbon-fluorine chains replace the attached fluorine atoms primarily at the four para-positions of the TPP core. The fluorine atoms at other sites are subsequently replaced by the individual side chains. A detailed overview over the synthesis of the different molecular libraries can be found in [59, 163–165].

As displayed in figure 4.1, TPPF<sub>84</sub> has four individual side chains (denoted by R2), attached in para-positions to the TPP core. The sum formula of the molecule is C<sub>84</sub>H<sub>26</sub>F<sub>84</sub>N<sub>4</sub>S<sub>4</sub> and the molecular weight is 2815 Da. TPPF<sub>120</sub> has a similar structure as TPPF<sub>84</sub>, but with a double-ended side chain (R3) at the para-position of the TPPF<sub>20</sub> core. The resulting sum formula can be written as C<sub>124</sub>H<sub>38</sub>F<sub>120</sub>N<sub>4</sub>S<sub>4</sub>. Due to these differences in chemical structure, the average molecular weight is 3991 Da. For the molecular libraries (3) and (4) the para positions of the TPP core are occupied by a varying number of additional side chains R2 (3) and R3 (4) attached to the phenyl rings. For compound (3) a sum formula of TPPF<sub>(20-x+17x)</sub> = C<sub>44</sub>H<sub>10</sub>F<sub>20-x</sub>N<sub>4</sub>(S(CH<sub>2</sub>)<sub>2</sub>C<sub>8</sub>F<sub>17</sub>)<sub>x</sub> is calculated, while (4) is described by C<sub>44</sub>H<sub>10</sub>F<sub>20-x</sub>N<sub>4</sub>(SCH<sub>2</sub>CH((CH<sub>2</sub>)<sub>3</sub>C<sub>6</sub>F<sub>13</sub>)<sub>2</sub>)<sub>x</sub>. For compound (3) the most probable number of side chains is x = 14 with a respective molecular mass of 7417 Da. In the molecular library (4) the number of side chains spans from x = 9-12 with the highest intensity found for x = 11 with a mass of 9363 Da.

A different approach in the molecular synthesis was taken for compounds (5) and (6): Since a higher number of chromophores enhances the VUV photoionization cross section of the molecule [166], the central part of the molecule was changed to a tetra-phenyl unit (5) and a TPP molecule (6). This core was used for linking the outer structure based on a four-fold porphyrin system, in case of structure of (5) ZnTPP units were bound to the periphery of the molecule. The most abundant number of side chains in the molecular library of compound (5) has an x=17 (R(ZnTPP)<sub>4</sub>F<sub>357</sub>) with a mass of 11,676 Da. For compound (6) the maximum of side chains peaks at x = 40 which corresponds to the molecule TPP(TPP)<sub>4</sub>F<sub>765</sub> having a mass of 22,152 Da.

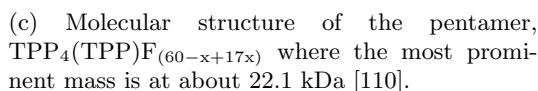
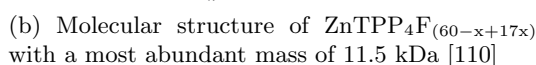
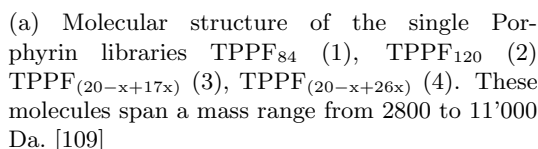


Figure 4.1: The molecular structures of the fluorinated porphyrin derivatives is shown. While the central core is identical for compounds (1)-(4)(4.1a), the number and composition of the side chains ('R') differs between the different molecules. In contrast to these molecules, the molecular library (5) (4.1b) is built from a central tetra-phenyl unit which links the four ZnTPP molecules. The outer four porphyrins in the molecular library (6) (4.1c) have again a TPP structure without the metal atom. Also the central binding structure is built from a TPP as well. These molecules were synthesized by J. Tüxen, L. Felix and M. Mayor (all University of Basel).

In the LD-SPI experiments described in the following all compounds - the chemically pure TPPF<sub>84</sub> and TPPF<sub>120</sub> as well as the different libraries - were used.

## 4.2 Experimental setup

For the measurement of the VUV photoionization properties of these molecules a dedicated TOF-MS beam line was set up, as shown in figure 4.2. Samples were pre-

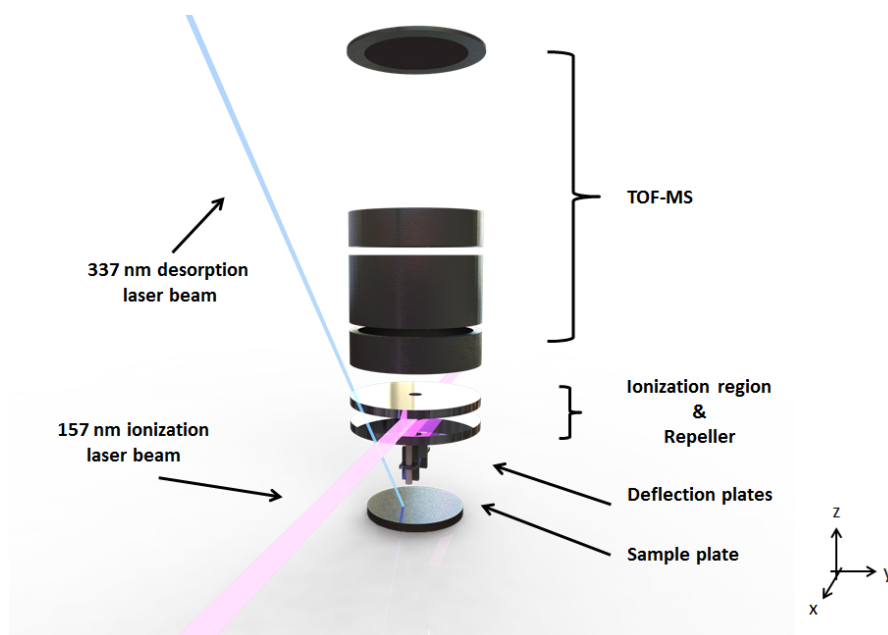


Figure 4.2: The molecular beam line for laser desorption and photoionization of porphyrin derivatives. The molecules are released from the sample plate by UV laser desorption and pass through a pair of deflection electrodes on their way to the ionization region. There 157 nm laser light ionizes the molecules and the cations are detected by a TOF-MS.

pared by dissolving the molecules in an appropriate solvent: Acetone for compound (1), (2) and ether for (3) and (4). For dissolving of molecular libraries (5) and (6) diethyl ether and butyl methyl ether were required as solvent, respectively. The LD sample consisted of a stainless steel plate, which was coated with the analytes, using the 'dried droplet' method [101]. Since neutral molecules were required, no acidic matrix was added.

UV laser desorption was used for the formation of a molecular beam: Thereby the laser beam from a nitrogen laser ( $N_2$ ) operating at 337 nm (VSL-337, Laser Innovations) was directed onto the sample plate under an angle of  $30^\circ$  to  $45^\circ$  degree. The

exact angle was dependent on the specific experimental setup. To create a dense particle beam, a laser pulse energy of about  $250 \mu J$  was focused on the surface of the sample. For compound (1)-(3) a convex lens with a focal length of  $f=+1000$  mm was implemented and the laser spot was focused down to  $w_x = 0.95$  mm and  $w_y = 1.2$  mm. The molecular library (4) was desorbed by using a focal spot size of  $w_x = 0.63$  mm and  $w_y = 1.55$  mm, created by a  $f=+300$  mm convex lens. A lens with even shorter focal length of  $f=+50$  mm was utilized for compounds (5), (6) which resulted in a laser spot size of  $w_x = 1.5$  mm and  $w_y = 0.5$  mm. The LD sample was mounted on a translational stage in such a way that a new sample spot was hit by each laser shot during the desorption process, helping to keep sample fluctuations on the recorded signal small.

After desorption the molecular plume was guided through two deflection plates (for measurements with (1) - (4)) set to appropriate high DC potential prior to the entrance into the ionization region of the TOF-MS to filter the ions from the LD plume. By deflecting the charged molecules of the plume the background signal in the mass spectrometer was reduced. The neutral molecule fraction entering the repeller region of the TOF-MS was photoionized by a pulsed VUV  $F_2$  excimer laser beam (EX5, GAM Inc.) The  $F_2$  laser operates at a wavelength of 157.6 nm with a pulse length of 5 ns and a maximal pulse energy of 1.5 mJ focused into a rectangular beam shape with the dimensions of about 1x8 mm ( $8 \times 0.6$  mm in case of *TPPF84/TPPF120/TPPF<sub>20-x+17x</sub>* and  $10.2 \times 0.4$  mm for *TPPF<sub>20-x+17x</sub>*). To reduce intensity losses, the laser beam path to the TOF-MS was purged with dry nitrogen and an anti-reflex coated  $CaF_2$  window was placed at the entry point of the vacuum chamber.

The formed cations were accelerated into the TOF-MS (Kaesdorf,  $m/\Delta m = 100$ ,  $U_{acc} = 18$  kV) and detected on a triple MCP, stacked in Chevron geometry. To decrease statistical fluctuations in the recorded signals, each mass spectrum was averaged over 16 to 30 laser desorption shots, depending on the molecule.

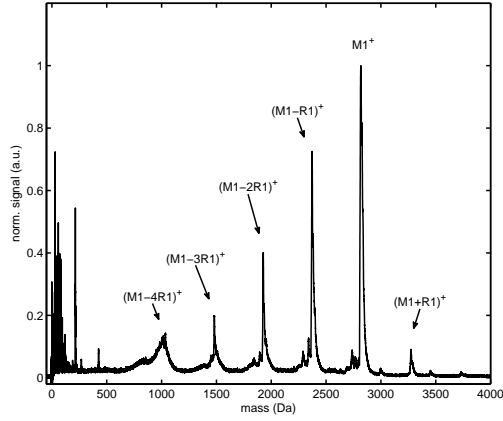
## 4.3 Experimental results

### 4.3.1 Mass spectra of perfluoroalkyl-functionalized porphyrin derivatives

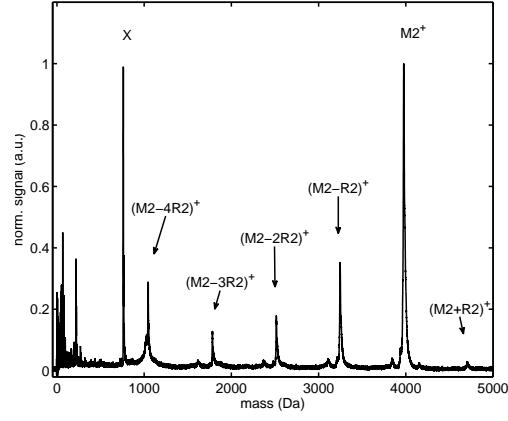
The mass spectra of the samples (1) - (4) as well as the molecular libraries (5), (6) are shown in figures 4.3 and 4.4. Generally, in all mass spectra the relative peak intensities depend on the delay time between the desorption  $N_2$  and  $F_2$  ionization lasers, e.g. the delay time after which volatilized molecules are ionized. Fragments are predominantly observed at a shorter delay time which corresponds to faster velocities of these low-mass ions. Intact molecules, having lower velocities, are mainly observed at longer delay times. This behavior is clearly shown by the velocity distributions in figure 4.5. The observed difference in the velocities could be an indication that a thermal fragmentation of the intact molecules is induced during the desorption process. For the fast and therefore, under the assumption of thermalization, hot molecules the correlation between internal and external degrees of freedom is a consequence of the higher internal temperatures and therefore of the fragmentation probability.

The mass spectra of TPPF<sub>84</sub> (figure 4.3a) shows the intact cation (M1) at a mass of about 2820 Da. Apart from the intact molecular ion several fragment peaks (denoted as  $M1 - (R1 - S)$  till  $M1 - 4 \cdot (R1 - S)$ ) are visible. The spacing corresponds to the mass of one single side chain, representing a loss of an individual fluoroalkylsulfonyl chain at the sulfur atom (see figure 4.1 for more details). Additionally, a cluster at higher mass than the intact molecular mass can be observed in the spectrum (M1+R1 in figure 4.3a) with a mass difference corresponding to the mass of a single side chain. The cluster (M1+R1) can only be explained by cluster formation in the desorption plume, because initial cross-reference analyte samples did not show this mass or any higher one in independent MALDI-TOF measurements [167]. Since such clusters were not detected in control measurements without photoionization laser, it seems that the clusters emerge from neutral molecules.

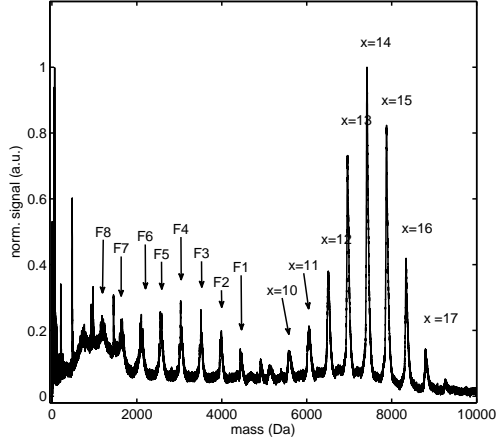
The mass spectrum of the second pure perfluoroalkyl-functionalized TPP molecule, TPPF<sub>120</sub>, gives a similar picture: In figure 4.3b the intact precursor ion (M2) is visible in addition to four distinct fragments  $[(M2 - R2) \text{ to } (M2 - 4R2)]$ . Again



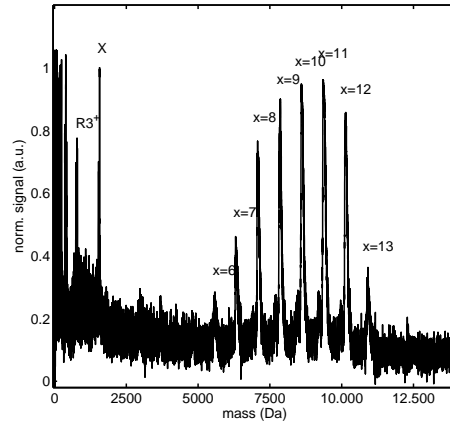
(a) The mass spectrum of TPPF<sub>84</sub>, showing intact molecule (M1) and individual side chains (M1-R).



(b) TPPF<sub>120</sub> shows a similar behavior in its mass spectrum. The intact molecule (M2) and its fragments (M2-R) are visible.



(c) Mass spectrum of the molecular library TPPF<sub>(20-x+17x)</sub> displays the variation of attached side chains (x=10-x=17) and clustering of individual side chains (F1-F8).



(d) A similar mass spectrum is observed for molecular library TPPF<sub>(20-x+26x)</sub>. The variation of the side chain is clearly visible (x=6-x=13).

Figure 4.3: Mass spectra of different perfluoroalkyl-functionalized TPP compounds ((1)-(4) in figure 4.1). In all spectra the ionization energy was kept identical to the maximal pulse energy of the  $F_2$  ionization laser. The delay time between the desorption process and the ionization laser was set to the maximum of the velocity distribution of the molecular plume, since peak intensities depended on the velocities of the molecules. Images taken from [109].

this can be explained similar to the case of TPPF<sub>84</sub> by a splitting of the side chains from the intact molecule. But compared to the previous mass spectrum an additional low-mass peak at a mass of about 760 Da is visible (X in figure 4.3b), which is consistent with the mass of a single side chain apart the sulfur atom, e.g.  $[R^3 - S]^+ = CH_2CH((CH_2)_3C_6F_{13})_2$ . On the high mass side of the spectrum the

cluster-formation of the intact precursor with an additional side chain ((M2+R2) in figure 4.3b) is seen, allowing for a similar hypothesis as previously.

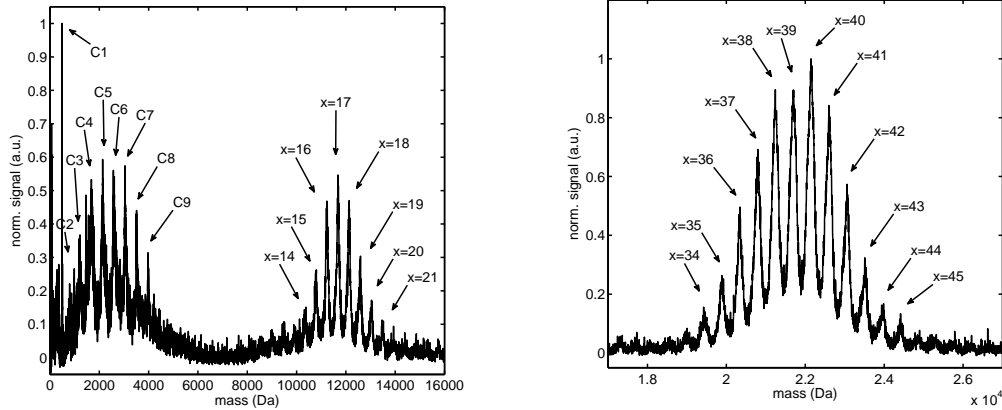
The mass spectrum of the first molecular library  $\text{TPPF}_{(20-x+17x)}$  ((3) in figure 4.1), reflects a distinct peak pattern of the side chain abundances as a result of the synthesis process of this molecule group. All molecules have an identical molecular TPP core, but a variable number of side chains R2 attached. The recorded spectrum shows a typical mass distribution with the number of side chains ranging from  $x=10$  to  $x=17$  with the most abundant for  $x=14$ . Each of the peaks represents one intact isomer, differing from the neighbors by the weight of one single side chain minus a single fluorine atom. In the mass spectrum, a fragmentation of the intact molecule is observed as well (F1-F8). Thereby each of these peaks has a mass difference of about  $478 \pm 40$  Da, which represents a cluster of side chains without the central TPP core.

The mass spectrum of the molecular library  $\text{TPPF}_{(20-x+26x)}$  (figure 4.3d) gives a similar spectra to the one of  $\text{TPPF}_{(20-x+17x)}$ . The side chain distribution observed runs from  $x=6$  to  $x=13$ , with  $x=11$  as the most probable number of attached side chains. Similar to the spectrum of  $\text{TPPF}_{120}$ , a single side chain can also be observed (R2) in figure 4.3d. But in comparison to  $\text{TPPF}_{(20-x+17x)}$  no clustering of side chains is seen, which is in contrast to molecular libraries having a linear side chain (see figures 4.1).

The porphyrin tetramer (figure 4.1b) and porphyrin pentamer (figure 4.1c) display a similar structure in the mass spectrum to the molecular library of the single TPP structure.  $\text{ZnTPP}_4\text{F}_{(60-x+17x)}$  (figure 4.4a) shows a distribution of eight well resolved mass peaks in the spectrum which correspond to the identical core with a varying number of side chains from  $x=14$  to  $x=21$ . Thereby the most probable number of side chains is  $x=17$ , corresponding to a mass of about 11,680 Da. The spacing between the different mass peaks is again  $450 \pm 10$  Da, indicating the mass of a single side chain (479 Da) minus a fluorine atom. On the low mass side of the spectrum a regular spaced distribution by  $457 \pm 18$  Da between two neighboring mass peaks (C1-C9) assumes a clustering of side chains also for this molecular library. Thereby C1 represents a single intact side chain followed by higher clusters of side chains.

The mass spectrum of  $\text{TPP}_4(\text{TPP})\text{F}_{(60-x+17x)}$  (figure 4.4b) shows an identical pattern to the spectra of the previous described libraries. For improved mass resolution

only the high end of the mass spectrum is displayed in figure 4.4b showing the characteristic side chain distribution ranging from  $x=34$  to  $x=45$  with the most prominent one at  $x=40$ . At the lower mass end of the spectrum a clustering of side chains can be seen again, similar to the ones shown in figure 4.3d. The results from



(a) Mass spectrum of ZnTPP<sub>4</sub>F<sub>(60-x+17x)</sub>, with the number of side chains spanning from  $x = 14-21$ .

(b) The mass spectrum of the molecular library TPP<sub>4</sub>(TPP)F<sub>(60-x+17x)</sub> with the number of side chains varying from  $x = 34-45$  is shown.

Figure 4.4: Recorded mass spectra of different perfluoroalkyl-functionalized TPP compounds: In all spectra the ionization energy was kept identical to the maximal pulse energy of the ionization laser. The delay time between the desorption and ionization laser was set to the maximum of the velocity distribution of the molecular plume since the peak intensities depended on the velocities of the molecules. Images taken from [109,110].

this experiment demonstrate that certain organic molecules with masses of up to 25 kDa are suited for photoionization if they display molecular structures as in the case of fluorinated porphyrins. This will be of interest not only for matter-wave interferometry where photoionization is a fundamental requirement (e.g. absorptive optical gratings [2]) but also in the detection stage of any neutral molecular beam experiment (like deflection experiments [168]).

### 4.3.2 Velocity distributions of laser-desorbed perfluoroalkyl - functionalized TPP libraries

In chapter 4.3.1 the volatilization of complex perfluoroalkyl-functionalized TPP molecules was shown. Another interesting aspect are the initial velocities of the molecules after volatilization, important in matter-wave interferometry experiments.

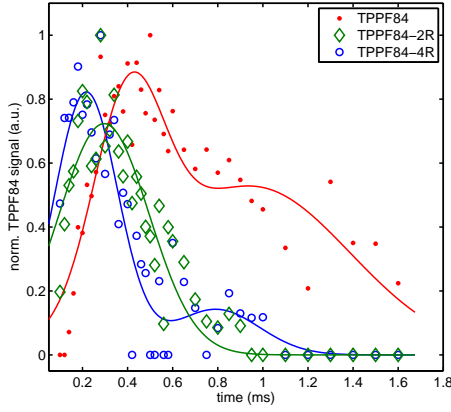
In matter-wave interferometry the wavelength of the particle is defined by the de Broglie wavelength,  $\lambda_{dB} = h/mv$ , which is inversely proportional to the velocity of the molecule. Current interferometers are compatible with a particle wavelength of  $\lambda_{dB}=300$  fm [2], which would require velocities in the order of 100 m/s in case of the molecular libraries  $\text{TPPF}_{(20-x+26x)}$  and below 50 m/s in case of  $\text{TPP}_4(\text{TPP})\text{F}_{(60-x+17x)}$ . Also other classical molecular beam experiments like molecular deflection [169,170] requires slow molecular velocities as well.

In the current experiment the molecular velocity distribution was recorded by measuring the time delay between the desorption and the ionization laser.

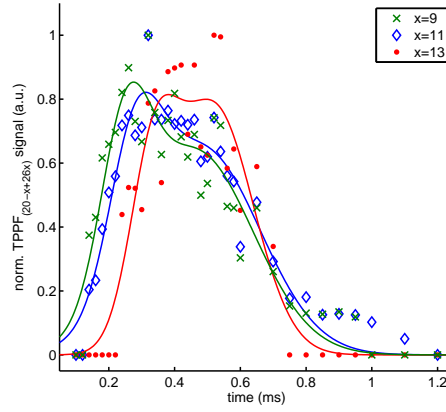
The smallest TPPF structure tested ( $\text{TPPF}_{84}$ ) shows a bi-modal, non-thermal velocity distribution (figure 4.5a) which can be fitted best by the sum of two Gaussian distributions, with the two most probable velocities of about  $v_{mp}=75$  m/s and  $v_{mp}=180$  m/s. In case of the lighter fragment ions a similar velocity distribution can be observed. A clear molecular size-dependent velocity slip can be observed, where the flight times of the fragment masses scales proportional to  $m^{1/2}$ . For the intact molecule the scaling factor is deviating from the this proportional factor. For the intact precursor ion a broad tail towards higher flight times is seen in the distribution, which shows that for  $\text{TPPF}_{84}$  strong molecular signals with velocities below 100 m/s are obtained.

A similar trend is observed for  $\text{TPPF}_{(20-x+26x)}$  (figure 4.5b) which shows a bi-modal, non-thermal Gaussian distribution, resulting in most probable velocities of about  $v_{mp}=150$  m/s,  $v_{mp}=260$  m/s and  $v_{mp}=140$  m/s,  $v_{mp}=215$  m/s respectively (for  $x=11$  and  $x=13$ ). The number of side chains in more complex porphyrin molecules obviously leads to slower velocities (figure 4.5b). This is shown in more detail in figure 4.6 for different number of sidechains present in the  $\text{TPPF}_{(20-x+26x)}$  library. Here a slip towards slower velocities with increasing molecular weight can be observed. Similar to  $\text{TPPF}_{84}$  a large fraction for velocities smaller than 130 m/s is detectable.

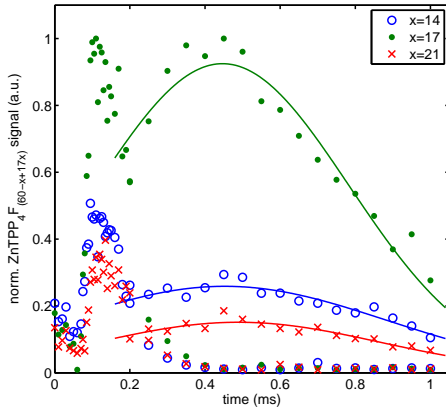
A similar spread of velocity can be observed in the case of the molecular libraries  $\text{ZnTPP}_4\text{F}_{(60-x+17x)}$  and  $\text{TPP}_4(\text{TPP})\text{F}_{(60-x+17x)}$ , shown in figures 4.5c and 4.5d. The fast fraction can be assigned to ions created in the desorption plume and was also observed when the  $F_2$  ionization laser was not in operation. Apart from the fast ions the data (figures 4.5c,4.5d) show a broad flight time distribution towards longer



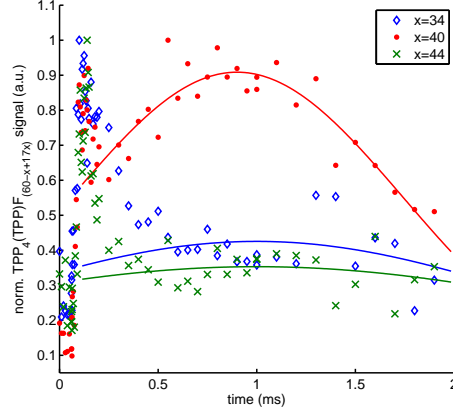
(a) Flight time distributions of the intact molecule (TPPF<sub>84</sub>) as well as two fragments (TPPF<sub>84</sub>-2R, TPPF<sub>84</sub>-4R)



(b) Time of flight curves of the desorbed molecular library TPPF<sub>(20-x+26x)</sub>. A relation between the number of attached side chains and molecular velocity can be identified.



(c) In the flight time distribution of the porphyrin tetramer two distinct peaks can be identified. While the slow component is attributed to the neutral molecules, the fast components are from ions created in the desorption process.



(d) For the porphyrin pentamer as similar time of flight distribution is observed. Again the initial ions from the desorption process can be observed as fast components of the time of flight distribution.

Figure 4.5: The velocity distribution of selected TPPF molecules are shown. This includes the lightest molecule TPPF<sub>84</sub> (figure 4.5a) as well as the molecular library TPPF<sub>(20-x+26x)</sub> (figure 4.5b). Furthermore the velocity distribution of the porphyrin tetramer and pentamer are presented (figure 4.5c,4.5d). All data are fitted by Gaussian distributions which are drawn as a guide for the eye. Generally strong signal strength can be observed even for velocities smaller than 100 m/s.

flight times, describing the photoionized neutrals. The fast ions are described best by a Maxwell-Boltzmann distribution, while the slow part is fitted by a Gaussian, the latter is shown as a guide to the eye. From the Gaussian fits a most probable velocity of  $v_{mp} = 90$  m/s can be deduced for the porphyrin tetramer and  $v_{mp} = 46$

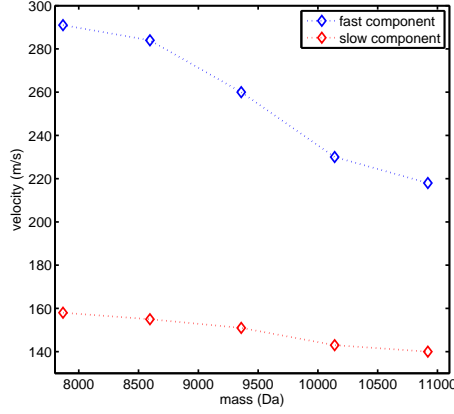


Figure 4.6: The extracted velocities of the intact molecules from the TPPF<sub>(20-x+26x)</sub> library are plotted against the mass for different numbers of sidechains present in these two libraries. A slip towards smaller velocities for increasing mass can be observed (within the library).

m/s for the porphyrin pentamer. The broad tail of the data towards longer flight times show that a substantial amount of signal is still present for velocities below 40 m/s (ZnTPP<sub>4</sub>F<sub>(60-x+17x)</sub>) and even below 20 m/s (TPP<sub>4</sub>(TPP)F<sub>(60-x+17x)</sub>). In comparison to the previous discussed time of flight distribution of TPPF<sub>(20-x+26x)</sub> no significant velocity shift towards slower velocities in dependence of the number of side chains can be observed for TPP<sub>4</sub>(TPP)F<sub>(60-x+17x)</sub>.

### 4.3.3 Ionization cross sections

In matter-wave interferometry a high photoionization cross section is required as well. The current OTIMA setup [2] requires a single-photon ionization cross section greater than  $5 \times 10^{-17} \text{cm}^{-2}$  [171] to ensure that the light grating is an absorptive structure for the passing particle beam. To test the ionization cross section of TPP derivative structures, the time delay between desorption and ionization was set to a fixed value corresponding to the highest observed signal and the 157 nm laser intensity was varied.

For the first four TPPF molecular libraries measured in this thesis ((1)-(4) in figure 4.1) the ionization process can be approximated in first order as a single photon process by the following equation [172]

$$S_{\text{PL}} = \rho \Delta V T \cdot (1 - \exp(-\frac{\sigma \Delta t P_{\text{L}}}{h\nu})) \quad (4.1)$$

where  $\rho$  is the number density of neutral species within the ionization volume  $V$ ,  $T$  denotes the transmission and detection efficiency of the TOF-MS,  $\sigma$  the ionization cross section, the laser power density ( $P_L$ ) with frequency  $\nu$  and the pulse duration  $\Delta t$ . Equation 4.1 can be used to describe our recorded data, provided that the laser intensity is high enough to drive the ion signal into saturation [173]. In this case the influence of different photoionization cross sections on the detection efficiency is eliminated.

Similarly to the velocity measurements, the ionization cross sections were determined for the lightest and heaviest single-TPP derivatives (TPPF<sub>84</sub>, TPPF<sub>(20-x+26x)</sub>) as well as the TPP tetramer and pentamer (ZnTPP<sub>4</sub>F<sub>(60-x+17x)</sub>, TPP<sub>4</sub>(TPP)F<sub>(60-x+17x)</sub>). The first two compounds show steady increasing signal strengths for low laser pulse energies while for more intense laser powers the signal saturates (figure 4.7), which is well described by the equation 4.1. From these data a fit for both molecules allows a

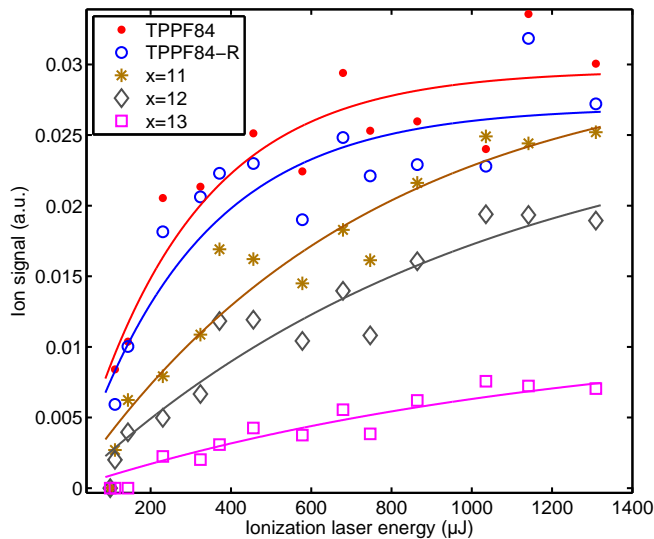


Figure 4.7: A variation of the VUV laser energy allows the determination of the ionization cross sections of the perfluoroalkyl-functionalized TPP derivatives TPPF<sub>84</sub> and TPPF<sub>(20-x+26x)</sub> ( $x=11$  to  $x=13$ ). From fits (solid lines) after equation 4.1 a single-photon ionization process can be assumed. Image adapted from [109].

calculation of the photoionization cross section of  $\sigma > 5 \times 10^{-17} \text{ cm}^{-2}$ . A summary of the ionization cross sections from TPPF<sub>84</sub>, TPPF<sub>(20-x+17x)</sub> and TPPF<sub>(20-x+26x)</sub> are found in table 4.1. The resulting cross-sections show that the higher the complexity of the molecules within its own library, the greater is its resulting photoionization cross section.

The number of absorbed photons  $N_{\text{abs}}$  from a molecule with a specific absorption

molecule	$\sigma(10^{-17}\text{cm}^{-2}) (\Delta\sigma)$
TPPF84	18 (1.8)
TPPF84-R	17 (1.8)
TPPF84-2R	14 (1.6)
TPPF84-3R	9 (1.5)
TPPF84-4R	4 (2)
TPPF <sub>(20-x+17x)</sub>	
x=10	$4 \times 10^{-2}$ (6)
x=11	$5 \times 10^{-3}$ (4.5)
x=12	1 (4)
x=13	5 (5)
x=14	7 (6)
x=15	8 (6)
x=16	9 (6.5)
x=17	10 (7)
TPPF <sub>(20-x+26x)</sub>	
x=9	2 (0.5)
x=10	5 (0.6)
x=11	7 (0.8)
x=12	5 (0.8)
x=13	5 (1)

Table 4.1: The ionization cross section of TPPF<sub>84</sub> (and its major fragments) as well as of the molecular libraries TPPF<sub>(20-x+17x)</sub> and TPPF<sub>(20-x+26x)</sub> are given.

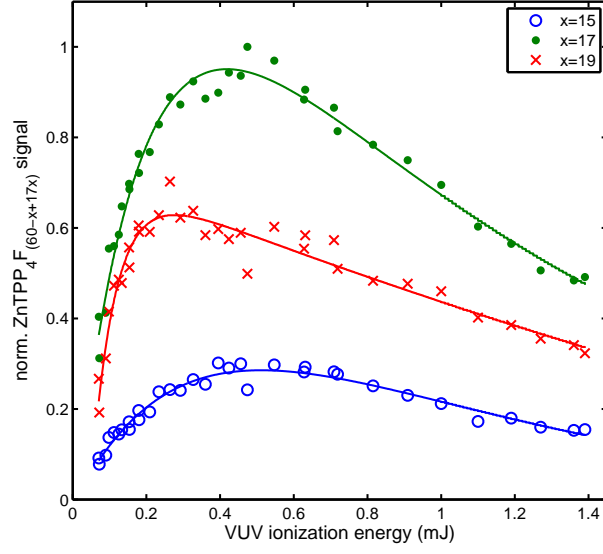
cross section can be estimated by

$$N_{\text{abs}} = \frac{\sigma_{\text{abs}} E_L}{\pi \omega^2 h \nu} \quad (4.2)$$

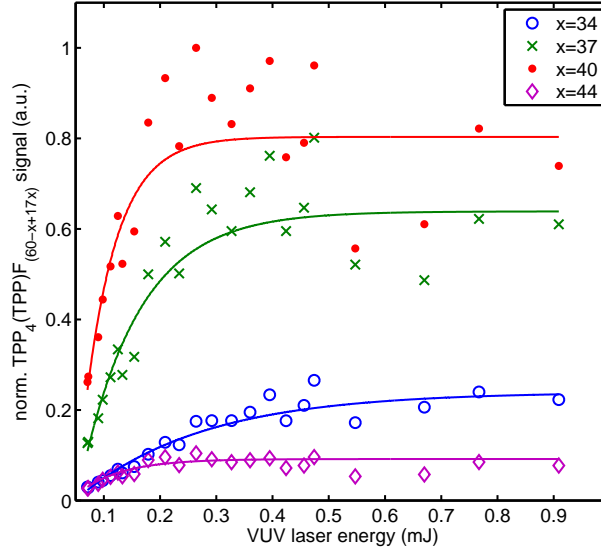
where  $E_L$  denotes the energy of the laser,  $\omega$  is the beam waist,  $\sigma_{\text{abs}}$  and  $\nu$  is the laser frequency.

With the absorption cross sections given above,  $N_{\text{abs}}$  is in the order of about 4 (for TPPF<sub>84</sub>) and 2 (for TPPF<sub>(20-x+17x)</sub>, TPPF<sub>(20-x+26x)</sub>) photons/pulse.

The TPP<sub>4</sub>(TPP)F<sub>(60-x+17x)</sub> library shows an increase of signal with laser intensity and a leveling-off similarly to the case of TPPF<sub>(20-x+26x)</sub>. In comparison, different results are seen for the TPP tetramer, shown in figure 4.8. This library shows an increased cross section with increasing VUV laser intensity until the saturation point is reached at about 400  $\mu J$ , followed by a decrease of the signal intensity, which can be explained by an increased photon-induced fragmentation of the molecule with



(a) VUV ionization dependence of  $\text{ZnTPP}_4\text{F}_{(60-x+17x)}$



(b) VUV ionization dependence of  $\text{TPP}_4(\text{TPP})\text{F}_{(60-x+17x)}$

Figure 4.8: The TPP tetramer  $\text{ZnTPP}_4\text{F}_{(60-x+17x)}$  (4.8a) and TPP pentamer  $\text{TPP}_4(\text{TPP})\text{F}_{(60-x+17x)}$  (4.8b) show a different behavior in their ionization properties. The tetramer signal decreases with increasing VUV laser energy which shows the onset of a photon-induced fragmentation process. In comparison, the TPP pentamer reaches a plateau when high 157nm laser energies are used. Adapted from [110]

higher light intensities. In comparison the  $\text{TPP}_4(\text{TPP})\text{F}_{(60-x+17x)}$  library shows an increase of signal with laser intensity and a leveling-off similar to the case of  $\text{TPPF}_{(20-x+26x)}$ .

In figure 4.7 another interesting feature can be observed. In the discussion on the mass spectrum of  $\text{TPPF}_{84}$  and  $\text{TPPF}_{(20-x+26x)}$  the source of fragmentation of the molecule could not be proven in a satisfactory manner. Since all masses plotted in figure 4.7 show an equal increase with increasing ionization energy, it suggests that the molecular fragments are produced mainly in the desorption process.

## Chapter 5

# Conclusion and discussion

This chapter presents results on laser desorption and photoionization (LD-PI) of complex organic molecules with molecular weights up to 25 kDa. In the experiments the neutral fraction of the desorbed LD plume was subjected to a post-ionization process by VUV laser radiation at 157 nm before detecting the produced ions in a time-of-flight mass spectrometer.

In these measurements perfluoroalkyl-functionalized tetraphenylporphyrin (TPPFx) molecules of different molecular structure and weight were used. These included not only chemically pure structures (like TPPF<sub>84</sub>) but also molecular libraries with variable numbers of side chains and different core structures (see figure 4.1 for more details).

A neutral molecular beam was produced by matrix-free laser desorption, post-ionized by the VUV ionization laser. From the recorded mass spectra only moderate fragmentation can be seen. For the cases where an overall increase in signal with increasing ionization energy can be observed, the fragmentation is occurring mainly during the desorption phase of the analytes. By varying the time delay between the desorption and ionization process the velocity distributions were determined, showing that the molecules were subject to a thermal desorption process with resulting velocities below 20 m/s. By changing the power of the ionization laser the photoionization cross sections of selected perfluorinated TPP compounds can be measured, showing a single-photon ionization behavior with cross-sections greater than  $\sigma > 1 \times 10^{-17} \text{ cm}^2$ .

### Coupling to a matter-wave interferometer

The final goal of the presented laser desorption study was to determine the suitability of LD-PI with TPPF molecules for matter-wave interferometry. Currently there are two operational near-field interferometers: the Kapitza-Dirac Talbot-Lau Interferometer (KDTLI) [44,174] is best suited for operating with continuous molecular beams. The OTIMA interferometer [2] uses pulsed light gratings, operating best with pulsed sources.

For coupling LDI to an interferometer OTIMA seems to be the optimal choice. The overall interferometer length of the OTIMA is only about 5 cm with no material gratings (in comparison to the KDTLI), which should increase the total beam flux. By mounting the particle source (e.g. the desorption sample) closer to the vicinity of the first grating, the overall length of the interferometer is reduced. Since OTIMA operates with timely pulsed gratings also pulsed particle sources can be readily coupled to the interferometer. Another advantage of the OTIMA setup is the intrinsic integration of photoionization during the particle detection, which will enhance the ionization efficiency, compared to the  $10^{-2} \dots 10^{-4}$  in case of electron impact ionization. A pulsed VUV light source can be well combined with the pulsed laser desorption source.

In a matter-wave interferometer from the OTIMA type optimal results are achieved when the particles are single-photon ionizable [2] at the grating wavelength. Although a recent theoretical work (unpublished) showed that also a two-photon absorption will allow the observation of quantum interference. When the molecules show photon-induced fragmentation in the grating [175], also this process can be used in the OTIMA. For the TPPF libraries the exact ionization potential is not known, but can be extrapolated from regular TPP. For the single TPP molecule the ionization is about 6.4 eV [161], which is well below the 157 nm VUV photon energy of 7.89 eV. For the TPPF libraries this is in accordance with the measured single-photon ionization curves (see figures 4.7,4.8) which also show that the TPPF libraries can be photoionized rather well at 157 nm, since saturated ion signals are observed for high VUV pulse energies. More work has to be invested into the optimization of the source design and the overall increase of the desorption efficiency (e.g. like sample preparation).

Finally, TPPFx molecular libraries in combination with a laser desorption source

could push the current mass limit in matter-wave interferometry towards higher mass ranges and more complex particles in an OTIMA type experiment. Since these molecular libraries show suitable desorption and photoionization properties, it might be interesting to push the mass limit of these molecular systems further. In a first step this might be possible by adding additional sidechains to the the molecular structure shown in figure 4.1b or 4.1c. Also the use of a double-strand chain similar to  $\text{TPPF}_{(20-x+26x)}$  could help in increasing the overall mass in such molecular libraries. In a further step one could envision also a replacement of the core in the molecular structure 4.1c: If instead of a TPP molecule small metal clusters are used, it should be possible to reach masses greater than  $10^5$  Da in such molecular libraries systems. Since the outer TPPF structures are still bonded to this new core, the photoionization properties should be intact.

## PartIII

### Ion traps for molecular studies

## Chapter 6

# Linear quadrupole ion traps

To push matter-wave physics to higher mass, cold and slow molecules are required. While desorption of functionalized molecules may eventually lead up to the lower 100 kDa range, interferometry experiments in the range of MDa and beyond require different sources. A low particle velocity is required, as can be seen by the de Broglie wavelength  $\lambda_{dB} = h/(mv)$ , but also the internal temperature of the molecules needs to be reduced. Otherwise the possible emission of thermal radiation could lead to decoherence [176]. To suppress vibrational photons it will be sufficient to equilibrate all internal states at 77 K. Cooling down to cryogenic temperatures of about 10 K shall reduce the particle velocity,  $v = \sqrt{(2k_B T)/m}$ , to about 1 m/s for  $10^6$  Da particles, i.e. values compatible with OTIMA interferometry.

As a new source for the creation of cryogenic particle ensembles an ion trap was pursued in this thesis. This device possesses several advantages:

- Compared to neutral molecules, ions have the advantage that they can be controlled more easily. Long-term trapping can be achieved independent of the internal molecular state. A neutralization mechanism could be implemented for instance via electron photodetachment of singly, charged anions [177].
- A quadrupole ion trap has the advantage of being mass selective. This allows to clean the molecular beam before the matter-wave interferometer.
- Since stable long-term trapping is readily achieved, it allows an efficient cooling of the ions in a buffer gas, even at low pressure.

In the following we will describe the design and setup of the linear quadrupole ion trap in our laboratory. Initial results will be presented as well as investigations into a new possible cooling mechanism for singly charged ions in the mass regime greater 1 MDa.

## 6.1 Overview over the fundamental ion trap parameters

Ion traps are unique tools, since they allow the confinement of ensembles or single particles over long time periods [178], covering a broad experimental field in both, chemistry and physics. The list of possible applications is long, covering mass spectrometry [179, 180], atomic and molecular cooling [181–183], quantum information processing [184], molecular spectroscopy [185], atomic clocks [186], nuclear physics [187] as well as investigations of antimatter [188].

To create a stable trapping field, electric and magnetic fields may be used. The Earnshaw theorem, based on the Laplace Equation  $\nabla^2\Phi = 0$ , states that electrostatic fields alone may only create saddle potentials but no stable trapping conditions in free space. By combining a static magnetic and an electric field or by alternating electrical fields stable trapping becomes feasible.

An electrostatic setup in a two-dimensional quadrupolar field will have only a confinement force in one direction (say along  $x$ ) but not simultaneously in both trapping axes. If an axial, static magnetic field is added, an additional confinement force is provided by the Lorentz force. Such a field configuration is realized in Penning traps, invented by Dehmelt [189]. Since in this case the ion trajectories are governed by the cyclotron frequency,  $\omega_{\text{cyc}} = eB/m$ , such confinement is mainly used when either trapping electrons, light or highly charged ions. Otherwise strong magnetic fields of several Tesla and beyond are required. An excellent written review on Penning traps and single particle physics can be found in [190].

In contrast to that, ion traps may exploit time varying electric potentials. This was first realized by Wolfgang Paul et al. [191, 192] using two-dimensional confinement fields,  $\Phi \propto x^2 - y^2$  (mass filter) or in all three dimensions,  $\Phi \propto r^2 - 2z^2$  (Paul trap).

A strong restoring force pushes the ions back towards the center of the field.

In a multipole expansion of the electric field, the first term showing a potential minimum in the center of the charge distribution is the quadrupole term. The potential

at any point then depends on the square of the distance from the origin.

In such a device the potential can be described by

$$\Phi(x, y, z) = A(\lambda x^2 + \sigma y^2 + \gamma z^2) + C \quad (6.1)$$

where A is a constant, C a fixed potential (either RF or DC) and  $\lambda, \sigma, \gamma$  are weighing factors. Since the electric field has to fulfill the Laplace equation in vacuum

$$\Delta\Phi(x, y, z) = 0 \quad (6.2)$$

it follows for equation 6.1

$$\Delta\Phi = A \cdot (2\lambda + 2\sigma + 2\gamma) \quad (6.3)$$

Since A is typically nonzero, the factors  $\lambda, \sigma, \gamma$  will comply with this equation by

$$\lambda = -\sigma, \gamma = 0 \quad (6.4)$$

$$\lambda = \sigma = 1, \gamma = -2 \quad (6.5)$$

Thereby the first line describes the condition for a linear quadrupole, while the second set is used for describing a three-dimensional quadrupole field structure. Since only two-dimensional quadrupole fields were used in this work, the three-dimensional case is not discussed any further.

### 6.1.1 The linear quadrupole trap

In comparison to the three-dimensional Paul trap, a linear ion trap confines the ions radially by an oscillatory RF field and axially by DC stopping potentials. The node of the RF field is the symmetry axis. The two-dimensional radial trap potential can be expanded in polar coordinates as [193]

$$\phi_n(r, t) = \Phi_0(t) \left( \frac{r}{r_0} \right)^n \cos(n\Theta) \quad (6.6)$$

$r$  and  $r_0$  describe the radial position of the ion and the inscribed radius of the ion trap. In Cartesian coordinates the same potential can be expanded into multipoles

in the form of

$$\Phi(x, y) = \sum_{N=0}^{\infty} A_N \Phi_N(x, y) \quad (6.7)$$

The resulting terms describe the constant potential ( $\Phi_0$ ), linear dipole ( $\Phi_1$ ), quadrupole potential ( $\Phi_2$ ), hexapole potential ( $\Phi_3$ ), octopole ( $\Phi_4$ ) etc. The first two potentials relevant for linear ion traps (omitting in the current consideration all higher order fields like the 22-pole), quadrupole or hexapole, can be written explicitly

$$\Phi_2(x, y) = \frac{\Phi_0}{2r_0^2}(x^2 - y^2) + C \quad (6.8)$$

$$\Phi_3(x, y) = \frac{\Phi_0}{r_0^3}(x^3 - 3xy^2) + C \quad (6.9)$$

$\Phi_0$  describes the potential difference between two neighboring electrodes and  $C$  is an integration constant.

The radial potential distributions given by equation 6.8, 6.9 are plotted in figure 6.1a, 6.1b. The 2D potential shape is fixed by the boundary conditions and depends on the shape and position of the trap electrodes.

The definition of the quadrupole potential (equation 6.8) displays an important aspect for a linear quadrupole ion trap. The ion motion inside such a potential will be decoupled between the two radial planes, which allows an analytical solution of the equation of motion. For higher order multipoles the motion in the two planes is generally coupled, making an analytical treatment difficult.

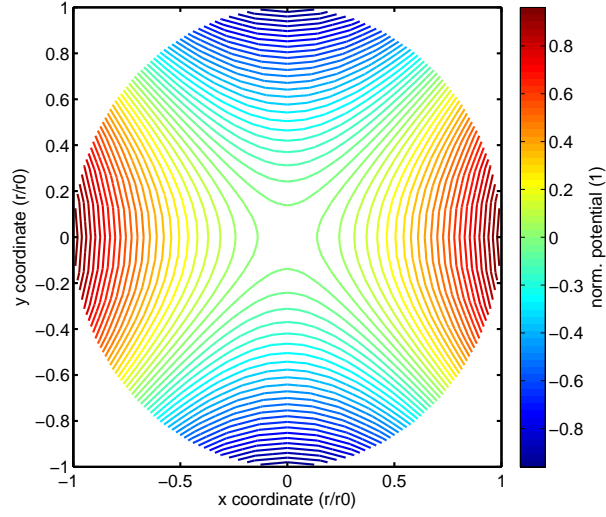
The full electric potential (in the radial and axial plane) of the linear quadrupole can be expressed by the following set of equations

$$\Phi_{\text{RF}}(x, y, t) = \frac{V_{\text{RF}}}{2} \left( \frac{x^2 + y^2}{r_0^2} \right) \cdot \cos(\Omega t) \quad (6.10)$$

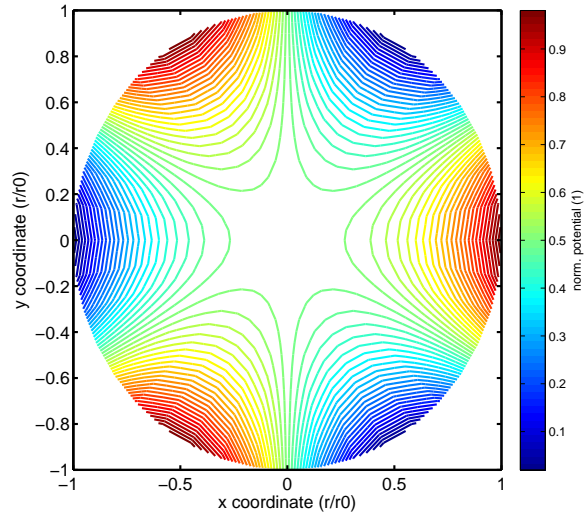
$$\Phi_{\text{EC}}(x, y, z) = \frac{\kappa U_{\text{EC}}}{z_0^2} \left( z^2 - \frac{x^2 + y^2}{2} \right) \quad (6.11)$$

$$\Phi_{\text{total}} = \Phi_{\text{RF}} + \Phi_{\text{EC}} \quad (6.12)$$

where  $V_{\text{RF}}$  describes the RF potential oscillating with the angular frequency  $\Omega$  and  $\kappa$  is a geometric factor, describing the shielding of the endcap potential in a given trap geometry. Figure 6.2 shows the schematic layout of such a linear trap. The dynamic trapping is achieved by applying RF voltages of equal amplitude but opposite polarity to the two diagonal sets of electrode pairs. To achieve an axial trapping,



(a)



(b)

Figure 6.1: The potential distribution in linear multipoles for two specific cases: a quadrupole (6.1a) and a hexapole (6.1b). For the hexapole an increased field-free region around the center can be observed. The potentials are normalized to  $(-1,1)$ .

an additional DC potential,  $U_{\text{EC}}$ , is applied to the electrodes on either side of the trap. The applied RF voltages define a saddle potential along the x-y planes of the trap, which flips with the RF frequency  $\Omega_{\text{RF}}$ . For any given set of RF parameters a well defined class of ions can be stable trapped within such an ion trap volume.

For the creation of an ideal quadrupolar electric field inside the ion trap hyperbolic

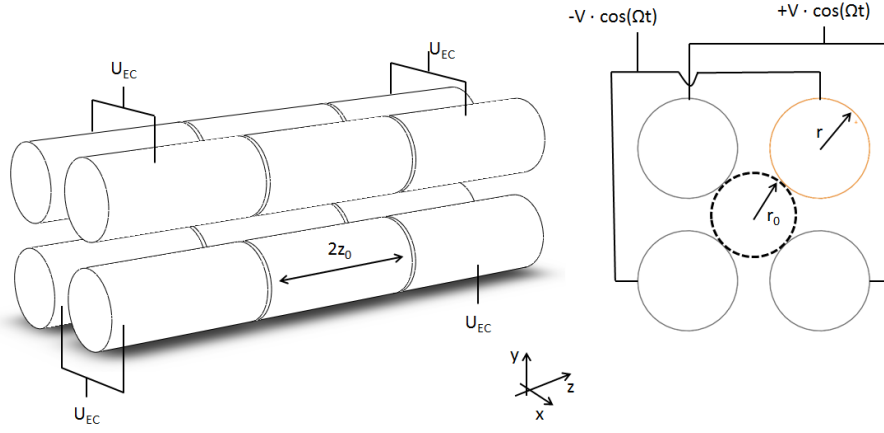


Figure 6.2: Schematic overview of a segmented linear quadrupole ion trap, showing the definition of the characteristic lengths  $r_0$ ,  $r$  and  $z_0$ . On the left side a side view of the trap is given, while on the right the cross section is shown. The trap rods are divided into electrically isolated segments, with a central electrode defining the trapping region. On each individual electrode the RF potential  $U + V\cos(\Omega t)$  is applied with the identical phase on each diagonal pair. Additionally an axial confinement potential, the end cap potential  $U_{\text{EC}}$ , is applied to the outer most electrodes.

electrode structures are required. While producing a slightly better quadrupolar field than round rods, the machining of such electrodes is quite difficult and the close proximity of neighboring electrodes at the rim in their outskirts can lead to enhanced sparking at high voltages. Therefore, in most cases linear ion traps are designed with cylindrical electrodes. To approximate the quadrupole field in the center of the trap the ratio of electrode radius  $r$  to inscribed radius  $r_0$  (shown in figure 6.2) should be  $r/r_0 = 1.148$  [194].

## Equation of motions

With a defined quadrupole potential the radial equation of motion  $F = -e\nabla\Phi$  can be defined (in this case explicit for the x coordinate) as

$$m \left( \frac{d^2 x}{dt^2} \right) = -2e \frac{(U_{\text{DC}} + V_{\text{RF}} \cos(\Omega t))x}{r_0^2} \quad (6.13)$$

The quadrupole field is a special case since the equation of motions can be reduced to a set of de-coupled one dimensional differential equations, the Mathieu equations:

$$\frac{d^2 u}{d\xi^2} + (a_u + 2q_u \cos(2\xi))u = 0 \quad (6.14)$$

where  $u=x,y$ ,  $\mathbf{a}_u, \mathbf{q}_u$  represent two dimensionless constants related to the physical parameters of the ion trap and  $\xi$  is a dimensionless recast of the frequency,  $\xi = \Omega t/2$ . By a direct comparison of the two equations 6.13 and 6.14 the dimensionless Mathieu parameters  $\mathbf{a}$ ,  $\mathbf{q}$  can be deduced:

$$q_x = -q_y = \frac{4eV_{\text{RF}}}{mr_0^2\Omega^2} \quad (6.15)$$

$$a_x = -a_y = \frac{8eU_{\text{DC}}}{mr_0^2\Omega^2} \quad (6.16)$$

If in the operation of the linear ion trap only an axial DC endcap potential is used instead of  $U_{\text{DC}}$ , the  $\mathbf{a}$  parameter can be re-written to [195]

$$a_z = \frac{8\kappa eU_{\text{EC}}}{mz_0^2\Omega^2} \quad (6.17)$$

$$a_r = \frac{4\kappa eU_{\text{EC}}}{mz_0^2\Omega^2} \quad (6.18)$$

where  $a_z$  describes the stability parameter for static confinement in the z axis, while  $a_r$  describes the radial plane. The parameter  $\kappa$  is a constant and is determined by the trap geometry. As long as  $a_z > 0$  and  $\mathbf{q}$ ,  $a_r$  lie within the stability regions, ions will have stable trajectories.

The description by the Mathieu equation has the advantage that the solutions are well known [196,197] and the stability of the resulting ion trajectories depends only on the two dimensionless parameters  $\mathbf{a}$ ,  $\mathbf{q}$  and not on the initial ion conditions

[193,198]. The general solution to equation 6.14 can be written as

$$u(t) = Ae^{i\omega_r t} \sum_{n=0}^{\infty} C_{2n} e^{in\Omega t} + Be^{-i\omega_r t} \sum_{n=0}^{\infty} C_{2n} e^{-in\Omega t} \quad (6.19)$$

where A and B are constants of integration and  $C_{2n}$  describe the amplitudes of ion motion depending on  $\mathbf{a}$  and  $\mathbf{q}$  only. When the characteristic exponent is imaginary, e.g. proportional  $i\beta$ , with  $\beta \notin \mathbb{N}$  (equation 6.19) the solution is periodic and stable. Otherwise the ion experiences instable trajectories and will escape the confinement volume of the trap within a few RF cycles. An in-depth treatment of this matter be found in [199].

The secular motion  $\omega_r$  corresponds to the motion of a harmonic oscillator and describes the ion motion within the RF potential. Terms with  $n \neq 0$  in equation 6.19 describe the ion motion driven by the RF field. This is the *micromotion*, representing a small 'wiggly' motion atop the slow-oscillating motion in figure 6.3.

The frequency of the secular motion in the radial plane can be calculated by

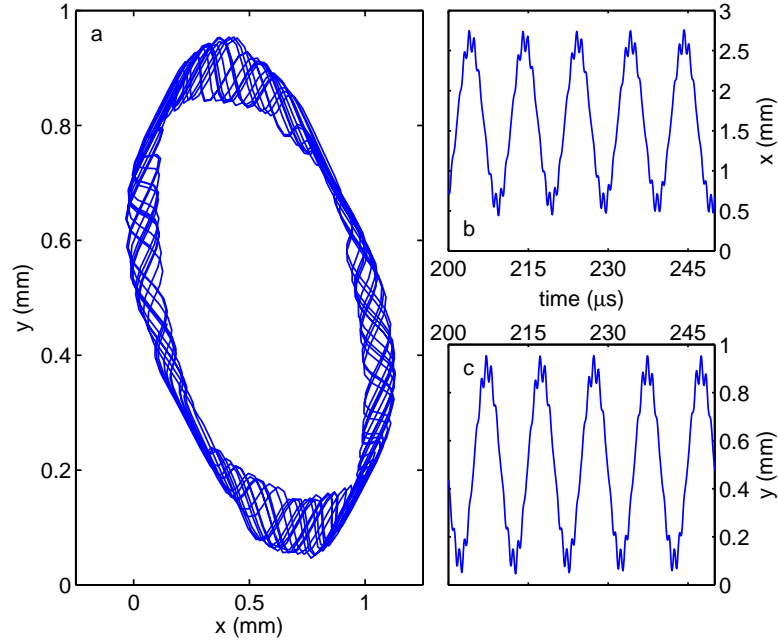


Figure 6.3: A simulated ion trajectory in the radial (x-y) plane (panel a). The temporal trend of the x and y component are presented in panel b and c respectively. The secular motion (low frequency) as well as the micromotion (low amplitude, fast oscillation period) can be identified in graph b, c. The Mathieu parameters in the simulation were chosen as  $\mathbf{a} = 0$ ,  $\mathbf{q} = 0.23$ . The ion trajectories were simulated in SIMION [200].

$$\omega_r = \frac{\Omega}{2}\beta \quad (6.20)$$

which depends only on the two Mathieu parameters  $\mathbf{a}$ ,  $\mathbf{q}$ . The Mathieu characteristic exponent  $\beta$  can be found numerically either by the continued-fraction expression in terms of  $\mathbf{a}$  and  $\mathbf{q}$  parameter or by the approximation [199]

$$\beta^2 = a_n - \frac{(a_n - 1)q_n^2}{2(a_n - 1)^2 - q_n^2} - \frac{(5a_n + 7)q_n^4}{32(a_n - 1)^3(a_n - 4)} - \frac{9(a_n^2 + 58a_n + 29)q_n^6}{64(a_n - 1)^5(a_n - 4)(a_n - 9)} + \mathcal{O}(q_n^8) \quad (6.21)$$

For operational conditions satisfying  $|\mathbf{a}|, \mathbf{q}^2 \ll 1$  and  $\beta \ll 1$  the secular motion in both trapping planes may be approximated by

$$\omega_r = \frac{\Omega}{2} \cdot \sqrt{\frac{q^2}{2} + a} = \frac{\Omega}{2} \cdot \sqrt{\frac{8e^2 V_{RF}^2}{m^2 r_0^4 \Omega^2} + \frac{8eU_{DC}}{m r_0^2 \Omega^2}} \quad (6.22)$$

$$\omega_z = \sqrt{\frac{\kappa e U_{EC}}{m z_0^2}} \quad (6.23)$$

Ions oscillate in the longitudinal direction of the trap with  $\omega_z$ , which is independent on the radial RF potential, but depends on the DC endcap potential, only.

The radial secular frequency  $\omega_r$  is not only determined by the trapping parameters, but also by the mass-to-charge ratio of the ion

$$\frac{m}{e} = \frac{2V_{RF}}{\sqrt{2}\omega_r r_0^2 \Omega} \quad (6.24)$$

This relationship is used for a selective mass scanning of the ion cloud [201, 202]: Since the ion motion can be regarded as a harmonic oscillation inside a potential well, additional irradiation with a radio-frequency resonant with the oscillation frequency ( $\omega_r$ ) leads to an increase in the kinetic energy of the ion and eventually to the loss of the ion from the trap. At the same time this technique also allows the isolation of ions of a specific mass-to-charge ratio  $m_i/e_i$ . Radiating notched RF waveforms by inverse Fourier transformation technique (e.g. white RF noise with a gap around the specific  $\omega_r$ ) into the trap will lead to a broad-band ejection of ions with the exception of the selected one with  $m_i/e_i$  [203].

The theoretical mass resolution in the resonant ion ejection can be directly related

to the frequency steps used in a measurement [204]

$$\frac{\nu}{\Delta\nu} = \frac{m}{\Delta m} \quad (6.25)$$

In the approximation of low  $\mathbf{q}$  ( $\mathbf{q} < 0.4$ ) the solution of equation 6.14 can be simplified to

$$u(t) = u_0 \cos(\omega_{\text{sec,u}}t + \phi_u) \left( 1 + \frac{q_u}{2} \cos(\Omega t) \right) \quad (6.26)$$

where  $\phi_u$  describes the phase on the oscillation and  $u_0$ ,  $\phi_u$  are determined by the initial conditions of the ion.

The composition of the ion motion from low-frequency secular frequency and micromotion is displayed in the equation. Thereby the amplitude of the micromotion is proportional to  $\mathbf{q}$  and the amplitude of the harmonic oscillation amplitude.

With the help of equation 6.21 the limits of stable motion can be found in the Mathieu stability diagram. Within these regions the ions have stable trajectories in both radial trapping axes. The lowest stability zone is shown in figure 6.4.

Since the stability diagram depends on the trapping parameters, it allows the esti-

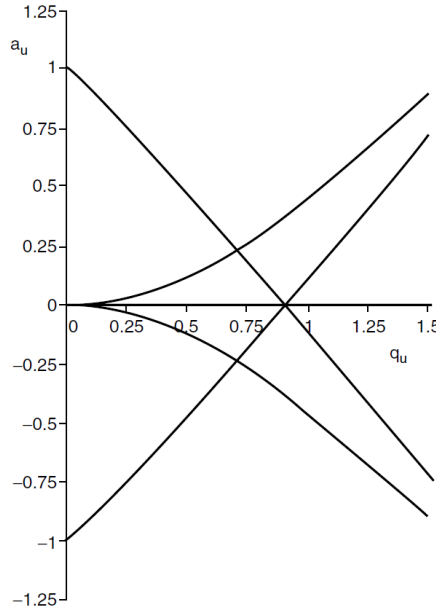


Figure 6.4: The first stability region in the Mathieu equation of a linear quadrupole trap spanning from  $\{\mathbf{a} , \mathbf{q} \} = \{0 - |0.237|; 0 - 0.9\}$ . The boundaries represent the limits for stable ion trajectories and satisfy the Mathieu equation. Image taken from [179].

mation of the parameters required for a stable confinement of an ion with mass  $m$ .

Furthermore it may be used to determine the mass-to-charge ratio of an unknown ion, since  $\{\mathbf{a}, \mathbf{q}\} \propto 1/m$ . In this case, experimentally either the RF amplitude  $V_{\text{RF}}$  is ramped down or a combination of DC and RF voltages is used to move the operation point of  $\mathbf{q}$  into the unstable region. In a similar approach the operational point of the ion trap can be moved to the tip of the (first) stability diagram, allowing stable trapping conditions for ions with only a narrow mass-to-charge ratio.

### 6.1.2 Pseudopotential approximation and trapping depth

When the amplitude of the RF field is nearly constant over the oscillation period of the ion, a useful approximation can be made. In this adiabatic approximation the secular motion of the ion can be treated as that of a particle in a time-independent effective potential, the effective- or pseudopotential  $V_{\text{eff}}$ . For a linear multipole ion trap of order  $n$  the pseudopotential can be written as [193, 205]

$$V_{\text{eff}}(r) = \frac{2n^2 e^2 V_{\text{RF}}^2}{16mr_0^2 \Omega^2} \cdot \left(\frac{r}{r_0}\right)^{2n-2} + \frac{e\kappa V_{\text{EC}}}{2z_0^2} (2z^2 - r^2) \quad (6.27)$$

The first term of equation 6.27 describes the time-averaged potential resulting from the oscillating RF field, the second term the influence of the static end cap potentials. Figure 6.5 displays the distribution of the radially effective potential for different multipole orders. Here the expected harmonic potential shape of the quadrupole can be observed. For increasing multipole order  $n$  the potential shape closest to the RF node gets more shallow while in the outskirts the electric field gradient increases with increasing  $n$ . This explains why a quadrupole is the optimal choice in experiments when well localized ion clouds are required (e.g. in case of optical detection by laser induced fluorescence or the controlled axial extraction of an ion beam from the trap). On the other hand, the shallow potential of higher order multipoles around the trap axis provides an ideal environment for cooling of large, extended ion clouds since micromotions are reduced. This is especially true in case of a 22-pole trap, which is widely used for cooling ion clouds to cryogenic temperatures [206].

For a linear quadrupole ion trap the pseudopotential can be described with the secular motions of the ion by the following relation

$$V_{\text{eff}}(r, z) = \frac{1}{2}m\omega_r^2 r^2 + \frac{1}{2}m\omega_z^2 z^2 \quad (6.28)$$

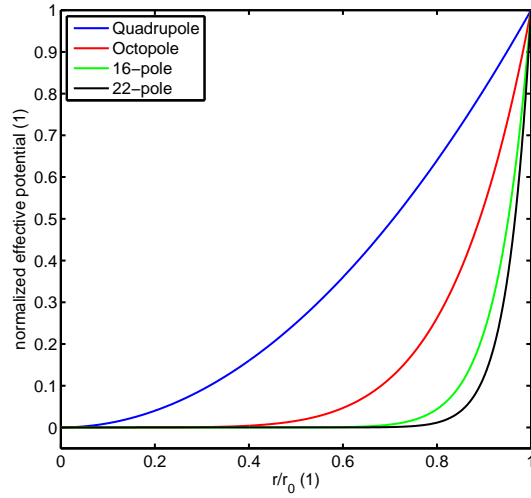


Figure 6.5: The distributions of the radial effective potential for different multipole order:  $n = 2$  (blue), 4 (red), 8 (green), 11 (black).

with  $\omega_r$ ,  $\omega_z$  corresponding to the secular frequencies of the trapped ion.

From equations 6.27, 6.28 the mass dependence of the effective potential can be seen. While the axial DC component has no mass dependence the radial potential is proportional to  $1/m$ , indicating that with increasing ion mass-to-charge (and constant trapping parameters) the radial potential will get more shallow. If two ions of different mass-to-charge ratio are trapped simultaneously, this will lead to a radial separation with the lighter ion trapped more closely to the trap axis [207,208], an important aspect when ions of different mass shall be trapped, as discussed in chapter 7.

An estimation (equation 6.28) shows that a trapping depth of a several eV can be reached. This is sufficient to routinely load a linear trap with ions created in a laser desorption source, especially if buffer gas cooling is used [209].

### 6.1.3 Trap capacity and space charge

When a large ion cloud is confined in a trap it will be influenced by the electrostatic ion-ion repulsion in addition to the RF field. This perturbs the ion motion and the storage capability of the trap. These repulsive forces counteract the effective potential [210,211] leading to shifts in the secular ion frequency [212,213] as well as an increase in the effective ion temperature [214] since the ions experience higher

RF field gradients in the outer region of the radial potential.

The effect of this Coulomb repulsion can be calculated in the low temperature limit ( $T \rightarrow 0$  K) with the averaged ion density by the Poisson equation

$$\nabla^2 \Psi = -\frac{\rho}{\epsilon_0} \quad (6.29)$$

The resulting repulsive force will counteract the attractive confinement force from the quadrupolar potential,  $F_{\text{Quad}} = -F_{\text{sc}}$ . The repulsive space charge force acting on an ion can be written as

$$F_{\text{sc}} = -e\nabla \Psi \quad (6.30)$$

By taking the second derivative and equating this with the Laplace of the effective potential (equations 6.27, 6.28) as well as with the Poisson's equation, the ion density can be explicitly written in terms of the trapping parameters. The density of a low-temperature plasma in a harmonic trap is constant and given by [215]

$$\rho = \frac{\epsilon_0 m}{e} (2\omega_r^2 + \omega_z^2) \quad (6.31)$$

While this equation is useful for an estimation of the trapped ion density, a more accurate treatment of the radial ion density distribution can be written as [213]

$$n(r) = \frac{N}{z_0} \frac{1}{2\pi a^2} \exp\left(\frac{-r^2}{2a^2}\right) \quad (6.32)$$

$$a = \frac{\rho_0}{2} \sqrt{\frac{4\pi\epsilon_0 k_B T + e^2 \rho_l}{2\pi\epsilon_0 e V_{\text{eff},r}}} \quad (6.33)$$

with  $N$  describing the total number of ions and  $\rho_l$  the line density of the ions.  $V_{\text{eff},r}$  denotes the radial effective potential and  $z_0$  the characteristic length of the ion trap (see figure 6.2).

For non-crystallized ions the kinetic energy of the ions is uniformly distributed in all three dimensions. It follows that the ion cloud surface will follow the equipotential surface between the repulsive space charge and the attractive pseudopotential. Therefore the ion cloud will be an ellipsoid with the ellipticity

$$\epsilon = \frac{z}{r} = \frac{\omega_r}{\omega_z} \quad (6.34)$$

## Estimations for practical experimental work

Using the previously derived equation for the ion density in the low temperature limit (equation 6.31), a prediction can be made for our linear ion trap. With typical operational values of  $\mathbf{q} = 0.23$  for an ion mass of 581 Da (Sulforhodamine B) the secular frequencies can be calculated as

$$\omega_r = 2\pi \times 101.07 \text{ kHz} \quad (6.35)$$

$$\omega_z = 2\pi \times 9.16 \text{ kHz} \quad (6.36)$$

which leads to an estimated charge density of

$$\frac{\rho}{e} = 2.7 \times 10^{14} \text{ ions/m}^3$$

In the experiment we are interested in trapping ions in the MDa range as well. Since the charge density is determined mainly by the trapping parameters (equation 6.31), similar charge densities are expected in this case as well.

### 6.1.4 Cooling of an ion cloud

Trapping of an ion cloud in a trap is not the only requirement which has to be met. Matter-wave interferometry additionally requires cooled ion species, which results in a decrease of the phase-space volume of the particle distribution with the consequence that the ion cloud concentrates around the RF node line. This reduces the anharmonicities in the trapping field 'felt' by the ion. At the same time the brightness of the ion cloud is increased. This has the consequence of a higher ion yield, for example when using the trap as source for an ion beam or by an increased signal-to-noise ratio when detecting the trapped particles by of fluorescence signal. Generally, cooling enhances the lifetime inside the ion trap [181].

Ions injected from an external source will have too much kinetic energy to be efficiently trapped, requiring a damping of the ion motion [216–218]. The initial energy has to be reduced to a value below the depth of the effective potential within the first passage of the ion trap.

A reduction of the kinetic energy will lead to a reduced amplitude of the secular

motion. Different to the secular motion, the micromotion is a coherent motion of the RF potential, which allows no direct cooling. The micromotion can only be reduced by keeping the local electric field around the ion cloud small, e.g. concentrating the ion cloud close to the node of the RF field. At this point the local RF field has a minimum, resulting in a small amplitude of micromotion. In case several ions are trapped simultaneously, in a collision process with either a neutral rest gas atom or a neighboring ion, an ion can be pushed off the trap axis and a phase-interruption in the micromotion takes place. Thereby work is done on the ion by the RF field, increasing the secular motion, leading to a heating of the ion cloud. This assumes a collisional partner of equal or larger mass than the ions mass. This will be a limiting factor in reaching the final temperature of a large trapped ion cloud [219].

The possibility of (selectively) reducing the micromotion by trapping the ion near the RF node is one of the advantages of the linear trap geometry compared to the 3D Paul trap. While a 3D trap exhibits only a point-like RF node, the RF node in a linear trap allows a more efficient cooling of large ion clouds.

Depending on the type of trapped ion (atom or molecule), the ion cloud size and the aimed experiment, different cooling techniques are available: These include laser cooling, buffer gas cooling, sympathetic cooling and resistive cooling, which have been described in numerous scientific articles and reviews, including the general description of cooling techniques [181, 220], as well as more specific papers related to laser cooling [182, 184], buffer gas cooling [221–225] and sympathetic cooling [226, 227].

For heavy molecules in a linear RF trap, typically buffer gas cooling or sympathetic cooling is the most efficient or only process. Since especially buffer gas cooling was operated in our experiments, it will be described in the following.

### **Buffergas cooling**

Since complex molecules (molecular structure greater than a diatom) do not show closed transitions due to their internal structure, laser cooling of such systems is not possible. This restricts the cooling in ion traps mainly to collisional processes. Thereby either ion-ion collisions (sympathetic cooling) or a neutral collision partner (buffer gas cooling) can be used. For buffer gas cooling a neutral gas at typical

pressures between  $10^{-5} - 10^{-2}$  mbar is leaked into the trapping volume, allowing collisions between the ions and the neutral particles. As long as the ion mass is much greater than that of the collision partner, the kinetic energy of the ion is reduced. When the mass of the ion is smaller, each collision will introduce a random phase in the micromotion, increasing the secular motion with the consequence of heating of the ions and eventual their loss. The cooling limit is thus the temperature of the buffer gas and given by the balance between RF-heating and cooling in ion-neutral collisions. For the former it could be shown that the final temperature is a constant of the applied trap potential [228].

The collisional cooling can be described as an average frictional damping force  $F = -Dv$  in the equation of motion of the ion

$$\frac{d^2u}{d\tau^2} + 2b\frac{du}{d\tau} + (a_u - 2q_u \cos(2\tau))u = 0 \quad (6.37)$$

with the damping constant  $b = D/m\Omega$ . With the transformation  $u = \omega \exp(-b\tau)$  equation 6.37 can be re-written into a modified Mathieu equation [197]

$$\frac{d^2\omega}{d\tau^2} + (a - b^2 - 2q \cos(2\tau))\omega = 0 \quad (6.38)$$

While the motion of the ion is still governed by this equation, the exponential factor leads to a modification: it could be shown [229, 230] that for high pressures the stability regions of the quadrupole trap are enlarged as well as shifted. This could enhance the mass range of a trap, while at the same time introducing new zones of instabilities. Generally, when operating an ion trap at low  $\mathbf{a}$ ,  $\mathbf{q}$  values, these effects do not influence the operation of the ion trap.

### Sympathetic cooling

Sympathetic cooling is a refined version of buffer-gas cooling. Here the hot ions are cooled by collisions with a cloud of cold ions. The major difference to buffer gas cooling is that the collisions are governed by the Coulomb interaction and the point of closest approach between two collision partners is further apart. This limits the cooling to the external degrees of freedom of the ions and it also guarantees that no clusters are formed. The internal energy of the molecular ion will stay close to its

initial value.

If laser-cooled atomic ions are used as a coolant, temperatures in the milli-Kelvin regime can be reached, allowing to even produce Coulomb crystals of molecular ions [231]. In a recent work [183] this cooling method was combined with neutral buffer gas cooling. Thereby a cooling of the rotational degrees of freedom of  $\text{MgH}^+$  to temperatures below 10 K could be shown, while the ions were crystallized in a Coulomb crystal.

To achieve a good cooling rate at the lowest possible temperature, the two participating ions should be as close as possible. This requires that the two ion clouds should not only be trapped inside the same pseudopotential, but also that their mass-to-charge ratio is similar. Otherwise the two ion clouds will be radially too far apart (the stratification effect [207]), eventually making the cooling process inefficient. Although the two ion clouds are overlapping, the motions of the individual ions are still decoupled from each other.

## 6.2 Laser induced fluorescence

In experiments where the ion trap is used as a particle source, an observation of the ion cloud prior the ejection of molecules could be useful. This requires a non-destructive ion detection instead of the charged particle detectors like channeltrons or Faraday cups. Also, standard charged particle detectors (electron multipliers, MCPs) show a decreasing detection efficiency with increasing mass/charge ratio of the ions in the typical kinetic energy region accessible for ion traps [232, 233]. This motivates the use of different detection principles as well. Thereby, an in-situ detection of trapped ions by laser induced fluorescence (LIF) is a feasible option. To illustrate the possibilities and the weaknesses of this detection techniques a short overview of molecular fluorescence will be given in the following. For more detailed information on fluorescence the reader is pointed to the references [234–236].

In a general statement, fluorescence describes the emission of a photon by a molecule upon absorption of electromagnetic radiation. With the absorption of a photon by the fluorophore, a chemical compound displaying fluorescence, an intra-molecular electronic transition is induced. As long as the photon energy is less than the ionization potential of the molecule, an electron will be shifted from the electronic

ground state ( $S_0$ ) to a higher state. In the subsequent electric dipole transition,  $S_1 \rightarrow S_0$ , a photon is emitted.

A scheme depicting such processes was first introduced by Jablonski [237]. It visualizes in a simple way the absorption, fluorescence, phosphorescence and internal conversion processes of a molecule, as shown in figure 6.6. The electronic states of the molecule are represented by bold solid lines.  $S_0, S_1, \dots$  denotes the singlet states while the triplet states are shown as  $T_1, T_2, \dots$ . The associated vibrational levels of each electronic state are displayed as well.

Vertical, solid lines show the intra-molecular transition upon the photon absorp-

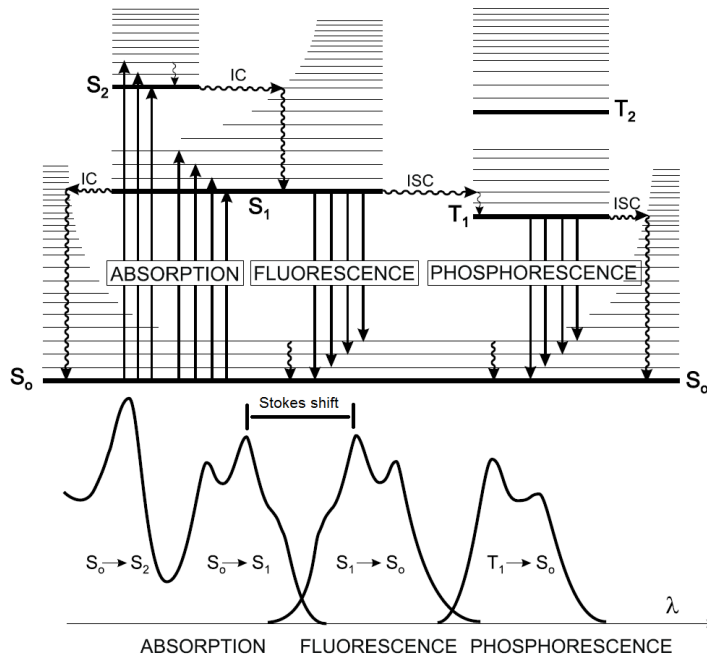


Figure 6.6: The Jablonski diagram displays the main activation and de-excitation routes in a fluorophore upon the absorption of a photon (excluding the photo-ionization process).  $S_x, T_x$  are the singlet and triplet states, ISC identifies the inter-system crossing and IC internal conversion. In the lower part of the image the wavelength range for different absorption and emission pathways is depicted. Image taken from [236].

tion, starting in the vibrational ground state of  $S_0$ , as described by the Boltzmann law for particles at 300 K. It must be noted that the vibrational level spacing can be very small, which leads to excitation from vibrationally excited states. This explains, why molecules may possess broad absorption and emission bands which also can be overlapping.

The fast absorption process, typically in the order of  $10^{-15}$  seconds, leaves the molecule an electronic and vibrational excited state. Eventually, the molecule will de-excite again towards the ground state, implied by the wiggly lines and the solid arrows directing towards the  $S_0$  state in figure 6.6. If the final excited state is greater than the lowest vibrational state in  $S_1$  the molecule will undergo internal conversion (for  $S > S_1$ ) and vibrational relaxation until this particular state is reached. Although a further internal conversion process into the  $S_0$  state can take place, the large energy difference between  $S_1$  and  $S_0$  makes this less likely. Generally, internal conversion is a non-radiative process, which takes place between two electronic states of the same spin multiplicity, as well as the non-radiative relaxation process inter-system crossing. Energy is transferred between two electronic states of different multiplicities, e.g. S and T. Generally this is only allowed between two isoenergetic vibrational levels, but spin-orbit coupling can lead to inter-system crossing between different vibrational states.

The de-excitation of the electron from the  $S_1 \rightarrow S_0$ , accompanied by the emission of a photon, is called fluorescence. With a few exception this process occurs only from the  $S_1$  state [236] and is therefore independent on the excitation energy. If the molecule makes internal conversion or vibrational relaxation prior fluorescence, the observable emission spectrum is shifted towards lower photon energies (higher wavelengths) than the absorbed photon, generalized by the Stokes rule. Also, the de-excitation by photon emission has its starting point always in the lowest vibrational level, while its final state must not reach the lowest vibrational level of  $S_0$ . This leads to a red-shift (Stokes shift) of the emission spectrum with respect to the absorption band, schematically shown in the lower part of figure 6.6.

The actual emission of the fluorescent photon is on the same time scale as the absorption. Since the excited state has a finite lifetime and other (competing) de-excitation processes can also take place beforehand, the recorded fluorescent intensity of a fluorophore population will always show an exponential decay with a characteristic time constant. An overview over the different major time constants in the absorption/emission process is given in table 6.1.

The wavelength dependencies of the different possible radiation processes in LIF are shown in the lower part of figure 6.6, depicting the Stokes shift between the two first absorption bands, the fluorescence band and the relationship between the peak

Absorption	$10^{-15}$ s
$S_1$ lifetime	$10^{-10}$ - $10^{-7}$ s
Vibrational relaxation	$10^{-12}$ - $10^{-10}$ s
Inter-system crossing	$10^{-10}$ - $10^{-8}$ s
Internal conversion	$10^{-11}$ - $10^{-9}$ s
$T_1$ lifetime	$10^{-6}$ - $10$ s

Table 6.1: The characteristic time constants of the intra-molecular processes after absorption of a photon [236]

structure and the different vibrational levels involved.

### 6.2.1 Properties of the absorption process

Before fluorescence is observed, the molecule has to reach the excited electronic state by absorption of a (single) photon, where the excitation rate  $W_A$  is given by

$$W_A = \frac{\sigma(\lambda)_{abs}}{A} \frac{I}{h\nu} \quad (6.39)$$

with  $\sigma(\lambda)$  denoting the wavelength dependent absorption cross section,  $I$  the intensity of the light source (laser power in Watts) and  $A$  is the cross section of the beam. In this context the absorption cross section has a simple geometric dimension. If the spontaneous fluorescence rate  $\gamma$  and the total absorption frequency  $\Gamma_{tot}$  are known for a molecule,  $\sigma_{abs}$  can be calculated for the absorption wavelength  $\lambda$  [238]

$$\sigma_{abs} = 2\pi \left( \frac{\lambda}{2\pi i} \right)^2 \cdot \frac{\gamma}{\Gamma_{tot}} \quad (6.40)$$

A different measure of the molecular absorption is the molar absorption coefficient  $\epsilon$  (expressed in  $Lmol^{-1}cm^{-1}$ ), which is introduced by the Lambert-Beer law

$$I = I_0 \exp^{-cd\epsilon} \quad (6.41)$$

$I_0, I$  are the initial and transmitted laser intensity,  $d$  is the optical path length through the sample and  $c$  is its concentration.  $\epsilon$  describes the suitability of a molecule to absorb light of a specific wavelength in a defined environment. Thereby a large value of  $\epsilon$  indicates a high probability of absorption, with values of 10000 - 30000  $Lmol^{-1}cm^{-1}$  for highly fluorescent probes. For strong emitters this value can be

even higher, reaching about  $9 \times 10^4 \text{ Lmol}^{-1}\text{cm}^{-1}$  as in the case of the fluorophore Rhodamine B [236].

With an experimentally determined molar extinction coefficient the absorption cross section of Rhodamine B can be calculated by [236]

$$\sigma_{abs} = \frac{\ln(10)\epsilon}{N_A} = 3.825 \times 10^{-19} \epsilon \quad (6.42)$$

In the last expression  $\sigma_{abs}$  is given in  $\text{cm}^2$  and  $N_A$  is the Avogadro constant.

Absorption cross sections can be quite different for each individual fluorophore, depending on the excitation wavelength. Furthermore the exact value of  $\sigma_{abs}$  is dependent on the molecular structure, the environment as well as on the interaction with other molecules. Changes in the solvent environment can lead to absorption shifts, either by moving the absorption maximum towards the blue (e.g. blue-shift or hypsochromic shift) or towards longer wavelengths (e.g. red-shift or bathochromic shift).

### 6.2.2 Properties of fluorescence emission

The lifetime of the excited state is defined by the two rate constants  $k_r, k_{nr}$  [236]

$$\tau = \frac{1}{k_r + k_{nr}} \quad (6.43)$$

where  $k_r$  describes the radiative deactivation and  $k_{nr}$  the non-radiative rate constant. The lifetime  $\tau$  is important for the description of the fluorescence quantum yield  $\Phi_{LIF}$ ,

$$\Phi_{LIF} = \frac{k_r}{k_r + k_{nr}} = k_r \tau \quad (6.44)$$

Basically  $\Phi_{LIF}$  is a measure of the (overall) fluorescence efficiency, defined by the ratio of the number of emitted fluorescence photons to the number of absorbed photons. For most measurements it is desirable to use molecules with high quantum yields, which is especially true for experiments when only a low density of fluorophores is expected (like observing an ion cloud in-situ inside an ion trap).

The environment of the fluorophore plays also a role in the de-excitation and has an impact onto the effective fluorescence rate of a molecule. As an example, oxygen

is well known for its quenching properties which reduces the quantum yield of a fluorophore. Furthermore the number of directly surrounding molecules and thus the number of available collision partners plays a crucial role on the fluorescence intensity. Due to the Stokes shift, the difference in energy between the absorbed and emitted photons is 'stored' inside the molecule, which will be released by collisions with background molecules (e.g. a buffer gas or solvent). If this is not possible, it eventually will lead to a photo-fragmentation of the molecule and the loss of the fluorophore. Also high illumination intensities will lead to a fast bleaching of the molecule.

Low fluorescence intensities and reduced fluorescence detectability may be a consequence of photo-bleaching of the molecule. An high-intensity illumination can lead to irreversible chemical reactions within the molecule. In most cases photo-bleaching is starting from a triplet state, which can be accessed by intersystem crossing (see figure 6.6). While this is primarily dependent on the illumination intensity, other effects like excited state absorption or collisions may also play a role.

### 6.2.3 Laser induced fluorescence of cations in the gas-phase

Although laser induced fluorescence of molecules in a liquid or solid environment is a broad and well developed field, fluorescence from neutral or charged fluorophores in the vacuum gas-phase has some advantages. Since the molecule has no solvation shell in vacuum, such a measurement allows to identify and study environmental effects such as, as an example, the bathchromatic shift of the emission maximum. Thereby it is possible to collect relevant chromophore information, which are required to fully understand the photophysics of these molecules. One could possibly investigate the correlation of  $\text{H}_2\text{O}$  on the emitted fluorescent light of a biological active molecule. The green fluorescent protein (GFP) should be mentioned as an example here. Recent measurements showed that 4-hydroxybenzylidene-2,3-dimethyl-imidazolinone (a model GFP chromophore) in vacuum has similar spectral features in its absorption than when bound inside the protein structure [239] and its photo-dissociation [240]. On the other hand, other work in literature [241] could demonstrate that the native form of rGFP (a recombinant variant of GFP) does not show fluorescence in vacuum, although the protein stayed intact and folded. The

authors concluded that due to the loss of the water shell around the protein, rGFP is completely inactivated and cannot be detected by LIF under vacuum conditions in the gas-phase.

With technical developments in ion trapping and fluorescence, it was only a matter of time until these two fields were combined for molecular fluorescence measurements in ion traps. Most recent work was performed in three-dimensional Paul traps [208, 242–249], in Fourier transform ion cyclotron resonance mass spectrometers (FTICR-MS) [250–252] as well as in-flight [241, 253]. In these cases soft-ionization methods were employed, like ESI [208, 247, 252] or MALDI (the following literature is mentioned as an incomplete overview [251, 254]). Most of the literature cited above used different dyes from the Xanthene family to test not only general LIF properties of trapped gas-phase ions, but also the LIF dependency on the buffer gas properties (neutral atom type [255] and pressure [244, 247, 252]), the photo-fragmentation of Rhodamine cations [242, 244] and Fluorescein anions [246]. Furthermore the general LIF properties like bathchromatic [244, 249, 252] as well as Stokes shifts [249] and prolonged fluorescence lifetimes of the gas-phase Rhodamine cations [248] were measured. At the same time LIF was used to investigate the ion dynamics of trapped ion clouds in RF traps [208, 242, 252]. Also fluorescence resonance energy transfer (FRET) measurements between two trapped fluorophores were measured in the case of mass-selected Polyproline peptides [245] and Rhodamines [250].

Apart from the measurements with common fluorescent molecules also experiments using nanoparticles were performed: Thereby charged, fluorescently labeled polystyrene nanobeads were either brought into the gas-phase by ESI [253] or by MALDI [243, 254]. Especially in [254] it could be shown that laser desorption of nanospheres produces mainly ions in low charge states (less than 10).

### 6.3 Design considerations for a linear ion trap

A broad range of different ion trap designs exist to choose from when experiments with trapped ions are set up. They range from confinement in RF fields (3D/linear) [192, 256] over Penning traps [257] to electrostatic traps [258]. The goal of this thesis is to prepare a (linear) ion trap that will be coupled to a future molecular matter-

wave interference experiment, eventually. The ion trap will be used as a particle source for complex and heavy molecules. This leads to specific considerations and experimental constraints, presented in the following.

For choosing the most favorable design of an ion trap for a molecular beam source the advantages and disadvantages of both, Penning and RF ion traps have to be considered in the context of the experiment. While Penning traps have the advantage of using static fields only, the (geometric) access to the center of such a trap is very limited, especially when considering optical detection methods. Also, when considering the confinement of molecules with a molecular mass of 1 MDa strong magnetic fields are required. In Penning traps a stable trapping condition can be defined by [197]

$$\omega_c^2 - \omega_z^2 > 0 \quad (6.45)$$

with the cyclotron and axial frequency, respectively

$$\omega_c = \frac{eB}{m} \quad (6.46)$$

$$\omega_z = \sqrt{\frac{2eU}{md^2}} \quad (6.47)$$

B, U are the magnetic field and the electric voltage used, m is the molecular mass of the confined particle and d describes the distance between the two endcaps. If dimensions in the order of about 1 cm and endcap potentials of less than 50 V are taken into consideration, an axial magnetic field of the order of 10 T or larger is required to fulfill the trapping condition (equation 6.45). While it is possible to increase the trap dimensions for a reduction of the required magnetic field B, it would also enlarge the resulting ion cloud, limiting the beam flux of an extracted ion beam from the ion trap.

Since the ion trap will be in close vicinity of a matter-wave interferometer, strong magnetic fields at the interference grating structure could have a negative influence on the observed interference contrast. A constant acceleration  $a$  of the then already neutral molecule due the magnetic field will lead to a fringe shift  $\Delta x = aT^2$  [8]. While such an overall shift alone will not destroy the interference pattern, all particles have to experience the identical shift. Otherwise the resulting interference pattern will be built from a mixture of shifts, reducing the visibility significantly.

For an extended trapping volume inside a Penning trap one can expect that the molecules will experience different magnetic field gradients  $dB/dz$  during ejection, which will result in a sum of different shifts  $\Delta x$ , reducing the observable interference contrast. This asks again for a small trapping volume, which would require large magnetic fields (see stability condition, equation 6.45).

As a final consideration point the cooling of ions inside a Penning trap should be mentioned. The reduction of the energy of an ion leads to an increase of the magnetron frequency (the motion perpendicular to the magnetic field axis) [181], which will eventually lead to ion losses by collisions with the trap electrodes. While this radial expansion can be controlled by the use of external correction fields, it will still lead to an increased ion cloud volume, which is unfavorable since the ions should be extracted as a tight packet into the interferometer.

This leads to the choice of RF driven ion traps. They have the advantage that they can be built very compact and by choosing the optimal trapping parameters the required trapping fields can be kept small. While also the electric fields of the RF trap will lead to a shift  $\Delta x$  in the observed interference pattern, electric fields can be switched-off more rapidly [259, 260] compared to a strong magnetic field, reducing the strength of the shift  $\Delta x$ . Electric fields can be shielded more effectively as well, which reduces their influence on the matter-wave interference even further.

In the considerations the geometric design has also to be fixed, either a 3D or a linear multipole RF ion trap will be used. In case of a linear geometry the order of the multipole has to be defined right at the beginning as well. For the present work the linear quadrupole geometry has been chosen for several reasons: The spatial extension of the confined ion cloud is larger in a linear quadrupole compared to a spherical shape in the 3D Paul trap. Additionally the 3D-Paul trap presents only a point-like field free region while in the linear trap this region is linear in axial direction, an advantage when considering cooling of a large ion cloud to cryogenic temperatures (as shown in chapter 6.1).

A further advantage of the linear ion trap is its greater trapping capacity compared to the 3D Paul trap [261]. Generally the space charge density in the linear trap is higher [261],  $N_{2d}/N_{3d} = (0.1)^2 r_0^2 l / (0.1)^3 z_0^2$ , allowing the confinement of larger numbers of ions before the influence of space charge takes overhand. This is an important aspect for future measurements in a matter-wave interferometer, where a

high flux of particles per interferometer cycle is required. In a linear trap the ions can be efficiently ejected along the RF node into, for example, an interferometer set-up. Alternatively, the linear trap geometry would also allow the implementation of a matter-wave interferometer of OTIMA type [2] inside the confinement volume itself.

The advantage for optical detection due to the more open geometry in the linear ion trap was already mentioned. Further advantages of this open geometry are a faster pumping speed of the buffer gas, which is required for the initial trapping and the cooling of the particles, but could be destroying the following matter-wave interference measurement by collisional decoherence [262].

For a future matter-wave interferometer a linear RF multipole seems to be suited compared to a 3D quadrupole. This leaves the question of the order of the multipole, which has still to be determined. The higher the order of the multipole, the larger the field-free region inside the trapping structure. While this can be of advantage for cooling [225, 263], a linear quadrupole possesses an intrinsic mass selectivity (see also chapter 6.1), an advantage when mass-selected ion beams shall be ejected into an experiment. Also, in lower order multipoles the distance between two neighboring electrodes is greater. This enhances the optical access to the ion cloud, thereby increasing the optical detection efficiency as well.

In this thesis a preparation stage was realized as a linear quadrupole ion trap with buffer gas cooling at 300 K, while future cooling stages to cryogenic temperatures shall be implemented in higher-order multipoles eventually. In the final experiment this should allow an efficient loading, coupled with intrinsic ion cloud cleaning (e.g. mass selection) and furthermore cooling to temperatures of about 10 K prior to matter-wave interference - either inside the trapping volume itself or outside of the ion trap.

## 6.4 The linear quadrupole ion trap - design

Prior the testing of the ion trap on its suitability for a possible coupling to a matter-wave interferometer, the design of the trap had to be determined. The question about the length and inscribed radius  $r_0$  of the quadrupole trap were answered in a first design step. The determination of the inscribed radius  $r_0$  of the ion trap is

guided here on the one side by the requirements for a good signal to noise ratio in the optical detection of the ion cloud. The trapping volume shall be wide enough to allow the confinement of large ion clouds (see equation 6.31), but at the same time the ion cloud diameter should be limited such that a good overlap with a laser beam for optical detection is given. This restricts the radial trap dimension to less than one centimeter and  $r_0$  is finally determined by the frequency and amplitude range of the available RF drive, where a stable ion motion is described by the Mathieu equations with  $\mathbf{q} < 0.9$ . The knowledge of the radio frequency  $\Omega_{RF}$  together with the mass of the captured ions allows us to determine  $r_0$  (see equation 6.16), since  $\mathbf{q} \propto V/m\Omega^2$ .

In figure 6.7 the stability parameter  $\mathbf{q}$  is plotted for different inscribed radii. In case

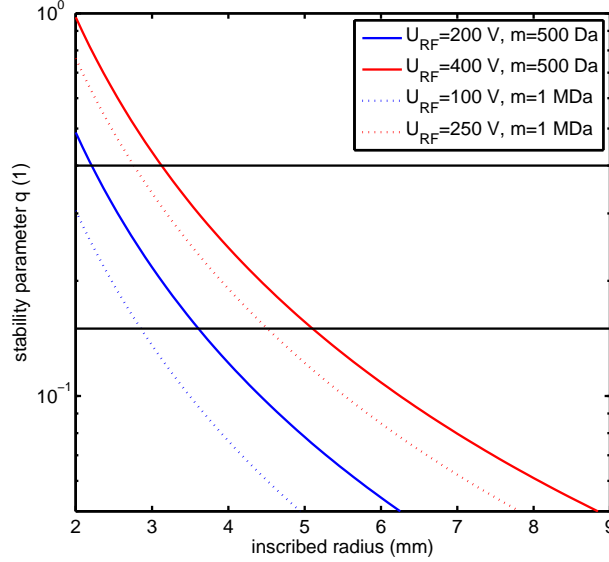


Figure 6.7: The calculated parameter space for the stability parameter  $\mathbf{q}$  at different possible radial trap dimensions is shown for two different applied RF voltages. The region between the two horizontal black lines at  $\mathbf{q} = \{0.15; 0.4\}$  show the region of optimal trapping. The RF frequency was assumed with  $\Omega_{RF} = 2\pi \times 1$  MHz and  $\Omega_{RF} = 2\pi \times 20$  kHz for an ion mass of 500 Da and 1 MDa, respectively.

of light ions (500 Da) the RF drive was assumed to have a frequency of  $2\pi \times 1$  MHz with an amplitude of 200 V (solid blue line) or 400 V (solid red line), respectively. For the ions with a mass of 1 MDa RF parameters were chosen with  $2\pi \times 20$  kHz and 100 V (dotted blue line) or 250 V amplitude (dotted red line). These values are well compatible with available RF power supplies.

From graph 6.7 we deduce that also from the RF parameters  $r_0$  should be in the

range between 3 and 9 mm. For smaller radii the stability parameter increases quickly towards the instable value of  $\mathbf{q} > 0.9$ . On the other side, a larger  $r_0$  leads to  $\mathbf{q}$  values below 0.1, resulting in very weak effective trapping potentials (see section 6.1 for more details). For  $\mathbf{q}$  between 0.15 and  $\leq 0.35$  optimal conditions for trapping and cooling of ions can be found with reduced micromotion. The two horizontal lines in figure 6.7 indicate the region between  $0.15 < \mathbf{q} < 0.4$ , which should be the standard operational region for a designed ion trap.

An inscribed radius between 3 and 4 millimeters should give the greatest operational flexibilities with the above mentioned constraints. Smaller trap diameters are not suited because in this case the open fraction between two neighboring rods limits an efficient optical detection of the trapped ion could. Larger inscribed radii would enhance the optical detection, but require higher RF amplitudes to reach similar effective potential depths (see also equation 6.27). With the chosen RF settings (and  $r_0$  value) the RF amplitude can be varied by about a factor of two without leaving the ideal region inside the stability diagram. For these assigned RF parameters the indicated radius is also optimal for retention of heavy ions as well, as shown in figure 6.7. With the chosen RF settings, the radial secular frequency (equation 6.23) of a trapped ion having a mass of 581 Da will be about 240 kHz (RF: 250 V, 1 MHz). While this could be limiting a cooling of the ion cloud, such high trapping potentials will increase the ion density inside the trap (see equation 6.31 as well as figure 6.9). With a readily available rod diameter of  $2r = 8$  mm, the inscribed trap radius would be  $r_0 = 3.48$  mm.

The considerations leading to the radial trap rod dimensions in figure 6.7 were based an estimated fixed ion mass of 500 Da. In this context this mass range was chosen, since here a large number of fluorophores are available. In a later experimental stage and especially in a future experiment, coupled to a matter-wave interferometer, ion masses in the MDa range will be used.

Since the trap radius  $r_0$  was defined, the available mass range which can be trapped within the first zone of stability (with  $\mathbf{a}=0$ ) can be deduced. A readjustment of the equation 6.16 leads to the following expression:

$$m = \frac{4eV}{\Omega^2 r_0^2 q} \quad (6.48)$$

With the fixed geometry and assumptions on the parameters of the RF electronics, the accessible mass range can be calculated as shown in figure 6.8. In this estimation similar RF parameters were taken: the RF frequency was chosen as  $\Omega_{\text{RF}} = 2\pi \times 1$  MHz and the amplitude was limited to 600 V. The shaded area of the plot (figure

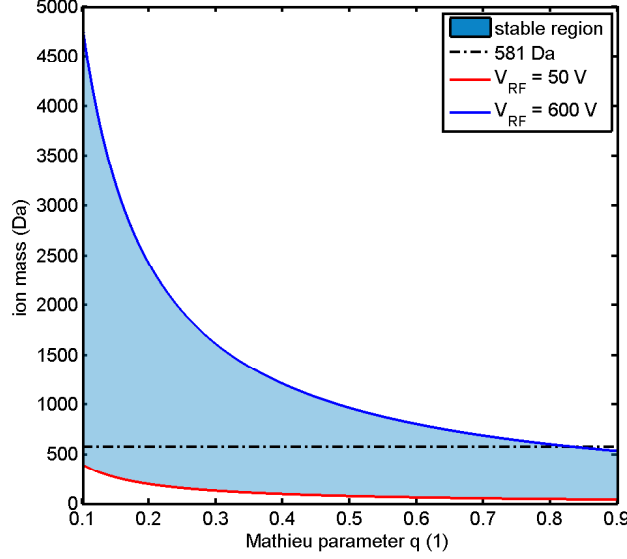


Figure 6.8: The accessible mass range of the planned ion trap with an inscribed radius of  $r_0 = 3.48$  mm is shown. The shaded region represents stable trapping conditions within the experimental parameters, the borders present the lowest (red line) and the highest (blue line) accessible RF amplitude in the experiment.

6.8) shows the mass range, which can be stable trapped in the underlying design layout and is bounded by the lowest and highest amplitudes of the RF drive. As a minimal value 50 V is taken (red line), since this amplitude should already allow a stable trapping field without too much influence of noise.

Figure 6.8 shows that the trap geometry will provide optimal stable trapping conditions in the envisaged low-mass region (of about 500 to 2000 Da), the mass region of small fluorophores. This is displayed by the dotted line in figure 6.8, which represents the mass of the fluorescent ion Sulforhodamine B (581 Da).

By adjusting the RF amplitude the accessible mass region is increased by a factor of four (up to approx. 2500 Da), allowing also to test (fluorescent) ions of higher mass without the need to change the experimental setup.

For the axial dimension of the linear ion trap the following considerations were taken into account: the ion trap should be capable of trapping a sufficiently high number of ions. In the following estimation the trap dimensions were taken from the finally

realized ion trap having an inscribed radius of  $r_0 = 3.48$  mm and characteristic length of  $z_0 = 10$  mm which should confine the ion cloud sufficiently to allow for a good overlap with laser beams. From the maximal ion density inside the linear quadrupole,  $n_{\text{imax}} = qV_{\text{RF}}\epsilon_0/er_0^2$  [264], the maximal ion number is estimated to be in the order of  $10^8$ . While in an actual experiment the number of ions will be limited to less than  $10^6$  (since the trap will be operating at 300 K and not in the low temperature limit), given by the space charge repulsion in such a large ion cloud. Figure 6.9 shows the maximum possible, calculated ion densities for the ion trap of chosen geometry with the accessible RF parameters (here 500 V for the low mass case, figure 6.9a, and 300 V for the heavy ions, figure 6.9b). For the light ions (graph 6.9a) a good part of the first stability zone is accessible, but the operation point for 1 MDa ions is more restricted (figure 6.9b). In both cases a similar number of ions can be stored in the ion trap, although, due to the low accessible  $q$  values, the numbers are a bit smaller for the heavy ions.

Another interesting feature is the shuffling and bunching of the ion cloud inside the ion trap volume, which requires a dedicated DC electrode structure along the trap axis to create multiple axial potential minima. For the axial confinement of the ions in the trap axial DC electrodes are required as well, but they can be identical to the ones required for a possible bunching of the ion cloud, if required.

In the final design an ion trap incorporating segmented trapping rods was defined. Figure 6.10 shows a drawing of the planned linear quadrupole ion trap together with its mounting structure.

The ion trap was built from polished stainless steel rods, dressed to a diameter of 8.0 mm. Only one pair of rods is cut into five segments, with the other pair being non-segmented. This design was chosen due to simplify the RF electronics. The RF can be applied to the non-segmented diagonal rod pair while the endcap potentials are applied to the different segments. Another advantage in this segmented layout is a reduced influence of RF fringe fields at the endcap sections, since the DC electrode 'sits' inside the RF field. The same holds true for the case that all four trapping rods are used for the RF drive, for which DC and RF power supplies have to be separated carefully (see also section 6.6.1).

The outer most segments (segment 1 and 5, figure 6.10a) had a total length of 25 mm while the three inner segment were trimmed to 20 mm. The different length

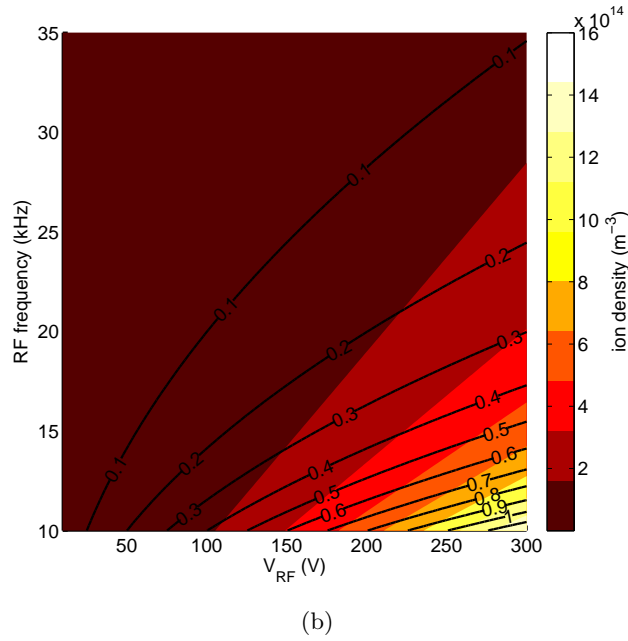
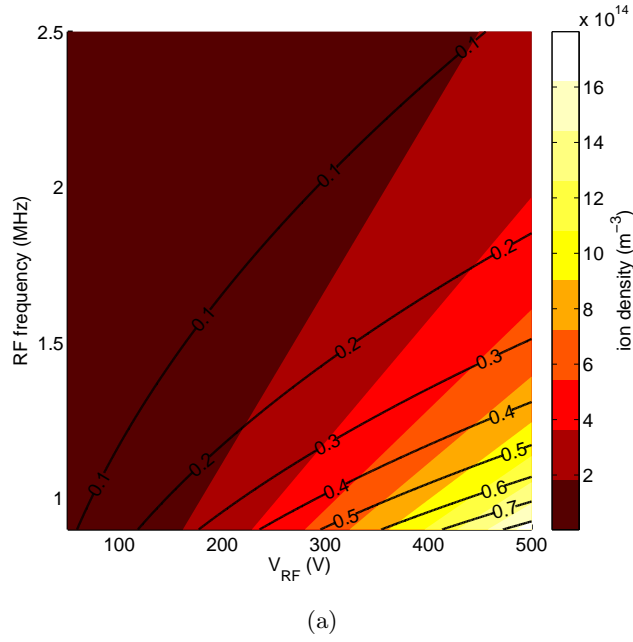


Figure 6.9: The maximum ion density for a linear ion trap with inscribed radius  $r_0 = 3.48$  mm is shown for the accessible RF parameter space. 6.9a shows the case for small fluorophores ( $m=581$  Da, Sulforhodamine B), while graph 6.9b assumes nanoparticles with a mass of 1 MDa. The solid black lines in both graphs show the corresponding Mathieu parameter  $q$ .

scales were necessary since segment 1 and 5 required more space for mounting the complete assembled rod to the support structure. The inner segment length was limited to 20 mm, since this allowed on the one hand to trap relatively large ion

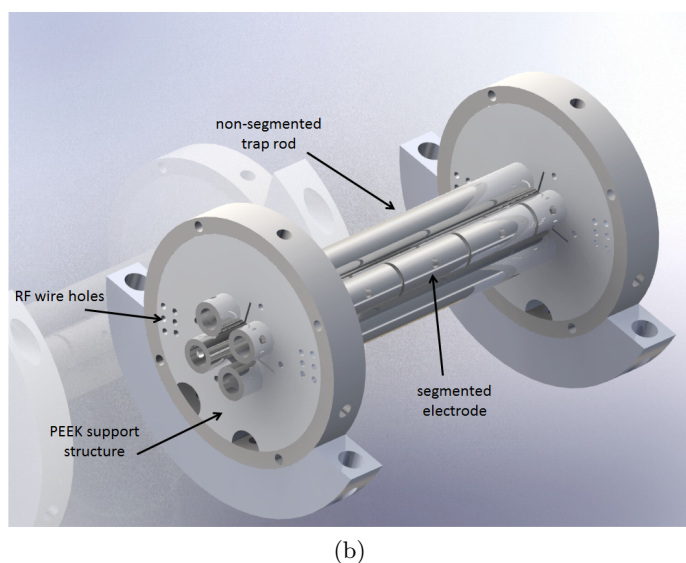
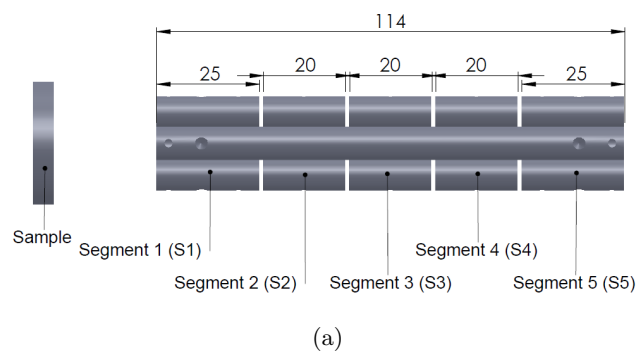


Figure 6.10: A CAD drawing of the segmented, linear ion trap setup is shown. Figure 6.10a shows on the left the molecular sample plate, while the segmented trap rods are shown at the top and the bottom. All dimensions are given in mm. A 3D view of the complete assembled linear quadrupole ion trap is presented in 6.10b.

clouds (see figure 6.9), while keeping the influence of the endcap potential in the center of the trap small (see figure 6.12). This fixed the total length of the ion trap to 114 mm.

To illustrate the design in more detail, the technical drawings of the different parts of the linear quadrupole are shown in the appendix 9.2 and the final assembled ion trap is presented in figure 6.11.

To connect the trap rods to the RF drive, 2 mm diameter Kapton insulated Cu

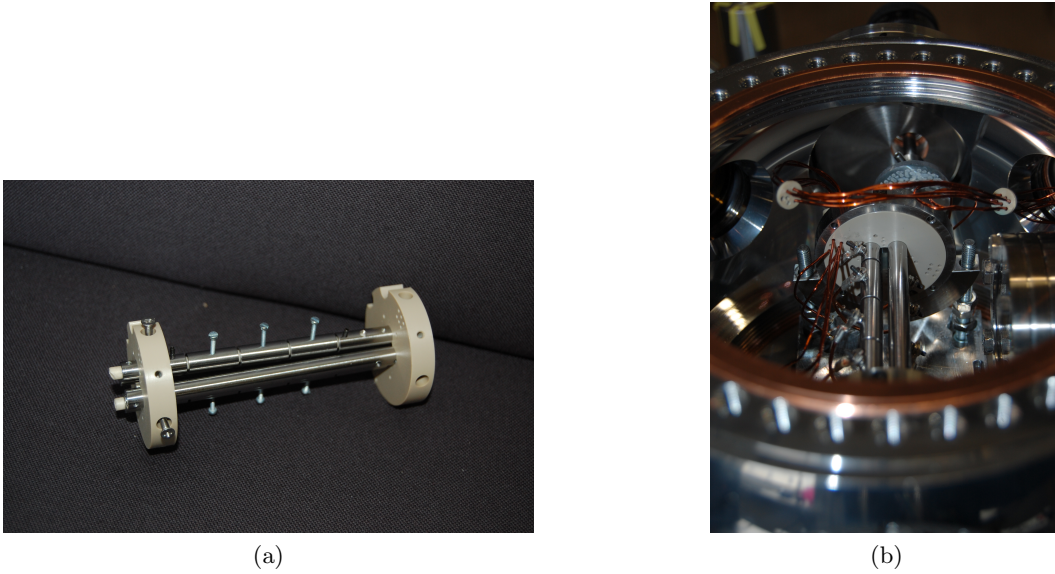


Figure 6.11: The linear ion trap is shown. 6.11a shows the assembled trap outside vacuum chamber, the image on the right (6.11b) shows the fully assembled ion trap inside the vacuum chamber. The RF wires (brown) are led from the electrical feedthrough of the vacuum chamber (top left corner) to the individual trap rods. Behind the ion trap a part of the sample disc is visible, while on the right edge an inverted view-port can be seen. The laser beam for LIF enters the chamber through the window left of the sample plate and passes under an angle of about  $45^\circ$  through the central trapping volume.

wires lead from the electrical feed-through to the quadrupole. The identical wires were used for applying the DC voltages as well, with the coupling of RF and DC done directly at the feed-through. Also care was taken that identical wire lengths were taken. All together, this should keep a mismatch of the RF between individual segments low, which could lead to a shift or weakening of the RF node inside the trapping volume. While stable trapping conditions can be still found in this case, it leads to an excess of micromotion [265, 266].

To estimate the influence of the endcap DC on the ion motion, the axial potential

distribution was computed with SIMION [200]. In this simulation the endcap voltage of 20 V was applied to segments S2 and S4 with the results for three different radial distances from the trap axis ( $r_0 = 0; r_0/2; r_0$ ) shown in figure 6.12.

Sometimes an axial harmonic potential shape of the endcap DC might be desirable,

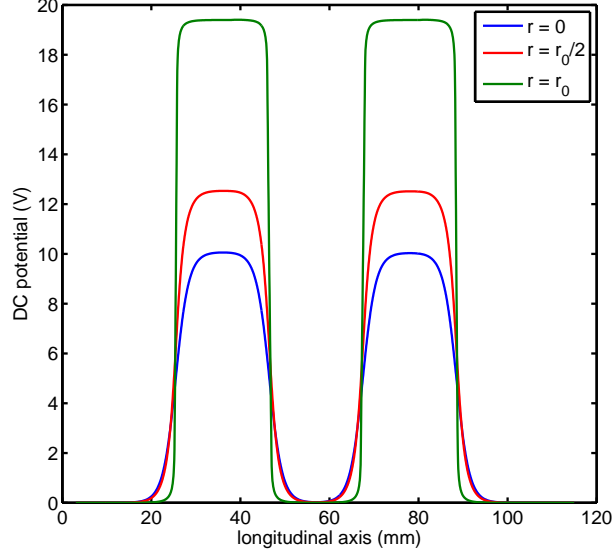


Figure 6.12: SIMION simulation for the electrical potential along trap axis ( $x = y = 0$ ). The voltage applied between to the segment 2 and 4 was 20 V. The center electrodes of the trap and the two outer most rod segments are grounded. The axial distribution of the endcap potential is shown for three different cases: One along the central axis of the ion trap (blue line), at  $r = r_0/2$  (red line) and finally at  $r \approx r_0$  (green line). The applied endcap potential was 20 V. The central trap structure (S3) is located between the axial position of 47 mm and 67 mm.

since it is of advantage when describing the ion dynamics and aspects ratios of an ion cloud [267]. In the current trap design the simulated axial field distribution shows that the endcap potential is not harmonic throughout the trapping segment. A trapped ion experiences a static saddle-point potential in the trap center of the form

$$\Phi_{stat}(x, y, z) \approx \frac{m}{2e} \omega_z^2 \cdot \left( z^2 - \frac{x^2 + y^2}{2} \right) \quad (6.49)$$

which weakens the radial pseudopotential [268]. Thus a steep axial potential gradient, given by the effective shielding by the neighboring rod segments, might be favorable in trapping large ion clouds.

Although literature shows that the truncation of the RF rods could lead to strong anharmonicities, thus limiting the available trapping volume [269], this effect should

be small in the existing setup since one pair of the trap rods is non-segmented. Also the layout of the RF circuit plays a role: If only one single RF phase is applied to the trap structure, the continuous RF rods cut back the influence of the anharmonicities since the ions observe no RF fringe fields at the axial turning points of the potential. If the RF is applied to all four rods, the simultaneous application of DC and RF on the endcap segments reduces the anharmonicities as well [269].

## 6.5 Detection of the ion cloud by laser induced fluorescence

A standard way to detect trapped ions is by ejecting them from the trapping volume. Afterwards the ion bunch is guided into a charged particle detector. But this detection method poses two problems: In the mass range beyond  $10^5$  Da, the ion detection with an electron multiplier becomes rather inefficient since the secondary electron generation typically requires ion velocities in the range of  $2 - 4 \times 10^4 \text{ ms}^{-1}$  [232]. This requires an acceleration voltage of several 10 keV, up to about 100 keV, depending on the ion mass. For our purposes the detection method should be non-destructive to keep the ions for subsequent measurements.

We have implemented laser induced fluorescence (LIF) in the experimental setup (see figure 6.13). The main advantage of LIF is that as long as the molecule is a fluorophore and the absorption/emission transitions are not quenched by the positive/negative charge attached to the molecular ion, LIF detection is independent on the ion mass. Furthermore, trapped molecules or nanoparticles can be detected in-situ and non-destructively.

Two different excitation laser wavelengths were used. A blue continuous laser diode at 445 nm (Warnlaser) with about 2 W optical power and a green continuous solid state laser at 532 nm with up to 1 W optical power (Wicked Laser). Since the green light is generated internally the laser by frequency doubling a 808 nm pumped 1064 nm beam, a laser line filter centered at  $530 \pm 10$  nm (FB530-10, Thorlabs) was required to block the remaining IR-light to reduce the light background inside the vacuum chamber. An optical shutter was used to block the laser light on demand. A laser beam telescope with a centered pinhole was installed for mode cleaning of

the laser beam. Additionally an iris is mounted into the beam path, reducing the beam halo of the laser beam after the telescope.

The 445 nm light did not require any additional line filters, since it is generated in a single diode and the recorded optical spectrum showed no additional side lines. A neutral density filter (ND) (ND0.5, Thorlabs) was mounted to reduce the optical power. In contrast to the green laser diode, the 445 nm diode emission could be remotely controlled and switched, which required no additional optical shutter.

A dichroic mirror (DM) (DMLP490R, Thorlabs) was mounted into the 532 nm

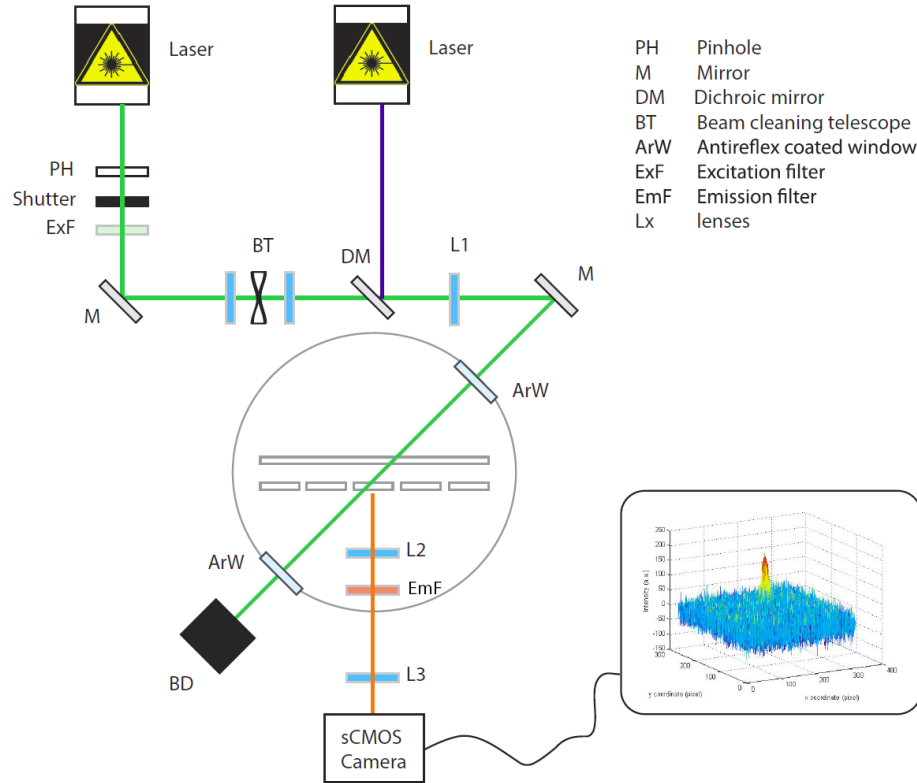


Figure 6.13: Optical setup for in-situ LIF detection of the trapped ions. The molecular ions are excited by a blue or green laser. The fluorescence light (shown in red) is guided and filtered by a bandpass (EmF) before it is detected by the sCMOS camera.

beam path, merging not only the two individual laser beams but also allowing the simultaneous two-color excitation of the ion cloud, if was required for the experiment.

A convex lens L1 ( $f=+200\text{mm}$ ) was mounted directly in front of the vacuum cham-

ber to focus the laser beam area down to approximately  $0.5\text{-}1\text{ mm}^2$ , small enough to pass between the trap rods for illumination of the ion cloud. The large Rayleigh length of the focused laser beam ensured that the laser beam illuminates the ion cloud homogeneously throughout its volume.

The laser beam is guided through an anti-reflection coated optical window (Laseroptik) (ArW) into the vacuum chamber where it crosses the S3 trap segment horizontally under 45 degrees. The beam leaves the trap chamber through a second anti-reflex coated window into a beam dump or a power meter. Independently which of the outer two segment pairs (S1/S5 or S2/S4) was used as endcap, this optical setup allowed an illumination of the ion cloud, located in the center of the trap.

The light emitted by the ion cloud is collected by an optical telescope (L2, L3) in the radial plane of the ion trap, as shown in figure 6.13. The emitted photons leave the vacuum chamber through an inverted view-port which allowed the placement of imaging optics to the confined ions as close as possible. Directly behind the window a convex lens L2 (Thorlabs) with a focal length of  $f=+50\text{ mm}$  collected the LIF light. A longpass filter with a cut-off wavelength of  $500\text{ nm}$  (FEL0500, Thorlabs) blocked the scattered laser light at  $445\text{ nm}$ . The  $532\text{ nm}$  excitation light was blocked by a notch filter with central wavelength at  $533\text{ nm}$  and FWHM of  $17\text{ nm}$  (NF533-17, Thorlabs). A concave lens (L3) projected the emitted light of the ion cloud onto a sCMOS (Andor NEO) detector (pixel size  $6.5\text{ }\mu\text{m}$ ).

The main advantage of using a camera chip over a photomultiplier tube in the planned experiment was the large detection area of the sCMOS chip ( $16.6 \times 14.0\text{ mm}$ ). Since the ion cloud can be trapped and excited over several LIF cycles (several hundreds or thousands), a fast detector in the  $\mu\text{s}$  to ns regime was not necessary. In contrast, the large two-dimensional detector matrix was needed to observe the spatial distribution of the ion cloud under different trapping conditions.

A high detection quantum efficiency over a large spectral range was important to study different classes of fluorescent ions in different spectral regions (e.g. Rhodamine 123, Nile Red with emission around  $500\text{ nm}$  and Sulforhodamine B mainly above  $550\text{ nm}$ ). The Andor NEO camera has a quantum efficiency above 30% throughout the spectral region of interest and even above 50% between  $500$  and  $700\text{ nm}$ . When cooled to its operational temperature of  $243\text{ K}$ , the low dark current ( $0.015\text{ e}^-/\text{pixel}/\text{sec}$ ) of the NEO camera also permits long exposure times and by

binning of pixels, the detection sensitivity is increased when observing very weak LIF signals.

An interesting aspect in the layout of the detection optics is the required magnification, maximum resolution of the system as well as to identify possible sources of background noise. The smallest resolvable structure is given by the Abbe diffraction limit [270]:

$$d = \frac{1.22\lambda}{2NA} \quad (6.50)$$

where  $d$  describes the distance between 2 point-like objects,  $NA$  is the numerical aperture of the optical system. With a calculated numerical aperture of  $NA=0.243$  and a central LIF emission wavelength of about 588 nm (Sulforhodamine B, [250, 271]) the possible optical resolution is about  $1.5 \mu m$ . Since an sCMOS chip is used in our experiments, the optimal achievable magnification ( $M$ ) is determined by the pixel size ( $P$ ) of the camera chip and the radius of the diffraction limited spot ( $r_{\text{diff}}$ ) [272]

$$M = \frac{2P}{r_{\text{diff}}} \quad (6.51)$$

which gives a magnification of  $M \approx 7$  in the described optical system. The estimated optical resolution could allow just the distinction of single ions (mean distance about  $10 \mu m$  in a Coulomb crystal [273]), but this was not in the aim of the experiment. Since the operational temperature of the experiment was at 300 K, the trapped ions would not be in a well defined, crystallized structure but just a thermal cloud distribution.\* To resolve a single ion within, a higher resolution and in fact better time-resolved detector would have been required. The conducted experiment covers mainly the installation and characterization of a linear ion trap in our laboratory with the LIF detection setup to record the complete spatial lengths of the illuminated ion cloud. Since this required no strong magnification, a factor of  $M \approx 2$  was finally used.

Another important aspect describing the imaging optics is the depth of field of the objective lens. This quantity can be calculated by

$$d_{\text{ob}} = \frac{n\lambda}{2NA^2} \quad (6.52)$$

---

\*The phase transition into an ordered, crystallized state is quantified by the plasma coupling parameter  $\Gamma = e^2/4\pi\epsilon_0 a_{\text{WS}} k_{\text{B}} T$  [274] and depends not only on the temperature, but also on the mass to charge ratio of the ions.  $a_{\text{WS}}$  is the Wigner-Seitz radius. For  $\Gamma > 150$  the ions form a Coulomb crystal.

where  $n$  is the index of refraction and NA is the numerical aperture of the objective. In the current setup depth of field was estimated to about  $5 \mu m$ .

Apart from the LIF signal an influence of different noise sources, forming the background in an recorded image, could be expected. The limiting factors on the signal included, next to the background noise were: the solid angle of the imaging optics, the transmission quality of the filters and lenses, thermal noise of the sCMOS chip, laser power as well as number of trapped fluorophores. Though not being a complete list, they represent the main sources for signal background and limitations and shall be discussed in the following.

The emitted fluorescence light from the ion cloud is isotropic, which makes the solid angle the collection path one of the strongest constraints for the LIF collection efficiency. A short calculation shows that the gap between two neighboring rods,  $g = 2.58 \text{ mm}$  at a distance  $d = 5.29 \text{ mm}$  from the trap node, poses a similar opening angle of about  $13.7^\circ$  as the imaging optics. This allows to calculate the solid angle of the system as [275]

$$\frac{\Omega}{4\pi} = \frac{1}{(4f/D)^2} \quad (6.53)$$

where  $f$  is the focal length of the lens ( $f=50 \text{ mm}$ ) and  $D$  is the lens diameter ( $1''$ ). For our imaging system about 1.5% of the emitted light can be collected.

The total number of absorbed and collected photons per ion,  $N_{\text{abs}}$  and  $N_{\text{col}}$ , can be evaluated by the following [58, 276]

$$N_{\text{abs}} = \sqrt{\frac{2}{\pi}} \cdot \frac{\sigma_{\text{abs}} P_{\text{Laser}} \tau}{A_{1/2} h\nu} \quad (6.54)$$

$$N_{\text{col}} = N_{\text{abs}} \eta \frac{d\Omega}{4\pi} t_{\text{Filter}} t_{\text{lens}} t_{\text{VP}} \quad (6.55)$$

where  $P_{\text{Laser}}$ ,  $A_{1/2}$  are the laser power and the radius of the beam waist at focus,  $\sigma_{\text{abs}}$  is the absorption cross section of the molecule,  $h\nu$  is the photon energy and  $\tau$  gives the effective exposure time of the ion in the excitation laser beam. Furthermore  $\eta$  represents the quantum yield of the fluorophore and  $t_{\text{filter}}$ ,  $t_{\text{lens}}$ ,  $t_{\text{VP}}$  describe the transmission factors of the optical filter, lenses and the viewport respectively.

The emitted fluorescence light from the trapped ions is expected to be weak (e.g. about 100 photons/sec in case of trapped Rhodamine 6G [255]) which requires a good signal-to-noise ratio in the detection. While equation 6.55 describes the overall

photon collection efficiency of the optical beam path, the signal-to-noise ratio can be described by [277]

$$\frac{S}{N} = \frac{D\Phi_{\text{LIF}}\sigma_{\text{abs}}Pt/Ah\nu}{[(D\Phi_{\text{LIF}}\sigma_{\text{abs}}Pt/Ah\nu) + C_{\text{b}}Pt + N_{\text{d}}t]^{\frac{1}{2}}} \quad (6.56)$$

where  $S$  describes the peak signal of a emitting fluorophore with quantum yield  $\Phi_{\text{LIF}}$ ,  $\sigma_{\text{abs}}$  is the absorption cross section,  $P$  is the laser power,  $h\nu$  is the photon energy,  $t$  is the effective interrogation time,  $A$  the laser beam cross-section at the position of the ion cloud,  $N_{\text{d}}$  is the dark count rate while  $C_{\text{b}}$  is the background count rate per watt excitation power. The detector efficiency  $D = \eta_{\text{quantum}}F_{\text{p}}F_{\text{f}}F_{\text{l}}$  consists of the quantum efficiency  $\eta_{\text{quantum}}$  of the sCMOS chip,  $F_{\text{p}}$  the solid angle of the system,  $F_{\text{f}}$  the fraction of LIF light passing the optical filters and  $F_{\text{l}}$  is the total transmission of the optical components and the chamber window.

For our experimental system, assuming trapped Sulforhodamine B, the different parameters can be specified in the following (table 6.2). From equation 6.55 the number of absorbed photons is estimated with about 1000 photons per ion and second. Estimated with the given experimental parameters (table 6.2) approximate 8-9 photons per ion and time  $\tau$  will reach the detector. Although this is quite a low number, a detectable LIF signal can be expected from an ion cloud having  $10^3$  to  $10^4$  ions. Similar, equation 6.56 yields an estimated signal-to-noise ratio of about 17 when a camera integration time of 2 seconds is taken. While this value shows that the ion signal should be easily detectable, the low number of total emitted photons shows that all possible background light sources should be reduced as much as possible.

External stray light was blocked at all optical ports into the vacuum chamber with a black anodized aluminum foil, except for the small gaps required for the different laser beams or for the imaging optics. For the excitation and imaging, the optical path of the LIF excitation path was completely encased by lens tubes. Also the pressure gauge on the side of the vacuum vessel needed to be blocked during a LIF measurement, since the thermal emission contributed to the image noise of the camera. Furthermore the light of the laboratory was reduced to a minimum during experiments.

---

<sup>†</sup>This value was determined by an estimated axial secular frequency of  $2\pi \times 6.3$  kHz taken from SIMION simulations.

parameter	value
$P_{\text{Laser}}$	0.5 W
$A$	1 $mm^2$
$\sigma_{\text{abs}}$	$1.5 \cdot 10^{-20} m^2$ [278]
$\eta$	0.8 [279]
$\tau$	0.017 s <sup>†</sup>
$t_{\text{lens}}$	0.97
$t_{\text{notch}}$	0.95
$t_{\text{filter}}$	0.87
$t_{\text{VP}}$	0.9
$\eta_{\text{quantum}}$	0.6
$N_d$	0.015 $e^-/\text{pixel}/\text{sec}$

Table 6.2: An estimation of the different factors determining the number of collected photons on the sCMOS chip in the LIF detection is shown for the case of Rhodamine dyes.

In conclusion, the estimations of the expected signal for our experimental optical setup show that LIF signals with a reasonable signal-to-noise ratio should be detectable. Since the LIF excitation was restricted to two single wavelengths (445, 532 nm) the choice of suitable fluorophores was limited. The molecular ions should have a high quantum efficiency for an efficient detection, while the fluorescence should not be quenched by the ion charge. In this case molecules from the family of Xanthene dyes are favorable (see section 6.7.1). To allow for a large number of excitation cycles of the trapped fluorophore, the Stokes energy needs to be removed from the ion (see section 6.2), otherwise the overall detection efficiency of the trapped ion cloud will be decreased. Such an energy transfer can be achieved by collision with light, neutral atoms, e.g. the buffer gas inside the ion trap (see [244, 255] as well as 6.1.4 and 6.7.5). If a sufficient high number of collisions is provided, a good ion signal should be detectable in our linear ion trap.

## 6.6 Design of electric circuits and timing sequences

As described in chapter 6.1, for trapping ions inside the designed linear quadrupole ion trap radio-frequency (RF) as well as direct-current (DC) fields are required. While the RF field traps the ions in radial direction, a DC field is essential for the axial confinement. DC potentials might also be necessary in case the trapped ion cloud needs to be radially shifted with respect to the on trap axis or for mass

selection.

The RF power supply source needs to fulfill the experimental requirements, since the required frequency range and amplitude of the RF is determined by the mass-to-charge ratio of the ion. In selecting the RF parameters, care has to be taken that a stable confinement field is created as determined by the stability parameter  $\mathbf{q}$  while also well defined frequencies and amplitudes are required for mass selection.

- Since in the different experiments it was planned to trap a wide range of masses ( $10^2$  Da - MDa) the RF drive needs to be tunable over a large frequency range, here from approximately 1.5 MHz down to 10 kHz. The high frequency is essential for low masses (few hundred Daltons), the low frequency is required for masses above  $10^5$  Da. Although it would be interesting to have the possibility of varying the frequency over the complete range (10 kHz - 1.5 MHz), a small band tuning range over 200-300 kHz (at  $2\pi \times 1$  MHz  $\Omega_{\text{RF,main}}$ ) were considered sufficient for the planned measurements.
- The depth of the pseudopotential is directly proportional to  $V_{\text{RF}}^2$  and the stability parameter  $\mathbf{q}_{\text{RF}}$ . For the envisaged high limit of the frequency range (about 1.5 MHz) for an ion mass of 581 Da, the minimal RF amplitude should not be less than about 50 V. Otherwise the effective potential depth is less than 1 eV, allowing only to trap few ions instead a large cloud. Although a high amplitude is in favor of deep trapping potentials, a maximal value below 1 kV should be sufficient for the envisaged experiments, higher voltages risk sparkovers.
- The ion trap and associated wiring is essentially a capacitive load given by the capacitance of the rods, while the influence of the inductance and resistive part can be neglected (former) or is given mainly by the wires (latter). The total capacitance of the linear quadrupole can be estimated by [280]

$$C_{\text{trap}} = \frac{4\epsilon_0 L}{r_0^2} \left( x \cdot \sqrt{x^2 - r_0^2} \right) \Big|_{x=r_0}^{x=(2\chi+1)r_0} \quad (6.57)$$

where L denotes the total length of the quadrupole (114 mm) and  $\chi$  is the ratio of the electrode radius, r, to inscribed radius,  $r_0$ . With the ion trap design parameters given above, the trap capacitance can be estimated to  $C = 41.8$

pF.

This capacitance value allows the calculation of the impedance at both RF frequency borders, 10 kHz as well as 1 MHz

$$Z_{C,1\text{MHz}} = \frac{1}{i\omega C} = 3.81k\Omega \quad (6.58)$$

$$Z_{C,10\text{kHz}} = 381k\Omega \quad (6.59)$$

Since we require high voltages ( $\approx 250$  V), the required driving power of the RF generator would be  $P = V^2/R = CV^2\omega/4\pi$ , or less than 10 W with  $C=41.8$  pF.

An application of RF voltages via a well-matched circuit (e.g. impedance matched) leads to a high Q of the circuit and thereby to high amplitudes at low driving powers (for the case of helical coil resonator see [281] or [282]). Although this can be a benefit, the matching itself can be difficult and time consuming [283]. Since we plan on varying the analyte mass, a new matching will be required with each change. This can be circumvented by using strong RF sources, where high amplitudes can be reached, even when driving into high impedances.

- It is often desirable to switch between a fully symmetric ion trap and a configuration where the RF is applied to one rod pair, only. This requires an RF source which allows switching between single-phase and dual-phase operation.

### 6.6.1 The RF power supplies

To fulfill all mentioned criteria two RF generators had to be used, as described in the following section.

#### Single phase RF drive

One of the RF drive schemes uses a low power RF signal, amplified with an RF amplifier and directly applied to the trap rods, as shown in figure 6.14.

The sinusoidal RF signal (Stanford Research Systems, DS345) can be varied in steps of 10 mV up to a value of 1 V (peak-peak) in a frequency range between 10

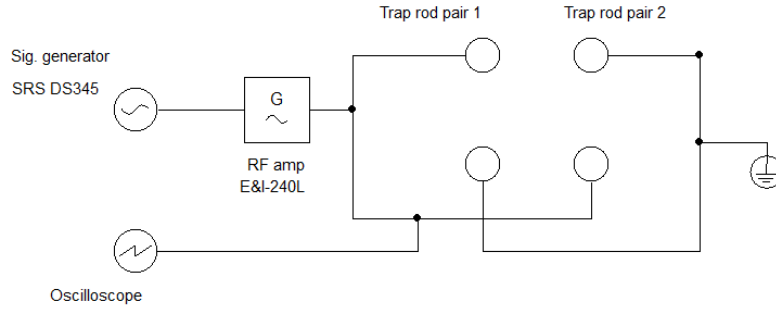


Figure 6.14: Schematic diagram of the RF circuit providing a single-phased RF to the linear quadrupole rods. The RF is generated in the signal generator and amplified afterwards. An online read-out of the RF amplitude was done with an oscilloscope via an HV probe.

kHz and 30 MHz, in steps of 1 Hz. These specific experimental values were limited by the amplifier switched behind the RF source.

A solid-state broad band power amplifier (E&I, model 240L) with a frequency span from 10 kHz to 12 MHz, a nominal output power of 40 W and a saturation power of maximal 100 W amplified the signal to typically 40 - 60 W (the specific values did depend on the RF settings). Its output signal was guided by a BNC cable to a vacuum feedthrough and to one pair of the quadrupole rods.

In order to switch the amplitude an external RF switch (MiniCircuits) was installed at the input of the RF amplifier, allowing a fast switching of the RF potential on the trap rods. A high-voltage probe (LeCroy, PP006A, 10:1, 500MHz, 10 M $\Omega$ ) was tapped to the electrical vacuum feedthrough and allowed to monitor the RF signal with an oscilloscope.

In order to test the linearity of the RF amplifier the input RF amplitude was varied, while the amplified signal was measured by the oscilloscope. The amplitude was determined by taking the mean over 100 subsequent sweeps of the oscilloscope, recorded under real-experimental conditions.

The data of figure 6.15 show a linear amplification behavior, the error bars are given by the standard deviation of the measured signal. Hardly any background noise was introduced by the RF amplifier. An identical behavior was observed at higher frequencies up to 1 MHz as well.

The RF amplifier had an output impedance of 50 Ohm, while the ion trap had an impedance of several k $\Omega$  (following equation 6.59 at a frequency of 10 kHz), which leads to a reflection of the RF power (greater 90%) by the load impedance

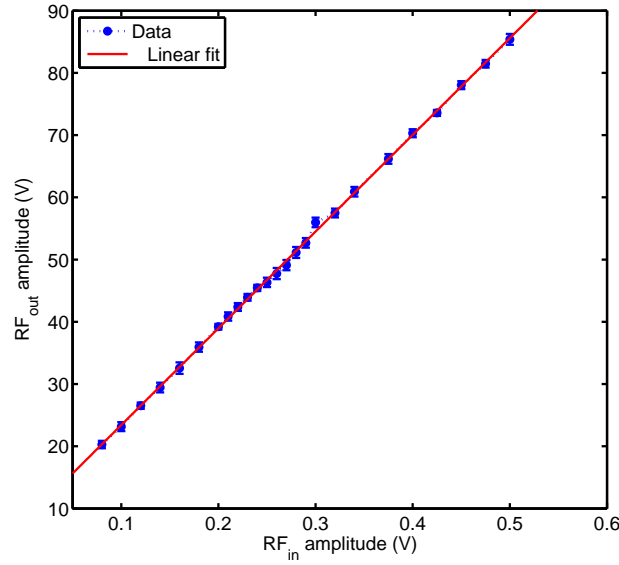


Figure 6.15: A scan of the RF signal shows a linear amplification of the input signal by the RF amplifier. The red line represents a linear fit as a guide for the eye. The RF drive frequency was 10 kHz.

back into the source. The amplifier could operate into any load, thereby accepting any reflected power without damage, allowing the generation of sufficiently high amplitudes ( $\approx 200$  V) for a stable confinement of the ions when experimentally needed. This made a daily change of different experimental settings (different ion species) possible, since no impedance matching was required.

In the presented setup, this source is generally limited in its output amplitude with a maximal amplitude below 200 V (zero-peak) and by the fact that only one single phased signal could be used. While this is sufficient for basic trapping experiments, independent on the ion mass, the effective pseudopotential is quite shallow in the order of few eV only.

### High power oscillator circuit as RF power source

A different path for driving the ion trap was chosen for the second RF driver in the experiment: An RF generator was designed and built, similar to [283,284], as shown in figure 6.16. Compared to the previously described circuit, the new design is a high voltage oscillator powered by a pentode transmitter tube connected in a push-pull

configuration. The oscillation frequency of this generator can be calculated by

$$f = \frac{1}{2 \cdot \pi \cdot \sqrt{C_{\text{tot}} L_{\text{tank}}}} \quad (6.60)$$

where  $L_{\text{tank}}$  is the inductance of the oscillator coil and  $C_{\text{tot}} = C_{\text{tune}} + C_{\text{load}}$  is the total capacitance with  $C_{\text{tune}}$  representing the capacitor in the oscillator circuit and  $C_{\text{load}}$  combining the combined capacitance of the ion trap and the vacuum feedthrough, the BNC cables and connectors.

This RF source was designed for trapping of ions in the mass range between 400 and 2000 Da, for which the required frequency in the presented ion trap geometry was estimated to be typically  $\Omega \approx 2\pi \times 1$  MHz (see figure 6.7). As discussed above, this device needs to be able to operate at high voltages of up to 600 V.

In the parallel LC circuit the capacitance is a mechanically controlled air-spaced variable rotary capacitor which could be continuously varied between  $C_{\text{var}} = 15$  and  $C_{\text{var}} = 430$  pF. An estimation showed that an inductance of 100 mH was required with a capacitance of 250 pF and  $\Omega = 2\pi \times 1$  MHz.

The tank coil is a cylindrical air-coil with a diameter of 5 cm and a total length of 20 cm. A 2 mm copper wire was wound  $N=60$  times around a cylindrical plastic tube. The construction allowed to tap the coil at any winding to vary the inductance. Since the diameter of the coil is small compared to its length  $l$ , the inductance of the coil could be calculated with equation 6.61

$$L = N^2 \cdot \frac{\mu_0 A}{l} \quad (6.61)$$

where  $\mu_0$  the vacuum permeability and  $A$  the cross section of the coil. Actually the resulting inductance,  $L \approx 45$  mH, appeared smaller than estimated from equation 6.60 ( $L = 100$  mH). Since the total capacitance,  $C_{\text{tot}}$  - the sum of the rotary capacitor, the capacitances of the load, feedthrough, BNC cables and other stray sources - determines the actual frequency, the inductance value was still sufficient to reach the aimed frequency.

To force the circuit to oscillate symmetrically, the coil of the circuit was center tapped. The taps at the outer ends of the coil were required to provide a feedback for sustaining the oscillation. The RF voltage was fed into the pentode tube, a dual end tetrode (SRS 4451), which, in contrast to similar RF generators [283], required

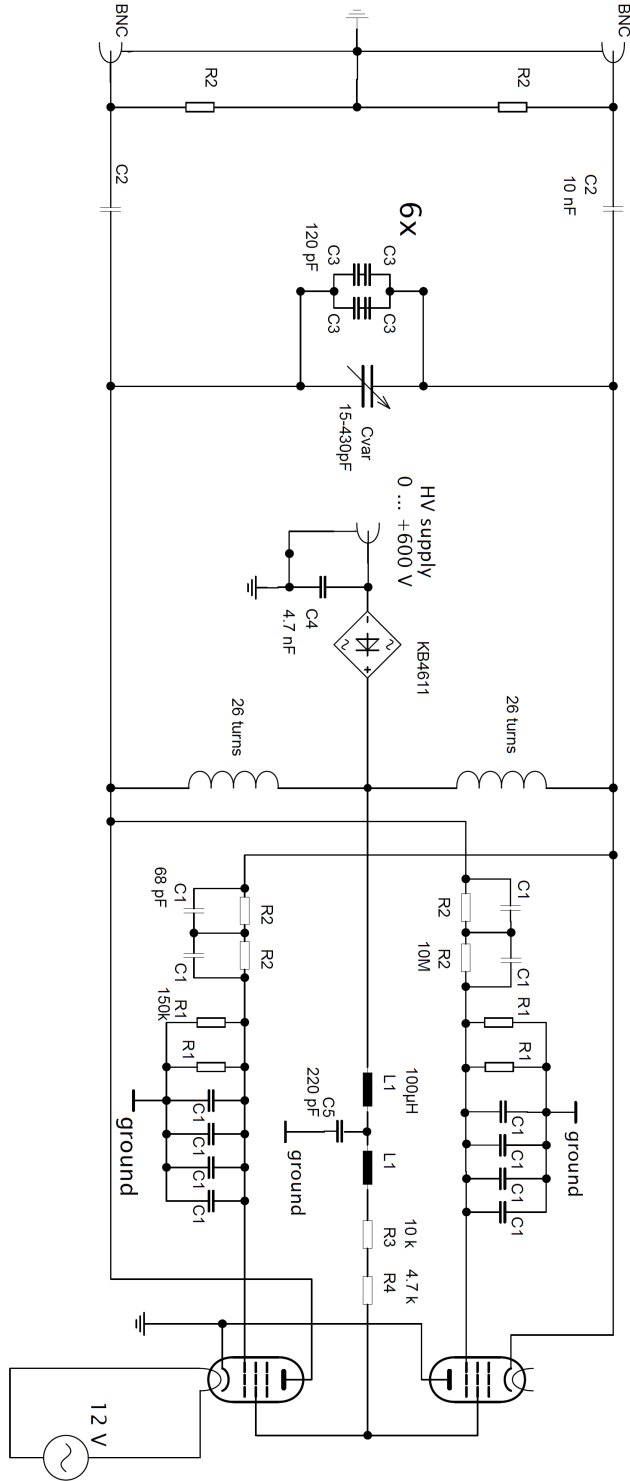


Figure 6.16: A schematic circuit diagram of the RF generator is shown, similar to [284]. The specific values of the different elements is given also in table 6.3.

only a single tube.

The resulting RF amplitude on the ion trap electrodes is about the same as to the plate voltage in this push-pull oscillator design. For the high voltage feed-in a high-voltage DC power supply capable of 700 V, 1 A output was used. The electron tube was able to deliver the requested voltage of max. 600 V. The resulting 1200 V between two neighboring ion trap electrodes provides a sufficiently deep effective potential. The electric power dissipated by the RF source was typically of the order of 50 to 120 W, depending on the chosen RF amplitude.

To prevent reflection of RF power into the driving DC supply, a bridge rectifier (KB4611) was introduced between the DC supply and the inductors as well as two connections to ground, blocked by a capacitor (C4, C5 in figure 6.16), which allowed a stable operation up to 700 V input voltage. A similar measure was taken at the output of the RF generator. In each of the two RF phases a blocking capacitor (C2) allowed to simultaneously apply the RF as well as a DC signal to the trap rods.

In measurements where larger  $q$  values at high RF amplitude were required (as an example see section 7), the frequency needed to be decreased to 800 - 900 kHz, requiring larger capacitance values  $C_{\text{var}}$ . A solution was found by soldering two 120 pF, 1 kV rated, capacitors (C3 in figure 6.16) in series. Two sets of these were combined in parallel, which resulted in a total value of 120 pF, but the overall amplitude rating was higher than the rated 1 kV, which allowed to reach the required RF amplitudes of 700 V without electrical break-down.

As shown in figure 6.16, a total of six sets of capacitors were introduced in parallel to  $C_{\text{var}}$ , which finally reduced the RF frequency to approximately 800 kHz, as required for measurements of the two-tone trap (see chapter 7).

The values of the different components (shown in table 6.3) in the circuit diagram (figure 6.16) provide an oscillation frequency between 800 kHz and 1.1 MHz.

Stable RF operation started between 25 and 30 V of the external DC power supply. With increasing DC potentials the RF amplitude grew linearly in strength with no saturation effects visible even for the highest potentials, shown in figure 6.17a. The linear increase of the RF amplitude is independent on the actual frequency value. A comparison of both measurements with the first bisecting line (shown in green in figure 6.17a) illustrates that with increasing DC potential the RF amplitude is dampened because of the current limit of the DC supply.

element	value
R3	10 k $\Omega$ , 10 W
R4	4.7 k $\Omega$ , 10 W
L1	100 mH
C1	68 pF
R1	150 k $\Omega$
R2	10 M
C2	10 nF
C3	120 pF
C4	4.7 nF, 2 kV
C5	220 pF, 1 kV

Table 6.3: Electrical elements used in the current RF generator, as shown in figure 6.16.

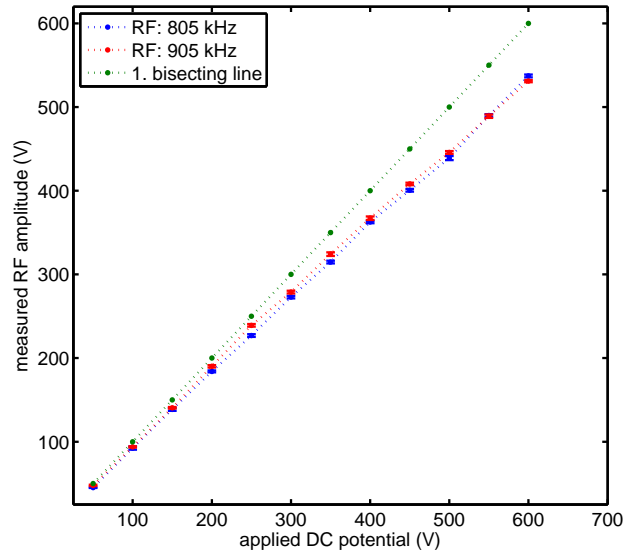
The complete electrical input power,  $P = U \cdot I$ , consumed by the RF generator is shown in figure 6.17b for two different RF frequencies. With increasing DC input, the dissipated power consumption increases quadratically, which can be understood from  $P = U^2/Z_{\text{tot}}$ . In the measurement we could observe a high stability of the RF amplitude, where short time fluctuations of the amplitude could be as large as  $\pm 4$  V, but in most cases they were limited to less than 0.2% of the output.

Variations could, however, be observed for the RF frequency during the first 20-30 minutes after switching-on of the RF power supply where the frequency increased by 10-15 kHz. Afterwards, the RF frequency was long-term stable, at the level of about 0.5%. This behavior can be explained by thermal effects of the pentode and/or tank coil during the initial time of operation, shifting the operational point of the RF generator.

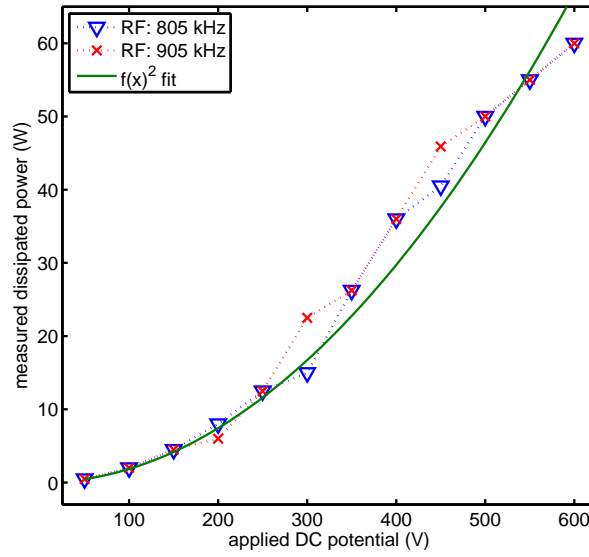
### 6.6.2 Endcap potentials

For an axial confinement of the ions, positive endcap voltages between 5 V and 80 V were sufficient, in most experiments typically only 20 V were needed for the axial confinement.

To allow a controlled switching of the endcap potential, a switching circuit was designed (figure 6.18): The segments are floating electrodes, which makes switching with a single transistor difficult. A solution was found in an optocoupler based transistor circuit. Here the NPN transistor was used to switch the optocoupler, which



(a)



(b)

Figure 6.17: The operation characteristics of the RF generator are shown. Graph 6.17a displays the linear increase of the RF amplitude, while 6.17b shows the dissipated power inside the RF generator. The green lines represent fits as a guide for the eye. For each data point the RF amplitude was measured over 200 subsequent sweeps on the oscilloscope. The RF generator showed a slow drift towards higher RF frequencies with increasing amplitudes due to thermal heating during the operation, which required that the actual frequency was adjusted and stabilized before each individual measurement.

in turn routed the positive endcap potential to the trap segments. For a separate operation of the two endcaps, two individual optocoupler circuits were installed, which allowed to switch the front and back endcap individually.

The rise time of the endcap potential was measured to be between 2.5 and 3.0  $\mu\text{s}$

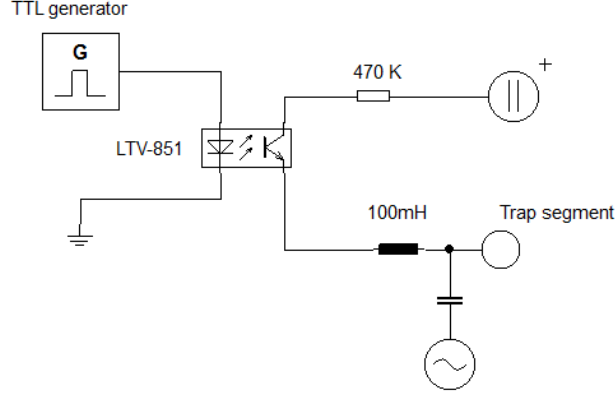


Figure 6.18: For the application of the axial DC potential a TTL switched a NPN transistor is used, which in turn controlled an optocoupler for applying the DC onto the trap segments.

with a decay time in the order of a few milliseconds. This measured switch-on time was determined to be fast enough for the entering of the ions into the trap, since the ion trap loading process consisted typically of several laser desorption pulses. Also the decay time was sufficiently fast for the experiment, since at the end of an experimental cycle the ion trap was emptied and the buffer gas pumped out (several seconds).

Since the ion trap segments were both used as RF electrodes and as DC endcaps, (figure 6.18) an inductance was installed directly at the vacuum feedthrough, separating the applied RF drive from the DC power supply. Similarly, a capacitor with 120 pF blocked the DC voltage from influencing the RF source.

### 6.6.3 TTL control and timing sequences

A complete experimental cycle of the ion trap requires a well defined pulse sequence for the activation and/or control of the different instruments or sequences. This included the application of the endcap potentials, the LIF lasers, the desorption laser. Two master trigger sources were used: A stand-alone digital delay / pulse generator (Berkeley Nucleonics Corporation, Model 575) and a PC controlled pulse

generator (NI, model PCI-6363). The former allowed a simultaneous triggering of up to 8 different devices with a time resolution of 250 ps up to 15 min. The latter was required when more complex experiments, like the double-mass trapping or two-color LIF detection (see chapter 7), requiring more than eight independent trigger signals, were performed. Thereby up to 32 independent TTL pulses could be created with a timing resolution ( $\approx \mu\text{sec}$ ) sufficient for our current experiments.

## 6.7 Experimental setup

Following the previous sections describing the design considerations as well as the chosen experimental design of the linear multipole, a description of the linear quadrupole ion trap experiment set up in the laboratory will be given here. A schematic representation of the different measurement steps in a trapping cycle is shown in figure 6.19. In short, the experiment will be able to trap ions, created externally in a

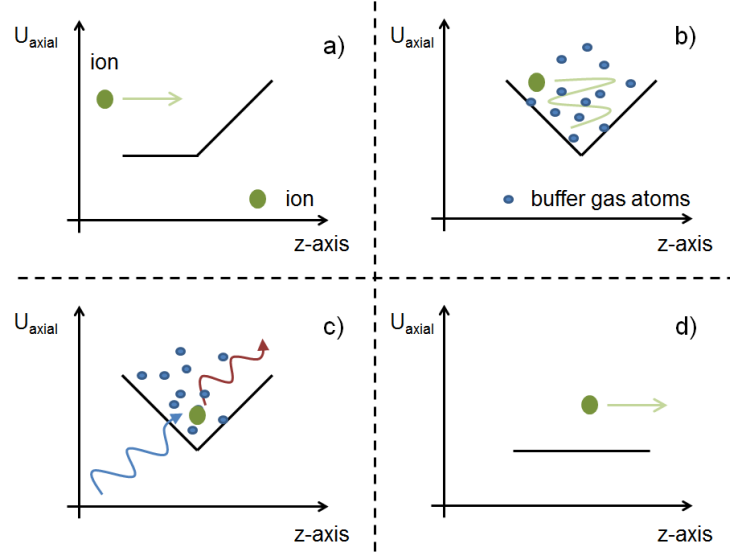


Figure 6.19: The different, basic steps during a measurement are shown schematically: Ions are loaded initially (a) and cooled in a buffer gas atmosphere (b). During the measurement the ions are excited by a LIF laser beam and the emitted photon is detected (c), in a final step the trap potential is lowered and the ion is ejected (d). The z-axis denotes the longitudinal trap axis.

MALDI source (a) and cool the ion's kinetic energy by buffer gas cooling (b). Upon the successful cooling, a measurement on the ion cloud takes place (described in the following) and the ions are subsequently detected by laser induced fluorescence (c).

In the final step the axial and radial ion trap potential is reduced and the ions are ejected (d).

In the experiment, the loading of the ion trap was based on MALDI: A pulsed UV laser operating at 337 nm (VSL-337) was guided towards the sample disc, having a diameter of 30 mm, located 25 mm in front of the ion trap ((1) in figure 6.20). Since the ions shall be injected parallel to the longitudinal axis of the ion trap, the surface of the sample was oriented perpendicular to the radial plane of the ion trap. Furthermore the sample was positioned such, that the desorption laser spot coincided with the longitudinal trap axis on the sample surface. The disc was mounted off-center on a rotational vacuum feedthrough to allow extended use of the sample. The UV laser beam was focused by an  $f = 500$  mm lens to a circular area of about

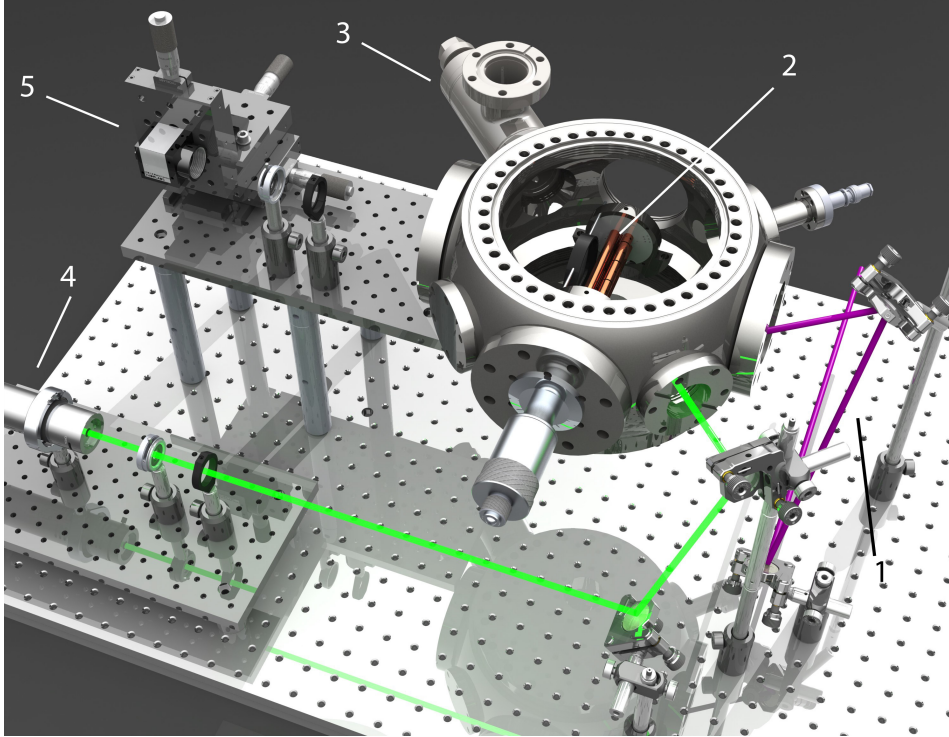


Figure 6.20: The laser desorption and ion confinement in the ion trap experiment. The ions are desorbed by a pulsed UV laser beam (1) and are trapped in the ion trap (2). Buffer gas for cooling of the ions is introduced by a leak valve (3). The trapped ion cloud is imaged using laser induced fluorescence (4,5).

$1 \text{ mm}^2$  at the sample surface. It hit the sample under an angle of about 40 degrees with respect to the longitudinal trap axis. In the desorption process the maximal pulse energy of the desorption laser of  $\approx 250 \mu\text{J}$  was used. Lower pulse energies for the MALDI process showed no significant benefit for the trapped ion signal,

while higher pulse energies or a tighter focus would have increased the probability of fragmentation of the analyte ions (as discussed in chapter 3.1 and the references given within). The  $N_2$  laser was operated typically with a repetition rate of 20 Hz. The sample disc was turned during loading to expose a fresh sample spot in every desorption shot. To enhance the ion transfer between the sample and the ion trap, a DC potential could be applied onto the sample plate.

During the desorption process the ions are released from the sample surface in a plume that moves into the ion trap with high speed of several hundred meters per second [113,114], which requires a dampening mechanism for their kinetic energy. We have realized a buffer gas cooling, since it is applicable to all sorts of particles, independent of their internal level structure. Helium was introduced as a neutral buffer gas through a TTL controlled metering valve ((3) in figure 6.20) which was opened in coincidence with the MALDI process to trap a large fraction of the desorption plume.

Two different valves were tested: a combination of an electrical controlled ball-valve together with a metering valve (VML, Hositrad) and a fast-pulsed valve (Parker Hannifin Corporation) mounted opposite of the sample on the trap axis in the vacuum chamber (not shown in figure 6.20). The helium created a controlled, 'quasi-continuous' buffer atmosphere with partial pressures of up to  $10^{-2}$  mbar, with the majority of the experiments conducted at pressures between  $2 - 3 \times 10^{-3}$  mbar. Higher pressures increased the risk of spark-overs and lower gas densities reduced the cooling and thereby loading efficiency.

When short buffer gas pulses were more advantageous in the experiments (like mass selection or double-mass trapping), gas pulses with a width between 300  $\mu s$  up to 3 ms were directed along the longitudinal trapping axis, counter propagating the ions created in the desorption process. The timing of the gas pulses was chosen in such a way that the majority of the desorption plume and the gas pulse overlapped within the trapping volume (figure 6.21). Compared to the continuous buffer gas, the short pulses had the advantage of shorter pumping times after the buffer gas input was stopped, allowing a faster change of the environmental conditions for the confined ion cloud. Also the peak gas density inside the gas pulse can be higher compared to a steady buffer gas, which allowed a more efficient reduction of the kinetic energy of the ions.

The buffer gas pressure was measured by a hot cathode - 'Bayard-Alpert' pressure gauge (Ionivac, Leybold), mounted on a side flange at the vacuum chamber. In the case of the continuous buffer gas, these readings should correspond to the actual pressure inside the ion trap. But in the case of the introduction of the pulsed buffer gas a higher gas density inside the trapping volume than the pressure readings must be assumed.

The radial confinement of the pre-cooled ions was realized via the RF potential: To trap the major part of the desorbed ions, the radio frequency is switched on prior the first desorption laser shot. The electrical RF circuit (LC tank circuit or RF amplifier) was chosen depending on the molecular ion used. For axial trapping the endcap potentials are applied according to timing scheme presented in figure 6.21.

At the end of the trapping cycle, the ion cloud was analyzed using LIF imaging, as presented in section 6.5. The ions needed to be cooled during the entire LIF period in order to counteract the internal heating of the molecules caused by repetitive deposition of Stokes energy in the fluorescence cycles.

For a successful measurement of the ion cloud a specific timing sequence of the different trigger pulses is necessary. The case of a typical loading-trapping-detection cycle of an ion cloud in the ion trap is shown in figure 6.21. An ion trap cycle is started by

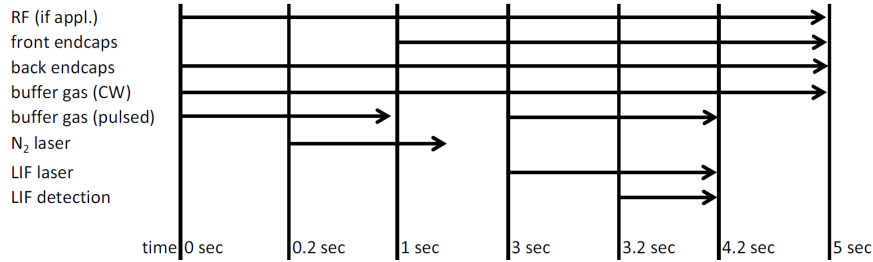


Figure 6.21: The time sequence of the different triggers active in a typical loading-detection experiment is shown. The complete time of the experiment was about 5 seconds.

applying the RF drive to the trapping rods. At the same time the endcap potential was applied to the desired trap rod segment furthest from the sample disc. Also, directly at the starting of the trapping sequence the buffer gas was introduced into the vacuum chamber. If a continuous gas atmosphere was used in the experiment, this marked the opening time of the buffer gas valve. In the case of a pulsed gas use, the trigger timing needed to be matched to the desorption laser. The optimal time

delay between the two pulses was when the desorbed ions interacted with the gas inside the trapping volume. This timing was determined experimentally and was found to be about 4.5 ms (for Sulforhodamine B).

The desorption laser was activated only 200 ms after the trap sequence started. This ensured that most of the MALDI sample desorption pulses happen at an already suitable buffer gas atmosphere (in case of the continuous gas scheme). The exact number of the TTL pulses in this sequence depended on the selected number of desorption shots and the chosen repetition rate of the laser. Typically 30 to 50 laser pulses at a frequency of 20 Hz were used for filling the ion trap with sample. Independently, the endcap close to the sample disc was activated at a time delay of 1 second.

In the following, the ions were stored inside the trapping volume for several seconds with the LIF laser beam exciting the molecules was switched on only after a time delay of 3 seconds. This waiting time was introduced for several reasons: On the one hand it allowed a variation of the number of sample desorption pulses between two subsequent measurements without the need to change the trigger sequence. More importantly, it also allowed the ions to thermalize with the buffer gas.

To take the switching times of the LIF lasers into account, a delay of 200 ms was introduced between the LIF lasers and the sCMOS, which had an exposure time of one second. Depending on the type of ion trapped or the size of the ion cloud, this time was prolonged up to 4 seconds. When the experiment was performed with a pulsed buffer gas, a second set of trigger pulses was sent to the valve at the same time as the LIF laser was started (figure 6.21).

The detection of the ion cloud concluded the trapping cycle and the RF as well as DC were switched off. Only the LC circuit required a manual reduction of the amplitude, thereby a longer time interval than indicated in the figure 6.21.

A similar timing sequence was implemented for mass selection measurements (figure 6.22). The TTL trigger sequence for the loading process was kept identical to the previous case. Since the mass selection required an additional trigger, the detection of the ion cloud was shifted towards a later point in time. Directly after loading and thermalization, the mass selection is initiated by irradiating the ion cloud with an auxiliary radio frequency (AUX RF) for 1-2 seconds, after which the AUX RF was switched off and the ion cloud was detected.

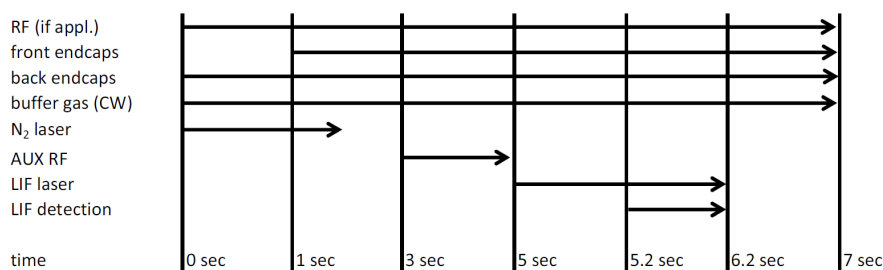


Figure 6.22: The required triggering sequence for the mass selection of the ion cloud. It is similar to the previous case (figure 6.21), but due to the required additional trigger, the overall timing sequence is prolonged.

### 6.7.1 Choice of particles

The first goal of the ion trap experiment was to explore volatilization of molecules and nanoparticles of different mass classes by laser desorption with subsequent confinement and detection in an RF field. The particle were selected according to the following criteria:

- The mass of the molecule should cover both ends of the region of interest from the lower  $10^2$  Da to  $10^9$  Da. It is known that MALDI can volatilize not only light ions in the mass range of  $10^2$  Da, but also massive nanoparticles [243]. Trapping of such ions in radio-frequency fields was also shown previously in this mass range [243,285,286]. Compared to nanospheres, molecules in the low mass range have the advantage of a limited mass in a defined small range. This defines the necessary ion trap parameters quite well, easing initial trapping attempts. The high mass range is of interest for later measurements, where the suitability of a linear ion trap for future matter-wave experiments will be investigated.
- Since the detection of all trapped ions was done via fluorescence, the charge on the molecule should not quench the fluorescence properties of the fluorophore. The ion should also possess high absorption cross sections at the available laser wavelengths (445, 532 nm). To detect a strong LIF intensity, the quantum yield should be high which, at the same time, keeps detection times short.
- The selected molecules should be thermally stable to survive the desorption without fragmentation. This could be a problem for high-mass bio-molecules.

Taking these criteria into account, different molecules were tested in the experiments: Two of the molecules fulfilled the above mentioned criteria and were therefore used as a 'working horse' in the presented measurements. On the low mass side, Sulforhodamine B was chosen while the mass range of greater  $10^6$  Da was explored with fluorescent polystyrene nanospheres. Apart from these particles, different other fluorescent molecules were tested as well, namely Rhodamine 123 and Sulforhodamine 101, both from the group of Xanthene dyes. Also Rhodamine-labeled Bovin Serum Albumin (BSA) was tested in an experiment. For all these molecules the recorded fluorescence signals were very weak, indicating that either the excitation laser wavelength was not matching well or the emission probability is reduced with the charging of the molecule. It was found that certain dyes display no or only low fluorescence as ions in the gas phase under the described experimental conditions, even when they are good fluorophores in solution [287]. One of these examples was the dye Phthalocyanine, where no LIF signal could be observed in the ion trap.

Sulforhodamine B, a Xanthene dye, is a well known laser dye with excellent LIF properties in the red. It is chemically stable, water-soluble and has a fluorescence quantum yield (in solution) of greater than 0.9 [250]. In its dry form it is a monosodium salt and has a molar mass of 580.65 g/mol. The corresponding molecular structure is shown in figure 6.23.

Similar to most of the fluorescent dyes the maximum of the emission and excitation

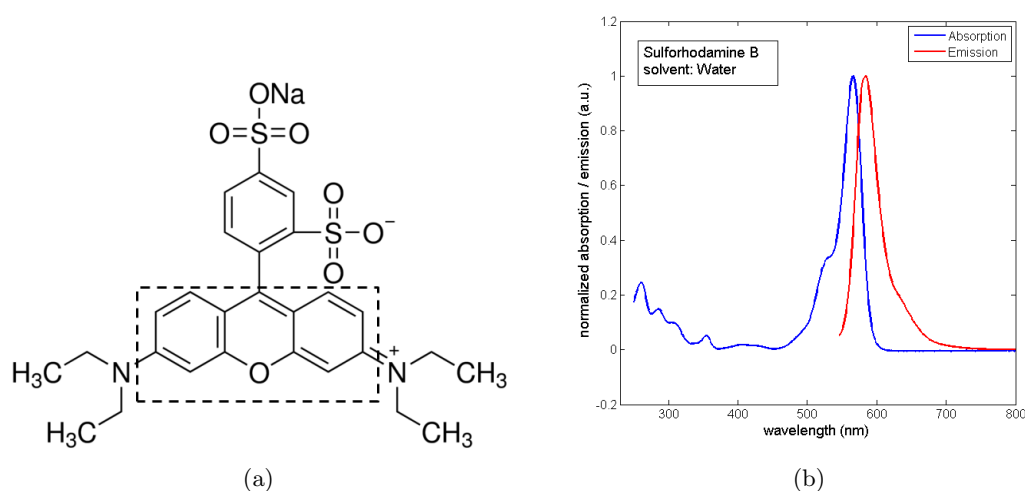


Figure 6.23: The molecular structure of Sulforhodamine B is shown in 6.23a. The Xanthene backbone is visible, indicated by the dashed box. The absorption/emission spectrum of Sulforhodamine B in water is shown in 6.23b [288].

line depends strongly on the solvent. An absorption/emission plot of the molecule in water is shown on the right side of figure 6.23. In a polar environment, like water, the excitation/emission are found at  $\lambda_{\text{ex}}=565/\lambda_{\text{em}}=586$  nm [234]. These values shift towards the blue for less polar solvents, in vacuum or gas-phase this can be more than 30 nm for different Xanthene dyes [242,247,249].

Strong LIF intensities of Sulforhodamine B ions trapped in an RF trap were reported in the literature when excited at a wavelength of  $\lambda_{\text{ex}}=514$  nm, while with an excitation wavelength of  $\lambda_{\text{ex}}=488$  nm less strong signals could be recorded [250]. Since the absorption band of this molecule is rather broad, it can be expected that an efficient excitation with our 532 nm LIF laser is possible.

Fluorescent polystyrene nanoparticles with a diameter of about 40 nm were chosen for the demonstration of ion trapping of particles with a high mass to charge ratio. Figure 6.24 shows a SEM image of the nanospheres.

We purchased nanobeads derivatized with the fluorophore Nile Red, which has

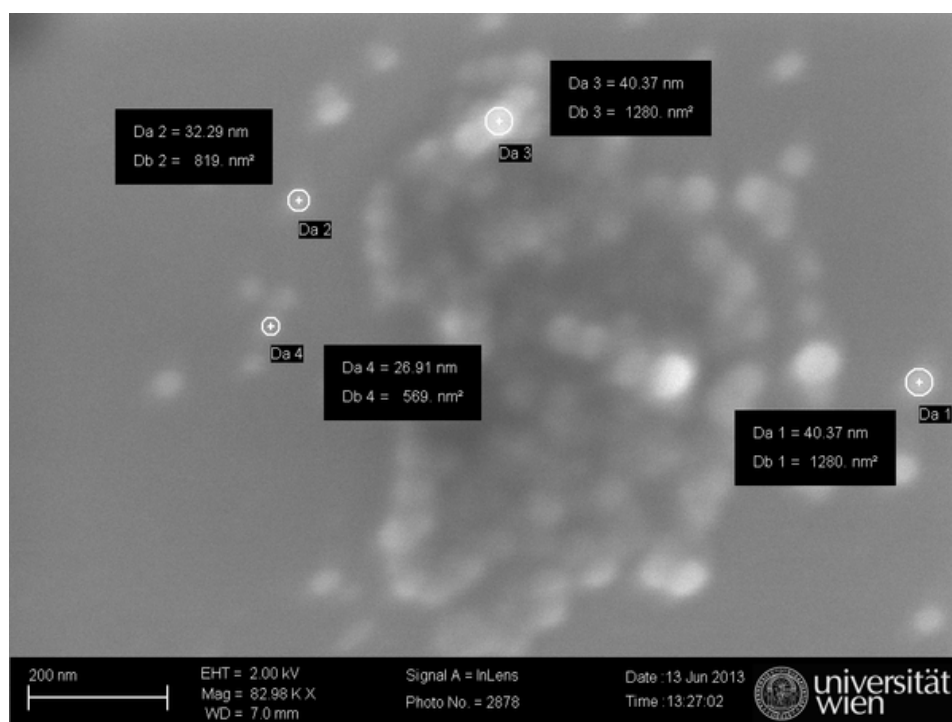


Figure 6.24: An SEM image of clustered polystyrene nanoparticles is shown. A mean diameter of about 40 nm can be identified, although the actual diameter can vary from bead to bead.

a broad spectral bandwidth with an excitation/emission maximum (in solution) of 525/560 nm. Similar to Sulforhodamine B, a strong dependence on the polarity

of the solvent has been discussed in the literature [289] as shown in figure 6.25, which lead to the assumption that the excitation maximum of Nile Red could also demonstrate a quite substantial shift towards the blue end of the spectrum in the gas phase. Since the vacuum can be described as a non-polar environment for the molecule, extrapolation from the data (fig. 6.25) leads to the conclusion that a good excitation at 445 nm could be expected.

From the supplier it was known that these particles were derivatized with a fluorophore which was either co-polymerized inside the nanoparticle or attached to the surface of the nanosphere. The actual process depended on the size of the nanoparticle, but no clear statement for our batch of polystyrene particles was made. In the latter case the dye should be shielded from the environment, reducing a possible negative influence on their fluorescent property, like the charge state of the molecule. This would be ideal for our measurements, since in this case also the Stokes energy should be removed effectively by the polystyrene matrix, which might allow measurements at lower buffer gas pressures.

The polystyrene nanobeads were bought from Kisker Biotech, having a specified

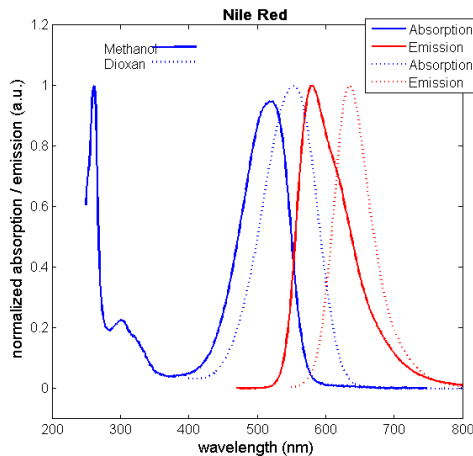


Figure 6.25: The LIF absorption/emission spectrum of Nile Red is shown. A strong dependence on the polarity of the solvent is visible. Data taken from [288].

mean diameter of  $40 \pm 4$  nm, suspended in water with a mass concentration of 1%. The number of nanospheres per mL of suspension could be determined by [234]

$$N_{\text{sphere}} = \frac{6C \cdot 10^{12}}{\rho \cdot \pi \cdot \Phi^3} \quad (6.62)$$

where  $C$  is the concentration of suspended beads in g/ml,  $\Phi$  the diameter (given in  $\mu\text{m}$ ) and  $\rho$  the density of the spheres. From the data sheet, the latter is  $\rho = 1.05$  g/ml [290]. For the 1% suspension a concentration  $N_{\text{sphere}} \approx 3 \times 10^{14}$ /ml can be calculated. To estimate the fluorescence intensity of stained nanoparticles, the so-called 'fluorescein equivalents' can be used. For our nanobeads this was estimated to be about 100 [234].

### 6.7.2 Sample preparation techniques

In the preparation of a sample for the measurements, the analyte particles required dissolving (or suspending) in well defined concentrations and the addition of a MALDI matrix. We used standard MALDI matrices, such as sinapic acid (SA), 2,5-dihydroxy benzoic acid (DHB) or  $\alpha$ -Cyano-4-hydroxycinnamic acid (CHCA). Typically 8 mg matrix was dissolved in 1 ml solvent, the type depending on the molecule. The molecular powder(s) were dissolved in either Ethanol (DHB) or Acetone (CHCA) and the solution was vortexed for at least 30 seconds.

In case of Sulforhodamine B, 20 mg were weighed and subsequently dissolved in 10 ml Ethanol. Also here the solution was vortexed prior to every use to ensure a complete mixing of both chemicals. The final measurement solution was prepared by mixing an aliquot of both previously prepared stock solutions in a 1:1 (vol) relation. A different approach was taken in the case of the polystyrene nanobeads: Initial experiments showed that strong ion signals from the nanosphere MALDI could be obtained if the bead concentration was low. Since the nanospheres were shipped suspended in water, the first step in this MALDI preparation was the dilution of the stock solution. Therefore 50  $\mu\text{l}$  were pipetted out and mixed with 500  $\mu\text{l}$  of distilled water, leading to a particle concentration in the order of  $10^{10}$  to  $10^{11}$ /ml. Parts of this solution were mixed again 1:1 (vol) with the dissolved MALDI matrix. In the case of the two-tone measurements (section 7), a 1:1:1 (vol) mixture of sphere : matrix : Sulforhodamine B solution was done.

In the final step of the sample preparation, the sample disc was cleaned thoroughly by wiping the surface with Acetone and Ethanol. Furthermore the sample was cleaned in Acetone for several minutes inside an ultrasonic bath and coated afterwards with the prepared MALDI solutions, using the dried-droplet method [291].

Prior to its introduction into the vacuum chamber the sample was dried in ambient air.

### 6.7.3 Trapping and detection of ion clouds

Although in the previous sections the basic measurement steps of ion trap confinement and detection have been described already, the experimental realization will be outlined shortly in the following.

After the introduction of a freshly prepared sample plate, the vacuum chamber was pumped to a pressure of better than  $5 \times 10^{-7}$  mbar. As soon as sufficient vacuum conditions were reached, the RF was applied to the trapping rods. For measurements at constant gas pressure, the pressure level was adjusted during this waiting time. After setting up the complete experimental basis and prior to any measurement with ions a background image was taken. This included the operation of the complete trapping cycle with the exception of the desorption laser to avoid the production of ions.

The loading and trapping of the ions was relatively straightforward at this point: When the correct experimental parameters were chosen, with the desorption laser properly aligned and the sample not depleted, a LIF image could be routinely recorded with Sulforhodamine B. Figure 6.26 shows a raw 2D image of trapped Sulforhodamine B. The LIF signal can be clearly identified in the central part of the image by the high signal intensity atop a strongly suppressed background. The ion cloud displays an ellipsoidal shape with its principle axis oriented along the longitudinal axis of the trap.

For the evaluation of the ion cloud images an analysis program was written in MATLAB: After the import of the raw LIF image, the corresponding background image was subtracted. This proved to be helpful for the identification of weak LIF signals in the midst of the constant scattered light. Since each recorded LIF image had to be analyzed individually and a single experiment could produce up to 200 images, the complete analysis in MATLAB was automated.

Finally the central section around the recorded ion cloud was identified and the signal intensities along the longitudinal trap axis was added up. The resulting 1D plot was fitted with a Gaussian distribution. If a large ion cloud was recorded, the signal

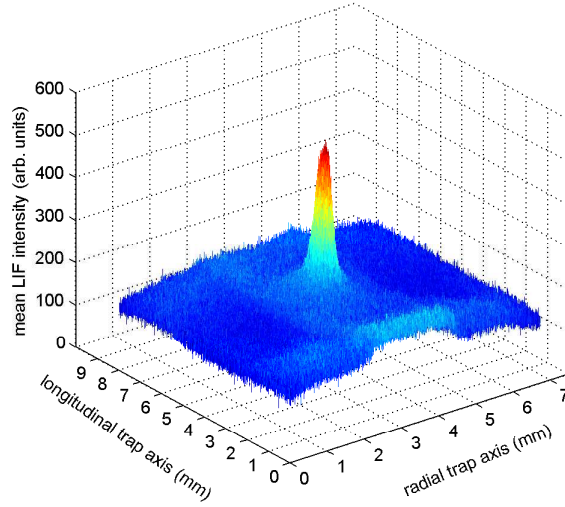


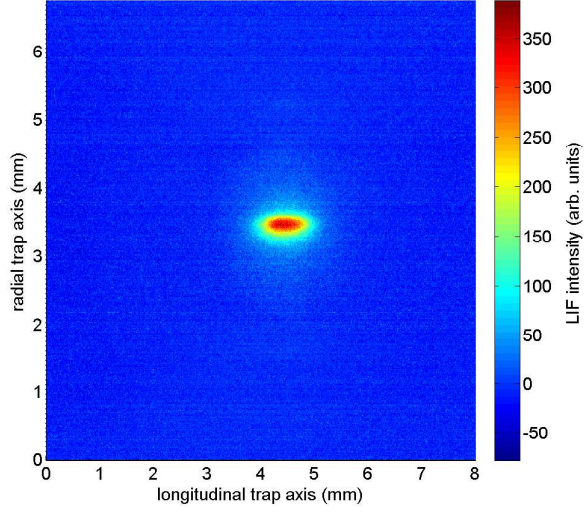
Figure 6.26: A raw image from the camera of the recorded LIF signal is shown. The recorded LIF intensity from the ion cloud is clearly seen above the light background inside the ion trap.

could display more than a single well defined peak. In this case a good fit could also be obtained by a sum of two Gaussians. Since for analysis of the measurements only the total intensity of the recorded ion cloud was of interest, this step was justified. A sample image is shown in figure 6.27a, where the background subtracted LIF image from figure 6.26 is shown. While the central ion cloud is still clearly identifiable, the scattered light is completely suppressed. The summed-up LIF signal is shown in figure 6.27b together with a double Gaussian fit. The final fit is shown as the red curve atop the blue data points.

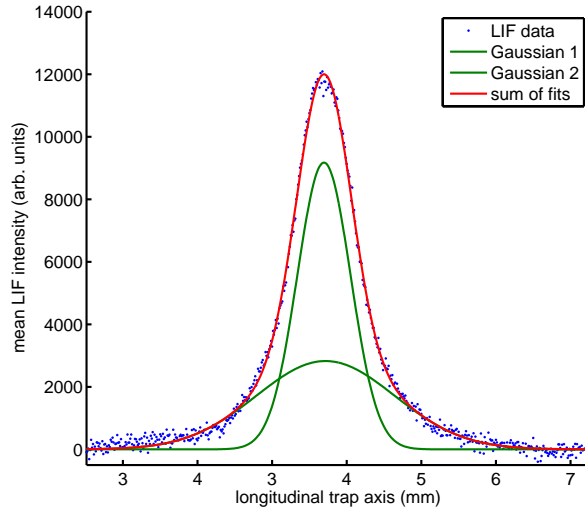
#### 6.7.4 Loading efficiency

An important information is the number of ions available in a measurement. This number is not only determined by the ion trap parameters and by the space charge, but it also depends on other ion trap parameters like the number of laser desorption cycles. The main direction of the initial measurements was to study to characterize the linear quadrupole ion trap. The results will influence a future ion trap design for matter-wave interferometry. Thus, the loading characteristics is determined by the design of the source region.

Figure 6.28 displays the filling curve for Sulforhodamine B. The experimental tim-



(a)



(b)

Figure 6.27: The background corrected LIF image from figure 6.26 is presented in 6.27a and 6.27b displays the summed-up signal distribution together with two fitted Gaussian distributions, where the red line shows the resulting fit. Chosen experimental parameters:  $2 \times 10^{-3}$  mbar He buffer gas pressure, 500 V RF amplitude, 900 kHz RF frequency, 35 laser desorption fill pulses and a 4x4 binning of the sCMOS chip.

ings were similar to those presented in figure 6.21. The RF drive was set to 900 kHz at 400 V, the endcap potential was kept at +20 V and a constant buffer gas pressure at  $2 \times 10^{-3}$  mbar was maintained. The ions were excited with the 532 nm laser beam for LIF detection. All trapping parameters were kept constant throughout the measurement, only the number of laser desorption pulses was varied.

During the desorption of the molecules care was taken that each laser shot hit a new

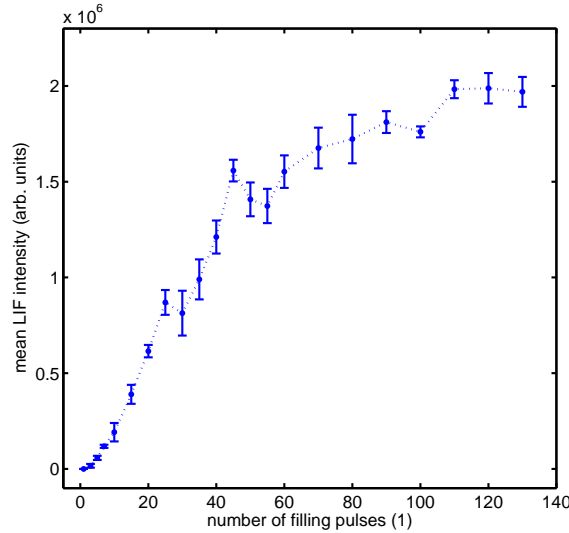


Figure 6.28: Measured fluorescence intensities for different numbers of MALDI desorption shots. For few loading pulses only the ion intensity increases quite strongly while it reaches a plateau for a large number of desorption shots

spot on the sample. To ensure that signal variations were not spoiled by fluctuations of the MALDI process or by irregularities of in the sample spot, the number of filling pulses was varied randomly throughout the measurement. To reduce statistical fluctuations, each data point was averaged over four subsequent trapping cycles.

The data in figure 6.28 show that one single desorption shot is insufficient for detecting any LIF signals, which is most likely due to two different processes: Once by the limited opening angle of the trap behind for the desorption plume, by which the number of ions being trapped in the linear quadrupole is reduced. The second limiting factor in the experiment was the LIF detection efficiency, as discussed in chapter 6.5.

An increase in number of desorption pulses results in a growing LIF signal intensity, which saturates at around 60 desorption pulses. Since the ions repel each other, they will tend to distribute throughout the confinement potential until the trap is

filled homogeneously. If the ion number is further increased, it becomes too large for the available effective potential and additional ions will be lost. In short, this equilibrium between confining RF potential and repelling space charge leads to the observed plateau in the ion LIF signal.

Another interesting parameter in the desorption process is the laser pulse energy. Its influence was tested in a similar experiment where no influence on the detectable LIF signal could be observed for Sulforhodamine B. The ion intensity stayed nearly constant until the pulse energy was lowered below the MALDI threshold at about 40-50  $\mu J$  and the signal was lost quickly.

Although the data analysis shows, that approximately 20-30 desorption shots are required for reaching a detectable LIF signal, this number can be reduced in a future setup. As discussed, one of the limiting factors was assumed to be the solid angle of the sample plate and with this the transfer efficiency between the MALDI desorption spot and ion trap volume. In a future setup this transfer efficiency could be increased by doing the laser desorption either directly inside the ion trap volume or by using a linear RF multipole of higher order as a guide between the MALDI sample and the linear quadrupole. Since a multipole RF field of order  $n > 2$  has a greater radial trapping efficiency, this could lead to an enhanced overall capturing efficiency. Generally it was shown, that a careful matching of the phase-space emittance of the source region to the acceptance of the linear trap the overall injection efficiency could be increased [292].

### 6.7.5 Ion signal dependencies on the buffer gas pressure

Efficient capturing of the externally created ions as well as detection by LIF requires slowing and cooling collisions in a neutral buffer gas. The gas density has to be sufficiently high such that the mean free path is shorter than the trap length. An estimation of the mean free path for Sulforhodamine B with a buffer gas density of  $10^{13}$  molecules/cm<sup>3</sup> gives a mean travel distance between two collisions of approximately  $\lambda \approx 8$  nm (size of Rhodamine 1 nm [293, 294], van der Waals radius Helium 0.14 nm [295]). While a Sulforhodamine B ion crosses the axial trapping volume between the two outermost trapping segments once, this mean free path length value should allow for enough collisions for reducing the kinetic energy sufficiently

to reflect the ion at the applied endcap potential furthest from the sample.

The buffer gas helps in confining the ions and the ion-atom interactions lead to a decrease of the ion temperature, allowing to cool the ions [221, 223–225, 296, 297]. This requires typically a large number of collisions between the ions and the neutral atoms, which is incompatible with a future use in an matter-wave interferometry experiment. For quantum experiments inside an ion trap, a base pressure of  $10^{-9}$  mbar or better will be required, which led to an investigation of the minimal required buffer gas pressure in the trapping volume.

LIF excitation of Sulforhodamine B results in a gradual gain of internal energy during successive photon absorption and emission cycles. As soon as the accumulated vibrational energy is higher than the weakest chemical bond in the molecular structure, the molecule can photo-fragment. Collisions between neutral buffer gas atoms and the ions, on the other side, will lead to a reduction of this internal energy built-up in the molecule. This increases the number of LIF transitions possible for the molecular ion. For Sulforhodamine B (in an  $\text{H}_2\text{O}$  environment) the energy difference between excitation and emission maximum, the Stokes shift, is about 67 meV. One likely fragmentation pathway in the Rhodamine is the split-off of an ethyl group, which has a bond dissociation energy of about 3.9 eV [298]. This indicates that a Rhodamine ion may undergo a maximum of 50 to 60 excitation cycles before too much internal energy will lead to photo-fragmentation. To allow the detection of strong LIF intensities in the experiment, cooling by neutral buffer gas atoms is required.

In the following experiment the two different buffer gas loading schemes were used to test the capturing efficiency of Sulforhodamine B. Prior to any measurement, the atmosphere was set to a constant pressure. The ion trap was then loaded and the ion cloud read out by LIF. Afterwards the trap was emptied and filled again. To reduce the influence of statistical fluctuations, data were averaged over 4 subsequent measurements. The experimental parameters were: 35 desorption pulses for loading in each trapping cycle, the RF parameters were chosen with 500 V amplitude at  $\Omega_{RF} = 2\pi \times 900$  kHz, the endcap potential was 20 V and the molecules were excited at 532 nm.

Figure 6.29 displays the resulting signal dependence on the buffer gas pressure: The loading of the ion trap at a constant buffer gas pressure is shown in blue, while the

influence of the pulsed buffer gas is displayed as the red curve. For constant He

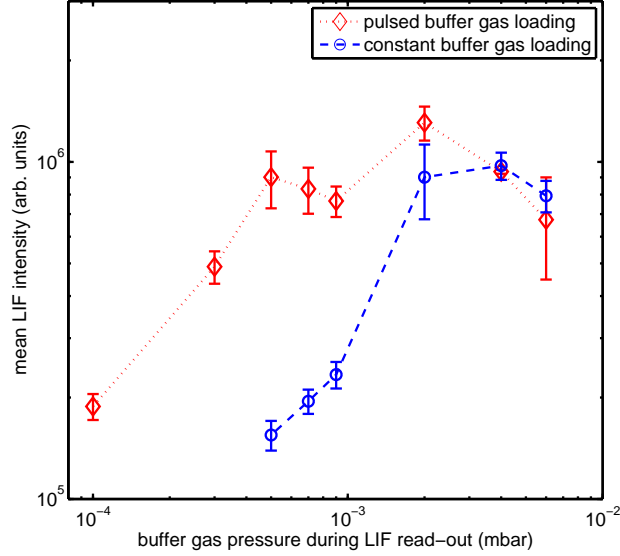


Figure 6.29: The LIF intensity of Sulforhodamine B vs the buffer gas pressure inside the trapping volume is shown for two different loading schemes: In one case a constant buffer gas atmosphere was used (blue), while in the other a pulsed buffer gas was used (red). For read-out the trap was filled with a constant buffer gas pressure again. The data show that a pressure of greater  $10^{-4}$  mbar of buffer gas is required for an efficient trapping and detection of the ion cloud. The lines are meant to guide the eye.

gas densities inside the ion trap, pressure greater than  $10^{-3}$  mbar result in nearly constant LIF signals which are slightly decreasing at more elevated pressures. In this regime the trap loading is quite efficient due to the high number of collisions the ions experience on their way into the ion trap, but also during the confinement time. When the buffer gas pressure at loading is decreased - in the case of constant buffer gas conditions the loading pressure was equal to the read-out pressure - the signal drops dramatically and for Helium pressures below  $3 \times 10^{-4}$  mbar no ion signal can be detected.

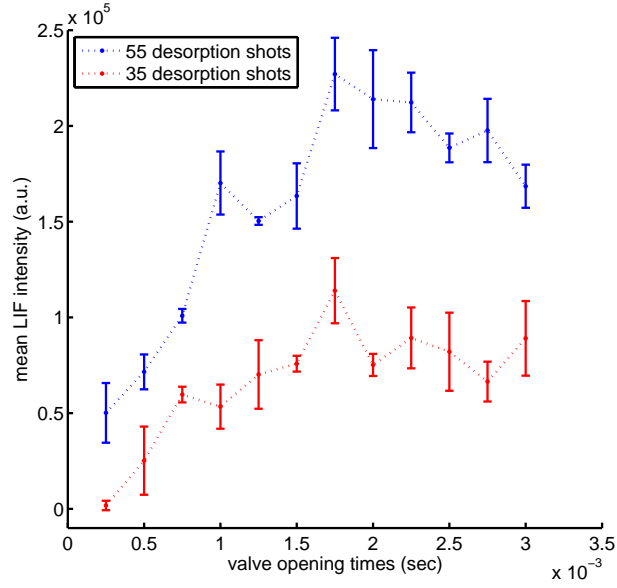
The use of a pulsed buffer gas (backing pressure on the valve: 1 bar) displays an efficient loading and trapping as well. In this case the observed LIF intensities fall off at lower pressures compared to the constant loading. While hardly any LIF signals can be observed for buffer gas pressures below  $6 \times 10^{-4}$  mbar under constant pressure loading conditions, the pulsed loading shows enhanced ion signals even at such low read-out He gas pressures. For lower pressures a decrease of the LIF intensities can be observed as well with a loss of LIF signal for read-out pressures

below  $8 \times 10^{-5}$  mbar. These trapping efficiencies can be explained by the increased (time-dependent) atom densities of the pulsed buffer gas.

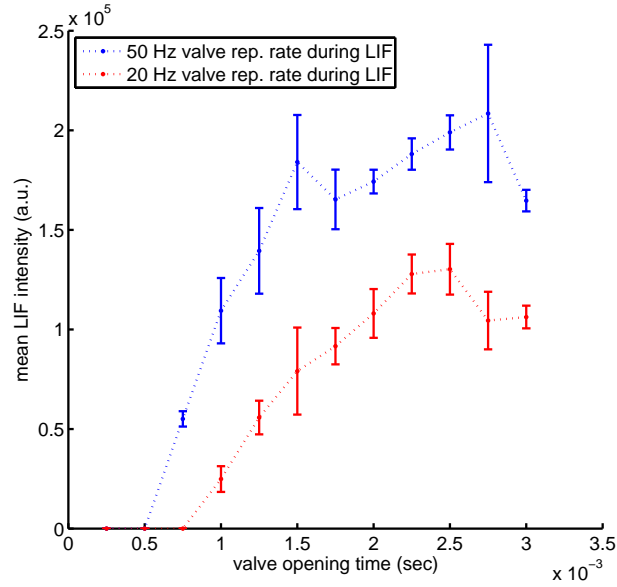
To further investigate the ion cloud behavior under pulsed buffer gas conditions, a second set of measurements were conducted. Thereby the influence of the valve opening times, e.g. the amount of gas available for ion-atom interaction, on the measured LIF signals was tested. In a first set of measurements the ions were loaded into the trap under pulsed gas conditions, while the LIF was read-out with constant buffer gas pressures in the low  $10^{-3}$  mbar. The second set of measurement used the pulsed buffer gas scheme for LIF read-out as well. In all measurements each data point was averaged over four consecutive trap fillings and similar RF parameters as before were used. To enhance the overall trapping efficiency of the ions, each gas pulse was introduced with an experimentally determined time delay of 4.5 ms in respect to the desorption laser. In this way the greatest overlap between the gas atoms and the ions was ensured.

The red (blue) curve in figure 6.30a shows the dependence when the trap was filled with 35 (55) MALDI shots. Although an even higher number of desorption pulses could be used, it would have only increased the rising slope of the signal, but the overall signal behavior would have stayed identical. In the recorded data a clear increase of the LIF intensity is observed with an increasing number of collision partners. This is in agreement with data published in literature [217, 247].

A similar measurement is shown in figure 6.30b. Compared to the previous experiment, the LIF detection was done under pulsed buffer gas condition as well. This translated that between the loading and the detection of the ions only reduced buffer gas pressures below  $10^{-4}$  to  $10^{-5}$  were present. A similar dependence of the gas pressure on the LIF intensity is clearly visible. The red (blue) curve was recorded with 35 (55) gas pulses again. In the LIF detection the opening frequency of the valve was changed between 20 and 55 Hz (red, blue in figure 6.30b, respectively). Also here a dependence of the LIF intensities on the available number of collision partners can be observed: The higher the number of buffer gas atoms (blue curve), the stronger the recorded signals can be. This is in agreement with the expected fluorescence behavior of molecules in the gas-phase (see also chapter 6.2).



(a)



(b)

Figure 6.30: Pressure dependence of the LIF signal with pulsed buffer gas. A pulsed valve was used for introducing the buffer gas into the chamber: In the first set of measurements (6.30a), the pulsed gas was used only during capturing. In a second experiment (6.30b) also the LIF read-out was performed under pulsed buffer gas conditions.

### 6.7.6 LIF dependence on the excitation power

Another important question is the dependence of the LIF signal strength on the excitation laser power. Although this depends on the specific fluorophore, specifically on the quantum yield, the absorption cross section, the thermal stability and intersystem crossing rates, it is generally interesting to know the laser dependencies for the current case, Sulforhodamine B.

In this specific measurement the trap was filled with an identical number of MALDI pulses at a constant buffer gas atmosphere of about  $2 \times 10^{-3}$  mbar for each individual measurement. After loading and trapping, the ion cloud was illuminated by the 532 nm LIF laser beam and the resulting image was taken. The LIF laser power was varied in power by placing neutral density filters into the laser beam.

Figure 6.31 shows the result of this experiment. Each data point consist of four

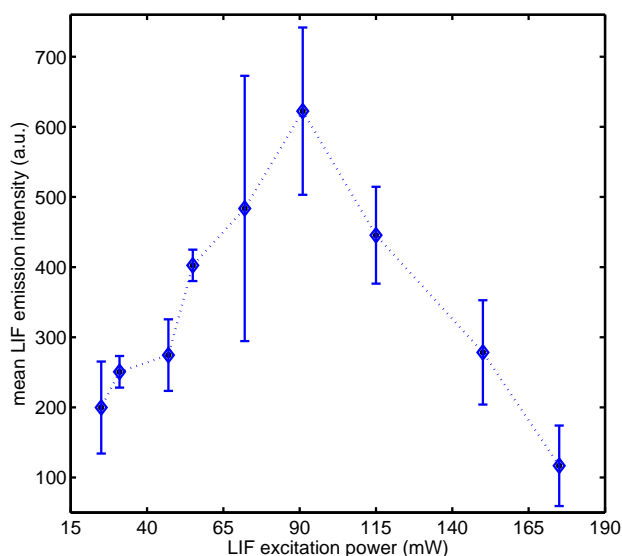


Figure 6.31: The LIF intensities are shown as a function of the excitation laser power under constant irradiation time and constant buffer gas pressure of  $2 \times 10^{-3}$  mbar.

individual measurements to reduce the influence of fluctuations during MALDI sampling. For low LIF powers the overall LIF intensity increases linearly with the laser power until at around 100 mW optical excitation power the LIF intensity plateaus. At even higher laser powers the absorbed optical energy can not be dissipated by radiative or collisional relaxation fast enough and the molecule dissociates or bleaches. This leads to the observable decrease of the LIF signal in figure 6.31.

The recorded intensity curve shows a similar behavior to [244, 299], where LIF signals from Rhodamine 6G and Rhodamine 575 cations were observed in an ion trap. Other trapped Rhodamine ions show photo-fragmentation upon the irradiation of visible light, with a resulting mass spectrum [252], which is similar to collision induced fragmentation [248]. Since Sulforhodamine B belongs to the same Rhodamine dye family, a similar behavior can be expected upon the irradiation with the LIF laser beam. In our data the LIF intensity decreases above 100 mW irradiation power due to photo-dissociation.

Another explanation of the plateau in the observed LIF signal could be that the fluorophore is saturated by the incident light. The saturation intensity can be estimated by [300]

$$I_{\text{sat}} = \frac{h\nu}{\sigma_{\text{abs}}\tau_{\text{LIF}}} \quad (6.63)$$

where  $h\nu$  describes the photon energy ( $\lambda = 532$  nm in our case),  $\sigma_{\text{abs}}$  the absorption cross section ( $1.5 \times 10^{-20} \text{ m}^2$  [278] in solution, no values for vacuum are available) and  $\tau_{\text{LIF}}$  is the effective fluorescence lifetime of the fluorophore (1.5 ns for Sulforhodamine [236] in solution, no values for vacuum are available). With these values and equation 6.63 the saturation intensity can be calculated to  $I_{\text{sat}} = 1.6 \text{ MW/cm}^2$ . This is much higher than the implemented experimental peak intensity of about  $18 \text{ W/cm}^2$ . This shows that the optical transition was not saturated in the course of the experiment. This is an indication that in our measurement the Sulforhodamine B cation did undergo photo-dissociation at high ( $> 100$  mW) laser powers.

### 6.7.7 Bleaching of the ion cloud

In the LIF process a molecule can not only absorb and re-emit a photon, but it can also be excited into a triplet state or photo-bleach. A triplet state displays no fluorescence for the duration of its state lifetime (typically  $\mu\text{s}$  up to ms [236]), while after a bleaching the molecule is permanently lost for LIF. While in principle the triplet state removes the molecule from the LIF detection temporarily, bleaching processes prevents its detection after a photo-chemical process permanently.

To observe this effect, the ion trap was filled with 35 desorption pulses in a constant helium atmosphere of  $2 \times 10^{-3}$  mbar. After confinement for several seconds, during which the ions could thermalize with the buffer gas at 300 K, the cloud was illumi-

nated with the LIF excitation laser beam at about 250 mW power. To monitor the bleaching, the time delay between the start of the LIF laser and the exposure on the camera was varied. The overall exposure time stayed constant for all measurements to reduce the influence of systematics during analysis.

Figure 6.32 shows the bleaching curve for Sulforhodamine B, where each data

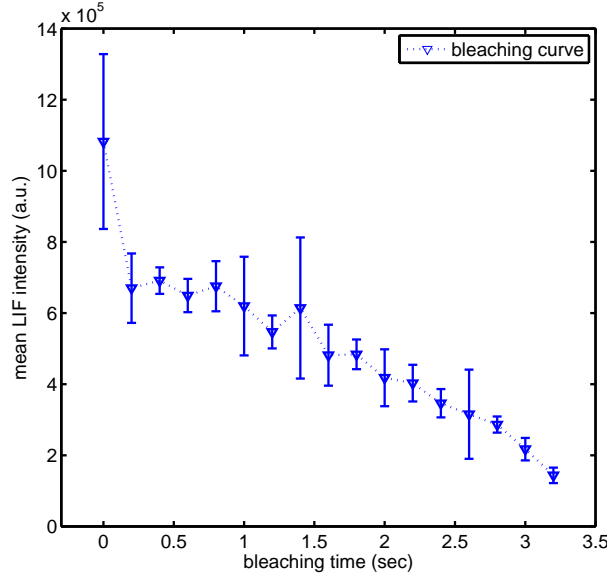


Figure 6.32: The fluorescence bleaching of Sulforhodamine B in a quadrupole ion trap with a constant buffer gas pressure of  $2 \times 10^{-3}$  mbar.

point is averaged over four consecutive measurements. A fast decay in the LIF signal within the first few milliseconds of detection is followed by a slower decrease. Thereby a linear decrease in the signal intensity can be observed. This is expected since the number of absorption processes is linear in time. The available signal strength indicates, however, that LIF detection can be done on a time scale that is sufficiently short to keep the effect of bleaching small.

### 6.7.8 Variation of the endcap potentials

In the linear quadrupole trap DC potentials on the endcap electrodes are required for a stable confinement of the ions. While this static field prevents the axial escape of the ions it weakens the effective potential in the radial plane (see equation 6.49), reducing the number of trapped ions and setting an upper bound for the maximal kinetic energy of the trapped ion. At the same time the endcap potential determines

which fraction of ions inside the MALDI plume can enter the trap, since only ions with a sufficient high kinetic energy can overcome this axial barrier.

To investigate the axial potential influence in this specific ion trap design, a measurement was conducted varying the endcap potential. All other parameters for loading, confinement and LIF read-out were kept similar to the previous measurements. The results are shown in figure 6.33.

At an endcap potential of about 20 to 30 V the observed LIF intensity has its

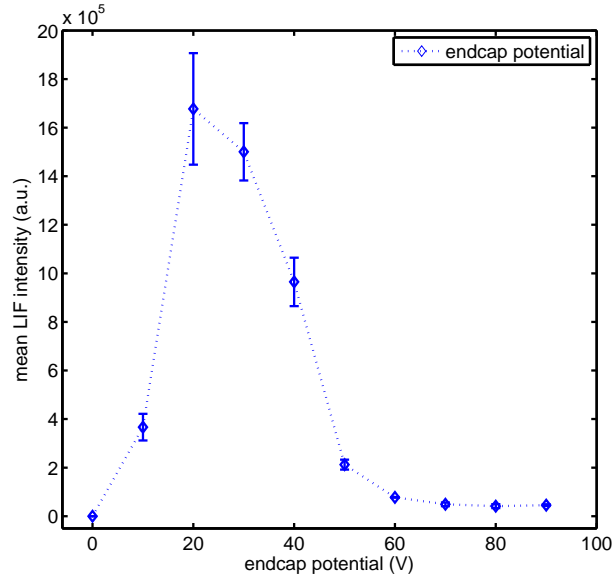


Figure 6.33: The influence of the endcap potential on the loading efficiency of Sulforhodamine B is shown. For the chosen RF parameters (500 V,  $\Omega_{RF} = 2\pi \times 900$  kHz), the radial effective potential is in the order of about 50 eV.

maximum, while it falls off quite rapidly for high and low potential values. In the case of low DC potentials, the axial trapping field seems to be too weak to confine a large ion cloud. On the other side, when high axial DC potentials are used, ion losses could be influenced by two different mechanisms. The Sulforhodamine B cations might be deflected from the high endcap potentials during loading. This decreases the injection efficiency, leading to lower observable LIF signals. On the other hand, the axi-symmetric quadrupole potential can be described by  $V_{DC}(r, z) = (U_{EC}/z_0^2) \cdot (z^2 - r^2/2)$  [217]. In our case, this shows that for endcap potentials values greater than 60 V, this potential is of similar depth at the RF node than the radial one. This could also be a limiting factor in the observable LIF intensities at high  $U_{EC}$  in figure 6.33.

## DC potential on the sample

Also the MALDI process itself can influence the coupling efficiency into the ion trap. If the MALDI sample plate is at an electrical potential the desorbed ions can either be accelerated or decelerated. However the ion signals showed no dependence on the applied polarity, even up to 125 V. As a result the sample was kept on ground for most of the experiments.

### 6.7.9 Radial ion cloud dimension

An interesting question for future experiments is the knowledge of the spatial dimensions of the ion cloud. In this measurement the LIF laser was introduced from below the ion trap and scanned along the radial trap axis, normal to the longitudinal one. Figure 6.34 presents the results of a radial LIF scan through the confined ion cloud. The chosen experimental parameters were: RF amplitude of 250 V at  $\Omega = 2\pi \times 980$  kHz, 35 laser desorption pulses for filling and a buffer gas pressure of  $1 - 2 \times 10^{-3}$  mbar.

The recorded fluorescence data (figure 6.34) show that the ion distribution around

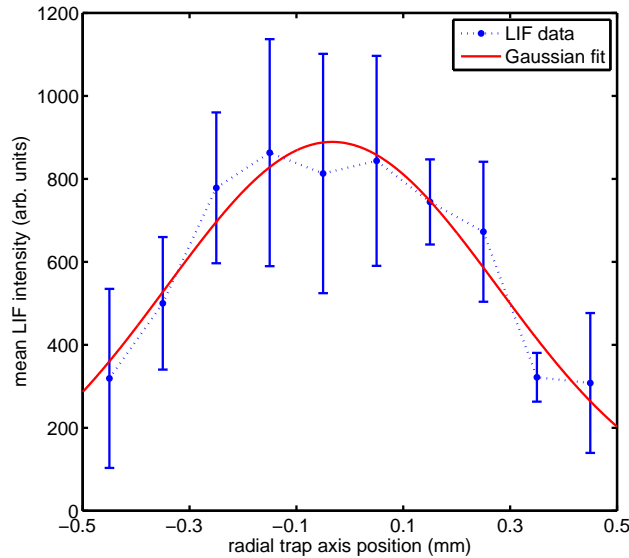


Figure 6.34: A scan of the vertical 532 nm laser beam through the radial plane of the ion trap showed an ion cloud width of about 0.6 mm around the center of the trap axis.

the RF node of the trap can be described by a Gaussian (shown in red in figure 6.34). This is comparable to previous work in literature, where also a Gaussian distribution of the ion cloud at room temperature could be observed (in case of Paul traps [208,228,301] as well as for a 2D radial trap potential [302]). For our data the Gaussian fit shows that the width of the ion cloud is around 0.65 mm FWHM.

With this measured ion cloud size, the number of trapped ions can be estimated following the work of [213]. It is assumed that about 90% of the axial trap length (e.g. 18 mm effective trap length) are accessible for the trapped ions (see also figure 6.12). With the RF parameters and the cloud radius given above the total number of ions can be estimated to  $N \approx 2 \times 10^6$  ions. Although this number seems a bit high, a comparison with the estimated charge density in our trap of about  $2.5 \times 10^5$  ions/mm<sup>3</sup> (see equation 6.1.3), leading to about  $5 \times 10^7$  ions in the trapping volume, the estimated ion number from the experiment is within this limit. While the total number of ions in the experiment will be less than the estimated one (due to, e.g., space charge or trap inharmonicities), it is safe to assume that about  $10^5$  ions were trapped in this measurement.

#### 6.7.10 Variation of the RF amplitude

The two parameters of the RF drive, its amplitude and frequency, influence the ion capturing as well as the trapping conditions of the ions. Thus an experiment was conducted to look into this relationship. Due to the design of the LC tank circuit, the frequency of the RF was fixed to 1.09 MHz and only the RF amplitude was varied. In this measurement the endcap potential was 20 V, applied to the trap segments 2 and 4. The other trapping parameters were kept constant throughout the measurement. To allow for the cooling of the ions, the buffer gas was kept at a constant pressure. Also, an identical number of loading desorption pulses were used. The result of this measurement are presented in figure 6.35, where each data point is the average over 3 consecutive measurements to reduce the influence of fluctuations in the MALDI process. As can be expected from theory, the trapped ion intensity increases with increasing RF amplitude on the trap rods. Since this correlates directly to the depth of the effective potential ( $V_{\text{eff}} \propto \mathbf{q}$ ), the enhanced ion signal can be explained by this way. The plotted fit is shown as a guide to the

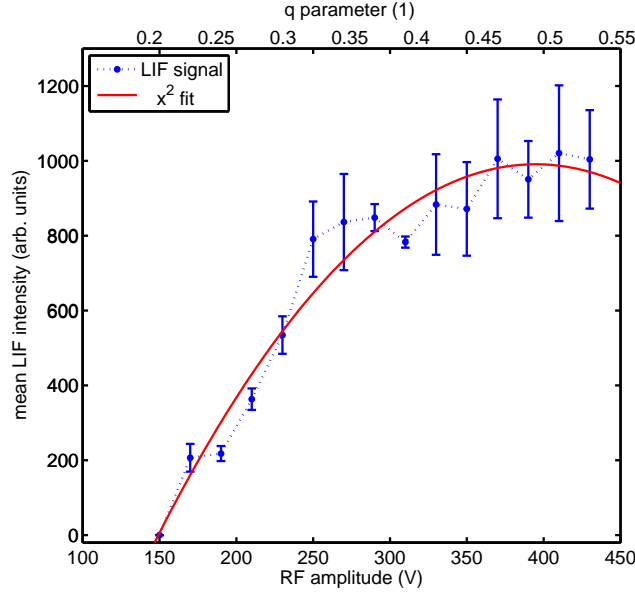


Figure 6.35: A variation of the RF amplitude shows that with increasing RF amplitude the LIF signal intensity increases quite strongly. For high amplitudes the signal saturates. The measurement was performed under identical loading conditions for each point.

eye. Due to technical reasons, it was not possible to increase the RF amplitude even further in this experiment. Otherwise a rapid decrease of the LIF intensity for  $\mathbf{q} \geq 0.85$  would have been expected.

The data show that a threshold RF amplitude of  $V_{\text{RF,thresh}} > 160$  V is required for stable trapping in our geometry. In comparison, the minimal required RF amplitude can be calculated by [217]

$$V_{\text{RF,min}} = \Omega_{\text{RF}} r_0^2 \cdot \sqrt{\frac{mU_{\text{EC}}}{2ez_0^2}} \quad (6.64)$$

which shows however, that a minimal RF potential of  $V_{\text{RF}} \approx 40$  V should be sufficient. A possible explanation for this discrepancy could be the external injection of the ions into the ion trap.

To investigate this matter further, SIMION simulations were performed for our ion trap geometry and parameters (buffer gas pressure, RF/DC parameters). The initial velocity of the ions was set to  $500 \text{ ms}^{-1}$  [114, 303] corresponding to a kinetic energy of about 0.7 eV, similar to the ones in [304], where similar mean velocities were shown in this mass class. Similar to previous SIMION simulations the starting points of the individual ions in the cloud was randomized as a 3D Gaussian distribu-

tion around the longitudinal axis (at the starting point) of the trap. When the ion cloud was initialized in the central (third) trap section, a minimum RF amplitude of about 40 V is sufficient to stably trap the ions. This is comparable to the RF amplitude as calculated from equation 6.64. Lower RF values led to an ejection of the ion while larger RF voltages resulted in a tighter confined ion cloud.

In comparison, if the ion cloud was started in the beginning of the second segment (the one carrying the endcap potential), a first successful ion transmission and subsequent trapping in the central part of the ion trap was observed for RF amplitudes of 165 V. This is in good agreement with the experiment. In the simulation even higher RF amplitudes increased the trapping efficiency and therefore the (theoretical) observable ion signal. This could be explained by the fact that a higher RF field leads to a stronger radial confinement of the ions, reducing the influence of the DC potential. Since in the experiment the ions were also introduced from an external source, this simulation results seem to explain the observable signals.

### 6.7.11 Mass selection

A key property distinguishing RF driven quadrupole ion traps from higher order multipole RF ion traps is that the intrinsic mass selectivity (see chapter 6.1 for details). This is of importance for future quantum experiments, whenever the detector is non-selective to mass, or when there is a risk for particle fragmentation in the manipulation process. This could be a problem in dissipative interferometer gratings. Generally, mass selection is advantageous for a correct interpretation of the experimental results. This offers the advantage to start future quantum experiments with a clean particle beam.

The motion of an ion in a linear quadrupole trap is determined by its specific oscillation frequencies, the secular motion and the micromotion. The dominant part is the secular frequency, given by  $\omega_{\text{sec}} = (2n + \beta)\Omega/2$ ,  $\beta^2 \approx 4eV_{\text{RF}}/\sqrt{2}mr_0^2\Omega^2$  [264], which is inversely proportional to the particle mass (see the theory section 6.1 for more details). Exciting this secular motion by an auxiliary AUX RF field on resonance at  $\omega_{\text{sec}}$  increases the kinetic energy of the ion up to the point where the particle is ejected from the confinement field. While this excitation scheme allows to determine the mass distribution of the ion cloud, an inverse excitation scheme will allow the

mass cleaning of the ion cloud. A notch-type auxiliary radio frequency centered around the specific  $\omega_{\text{sec}}$  will lead to the simultaneous ejection of all ions except for the wanted mass.

The above described mass selection technique was chosen over the RF/DC ion isolation known from the quadrupole mass filter, since the former was expected to be a more straightforward method. For RF/DC mass selection after initial ion trapping, changes in the RF frequency and/or potential as well as DC potential are required to reach the apex point of the stability diagram. Since a low  $\mathbf{q}$  value is required for post mass selection again, the RF and DC would need to be changed once more. These changes could lead to heating effects, which might increase the loss of trapped ions. Also, as discussed in [305], the application of a DC potential leads to ion instabilities in one specific trap axis only. This could also lead to increased heating effects and losses of the trapped ions.

Mass selection was measured in the current setup, where the dipolar excitation scheme for ion ejection was chosen. This required the application of the AUX RF onto a single diagonal trap rod pair, as shown in figure 6.36. In the experiment, compared to the previous described ones, only one single phase of the main RF drive was applied to one pair of the trapping rods. The other one was connected to ground with respect to the RF potential. The AUX RF signal was generated

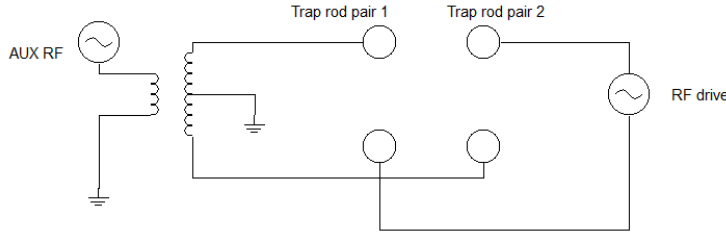


Figure 6.36: The circuit diagram for the excitation of the secular motion of the trapped ion is shown. The ideal transformer identity was estimated with  $a = 0.25$ .

by a signal generator and coupled to a transformer, center-tapped on the secondary side. Similar to the situation of the RF generator (in chapter 6.6.1), this created two RF phases of identical frequency and amplitude but  $180^\circ$  phase-shifted. This way a sinusoidal dipolar excitation waveform with an excitation amplitude of up to 5 V could stimulate the trapped ion, when required for the measurement. When this splitting of the two RF drives was not needed, the center tap on the coil was connected to the second phase of the main RF drive.

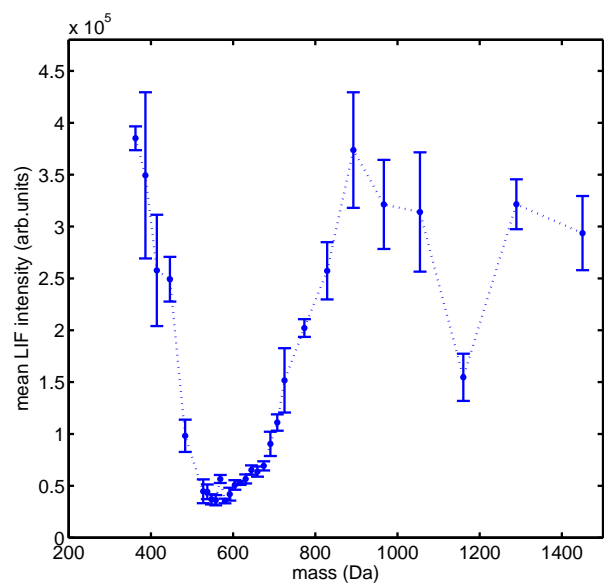
For this measurement the pulsed buffer gas scheme was applied for ion loading and LIF detection, since the secular excitation was performed best under vacuum conditions. Otherwise, in case of a constant buffer gas atmosphere the secular ion motion would have still been excited, but resulting only in a forced, damped oscillation. To eject the ions a stronger AUX RF amplitude would have been necessary in this case. At the same time collisions with the buffer gas atoms under the influence of the external field would have increased the probability of collision induced fragmentation (CID) [306,307]: Excitation in a buffer gas environment leads to a competition between ion ejection and fragmentation. The fragmentation depends besides of the molecular structure of the ion on the AUX RF parameters as well.

During measurements the ion trap was loaded with Sulforhodamine B under the optimal field settings (RF amplitude 400 V and  $\Omega = 2\pi \times 980.6$  kHz) while the AUX RF amplitude was set to 1.0 V (peak-peak). After loading the ions a trapping cycle was applied as presented in figure 6.22. It consisted of loading the ion trap followed by a short waiting time to allow the pumping-out of the buffer gas and subsequently the AUX RF was activated for about 3 seconds. The secular excitation was then directly followed by the readout of the ion cloud. Finally the trap was emptied and a new trap cycle was started.

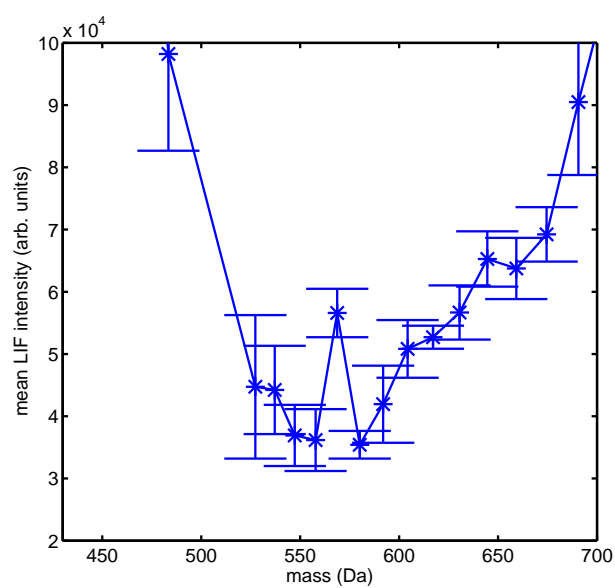
The resulting mass spectrum is shown in figure 6.37 as a depletion spectrum where the excitation frequency is already converted to the ion mass by (with a single-phased main RF only)

$$m = \sqrt{\frac{4e^2V^2}{\sqrt{2}r_0^2\Omega^2\omega_{\text{sec}}^2}} \quad (6.65)$$

Each data point is an average over 4 subsequent ion trap cycles. For reducing the influence of inhomogeneities or depletion effects of the MALDI sample, the AUX RF frequencies were chosen in a random order during the course of the experiment. On the left side of figure 6.37 the recorded mass spectrum displays a distinct dip as well as a smaller one on the high mass side. These indicate that ion losses had occurred during the excitation of the ion. The dominant mass peak is centered around 570 Da, which is in close proximity of the nominal mass of Sulforhodamine B. Because the molecule was bought as a monosodium salt having the molecular weight of 580.6 Da, it must be assumed, that the sodium ion was dissociated during the solvation of the molecules. This reduces its mass to 557 Da, which is still within the measured



(a)



(b)

Figure 6.37: A mass scan of Sulforhodamine B by dipolar excitation method. While 6.37a shows the complete recorded mass spectrum, figure 6.37b displays a zoom into the region of 570 Da.

mass distribution. Therefore ions of both masses are measured within this mass peak, as displayed on the right hand side of figure 6.37. The graph shows a zoom into the central section of the mass dip centered around 570 Da. One can clearly observe that in the central section of the peak the observed LIF intensity is slightly increased compared to the data points on the left and the right. Since each data point is given by the average of four independent measurements, this increase in ion intensity is most likely not due to random signal fluctuations (as shown by the error bars). The data points directly to the left and right represent a mass of 557 and 580 Da, respectively. They correspond to Sulforhodamine B in its native form (557 Da) and as a monosodium salt (580 Da). This shows that it was possible to resolve these two masses within this mass selection measurement. From the recorded spectrum a mass resolution of  $m/\Delta m \approx 10$  can be deduced. This is similar to the expected mass resolution given by the frequency step of 2 kHz in the experiment and equation 6.23.

The fragmentation properties of Sulforhodamine B might also have a consequence onto the low mass resolution of the observed peak. The breaking of chemical bonds in the periphery of the molecule will lead to a change in the molecular mass, leaving the LIF properties intact. As example, the loss of a methyl- or an ethyl group will not influence the fluorescence properties of the molecule (see also figure 6.23a). Fragmentation of Sulforhodamine B could happen during MALDI or even during collisions with rest gas atoms during secular excitation with a high AUX RF amplitude (see figure 6.39). Due to the effective potential such fragment ions will be trapped as well. While the intact ions are ejected from the trap during the mass selection, under these conditions fragment ions will still remain trapped. The fluorescent light observed in the subsequent detection will lead to a broadening of the detected mass peak, since the fragments will not be distinguished from the intact ions by LIF observation.

Although the obtained mass resolution is still not sufficient to use such a setup as particle source for a molecular matter-wave interferometer, this experiment can prove the fundamentals for a further concept, since a higher mass resolution using this mass selection concept was recently shown [285].

A second mass dip in figure 6.37 is centered around 1160 Da. Compared to the previously discussed mass peak, the decrease in signal intensity is not as large. Fur-

thermore this mass peak is, unfortunately, given by a single data point only, but since the data point (including errorbar) is much less intense than the neighboring ones, a random signal fluctuation can be excluded again. The broad width of the peak is due to the chosen larger frequency step in between two neighboring AUX frequencies.

From its peak data value, the mass of 1160 Da corresponds quite well to twice the mass of Sulforhodamine B. It therefore might represent a double Sulforhodamine B cluster. This could also explain the less strong depletion of the observed signal, since a lower percentage of clusters compared to single molecules are present in the MALDI plume.

To test the validity of the observed mass spectrum (figure 6.37) a control experiment was conducted with a dedicated TOF-MS setup. For this measurement a sample was prepared, using the identical analyte solutions and MALDI target preparation steps. MALDI was conducted under the same conditions and ions were detected using TOF-MS (Kaesdorf,  $\frac{m}{\Delta m} \approx 100$ ). A detailed description of the experimental setup is given in chapter II. The resulting mass spectrum is shown in the following figure 6.38. The most prominent peak in this spectrum is given by the single Sul-

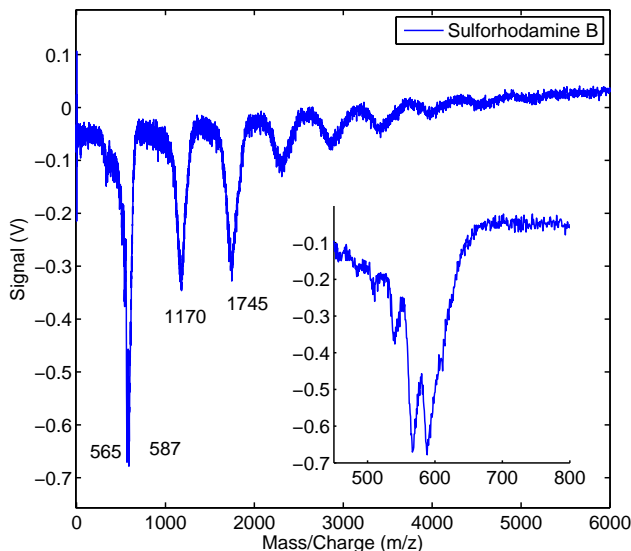


Figure 6.38: MALDI TOF-MS mass spectrum of Sulforhodamine B. A strong clustering of the molecules can be seen. At the same time the low mass region of the spectrum resembles the ion trap data (figure 6.37). The inset shows the main peak. A clear separation into Sulforhodamine B and its monosodium salt and fragments is given.

forhodamine B molecule at about 570 Da. The zoom-insert in the figure shows that this peak is again a double peak with two maxima at 565 and 587 Da, representing the Sulforhodamine B monosodium salt and Sulforhodamine B or a fragment of the monosodium salt. Apart from this signal a series of clustering up to seven-fold can be observed. On the low mass end of the spectrum a further peak of lower intensity at about 330 Da can be identified. This is most likely a fragment of Sulforhodamine B which is produced in the MALDI process. The calculated mass for the first two clusters is indicated in the graph. For the measured double cluster the two mass values (ion trap, TOF-MS) can be assumed identical within the experimental errors. The high signals show that even under high-vacuum conditions clusters of the analyte molecule are produced by MALDI-ionization. Therefore it seems that the clustering is independent of the external buffer gas atmosphere and rather driven by the high density in the MALDI plume.

The comparison with the mass spectrum from the ion trap (figure 6.37) proves that a dipolar excitation method in the ion trap provides correct mass values of the ion cloud within the error margins, but (up to now) with a very broad mass width. To explore the possible influences of experimental parameters on the observed peak width, the amplitude of the AUX RF was scanned, while all other experimental parameters were kept identical to the previous mass scan, as well as the frequency step of the AUX RF, except for the case of very low RF amplitudes. In this case a smaller width in the mass peak was expected and therefore smaller steps were chosen. The resulting mass spectra are shown in figure 6.39.

Compared to the previous scan with an AUX RF amplitude of 1 V (blue), the increase to 3 V (red) shows a larger width of the scanned mass distribution while the center of the mass peak does not shift. The saturated mass peak shows a very efficient coupling of the AUX RF to the ion secular frequency, even for near-resonance cases. This leads to an energy increase with subsequent ion loss even when neighboring  $\omega_{\text{sec}}$  were tested. Also the fragmentation of the intact molecular ion could lead to such a broadening since the fragmentation probability increases with increasing AUX RF amplitude.

A similar picture can be seen on the high mass side of the spectrum. But since the signal intensity is rather low in this spectral region, the observed dip in the LIF signal is not as clearly visible as in case of the monomolecular Sulforhodamine B.

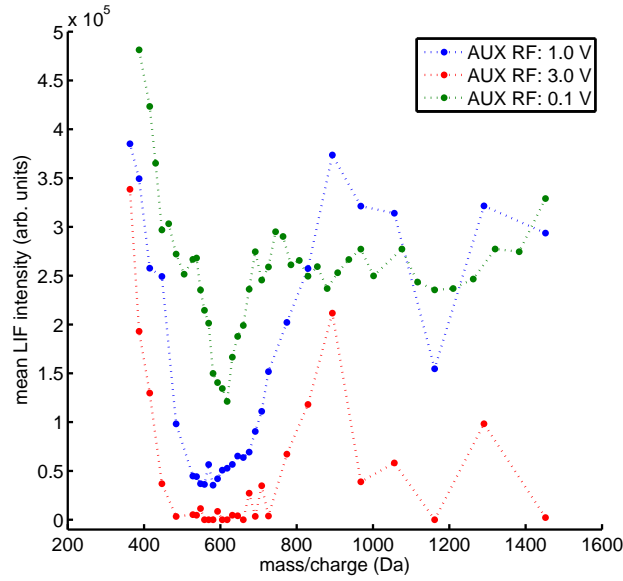


Figure 6.39: Dipolar excitation of trapped Sulforhodamine B cations under different AUX RF conditions. With increasing AUX RF amplitude the width of mass peaks increases as well.

A similar mass spectrum can be observed for low amplitude AUX RF excitations (blue line in figure 6.39). For this measurement the dipole excitation amplitude was lowered to 100 mV (peak-peak), also a higher number of laser desorption pulses were used. Since the amplitude was smaller compared to the previous two measurements, the ion cloud irradiation time was prolonged to a total of 10 seconds to ensure an efficient ion ejection. To reduce the noise in the recorded spectrum, the data in figure 6.39 were smoothen over five neighboring points. In the data a distinct mass peak at about 615 Da can be observed, which corresponds to a shift of about 30 Da towards higher mass in comparison to the previous discussed spectra (figure 6.37,6.38).

This observed mass shift is most likely given by the ion cloud itself and not due to the AUX RF. Since a higher number of desorption pulses was used in this measurement, a higher trapped ion number than in the previous experiments can be expected. This could have led to a space-charge dependent mass shift in the secular frequency of the ion, as shown in literature [202, 308]. Especially in 3D Paul traps it could be shown that the secular motion of the ions are shifted towards lower frequency for increasing space charge [309]. Since  $\omega_{\text{sec}} \propto m^{-1}$ , this leads to a higher observed mass than the one calculated from the ion trap parameters of a single ion.

Compared to the other two spectra, the width of the low-amplitude excitation mass

peak in figure 6.39 is narrower, which reflects an increased mass resolution. This shows that for a mass spectrum with high mass resolution the dipolar excitation amplitude has to be kept low.

### 6.7.12 Trapping of nanospheres

A future experimental setup for a matter-wave interference of particles in the ultra-high mass regime ( $m > 10^6$  Da) could consist of a MALDI (or ESI with charge-reduction stage) loaded, cryogenic buffer-gas cooled ion trap, for which the loading and trapping of very high masses in the current ion trap experimental setup had to be investigated. The outcome could be a first step to show if an ion trap could be of use as possible source for such planned high-mass and ultra-high mass matter-wave experiments. For this purpose we chose as test particles fluorescent polystyrenes spheres with a nominal diameter of  $40 \pm 4$  nm. This corresponds to a mass of approximately 25 MDa [253]. The beads are labeled with Nile Red fluorophores which can be excited with blue (445 nm) as well as with the green light (532 nm). A more detailed description on these particles is given in chapter 6.7.1.

Since the expected mass to charge ratio of these particles was much larger than that of Sulforhodamine B, the RF electronic circuits needed to be adapted. For moderate RF amplitudes ( $V \leq 200$  V) the frequency needed to be lowered to several kHz. In the following measurements the single-phased, amplified RF drive was used, as described in section 6.6.1.

In a first experiment, the RF parameters were varied to investigate the optimal settings. Thereby the RF frequency was scanned over 10 trap cycles. The resulting trapping distribution is shown in the histogram in figure 6.40. It shows that the highest number of successful injected trap cycles can be found at around 40 kHz. From the  $m/z$  ratio in this frequency range and Mathieu's stability parameter  $\mathbf{q}$ , a lower mass-to-charge limit of  $m/z > 500$  kDa was derived.

This is less than previously estimated and might be due to several reasons:

- The nanospheres might leave the MALDI plume in higher charge states than expected. In literature it is suggested that in MALDI this is probable for heavy ions [92, 310].

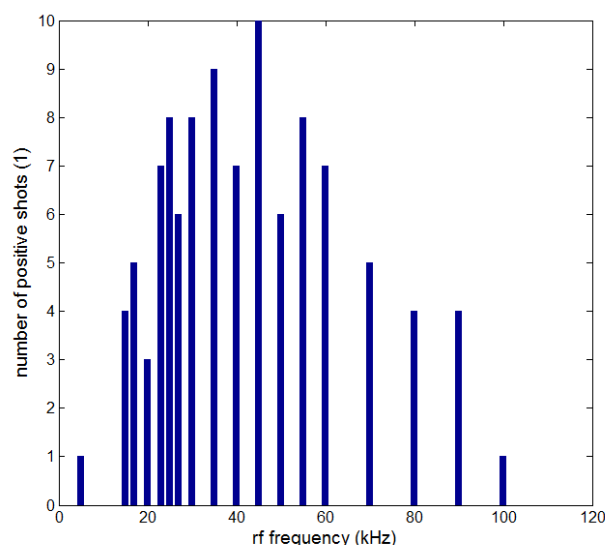


Figure 6.40: A scan over the RF drive frequency shows that the optimal trapping conditions can be found at about 40 kHz. This leads to a slightly lower mass than when calculated.

- During particle growth in the production process, a lower percentage of divinyl benzene leads to a lower mass density of the nanospheres. Since this proprietary manufacturer information was not disclosed to us, it is possible that the initial mass estimation was too high.

### 6.7.13 Fluorescence of the polystyrene nanospheres

Since the polystyrene spheres are doped with Nile Red a good fluorescence excitation could be observed, both in the green (532 nm) and in the blue (445 nm). The LIF excitation intensity is very high and surprisingly independent of the two excitation wavelengths. The fact that the fluorophore are incorporated inside the nanospheres could provide a good environment for the chromophores to rapidly release their Stokes energy to the polystyrene environment. Also each nanoparticle can carry more than a single LIF center (as shown in chapter 6.7.1). Because of the high fluorescence intensity, short exposure times of 200 ms or less could be used. This allowed the recording of a kinetic image series of the trapped ions. A detailed analysis of each individual frame results in a bleaching curve for the nanospheres, shown in the lower part of figure 6.41. Although the data scatter, a tendency for a decrease of the LIF intensity is visible, which is indicated by the plotted line (drawn

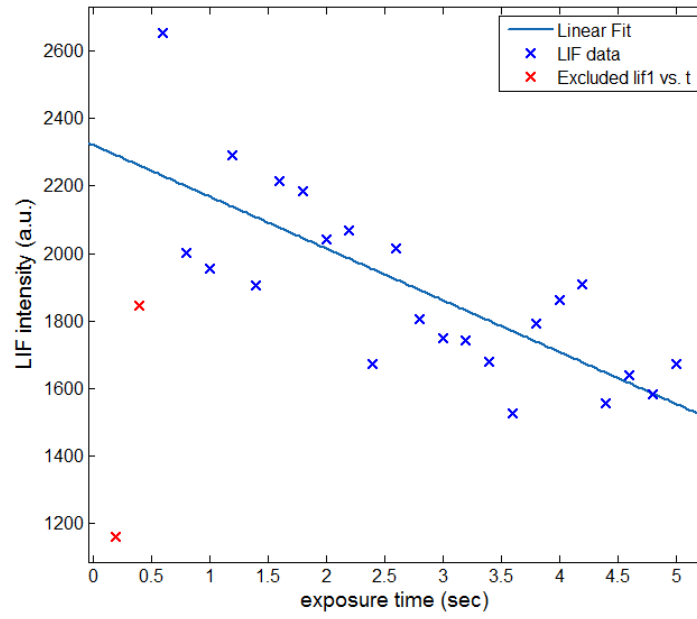


Figure 6.41: A scan of the emitted LIF intensity of a single ion cloud recorded by a kinetic series of an ion cloud. The ion trap was loaded in the positive ion mode. An exponential fit is included as a guide to the eye.

as a guide for the eye).

## Chapter 7

# Two-tone quadrupole trap

### 7.1 Cooling of molecular ions

Laser cooling and BEC physics [4] as well as the laser cooling of cold di-atomic molecules [311] has enabled to study new phenomena in quantum physics [312,313], ultracold chemistry [66,274,314–316] and ultracold collision of molecules [314,317]. One problem in cooling large molecules using 'classic' laser schemes [3] is the large number of internal vibrational and rotational levels and the impossibility of closed cycling transitions, which would allow to exchange many hundred thousand photons, as in the case for atoms. Although, in recent experiments the cooling of simple di-atomic molecules into the vibrational [318] or the rotational ground state [183] has been demonstrated, there is no straightforward concept for more complex molecules. For matter-wave interferometry experiments with molecules exceeding  $10^5$  Da cooling of the translational degrees of freedom becomes an important requirement. Sympathetic cooling of singly charged, heavy molecular ions ( $m > 1$  kDa) to mK temperatures by collisions with laser cooled atomic ions would be a big step forward, if ever it could be realized. This question triggered the idea to look into the possibility of sympathetic cooling of singly charged nanoparticles with molecular masses exceeding  $10^5$  Da, similar to ones discussed in chapter 6.7.1.

## 7.2 Simultaneous trapping of two ion species with large mass difference in a single-frequency RF trap

Although temperatures below 1 K may be reached by sympathetic cooling, a major drawback is the requirement that the molecular ion and the cooling ion should have similar mass to charge ratios ( $m/z$ ) [319]. For light ions a limit for efficient cooling was found for mass ratios of  $m_{\text{molecule}}/m_{\text{lasercooledion}} > 0.53$  [226]. Although, with a carefully choice of the ion trap parameters, even lower mass ratios can be cooled to mK temperatures [320,321]. For mass ratios  $> 1$  the cooling efficiency decreases with increasing molecular mass, since the ion clouds separate radially within the trap, scaling as  $r_1/r_2 = \sqrt{e_2 m_1 / e_1 m_2}$  (with  $r_1$  being the outer radius of the ion cloud of the lower mass-to-charge ratio ( $m_1/e_1$ ) and  $r_2$  the inner radius of the higher mass-to-charge ratio) [207,322]. With increasing radial separation the collision probability between atomic and molecular ions decreases, raising the final temperature of the molecular ion. This was shown for a mass ratio of about 5-6 between the two ion species [322] and with mass ratios greater than 10:1, temperatures below 1 K will not be reached.

To cool ions around 1 MDa with laser cooled atomic ions (around 100 Da), it will require  $10^3$  to  $10^4$  charges on the heavy ion to keep the radial ion cloud separation small within the trap. With such large charge numbers it will be virtually impossible to neutralize the ion after the cooling process as required for interference experiments.

Even if a heavy ion with low charge state could be cooled, another limitation in its realization will be the different ion dynamics of the two ion species inside the identical RF potential. Two significant criteria from ion trap theory have to be satisfied for stable trapping: First, the mass limit inside a linear quadrupole is given by

$$\frac{m}{e} > \frac{4V_0}{r_0^2 \Omega^2 \mathbf{q}} \quad (7.1)$$

where  $V_0$  and  $\Omega$  are the amplitude and frequency of the RF drive, respectively and  $\mathbf{q}$  is one of the two Mathieu parameters. The second criterion is given by

$$E_{\text{Kin}} < \frac{e^2 V_0^2}{4m r_0^2 \Omega^2} \quad (7.2)$$

stating, that the kinetic energy of the ion has to be smaller than the depth of the effective potential of the quadrupole ion trap.

A closer look onto equation 7.1 shows that it represents only a lower mass limit, but with increasing mass the effective trapping potential is gradually reduced. In short, the effective potential of the linear trap is proportional to the inverse of the ion mass,  $V_{\text{eff}} \propto 1/m$ . This reduces the potential depth by which the ion can be trapped stably. The resulting stratification effect [207] also reduces the spatial overlap between the two ion clouds. Together with the stability criterion this causes a difficulty when attempting to trap ions of very different mass-to-charge ratios simultaneously.

A closer inspection of equation 7.2 shows that with increasing difference in the two

RF amplitude	RF frequency	q	eff. potential	eff. potential
200 V	$2\pi$ 3.5 MHz	0.3	3.75 eV	$1.6 \times 10^{-4} \text{ eV}$

Table 7.1: Estimation of the (radial) trapping parameters for simultaneous trapping of two different mass-to-charge ratios inside the identical RF trapping potential. For a successful trapping of the heavy ion, a very low kinetic energy is required.

mass-to-charge ratios, the kinetic energy of the high-mass ions needs to be very low to be held inside the same effective potential. A short estimation for the ion  $^{43}\text{Ca}$  as cooling ion and for a particle with  $10^6$  Da (singly charged) as hot ion, leads to the following parameters (table 7.1).

The potential depths given in table 7.1 emphasize the very shallow potential for heavy ions trapped at RF parameters that are necessary for the light mass ions. Assumed that an ion has been completely thermalized, the ion kinetic energy would be less than 2 K. While this is not unrealistic even for ions with  $m=10^6$  Da, it might only be feasible for a small number of heavy ions, since for large ion clouds the space charge will lead to increased ion losses.

The necessary electric field of the endcaps will further reduce the depth of the effective potential (see equation 6.28), with a negative impact onto the confinement of the heavy ions ( $m=10^6$  Da), reducing the trapping probability.

Therefore a single-tone trapping of ion species with large  $m/z$  differences seems not to be a successful approach for ion cooling.

### 7.3 Two-tone trapping

A different approach towards the simultaneous trapping of two ion species with large difference in  $m/z$  ratios is when applying two different radio frequencies to the trap rods [323, 324]. Thus, two individual effective potentials would be created inside the same trapping volume, deep enough to stably confine ions with their respective mass-to-charge ratio. Since each ion 'feels' now 'its own' RF drive (at least to the lowest order), all ions should gather close to the RF node, thus increasing the spatial overlap between the two ion clouds. This could eventually allow the sympathetic cooling of ions with very different mass-to-charge ratios.

Following closely the work of [323], the two-frequency potential can be described by the following equation:

$$\Phi = (U_0 + V_1 \cos(\Omega_1 t) + V_2 \cos(\Omega_2 t)) \frac{x^2 - y^2}{2r_0^2} \quad (7.3)$$

(throughout this chapter, '**1**' describes the light ion and '**2**' the heavy ion). Using the potential of equation 7.3 the motion in the radial planes are described by a set of modified equations of motion, given for the light ion by:

$$\frac{d^2 x}{dt^2} + \frac{e}{m_i r_0^2} (V_i \cos(\Omega_i t) + V_j \cos(\Omega_j t) + U_0) x = 0 \quad (7.4)$$

$$\frac{d^2 y}{dt^2} - \frac{e}{m_i r_0^2} (V_i \cos(\Omega_i t) + V_j \cos(\Omega_j t) + U_0) y = 0 \quad (7.5)$$

where  $i=1, j=2$  and vice-versa for the heavy ion.

As shown in chapter 6.1, the motion of an ion in a linear quadrupole trap can be described by the Mathieu equation (equation 6.14) with the stability parameters **a** and **q**. From a direct comparison of the Mathieu equation and the equation of motion (in the following shown only for one radial plane, the light ion and  $U = 0$  V),  $-\frac{\Omega^2}{4}(a - 2q \cos(\Omega t)) = -\frac{2e}{m r_0^2}(V_1 \cos(\Omega_1 t) + V_2 \cos(\Omega_2 t))$ , the two modified stability parameters for the light mass ions can be deduced:

$$q = \frac{4eV_1}{m_1 \Omega_1^2 r_0^2} \quad (7.6)$$

$$a = \frac{8eV_2 \cos(\Omega_2 t)}{m_1 \Omega_1^2 r_0^2} \quad (7.7)$$

With this set of stability parameters, the secular frequency can be calculated. In the simplest approximation with the DC potential set to  $U = 0$  V, it can be written as:

$$\omega_{sec} = \frac{\Omega_1}{2} \cdot \sqrt{\frac{8e^2V_1^2}{m_1^2\Omega_1^4r_0^4} + \frac{8eV_2\cos(\Omega_2t)}{m_1\Omega_1^2r_0^2}} \quad (7.8)$$

From the applied two-tone potential (equation 7.3) and the secular frequency (equation 7.8), it can be seen that the second RF voltage is a disturbance force for the light mass ion  $m_1$ . This is especially evident in equation 7.7, where the amplitude  $V_2$  appears in the  $\mathbf{a}$  parameter, which usually describes the influence of the DC potential onto the ion motion. Here  $V_2$  acts like a slowly time varying amplitude perturbation on the trajectory of ion<sub>1</sub>.

The effective potential for the low-mass ion is influenced by the second RF as well. The modified effective potential can be deduced from the kinetic energy of the ions,  $E_{kin} = m\omega_{sec}^2r_{max}^2/2$ , as

$$V^* = \frac{e^2V_1^2}{m_1\Omega_1^2r_0^2} \cdot \left(\frac{r}{r_0}\right)^2 + V_2\cos(\Omega_2t) \quad (7.9)$$

For a given pseudopotential we can formulate a necessary condition for the stable confinement of the light ion:

$$\frac{eV_1^2}{2m_1r_0^2\Omega_1^2} >> V_2 \quad (7.10)$$

Generally, the motion of the light ion will be perturbed by the second RF potential, which acts as destabilizing force. As long as  $V_2$  is weaker than the depth of the effective potential for  $m_1$  (equation 7.10), the light ion should nevertheless stay confined.

These criteria give only the limit for stable confinement and not for the radial amplitude of the light ion. Due to the influence of  $V_2$  one can assume, that the light ions will have strong excursions which requires strong cooling forces. Generally, four criteria can be derived from the above equations, which need to be fulfilled for stable trapping of low-mass ions in a double RF potential:

1. The kinetic energy of the ion must be smaller than the depth of the effective potential.

2. The RF parameters for the light mass have to lie within the stable region, e.g.,  $\mathbf{q} < 0.9$ .
3. The influence of the 'quasi-DC' (e.g. the second RF amplitude) must be small: The modified  $\mathbf{a}$  parameter, with  $\mathbf{a} = (8eV_2)/(m_1\Omega_1^2r_0^2)$ , should stay within a stable region for the light ion.
4. The secular frequency of the light ion should not be identical or close to the frequency of the second RF. Otherwise a resonant excitation similar to dipolar resonant excitation is to be expected.

Different to the light ion, the motion of the heavy ion ( $m_2$ ) cannot be described in this perturbative treatment. For  $m_2$  the following two conditions apply for a stable confinement:

$$\frac{eV_1^2}{2m_2r_0^2\Omega_1^2} < V_2 \quad (7.11)$$

$$\frac{eV_2^2}{2m_2r_0^2\Omega_2^2} < V_1 \quad (7.12)$$

These conditions show that the trajectories of the heavy ions are influenced by both RF potentials equally. The fast oscillatory RF ( $\Omega_1$ ) still allows stable trapping conditions since the stability parameter  $\mathbf{q}$  describes only a low mass cut-off.

In the following the dynamics of such a two-tone setup is explored, using the existing ion trap geometry (see section 6.4). The estimated parameters in table 7.2 show that the RF parameters are all within a practical experimental range.

## 7.4 SIMION simulations investigating trapping in a two-frequency ion trap

The theoretical estimations show that the simultaneous trapping of two ions with a large difference in their mass-to-charge-ratio should in principle be possible in a linear quadrupole trap. A set of ion trajectory calculations were performed in SIMION 8.1 [200] to estimate the correlations of the two RF parameters for the interpretation of later measurements.

parameter	value
$m_1$ (Sulforhodamine B)	581 Da
$m_2$	$10^6$ Da
$e_{1,2}$	+1
$V_1$	600 V
$\Omega_{\text{RF},2}$	$2\pi \times 15$ kHz
<b>q</b> operation point for mass $m_1$	0.35
$\Omega_{\text{RF},1}$	$2\pi \times 1.089$ MHz
max. $V_2$ (from eqn. 7.10)	52 V
use $V_2 = 50$ V	
<b>a</b> <sub>m1</sub>	0.058
$\omega_{\text{sec},1}$	$2\pi \times 131.6$ kHz
$V_1^*$	51 eV
<b>q</b> operation point for mass $m_1$	0.63
$\Omega_{\text{RF},1}$	$2\pi \times 812$ kHz
max. $V_2$ (from eqn. 7.10)	94 V
use $V_2 = 45$ V	
<b>a</b> <sub>m1</sub>	0.095
$\omega_{\text{sec},1}$	$2\pi \times 124.85$ kHz
$V_1^*$	70 eV

Table 7.2: Calculated parameters to achieve stable trapping of two ions of different mass-charge-ratios in a two-tone RF quadrupole trap. Calculations are based on the experimental ion trap parameters, presented in this thesis, as well as on the equation presented above and in [323].

### Simulation settings

Our ion trap geometry was implemented into SIMION, as displayed in figure 7.1. It displays a simulation result for the combined trapping of Sulforhodamine B (581 Da) and a polystyrene sphere at  $10^6$  Da. Since ion loading by MALDI cannot be described by SIMION in a realistic way, the loading of the trap was not simulated, instead all ions start in a volume element in the central trap section (S3). They are randomly positioned in a 3D Gaussian distribution, with a standard deviation of about 1.5 mm. The initial kinetic energies for the two different ion groups are about 1 eV for Sulforhodamine B and 0.1 eV for the heavy ions. Values from table 7.2 were used for the two RF potentials, since these resulted in stable trapping conditions. To simulate the current experimental conditions, a buffer gas atmosphere with Helium at a constant pressure of 0.3 Pa and 300 K was implemented. Buffer gas is introduced at the beginning of the simulation without a pressure gradient. To describe the ion collisions the SIMION Hard Sphere Collision Model (HS1) routine

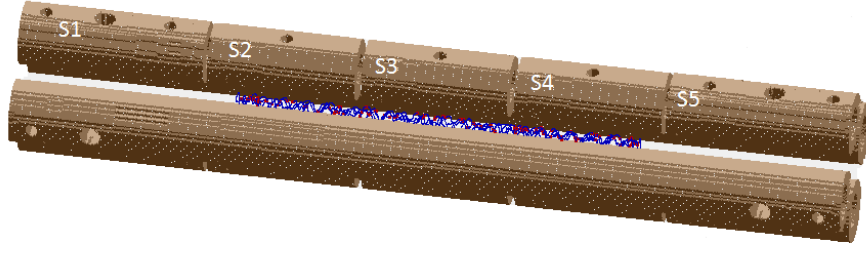


Figure 7.1: An image of the linear quadrupole geometry from a SIMION simulation is shown. The  $RF_1$  parameters were applied to the non-segmented rods, while the RF required for high mass trapping was applied to the segmented rods (labeled S1 to S5). In this simulation the endcap potentials were also applied to S1 and S5. At the beginning of all simulations the initial phase of the RF is set to zero and the relative phase between the two RF frequencies is neglected. Sample trajectories of the ions are shown in blue in the center of the ion trap.

was used.

For a better overview the most important simulation parameters are summarized in table 7.3.

parameter	value
$V_1$ (on non-segmented rods)	600 V
$\Omega_1$	$2\pi \times 812/900/1050$ kHz
$V_2$ (on segmented rods)	30 - 70 V
$\Omega_2$	$2\pi \times 15$ kHz
endcap potential	40 - 80 V
buffer gas temperature	300 K
buffer gas pressure	$3 \times 10^{-3}$ mbar
collision cross section	$2 \times 10^{-18}$ m <sup>2</sup>
initial energy light ion	1 eV
initial energy heavy ion	0.1 eV
simulation time	50 ms
number of light/heavy ions	40 each

Table 7.3: The most important parameters for the two-frequency ion trap simulations are given.

#### 7.4.1 SIMION simulation results

The analysis from SIMION simulations proved that stable trapping conditions for ion clouds of different mass to charge ratio could be obtained in a double frequency RF trap.

In order to determine practical parameters the  $\mathbf{q}$  parameter of the light ion was var-

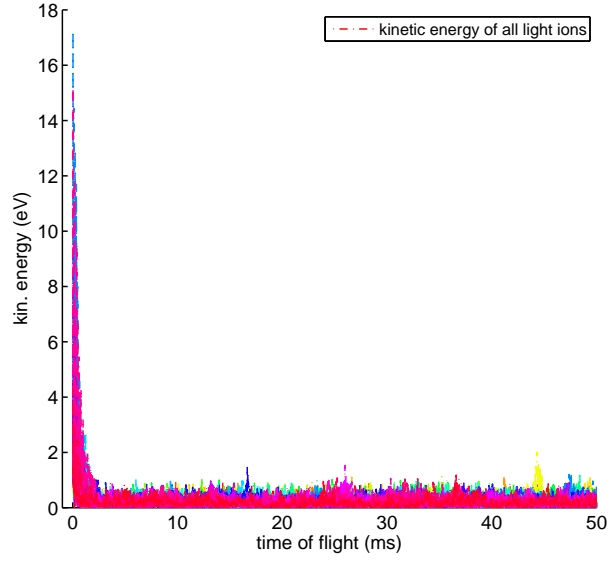
ied by simulating at three different RF<sub>1</sub> frequencies, namely 812 kHz, 900 kHz and 1050 kHz. These RF parameters corresponded to  $\mathbf{q}$  values of 0.63, 0.51 and 0.37, covering regions of different  $\mathbf{a}$  values and thus to RF<sub>2</sub> amplitudes with the highest acceptable RF<sub>2</sub> amplitudes expected at the lowest RF<sub>1</sub> frequency.

In a first set of simulations the radio-frequency for the heavy ions was applied to the three innermost segments only (S2, S3, S4, see also figure 6.10) while the outer segments S1, S5 were connected to the end-cap potential. The RF<sub>1</sub> amplitude level was kept constant at 600 V throughout the simulations, while the influence of the RF<sub>2</sub> amplitude was varied between 30 V and 70 V.

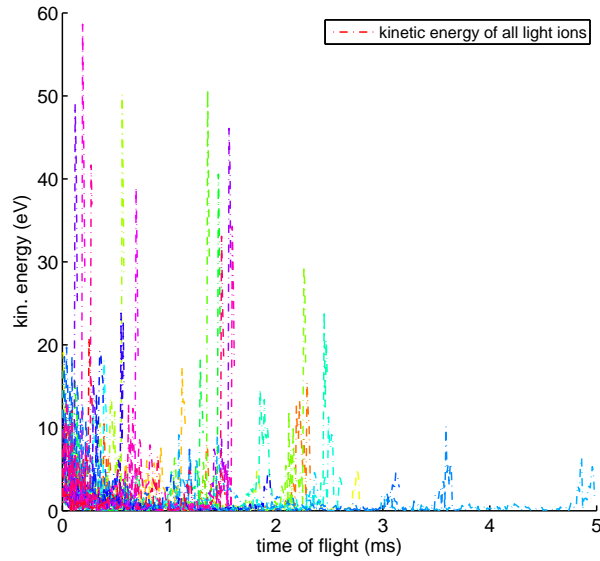
For low RF<sub>2</sub> amplitudes a stable confinement for light ions was found, as shown in figure 7.2a (RF<sub>1</sub> frequency: 900 kHz). The light ions loose kinetic energy within the first few hundred  $\mu s$  because of the buffer gas cooling and reach an equilibrium state with a mean kinetic energy of  $\langle E_{\text{kin}} \rangle < 1$  eV. The ions stay confined until the end of the simulation at 50 ms. A detailed analysis of the different trajectories supports the conclusions that light ions can be stably trapped at a low amplitude of the low frequency RF<sub>2</sub>.

Increasing the amplitude of RF<sub>2</sub> strongly influences the kinetic energy of the light ions: The kinetic energy increases with increasing flight time, as the ions appear to receive random 'kicks', leading to increased ion loss in the course of the simulation time. This behavior is displayed in figure 7.2b for the highest simulated RF<sub>2</sub> amplitude (70 V) simulated. The light ions have no stable trajectories and are ejected from the ion trap nearly instantaneously, with more than 50% of the ions lost within the first four milliseconds and the rest shortly afterwards. Even continuous buffer gas cooling is not sufficient for a stable long-term confinement in this case.

A similar trend is seen in the simulations for the two other RF frequencies (812 kHz, 1050 kHz) as well. In figure 7.3 the trapped ion fraction at different flight times are shown for two simulated RF<sub>1</sub> frequencies. Stable trapping of the light ion cloud can be achieved for RF<sub>2</sub> amplitudes below about 55 V. Above this level an increased ion loss is observed, the rate depending on the RF<sub>1</sub> frequency which is clearly seen when comparing 1050 kHz (figure 7.3b) and 812 kHz (figure 7.3a). For the former an amplitude of  $V_{\text{RF2}} = 60$  V decreases the trapped ion population to 25 % within the first 16 ms flight time. Contrary, at the lower frequency (812 kHz) still more than 80 % of the ions are still confined at this run-time. For the longest simulated flight



(a)  $\text{RF}_2$  amplitude: 30 V. All light ions stay trapped throughout the simulation period.



(b)  $\text{RF}_2$  amplitude: 70 V. Compared to the lower  $\text{RF}_2$  amplitude, a strong loss of light ions can be observed.

Figure 7.2: Distribution of the kinetic energy of all (40) light ions trapped inside the two-tone RF potential with frequencies of 900 kHz and 15 kHz and the two RF amplitudes:  $\text{RF}_1$  600 V and  $\text{RF}_2$  30 V (7.2a) or 70 V (7.2b). All other trapping parameters were used as in table 7.3. For low  $\text{RF}_2$  amplitudes light ions are stably confined throughout the simulations, with increasing amplitudes losses of the light ions will occur.

time (50 ms) more than 50% of the ions stay trapped for  $\text{RF}_1 = 812$  kHz. Increase of the  $\text{RF}_2$  amplitude further leads to rapid light ion losses also in this case.

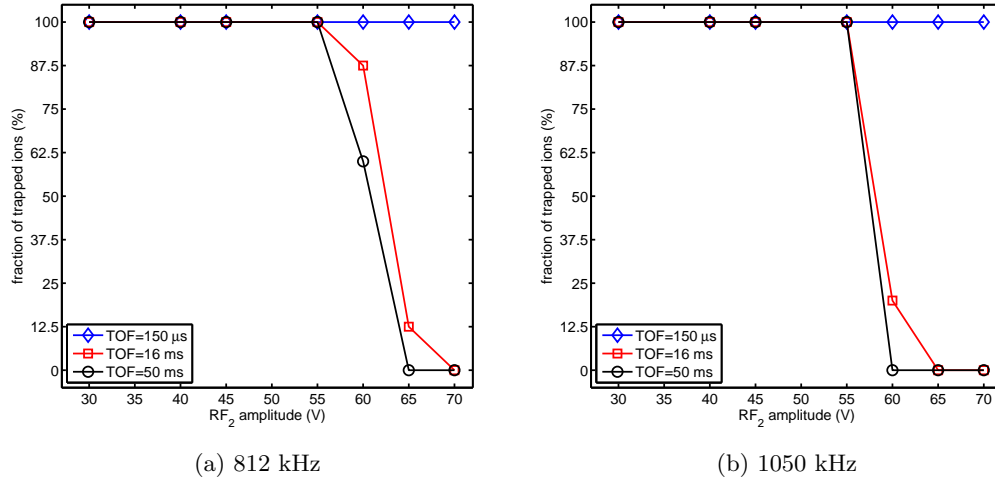


Figure 7.3: The fraction of trapped light ions for different  $\text{RF}_1$  frequencies (812 kHz in 7.3a and 1050 kHz in 7.3b) and different  $\text{RF}_2$  amplitudes. Simulation parameters were identical to the ones in table 7.3. The trapped ion population is shown at different simulation times (0.15, 16 and 50 ms). An influence of the  $\text{RF}_2$  amplitude is evident (e.g. loss of ion population with increasing RF amplitude). Increased trapping stability due to increased  $\mathbf{a}$  when decreasing the  $\text{RF}_1$  frequency is observed. At  $\text{RF}_1 = 900$  kHz results are similar to  $\text{RF}_1 = 812$  kHz (not shown).

The increased trapping stability at lower  $\text{RF}_1$  frequencies can be explained by the Mathieu parameter  $\mathbf{a}$ . Due to the decreasing frequency value the stable trapping region in the  $\mathbf{a} - \mathbf{q}$  plane increases. This allows an increase of the  $\text{RF}_2$  amplitude while the light ions are still kept confined in the ion trap.

The results of figure 7.3 indicate that the  $\text{RF}_2$  amplitude influences the stability of the light ions strongly. A possible explanation could be how and in which strength the endcap potential is applied. With rising  $\text{RF}_2$  amplitude the effective potential for the light ions is growing too shallow in comparison to their kinetic energy, leading to losses along the longitudinal axis of the ion trap. This is shown in figure 7.4, where the trajectories of 40 light ions are shown in a cut through the axial-radial plane of the ion trap. In this simulation the ions expand over a quite large fraction of the radial plane, but nevertheless are distributed evenly throughout the axial trap volume (indicated by the high density of plotted ion trajectories) for most of the simulation time. Eventually they escape the trapping volume along the axial direction of the trap, indicating that a high  $\text{RF}_2$  amplitude 'pushes' the ions over the endcap barrier.

To further investigate this cause of ion loss, a second set of simulations was per-

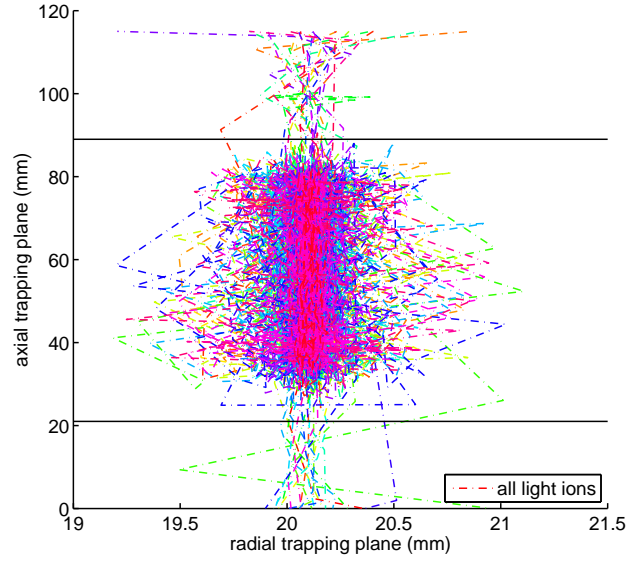


Figure 7.4: Ion trajectories of the light mass ions (shown in the radial-axial plane) demonstrating a major ion loss along the axial direction of the trap. Hardly any light ions are lost in the radial direction. In this simulation the  $\text{RF}_2$  amplitude was 70 V as well as the endcap potential which was applied to electrodes S1, S5. The inner edges of the endcaps are marked by the two black horizontal lines and the RF node is at about 20 mm in the radial plane.

formed, keeping the basic simulation parameters identical to previous simulations (see table 7.3), but applying simultaneously  $U_{\text{DC}}$  and  $\text{RF}_2$  to segments S1, S5. For  $\Omega_1 = 2\pi \times 1050$  kHz the results are shown in figure 7.5 in comparison to the previous simulation (see figure 7.3b) indicating more stable trapping conditions to the previous case (no  $\text{RF}_2$  on S1, S5). Although a larger fraction of ions is still trapped at the different simulation times, nevertheless, also for  $\text{RF}_2 > 60$  V no long-term trapping is observed. The other two  $\text{RF}_1$  frequencies, 812 kHz and 900 kHz, present a different picture: No indications of ion losses even at  $\text{RF}_2$  amplitudes of 70 V is seen.

For the heavy ions stable trapping was identified throughout the complete parameter space investigated in the simulations. The value of  $\Omega_{\text{RF}_1}$  has no significant influence on the results for all the three frequencies studied (812 kHz, 900 kHz, 1050 kHz), with no ion loss to be observed. This was expected from the theoretical considerations above: The high frequency RF contributes not much to instability since  $\mathbf{q}$  of  $\text{RF}_1$  determines only a low-mass cut-off and the high-frequency  $\text{RF}_1$  produces an attractive - though weak - trapping potential.

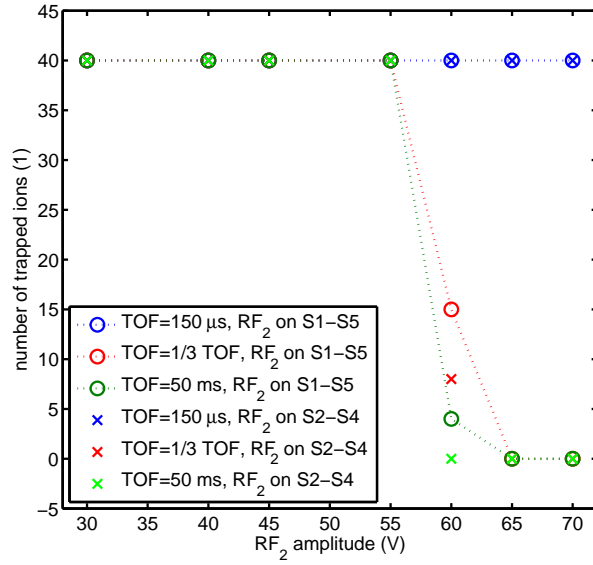


Figure 7.5: Comparison of two simulations at  $\Omega_1 = 2\pi \times 1050$  kHz (RF<sub>2</sub> and DC on S1, S5 - connected data points). For comparison the simulation (only DC on S1, S5) is plotted with individual data points. All other simulation parameters were identical to table 7.3.

The kinetic energy distributions of heavy ions throughout the different simulations are shown in figure 7.6, with a stable confinement of ions being nearly independent on the RF<sub>2</sub> amplitude. For low radio-frequency amplitudes (RF<sub>2</sub> = 30 V, figure 7.6a), the kinetic energy of the trapped ions show a slight raise with increasing flight times. But this energy increase is still not high enough to eject the ions from the ion trap. An identical distribution is seen for comparison in figure 7.6b for RF<sub>2</sub> = 70 V, where the overall kinetic energy of the heavy ions remains dampened throughout the whole simulation time.

### The effect of the endcap potential in a two-tone RF trap

To investigate ion losses depending on the endcap potential strength, two additional simulations were performed varying the endcap potential between 30 V and 80 V. RF<sub>1</sub> was set to 900 kHz at 600 V (light ions) and RF<sub>2</sub> to 15 kHz at 50 V (heavy ions), all other settings were identical as in table 7.3.

As long as the endcap potential is much greater than the RF<sub>2</sub> amplitude (by more than 10 V) stable trapping of the light ions is possible. Otherwise the number of trapped ions decreases with prolonged simulation time and, as soon as the endcap

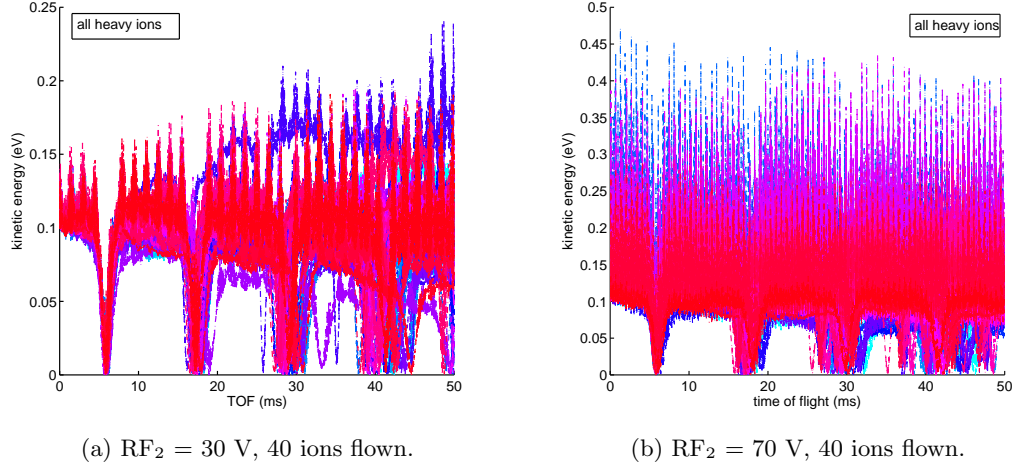


Figure 7.6: Temporal evolution of the kinetic energies of the heavy ions inside the two-tone RF field. A weak amplitude (30 V) (7.6a) leads eventually to an overall increase in kinetic energy of the ions, higher RF amplitudes (70 V) show no such energy increase (7.6b). Simulation parameters were identical to the ones in table 7.3.

is equally or less strong than the  $RF_2$  amplitude, no stable trapping of the light ions is possible, since the  $RF_2$  amplitude acts like a 'quasi-DC' onto the light ions. If the axial confinement field becomes weaker than the central 'quasi-DC', the ions can escape along the longitudinal axis of the ion trap. For the heavy ions no strong influence of the endcap potential can be observed, and similar to earlier simulations, all trapped ions remain trapped throughout the whole simulation time.

#### 7.4.2 Spectral analysis of the ion motion in a double RF potential

For a more detailed picture of the ion dynamics inside a two-tone trap, a spectral analysis of the simulated trajectories was performed. The RF drive parameters were set to  $RF_2 = 70$  V, 15 kHz and  $RF_1 = 600$  V, 900 kHz with a DC of 70 V on the endcaps. All other ion trap and (internal) SIMION parameters were kept as in the previous simulations (table 7.3). To obtain a good spectral resolution, a time step of  $0.1 \mu s$  was chosen.

Results for the radial secular motion of an ion with heavy molecular weight is shown in figure 7.8. The most prominent peak is visible at about 740 Hz, which corresponds to the fundamental radial secular frequency  $\omega_0$  of the ion. The strong amplitude indicates the dominant frequency fraction of the ion motion. Apart from  $\omega_0$ , first

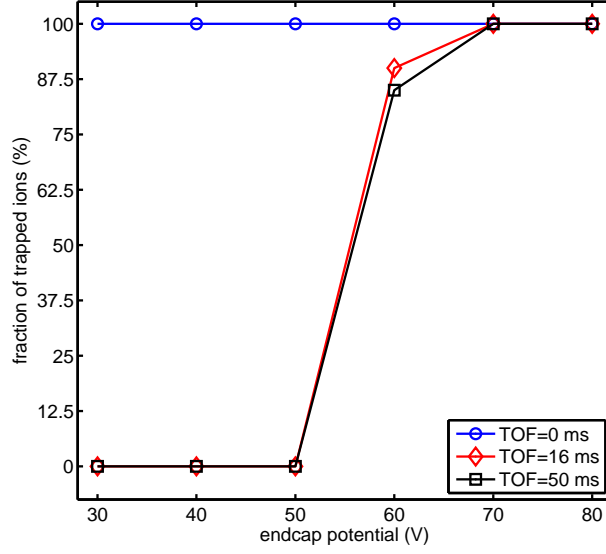


Figure 7.7: A major loss channel for light ions is given by the strength of the endcap potential. With a potential equal or less than the  $\text{RF}_2$  amplitude, no trapping is possible. Endcap potential was applied to segments S1, S5 and RF values were chosen as described in the text.

higher order frequency modes in the vicinity of 15 and 30 kHz can be identified, as can be calculated from theory by  $\omega_n = (\beta + 2n) \times \Omega/2$ . A detailed list of all identified frequencies is given in table 7.4.

In the double RF trap a new set of oscillations appears at the high end of the power spectral density (PSD) plot. This peak group consists of two sets of individual frequencies, equally spaced around 900 kHz, showing the influence of the  $\text{RF}_1$  on the heavy ions. This result demonstrates that ion trajectories are more complex in a two-tone trap than in standard linear quadrupole experiments.

The influence of  $\text{RF}_1$  on the actual ion trajectories was investigated further by comparing directly different applied  $\text{RF}_1$  potentials, as shown in figure 7.9. For better legibility, the data for 300 V (blue line) as well as for 500 V (green line) have been scaled by a factor of  $10^{-4}$  and  $10^{-9}$ , respectively.

If only  $\text{RF}_2$  is present, the FFT analysis shows the oscillation modes of the heavy ions as expected from ion trap theory, namely  $\omega_0, \Omega_{\text{RF}} \pm \omega_0$  as well as  $2 \cdot \Omega_{\text{RF}} \pm \omega_0$ .

With the introduction of  $\text{RF}_1$ , new spectral patterns appear at the high frequency side of the FFT plot. These are mainly due to new oscillation modes at the frequencies of  $\Omega_{\text{RF1}} \pm \omega_0$ . Furthermore the noise floor at frequencies greater than 1 MHz increases. The ion motion induced by the  $\text{RF}_2$  remains independent from the

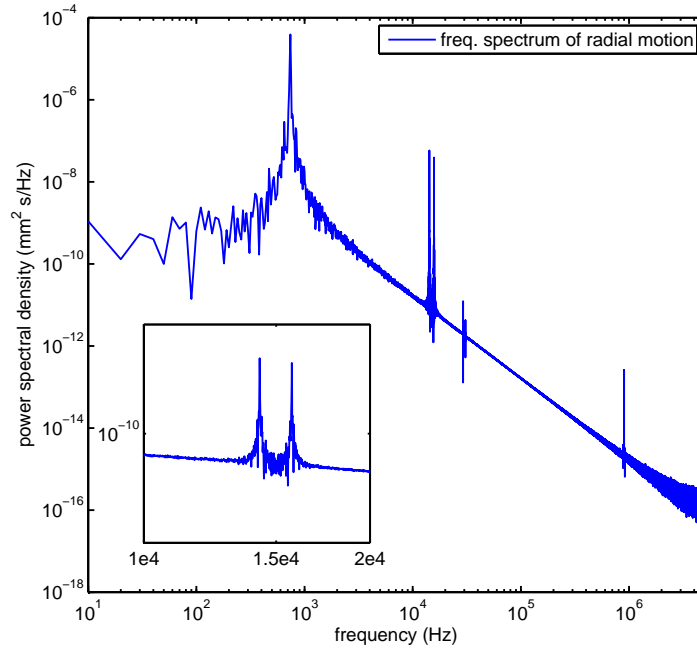


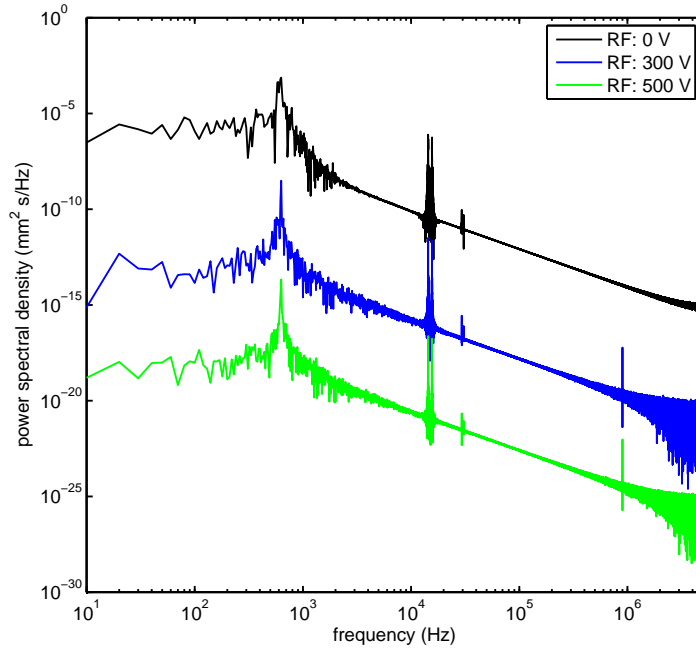
Figure 7.8: Spectral analysis of the radial secular motion of the heavy ions inside the double-frequency trap with RF frequencies of 15 kHz, 900 kHz and amplitudes of 70 V, 600 V. The different oscillation modes of the ions are easily identifiable. For details of the higher oscillation modes a section around  $\omega_{\pm 1}$  was zoomed in the inset. The two secular frequencies spaced equivalently around the RF drive frequency are clearly visible, while the RF frequency itself is absent.

influence of the  $\text{RF}_1$ .

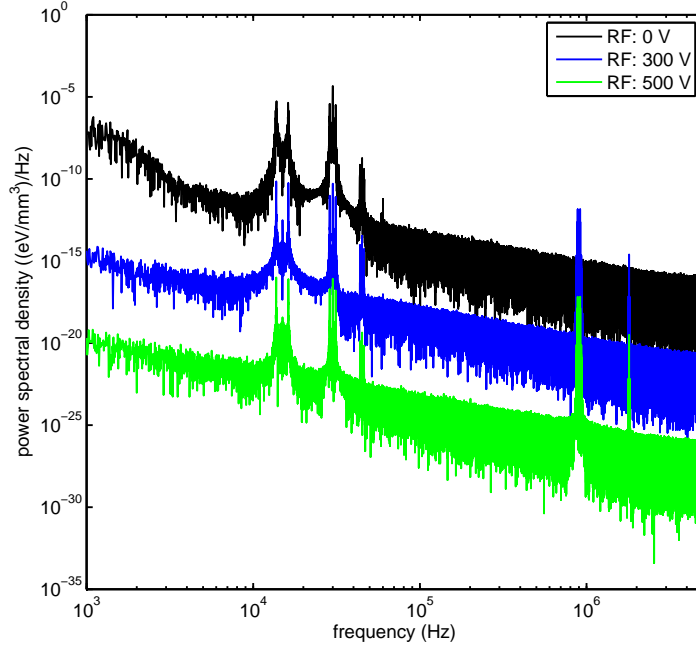
A similar observation can be made in the analysis of the kinetic energy (figure 7.9b). Without  $\text{RF}_1$  only the fundamental ion oscillation modes are seen. With the introduction of  $\text{RF}_1$ , additional spectral lines appear in the high-end of the spectra, which are given by a combination of  $\Omega_{\text{RF}1} \pm \omega_0$ .

From these simulations we conclude again that a stable trapping of heavy mass ions should be possible in a two-tone trap. The observed influence of the second RF on the kinetic energy could limit the effect of any external cooling mechanism, thus cooling to cryogenic temperatures will be necessary to confine the ions more closely to the RF node.

Our simulations proved that also light ions can be stably trapped in a two-tone RF potential, but their detailed ion motion needed still to be explored. A FFT analysis of the secular motion and of the kinetic energy was performed for varying trap parameters ( $\text{RF}_2$  amplitudes: 0, 30 and 60 V), shown in figure 7.10. For  $\text{RF}_2 = 0\text{V}$ , the secular frequency is  $\omega_0 = 1.937 \times 10^5$  Hz, peaks at higher frequencies are due to



(a) FFT spectrum of the radial motional amplitude



(b) FFT spectrum of the kinetic energy

Figure 7.9: FFT analysis of the simulated radial motion of a heavy mass ion trapped inside a double RF frequency potential of different strengths. 7.9a shows the radial secular motion of the ions, while 7.9b the respective FFT analysis of the ion kinetic energy. For a better comparison, the curve for the 300 V (blue) and the 500 V (green) RF amplitude was scaled by a factor of  $10^{-5}$  and  $10^{-9}$  respectively, in both plots. RF parameters were 15 kHz and 0 - 500 V (heavy ion) as well as 900 kHz and 600 V, all other simulation parameters were identical to the ones given in table 7.3.

frequency (Hz)	description
740	fundamental secular frequency, $\omega_0$
$1.426 \cdot 10^4$	$\Omega_{RF2} - \omega_0$
$1.574 \cdot 10^4$	$\Omega_{RF2} + \omega_0$
$2.926 \cdot 10^4$	$2 \cdot \Omega_{RF2} - \omega_0$
$3.073 \cdot 10^4$	$2 \cdot \Omega_{RF2} + \omega_0$
$8.993 \cdot 10^5$	$\Omega_{RF1} - \omega_0$
$9.007 \cdot 10^5$	$\Omega_{RF1} + \omega_0$
$8.843 \cdot 10^5$	$\Omega_{RF1} - \Omega_{RF1} - \omega_0$
$8.857 \cdot 10^5$	$\Omega_{RF1} - \Omega_{RF1} + \omega_0$
$9.143 \cdot 10^5$	$\Omega_{RF1} + \Omega_{RF1} - \omega_0$
$9.157 \cdot 10^5$	$\Omega_{RF1} + \Omega_{RF1} + \omega_0$

Table 7.4: From an analysis of the power spectral density plot (figure 7.8) the radial secular frequency spectrum from the ion can be deduced. The low frequency values are given by the influence of the RF<sub>2</sub>, while the high frequency peaks are given by the influence of the second RF drive.

the higher orders of the secular motion.

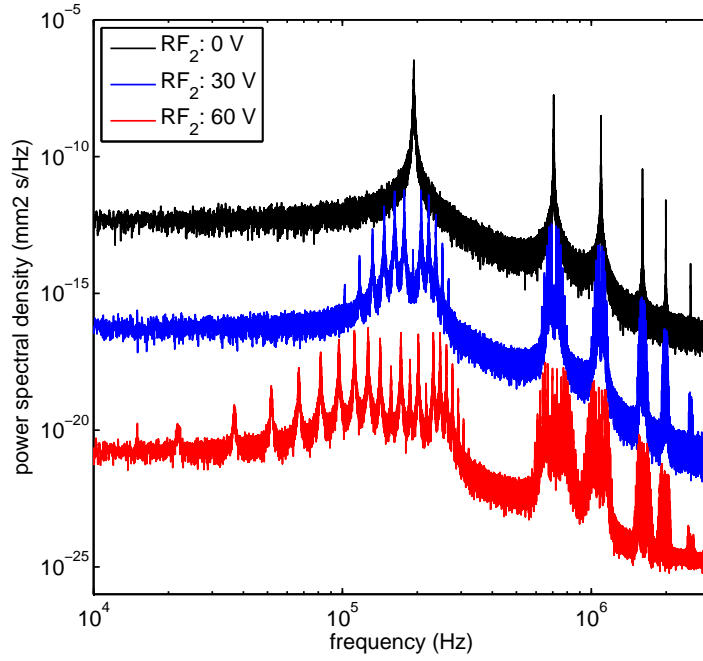
Setting RF<sub>2</sub> to 30 V creates a more complex frequency spectrum (shown in blue, figure 7.10a). Generally, a few distinct frequency cluster can be identified. Apart from the central frequency in each cluster additional oscillations are seen with respect to the unperturbed ion motion. The frequency difference between two neighboring peaks has a value of 15 kHz, which corresponds to the RF<sub>2</sub> frequency.

For even larger V<sub>RF2</sub> values (e.g. 60 V) the oscillation modes get even more complex. Furthermore additional peaks appear in the spectrum, which indicates that the kinetic energy of the ions will increase with increasing RF<sub>2</sub> amplitude.

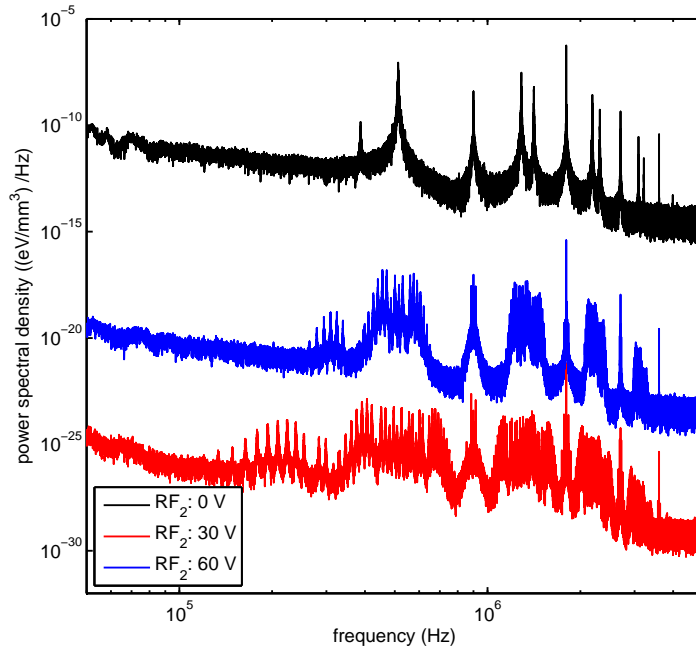
This can be observed in the PSD plot of the kinetic energy as well (figure 7.10b). Additional frequency peaks, spaced by the RF<sub>2</sub> frequency appear with increasing RF<sub>2</sub> amplitude. The strong increase of additional modes and their amplitudes indicates again that the light ions will be heated by the RF<sub>2</sub> amplitude. This emphasizes the need for a strong cooling mechanism for the light ions inside a double RF potential.

## 7.5 Experimental tests of a two-tone trap

The theoretical model showed that a simultaneous, long-term stable confinement of two vastly different ion masses (by factor 1000 or more) should be possible. In the following, we will present first experimental tests of this idea in our linear quadrupole



(a) FFT of the radial motional amplitude



(b) FFT of the kinetic energy

Figure 7.10: FFT analysis of the radial motion and kinetic energy of the light ion trapped in a two-tone trap. With increasing  $\text{RF}_2$  amplitude additional oscillations modes appear in the spectra. These are spaced by the  $\text{RF}_2$  frequency (e.g. 15 kHz) (for a better comparison, two of the curves are scaled: blue ( $10^{-4}$ ) and red ( $10^{-9}$ )).

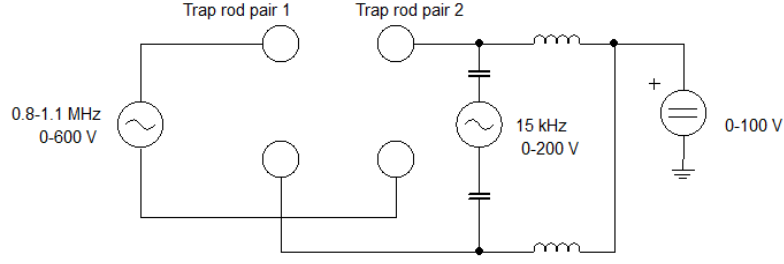


Figure 7.11: Circuit diagram of the electric wiring for measurements in the two-tone RF setup. Rod pair one is the non-segmented one, while rod pair 2 is the segmented. The DC connection was inserted only at the trap segments 1 and 5, which were used as endcap electrodes simultaneously.

ion trap.

### 7.5.1 Experimental setup

For that purpose the ion trap setup of section 6.7 was modified according to the predicted parameters. The calculated parameters for the light ion are presented in table 7.2, which could be realized with the available equipment in the laboratory. For the heavy ions the two stability conditions (equations 7.11, 7.12) can be calculated to  $eV_1^2/2m_2r_0^2\Omega_1^2 = 0.055$  V and  $eV_2^2/2m_2r_0^2\Omega_2^2 = 1.12$  V with  $\Omega_{RF1}=812$  kHz. Both values are lower than the estimated RF amplitudes, indicating that heavy ions should also be stably trapped under these conditions.

The wiring of our trap was adapted to apply a two-frequency RF potential, as shown in figure 7.11. Each of the two RF sources was connected to one of the two pairs of trap rods. The non-segmented rods were connected to one of the outputs of the LC tank coil circuit (see chapter 6.6.1), the second output, carrying the  $180^\circ$  phase-shifted RF signal, was grounded by a Faraday cage. The amplitude could be varied between 0 and 600 V and the frequency could be set between 800 kHz and 1.1 MHz. This allowed stable trapping of the fluorophore Sulforhodamine B within  $0 < \mathbf{q} < 0.63$ .

On the segmented trap electrodes the RF potential was obtained by the amplified output of a signal generator. With this combination a variable  $RF_2$  tuning over a large trapping parameter space was possible. The RF amplitudes were limited to  $< 200$  V. As estimated in section 7.3, only moderate RF potentials are necessary to generate the pseudopotential necessary for high-mass particle trapping, since

otherwise light ions would be forced out of the trap.

Axial confinement was reached by connecting the outermost segments (S1, S5) to the DC power supply with up to +150 V. To prevent interference between the two power sources an LC link was introduced in the wiring of segments S1, S5 (see figure 7.11). A 120 pF, 1 kV (DC) rated capacitance was wired as two pairs of 120 pF individual capacitors in series, blocking the DC entering the RF supply. To block off the reflected RF into the DC supply, a series of two 100 mH inductors (Murata) were used for shielding.

To test the influence of the low frequency  $RF_2$  on low mass ions, Sulforhodamine B was used as a low molecular test compound and polystyrene particles with a nominal diameter of  $40 \pm 4$  nm, stained with fluorophore Nile Red as high molecular compound. The trap was filled using a MALDI source, as already described in section 6. Samples were prepared in the following way:

- 8 mg 2,5-Dihydroxybenzoic acid, dissolved in 0.5 ml Ethanol
- 5 mg Sulforhodamine B, dissolved in 1 ml Ethanol
- 50  $\mu$ l polystyrene solution (1% $w/v$ ) was further diluted with 500  $\mu$ l  $H_2O_{\text{dest.}}$
- All stock solutions were mixed in a 1:1 (vol.) ratio prior spotting onto the MALDI sample plate

A trapping cycle was started by loading ions into the trap under a constant buffer gas atmosphere (typically  $2 \times 10^{-3}$  mbar Helium at room temperature). Generally 30 to 40 desorption laser pulses were utilized in MALDI desorption. Ions were kept typically in the trap for about three to five seconds before a read-out with the LIF lasers was started. Depending on the measurement the laser wavelengths 445 nm, 532 nm, or both wavelengths simultaneously could be chosen. The trapping cycle was completed by lowering the endcap potentials to zero, removing the buffer gas and switching off the low-frequency RF.

### 7.5.2 Experimental results

To find the optimal parameter space for a stable confinement the compounds were tested also individually in a two-tone RF potential.

## Influence of the high mass radio-frequency onto the trapping performance

At first, the influence of the low-frequency RF ( $\text{RF}_2$ ) on the light ions was tested. Sulforhodamine B was loaded into the trap with an  $\text{RF}_1$  amplitude of 450 V and frequency of 1.081 MHz, which corresponds to a stability parameter  $\mathbf{q} \approx 0.27$ . The  $\text{RF}_2$  amplitude needed to be restricted to below 15-20 V, to keep the  $\mathbf{a}$  parameter (equation 7.7) at values of about 0.02 and therefore within the first stability region. With the low  $\text{RF}_2$  amplitude, a small endcap potential of 25 V was applied to the trap segments one and five.

Helium as buffer gas pressure was kept at a constant pressure of  $3 \times 10^{-3}$  mbar. Identical numbers of desorption pulses were used for loading. Each measurement was repeated three times to reduce the influence of statistical fluctuations. The  $\text{RF}_2$  drive was switched off during the loading of the ion trap.

Immediately after the ion confinement and after 3 seconds, a first LIF image was taken to quantify the ion cloud. Then the  $\text{RF}_2$  amplitude was switched on and a further LIF image was taken. The resulting changes in LIF intensity for various  $\text{RF}_2$  frequencies are shown in figure 7.12.

Compared to the ion loading signal, the second LIF read-out shows another new

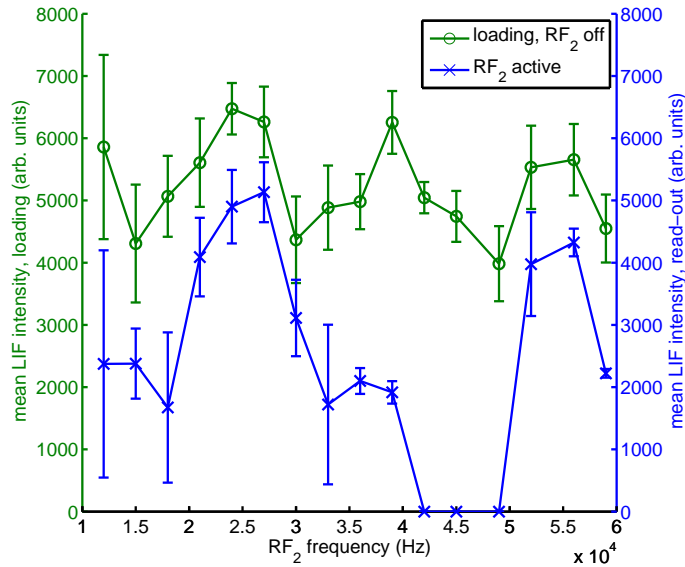


Figure 7.12: A variation of the frequency of the low frequency RF shows a distinct influence on the ion signal of the light-mass ions. The loading curve (green) shows a relative stable signal as long as  $\text{RF}_2$  is still off. The LIF signal after the onset of the  $\text{RF}_2$  is shown in blue.

trend: After application of  $\Omega_{\text{RF}2} = 2\pi \times 10$  to 30 kHz, the detected signal follows the general trend seen for the loading curve, e.g. with increasing initial LIF intensities also the second LIF signal increases, but at higher RF<sub>2</sub> frequencies (around 40 to 50 kHz) the observable LIF drops. At even higher frequencies ( $> 50$  kHz) both curves follow each other again.

The signal loss between 40 and 50 kHz could be influenced by different loss mechanisms: sample fluctuations during loading of the trap, bleaching of the ion cloud and the influence of the RF<sub>2</sub> potential.

The observed loading curve in figure 7.12 (green) shows a low fluctuation over the recorded frequency range. Furthermore each data point represents the average over three individual measurements. This makes an influence of the sample and MALDI process on the mentioned signal loss unlikely.

Another process which could influence the detected LIF intensities is bleaching of the ion cloud. While this cannot be ruled out to limit the signal intensities, the second LIF curve (blue line in figure 7.12) does not indicate it. While the blue curve has overall smaller intensities compared to the green one (given by ion losses or bleaching), bleaching cannot describe such a sudden drop in the LIF intensity. Also the influence of higher order secular frequencies for Sulforhodamine B ions can be ruled out for creating such specific signal loss.

Therefore it is assumed that signal losses between 40 and 50 kHz are due to the influence of the second RF drive. Although this signal behavior at these RF<sub>2</sub> frequencies cannot be explained in detail by theoretical estimations (see equations 7.10, 7.7), it shows first ion cloud behavior under the influence of a second RF potential. Furthermore, it demonstrates that the motion of light ions inside a two-tone RF potential is more complex than estimated.

While the frequency scan of the RF<sub>2</sub> drive showed that the Sulforhodamine B ions can be stably trapped in a two-frequency potential over several seconds (see fig. 7.12), similar measurements were conducted to investigate the influence of the RF<sub>2</sub> potential onto the trapping time of the ions. Sulforhodamine B alone was introduced into the vacuum chamber, keeping all other experimental parameters, i.e. buffer gas, electrical connections, LIF excitation wavelength, identical. The ion dynamics was observed by recording a series of LIF images, each with a time of 7 seconds to the previous one. The measurement was repeated for RF<sub>2</sub> = 25, 29, 32

and 34 kHz and the resulting LIF intensity signals are plotted in figure 7.13.

Over the first ten seconds a strong LIF intensity can be observed. It falls over time

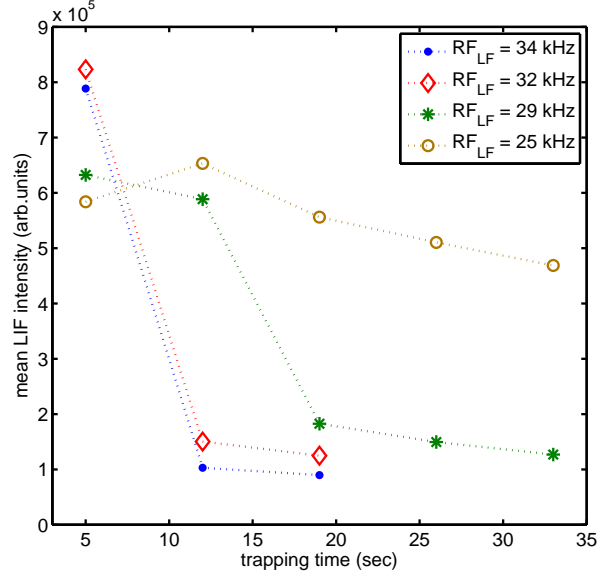


Figure 7.13: The trapping times of a Sulforhodamine B ion cloud is shown for different  $\text{RF}_2$  frequencies. A similar trend to the previous measurement (figure 7.12) can be seen.

as a consequence of ion losses. While bleaching can also have an effect, RF ejection is the dominant loss mechanism. For the two measurements at  $\Omega_{\text{RF}} > 2\pi \times 30$  kHz, the signal shows a fast decay while even detuning the trap by only 20% allows to see molecular fluorescence for almost an order of magnitude larger.

These results confirm the results of figure 7.12 that stable trapping of light ion clouds inside a two-tone RF potential is possible at suitable frequencies.

### Massive ions in a double-frequency RF potential

To investigate the effect of a double-frequency RF potential on heavy ions similar experiments were conducted with polystyrene nanobeads. The RF parameters were chosen to be  $\text{RF}_1$ : 1.02 MHz and 300 V as well as  $\text{RF}_2$ : 45 kHz and 150 V. All other experimental parameters were kept identical to the previous measurements. For detection the ion cloud was illuminated by the LIF laser for one second. The trap was loaded with  $\text{RF}_2$  only and the ion cloud was detected by laser induced fluorescence after 5 seconds. Directly afterwards  $\text{RF}_1$  was applied and the evolution

of the ion cloud was monitored every seven seconds as shown in figure 7.14.

We observe trapping for more than 120 seconds, i.e. essentially permanently. The

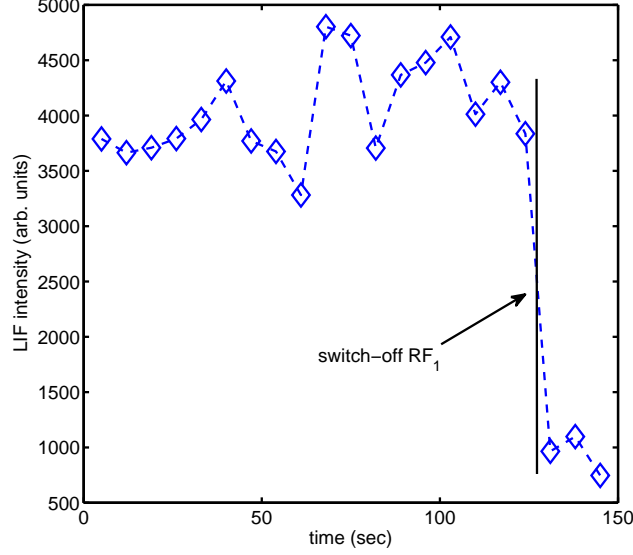


Figure 7.14: Long term trapping of polystyrene spheres under the influence of the high-frequency  $\text{RF}_1$ . Although the data scatter around the mean LIF intensity, a stable trapping of the nanoparticles in the two-tone RF trap can be seen.

activation of the  $\text{RF}_1$  does not lead to a detectable ion loss. The fluctuations in the signal could be given by the on movement of the ion cloud through the LIF laser focus. At the end of the measurement the  $\text{RF}_1$  potential was switched-off again, resulting in the total disappearance of almost all trapped ions, as indicated by the vertical black line in figure 7.14.

The experiment shows that adding an  $\text{RF}_1$  amplitude to the effective trapping potential after loading and buffer gas cooling does not disturb the heavy ion cloud. Removal of  $\text{RF}_1$  however, results in its ejection. Ramping the  $\text{RF}_1$  amplitude to its maximal value requires several seconds. This quasi-adiabatic process seems not to disturb the trapped ions, while on the other hand, the fast switching-off process has a negative impact on the ion motion.

### Variation of the endcap potential

We finally analyze the parameter space for stable trapping of light ions inside the two-tone frequency potential. Our SIMION simulations (see section 7.4) showed

that the  $\text{RF}_2$  amplitude can be raised to adequate trapping values (e.g. about 70 V) without losing the low mass ions. But in practice further factors also influence the ion motion. This stimulated experiments following the light ion signal dependency on the endcap strength at:  $\text{RF}_1 = 900$  kHz and  $U_1 = 600$  V,  $\text{RF}_2 = 20$  kHz and  $U_2 < 60$  V. Both RF potentials were switched on prior to the injection of Sulforhodamine B ions. The ion trap was always loaded with the same number of MALDI shots, the endcap potential was varied and the ion cloud was detected in LIF using 532 nm excitation. Figure 7.15 shows the ion signal in dependence of the  $\text{RF}_2$  amplitude for different endcap potentials.

With increasing  $V_{\text{RF}_2}$  the ion signal decreases and when the  $\text{RF}_2$  amplitude ap-

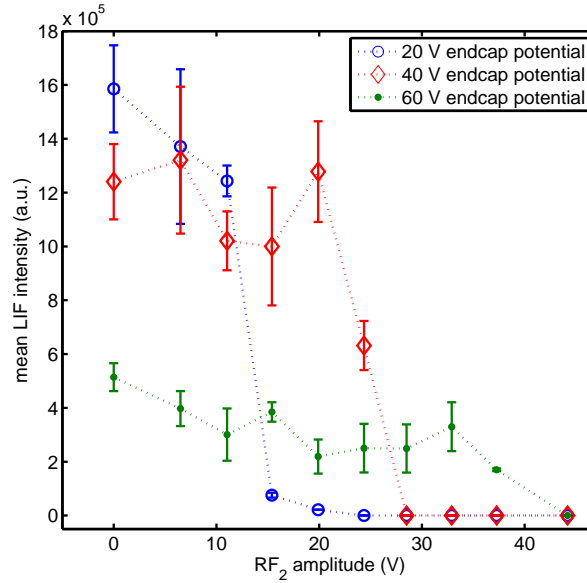


Figure 7.15: Laser induced fluorescence of Sulforhodamine B for different endcap potentials and  $\text{RF}_2$  amplitudes. Ions are preferentially lost at high  $\text{RF}_2$  potentials.

proaches the endcap potential, a fast drop in fluorescence can be observed. The ion signal disappears when the  $\text{RF}_2$  reaches a potential still smaller than the DC voltage on the endcaps. This is consistent with our simulations in section 7.4.

The experiments show, that ions are already lost at low amplitudes and it must be assumed that additional sources are responsible for ejection of ions. In the experiment  $\text{RF}_2$  amplitudes of about 40 V (green line in figure 7.15) still allow trapping of Sulforhodamine B. This RF amplitude is already sufficient to trap heavy ions.

We can thus demonstrate that light- and heavy ions can be trapped simultaneously under the same effective potentials. The detectable laser induced fluorescence in-

tensity drops with increasing endcap potentials. This might can explained by the kinetic energy distribution of the ions during the loading process: With the endcap potential 'on' during loading, the endcaps deflect more ions from the trap axis when the endcap potential is higher (similar to the data shown in figure 6.33).

### Simultaneous two mass trapping

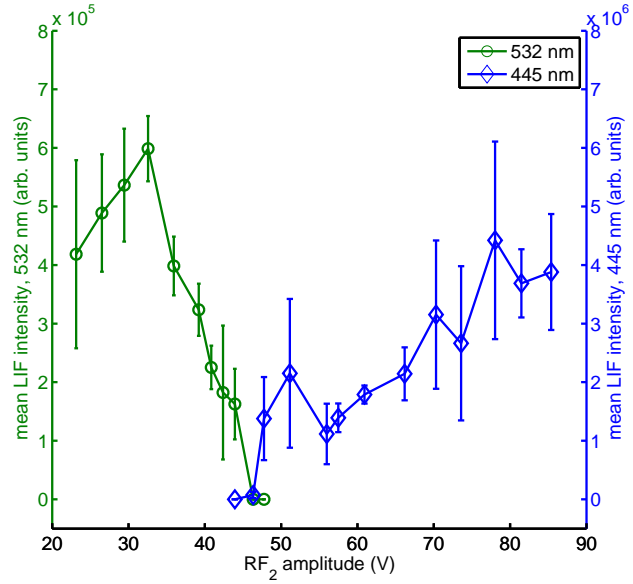
The experiments already discussed in this chapter demonstrated that a stable trapping of light or heavy ions inside a two-tone RF potential is feasible. We now ask if stable confinement of two ion species with a large separation in mass-to-charge ratio can be achieved simultaneously.

Sulforhodamine B and polystyrene nanobeads, were spotted onto the MALDI sample plate, as described in chapter 6.7.2. The ion trap was operated under similar conditions as described in section 7.5.2.

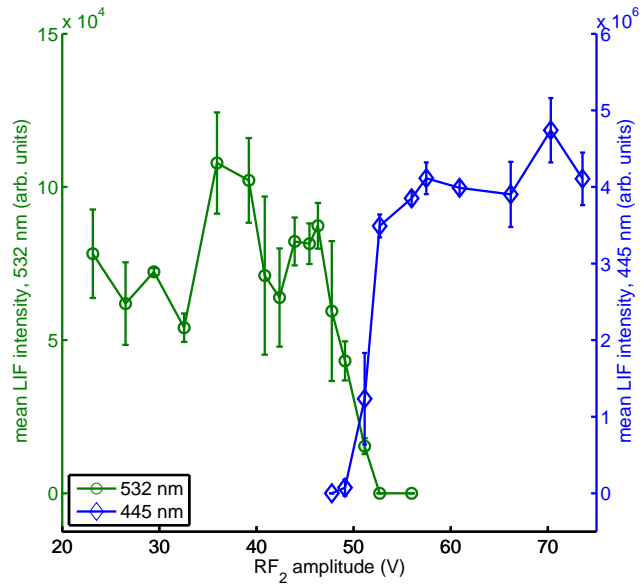
Figure 7.16a shows the ion trap at an endcap voltage of  $U_{EC} = 60$  V, while the curves in 7.16b were taken with  $E_{EC} = 70$  V.

The  $RF_2$  amplitude was varied and a similar trend is seen in both data sets (figures 7.16a, 7.16b): At low  $RF_2$  amplitudes fluorescence was visible upon excitation at 532 nm (green line). This is attributed to trapped Sulforhodamine B. We find a continuous signal reduction in signal intensity for increasing  $RF_2$  amplitudes. This is consistent with the expectations for Sulforhodamine B ions (see figure 7.16 above). No signal was detected for identical RF settings upon excitation with 445 nm light. However, with increasing  $RF_2$  amplitude strong fluorescence signal can be observed (at 445 nm excitation), which indicates that the light is emitted by polystyrene ions.

When both fluorescence curves are plotted (for  $U_{EC} = 60$  V in figure 7.16a), no intercept point is visible. This indicates that the required  $RF_2$  for stable confinement of Sulforhodamine B is too weak to allow loading/trapping of polystyrene nanobeads. From a different view: before a suitable trap depth for the polystyrene ions is reached, all light ions are (already) ejected from the ion trap due to the second RF potential! When the endcap potential is increased to 70 V, the two curves start to overlap (figure 7.16b). At  $RF_2 = 50$  V the 532 nm excitation curve still shows a significant signal together with the 445 nm excitation curve (blue line).



(a) 60 V endcap potential



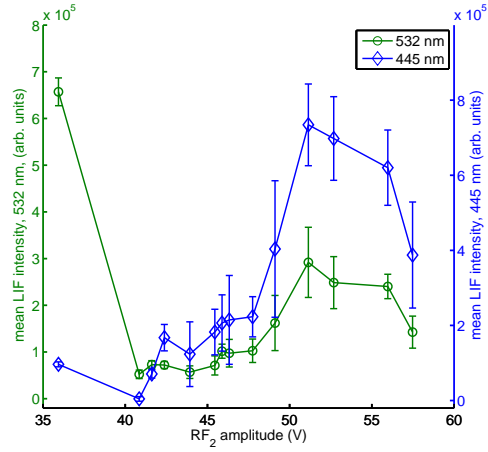
(b) 70 V endcap potential

Figure 7.16: Experimental results of a mixed ion cloud inside a double-frequency RF potential. 7.16a shows the case with  $U_{EC} = 60$  V, 7.16b represents the measurement with an endcap potential of 70 V. Note the difference in signal strength between the 532 and 445 nm LIF data.

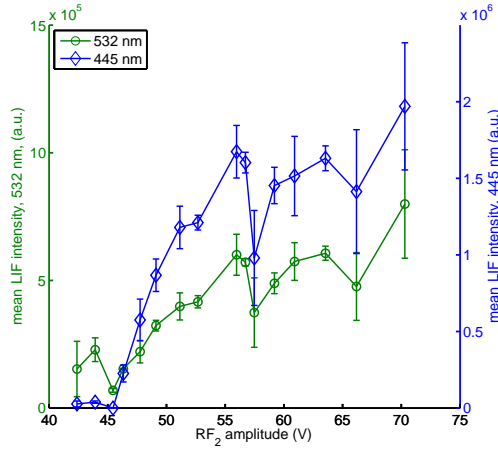
The intersection of the two curves indicate that stable trapping of the two ion clouds is possible in spite of their enormous difference in mass-to-charge ratio. Unfortunately this fact could not be corroborated with absolute certainty. As pointed out in section 6.7.1, the fluorophore of the polystyrene beads (Nile Red) can also be excited by 532 nm light. This prevents to clearly distinguish the emitting species when both ion species are trapped simultaneously (figure 7.16b). But figures 7.16a and 7.16b seem to rule out this possibility, since for an endcap voltage of 60 V the two curves do not cross. If the excitation of the nanospheres at 532 nm plays a significant role, the green line should extend to  $U_{RF2}$  values greater than 50 V.

To shed more light on this question, laser induced fluorescence cycle was inverted to reduce the influence of bleaching in Sulforhodamine B. The first LIF image was taken with the 445 nm laser beam, while for the second image only 532 nm light was used. Figure 7.17 shows the resulting ion signals for three different endcap potentials.

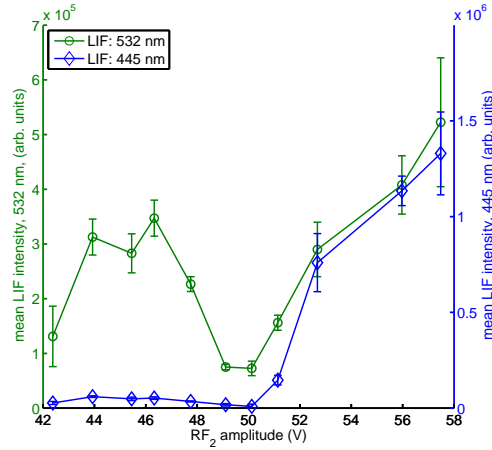
All three plots allow a generalizing observation: With increasing endcap voltages the signals in the 445 nm plots (blue lines) appear at higher  $RF_2$  amplitudes, similar to our SIMION simulations (section 7.4). For Sulforhodamine B ions the opposite behavior is seen (similar figure 7.15): For increased endcap voltage the 532 nm signal is extended towards higher RF amplitudes. Still an overlap between the two curves is detectable. Similar to the previous measurements (fig. 7.16), with increasing  $RF_2$  strength an increase in 532 nm emission is observed. This is again attributed to the absorption band of Nile Red in the polystyrene particles. This question may only be finally solved in (future) experiments using fluorescent dyes with a more widely separated spectrum.



(a) 60 V endcap potential



(b) 70 V endcap potential



(c) 80 V endcap potential

Figure 7.17: The recorded ion signals in a two-frequency RF potential well and different applied endcap potentials: 60 V (fig. 7.17a), 70 V (fig. 7.17b) and 80 V (fig. 7.17c). For the detection of the ion cloud two different laser wavelengths, 532 nm and 445 nm, were used sequential. Note the difference in scale between the green and blue curves.

## 7.6 Conclusions and outlook of the two-tone trapping experiment

Recent literature [323, 324] and theoretical estimations of the ion motion inside a linear quadrupole field driven by two different RF frequencies indicate that a stable confinement of two ion species with a large mass difference should be possible. Detailed SIMION simulations allowed us to identify the suitable set of RF parameters for trapping. But these simulations also indicate that cooling to cryogenic or even mK temperatures will become difficult in a two-tone trap (see section 7.4).

To test out simulations detailed experiments were set up using the linear ion trap described in this thesis. While trapping the ion species individually, we could identify stable trapping for light and heavy ions inside a two-tone trap. The simultaneous trapping of both ion species did not allow a final conclusion if both, light and heavy ions, were trapped at the same time. This was due to the broad spectroscopic absorption characteristics of the heavy ion species (Nile Red). In future experiments fluorescent dyes with a more widely separated spectrum could be used to identify simultaneous trapping in a two-frequency ion trap.

## Chapter 8

# Conclusions and future prospects on the ion trap experiment

In the context of this thesis a first linear quadrupole ion trap was designed and built in our laboratory as a first investigation towards a source for cold and slow molecules for future matter-wave interferometry in the mass range beyond  $10^5$  Da. The design and first results of this experiment were presented. MALDI was chosen for loading the ion trap, it has the advantage of being a 'soft ionization' source - e.g. the fragmentation rate is low. It is also suitable for complex, heavy molecules and nanoparticles in the mass regime greater than 1 MDa. Furthermore, in strong comparison to ESI, the charge state of the produced ions is low. Typically they carry about one to three charges.

A segmented, linear RF quadrupole ion trap is intrinsically mass selective and confines the ions close to the RF node which is of advantage for extraction or optical detection of the ion cloud. For an efficient loading of the externally created ions and their cooling room temperature Helium was introduced as a neutral buffer gas.

For ions with a large mass-to-charge ratio the detection efficiency of common charged particle detectors is rather poor. We have therefore implemented in-situ, gas-phase optical detection by laser induced fluorescence (LIF), a method that is well scalable to large bionanomaterials, stained nanobeads and quantum dots alike. This detection has the advantage of being insensitive to the mass of the nanoparticles as well as being non-destructive. Especially the latter is of interest for a possible future

coupling of an ion trap to a matter-wave interferometer.

In the current experimental setup the MALDI loading and trapping showed promising results. With the fluorophore Sulforhodamine B (581 Da) the ion trap was tested. Also the loading of heavy ions with a mass  $> 10^5$  Da was seen in dedicated experiments, where stable confinement could be achieved. The measurements show that the linear ion trap is a suitable accumulation and testing device for experiments with heavy ions. The information gained in the experiments will help in designing an ion trap for future high mass matter-wave interferometers.

In a next-generation several improvements for the experimental setup can be envisaged:

- **The detection of the ions**

In comparison to the current setup an axial excitation laser would allow a more homogenous illumination of the ion cloud. Although care has to be taken to remove the ion source from the laser beam path to avoid bleaching of the sample prior to their loading into the ion trap.

A limiting factor in the described experiment turned out to be the fixed wavelength of the excitation light source. A dye laser or an OPO will increase the number of accessible molecules since the bath-chromatic shift of the excitation maxima can be compensated.

One may also consider the implementation of specialized charge particle detectors. Here either Superconducting Single Photon Detectors (SSPD) could be used as LIF or particle detectors. Due to the small size of the SSPD chips one could install the detector much closer to the trapping volume which would increase the LIF emission detection efficiency. If, on the other hand, the ions are extracted from the ion trap, such an SSPD chip could also be used for the detection of charged particles [325,326]. Also neutral particles might be detected this way [327,328], which would allow experiments on neutralization cross sections and rates for trapped anions. Another suitable technique for the detection of charged particles might also be an improved future version of an IonCCD [329].

- **Ion creation and cooling**

With a re-design of the experiment also the ion source should be improved.

To enhance the injection and trapping efficiency of the external created ions, a higher-order multipole (typically hexapole or octopole) should be introduced between the MALDI plate and the entrance to the linear quadrupole. In comparison to the quadrupole, a higher order linear multipole has an enhanced radial confinement efficiency, which helps in guiding the ions from the sample plate into the ion trap. This would increase the overall ion injection efficiency of the system.

Another experimental feature which is directly connected to matter-wave interferometry is the temperature of the ions. For interferometry with molecules in the mass range of  $> 100$  kDa, molecule or nanoparticle velocity (e.g. external temperature) must be small to still have a reasonable large de Broglie wavelength. Also the internal particle temperature must be small to decrease the probability of ro-vib transition with emission of thermal photons, leading to decoherence effects. The required particle temperature can be estimated by

$$T = \frac{h}{2mk_B\lambda_{dB}} \quad (8.1)$$

with  $h$  being the Plank constant,  $\lambda_{dB}$  the de Broglie wavelength (about 300 fm in the current setups [2]) and  $k_B$  Boltzmann constant. In the case of 10 MDa molecules a temperature below 6 K is required. This shows that a cryogenic setup (incl. buffer gas) operating at 4 K will be needed. Since higher order RF multipoles have, in comparison to RF quadrupoles, extended radial field-free regions lower final temperatures can be expected and therefore such a device can be beneficial.

- **Mass selection**

The mass resolution shall be improved in a further setup. Although a mass scanning by sweeping a DC/RF voltage ratio (regular mass scans in quadrupoles) sounds to be an easier option (compared to the resonance enhanced mass selection), it might not be the best choice since the mass resolution  $\mathfrak{R}$  in this scans method is typically limited to the 10-fold unit resolution [135].

On the other hand, the resonance enhanced mass selection as tested in this work is capable of obtaining an overall higher resolution. For this method resolutions can be typically at about  $\mathfrak{R}=30000$  at 500 Da [330] and even mass

resolution in the ppm range can be reached [285].

In conclusion, it could be shown that a linear quadrupole ion trap could be built and put into operation in our laboratory. Its basic trapping capabilities could be shown and tested. Although further steps are required for coupling such a device to a matter-wave interferometer, it could be shown that an ion trap might be a suitable source for a future experiment.

## Chapter 9

# Appendix

### 9.1 Derivation of the Mathieu parameter $a, q$

The ion motion inside a linear quadrupole ion trap can be described by the Mathieu equations. Their canonical form is

$$\frac{d^2 u}{d\xi^2} + (a - 2q \cos(2\xi)) \cdot u = 0 \quad (9.1)$$

In the context of quadrupolar RF fields,  $\mathbf{a}$ ,  $\mathbf{q}$  are dimensionless and describe the stability parameters,  $\xi$  is a dimensionless parameter related to  $\Omega t/2$  and  $u$  represents the coordinates  $x, y$ .

The Mathieu parameters can be determined by a comparison of the Mathieu equation and the equation of motion in its normal form. In a first step it can be shown that the following holds true:

$$\frac{d}{dt} = \frac{d\xi}{dt} \frac{d}{d\xi} = \frac{\Omega}{2} \frac{d}{d\xi} \quad (9.2)$$

$$\frac{d^2}{dt^2} = \frac{d\xi}{dt} \frac{d}{d\xi} \left( \frac{d}{dt} \right) = \frac{\Omega^2}{4} \frac{d}{d\xi^2} \quad (9.3)$$

If this differential is now inserted into the Mathieu equation, the following equation can be written down:

$$\frac{d^2 u}{dt^2} = - \left( \frac{\Omega^2}{4} \cdot a - 2 \frac{\Omega^2}{4} \cdot q \cos(\Omega \cdot t) \right) u \quad (9.4)$$

With equation 9.4 and the equation of motion

$$\frac{d^2x}{dt^2} = - \left( \frac{2eU}{mr_0^2} + \frac{2eV \cos(\Omega t)}{mr_0^2} \right) x$$

the stability parameters can be expressed by the following equations:

$$a = \frac{8eU}{mr_0^2\Omega^2} \quad (9.5)$$

$$q = \frac{4eV}{mr_0^2\Omega^2} \quad (9.6)$$

With this derivation the relationship between the trapping parameters in the experimental setup and the ion motion could be shown.

Another aspect of the stability parameters should be mentioned as well. In literature  $\mathbf{q}$  is sometimes defined as  $\mathbf{q} \propto 2 \text{ V}$ , while  $\mathbf{q} \propto 4 \text{ V}$  is given in different work. This discrepancy by a factor of two arises from the different definitions of the RF potentials in the respective work. E.g. amplitude defined as zero-peak or peak-peak.

## 9.2 Description of the ion trap design

In the following a more detailed description of the ion trap design will be given, than already described in the previous sections.

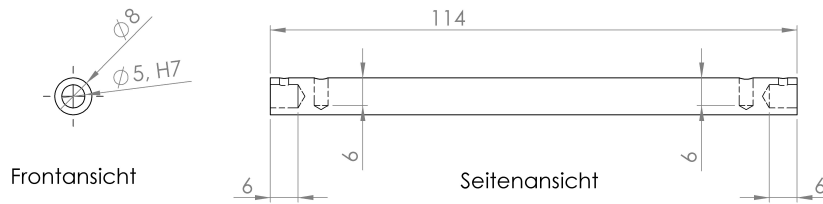
To mount the ion trap rods in the experiment, an axial hole (5 mm in diameter) was drilled through the complete length of the inner three segments, while segments 1 and 5 were only partially drilled, since a tapped thread hole was required for mounting purposes close to the outer edge S1, S5. For the assembly of a complete trapping rod the individual segments were strung onto an  $Al_2O_3$  rod of 5 mm diameter, holding all five segments. The ceramic rod provides an alignment of the trap electrodes together with an electrical isolation between the different segments. A gap of 1 mm was chosen between neighboring electrode segments to prevent sparking when using high RF amplitudes.

To complete the quadrupolar structure of the trap, a circular support structure with an outer diameter of 50 mm was machined from PEEK. This allowed the mounting of the electrodes in the previously determined inscribed radius  $r_0$ . Care was taken to have free axial access from both ends, to allow loading from an external ion sources

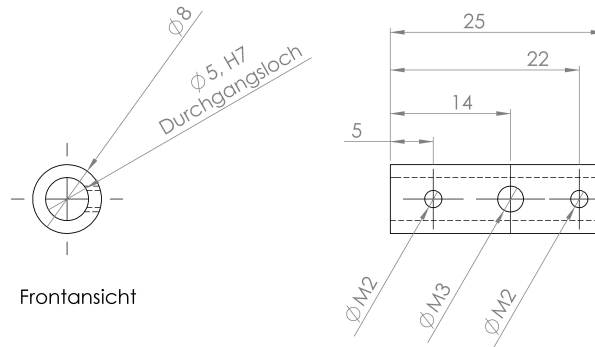
as well as ejection into an axial detector (when required). PEEK has the advantage of being an electrical insulator, it is hard and has, at the same time, good machining properties. Furthermore its outgassing rate in vacuum is low.

To show the design of the linear ion trap in more detail, the technical drawings of the most important elements are presented. All dimensions are in mm. The three different trap rod schemes, required for setting up the ion trap presented in this thesis are shown in figure 9.1.

In the following figure the ion trap mount structure is shown in detail. While this



(a) Technical drawing of the non-segmented trap rods



(b) Technical drawing of trap rod segments for segmented rod pairs

Figure 9.1: The technical drawings of the different on trap rods are presented. 9.1a shows the non-segmented rod pair, while in 9.1b the different electrodes of the segmented trp rods can be seen. All dimensions are given in mm.

structure should be an electrical insulator, rigid and vacuum stable (e.g. low outgassing rates), the material should also be machinable. A suitable building material was found in PEEK.



## Chapter 10

# Acknowledgments

This presented work would not have been possible without the support and help of other persons, which should be mentioned here.

I would like to express my thanks to Prof. Markus Arndt, who gave me the opportunity to work on my PhD thesis in his group. Thank you for showing me all the different and important facets and skills required for working as a scientist. I also thank you for the constant support and motivation throughout the up and downs in the experiments.

Here I want to thank Prof. Mayor, Jens Tüxen and Lukas Felix for the synthesis of the fluorinated TPP molecules. Another thanks goes to Prof. Willitsch who provided helpful discussions and information regarding our RF driver for the experiment.

I want to thank the master students who worked together with me throughout the years in the laboratory. Here I would like to single out Ugur Sezer. He had many great ideas and knew how to implement them. I had a good time working with him. Also, I would like to thank the members of the Vienna Quantum Nanophysics group, especially Nadine Dörre and Sandra Eibenberger who always had time to discuss physics or other topics over a cup of coffee.

Finally I would like to present my gratitude to my family who supported me throughout the years in all possible ways. Here I want to especially mention my parents and my wife Hedwig.



# Bibliography

- [1] L. de Broglie, “Waves and quanta,” *Nature*, vol. 112, pp. 540–540, 1923.
- [2] P. Haslinger, N. Dörre, P. Geyer, J. Rodewald, S. Nimmrichter, and M. Arndt, “A universal matter-wave interferometer with optical ionization gratings in the time domain,” *Nature Physics*, vol. 9, pp. 144–148, 2013.
- [3] W. Phillips, “Laser cooling and trapping of neutral atoms,” *Reviews of Modern Physics*, vol. 70, pp. 721–741, 1998.
- [4] E. Cornell and C. Wieman, “Nobel Lecture: Bose-Einstein Condensation in a Dilute Gas, the First 70 Years and some Recent Experiments,” *Reviews of Modern Physics*, vol. 74, pp. 875–893, 2002.
- [5] I. Bloch, “Ultracold Quantum Gases in Optical Lattices,” *Nature*, vol. 1, pp. 23–30, 2005.
- [6] A. Aspuru-Guzik and P. Walther, “Photonic quantum simulators,” *Nature Physics*, vol. 8, pp. 285–291, 2012.
- [7] M. Arndt and K. Hornberger, “Testing the limits of quantum mechanical superpositions,” *Nature Physics*, vol. 10, pp. 271–277, 2014.
- [8] K. Hornberger, S. Gerlich, P. Haslinger, S. Nimmrichter, and M. Arndt, “Colloquium: Quantum interference of clusters and molecules,” *Reviews of Modern Physics*, vol. 84, no. 1, pp. 157–173, 2012.
- [9] C. Davisson and L. H. Germer, “The scattering of electrons by a single crystal of Nickel,” *Nature*, vol. 119, pp. 558–560, 1927.
- [10] G. P. Thomson, “The Diffraction of Cathode Rays by Thin Films of Platinum,” *Nature*, vol. 120, pp. 802–802, 1927.
- [11] I. Estermann and O. Stern, “Beugung von Molekularstrahlen,” *Zeitschrift für Physik*, vol. 61, pp. 95–125, 1930.
- [12] H. von Halban and P. Preiswerk, “Experimental evidence of neutron diffraction,” *C.R. Hebd. Séances. Acad*, vol. 203, p. 73, 1936.
- [13] M. A. V. Hove and S. Y. Tong, *Surface crystallography by LEED*. Springer-Verlag New York, 1979.
- [14] D. L. Price, *Neutron Scattering, Part B, 23 Experimental Methods in the Physical Sciences*. Academic Press Inc., 1996.

- [15] A. H. Zewail, “4D ultrafast electron diffraction, crystallography, and microscopy,” *Annual Review of Physical Chemistry*, vol. 57, no. 1, pp. 65–103, 2006.
- [16] A. D. Cronin, J. Schmiedmayer, and D. E. Pritchard, “Optics and interferometry with atoms and molecules,” *Reviews of Modern Physics*, vol. 81, pp. 1051–1129, 2009.
- [17] T. Li, S. Kheifets, and M. G. Raizen, “Millikelvin cooling of an optically trapped microsphere in vacuum,” *Nature Physics*, vol. 7, pp. 527 – 530, 2011.
- [18] J. Gieseler, B. Deutsch, R. Quidant, and L. Novotny, “Subkelvin Parametric Feedback Cooling of a Laser-Trapped Nanoparticle,” *Physical Review Letters*, vol. 109, no. 10, p. 103603, 2012.
- [19] P. Asenbaum, S. Kuhn, S. Nimmrichter, U. Sezer, and M. Arndt, “Cavity cooling of free silicon nanoparticles in high vacuum,” *Nature Communications*, vol. 4, p. 2743, 2013.
- [20] R. Kaltenbaek, G. Hechenblaikner, N. Kiesel, O. Romero-Isart, K. C. Schwab, U. Johann, and M. Aspelmeyer, “Macroscopic quantum resonators (MAQRO),” *Experimental Astronomy*, vol. 34, pp. 123 – 164, 2012.
- [21] O. Romero-Isart, “Quantum superposition of massive objects and collapse models,” *Physical Review A*, vol. 84, p. 052121, 2011.
- [22] O. Romero-Isart, M. Juan, R. Quidant, and J. Cirac, “Toward quantum superposition of living organisms,” *New Journal of Physics*, vol. 12, p. 033015, 2010.
- [23] O. Romero-Isart, A. C. Pflanzer, M. L. Juan, R. Quidant, N. Kiesel, M. Aspelmeyer, and J. I. Cirac, “Optically levitating dielectrics in the quantum regime: Theory and protocols,” *Physical Review A*, vol. 83, no. 1, 2011.
- [24] S. Nimmrichter, K. Hornberger, P. Haslinger, and M. Arndt, “Testing spontaneous localization theories with matter-wave interferometry,” *Physical Review A*, vol. 83, p. 043621, 2011.
- [25] S. Nimmrichter and K. Hornberger, “Macroscopicity of Mechanical Quantum Superposition States,” *Physical Review Letters*, vol. 110, p. 160403, 2013.
- [26] J. Bateman, S. Nimmrichter, K. Hornberger, and H. Ulbricht, “Near-field interferometry of a free-falling nanoparticle from a point-like source,” *Nature Communications*, vol. 5, p. 4788, 2014.
- [27] A. Bassi and G. Ghirardi, “Dynamical Reduction Models,” *Physics Reports*, vol. 379, pp. 257–426, 2003.
- [28] L. Diosi, “Models for universal reduction of macroscopic quantum fluctuations,” *Physical Review A*, vol. 40, pp. 1165 – 1174, 1989.
- [29] G. C. Ghirardi, A. Rimini, and T. Weber, “Unified dynamics for microscopic and macroscopic systems,” *Physical Review D*, vol. 34, pp. 470–491, 1986.

- [30] D. Giulini and A. Großardt, “Gravitationally induced inhibitions of dispersion according to the Schrödinger-Newton Equation,” *Classical and Quantum Gravity*, vol. 28, p. 195026, 2011.
- [31] R. Penrose, “On gravity’s role in quantum state reduction,” *General Relativity and Gravitation*, vol. 28, pp. 581–600, 1996.
- [32] G. Amelino-Camelia, K. Aplin, M. Arndt, J. D. Barrow, R. J. Bingham, C. Borde, P. Bouyer, M. Caldwell, A. M. Cruise, T. Damour, P. D’Arrigo, H. Dittus, W. Ertmer, B. Foulon, P. Gill, G. D. Hammond, J. Hough, C. Jentsch, U. Johann, P. Jetzer, H. Klein, A. Lambrecht, B. Lamine, C. Lämmerzahl, N. Lockerbie, F. Loeffler, J. T. Mendonca, J. Mester, W. T. Ni, C. Pegrum, A. Peters, E. Rasel, S. Reynaud, D. Shaul, T. J. Sumner, S. Theil, C. Torrie, P. Touboul, C. Trenkel, S. Vitale, W. Vodel, C. Wang, H. Ward, and A. Woodgate, “Gauge: the grand unification and gravity explorer,” *Experimental Astronomy*, vol. 23, no. 2, pp. 549–572, 2009.
- [33] M. Hohensee, S. Chu, A. Peters, and H. Müller, “Equivalence Principle and Gravitational Redshift,” *Physical Review Letters*, vol. 106, no. 15, p. 151102, 2011.
- [34] G. Varoquaux, R. Nyman, R. Geiger, P. Cheinet, A. Landragin, and P. Bouyer, “How to estimate the differential acceleration in a two-species atom interferometer to test the equivalence principle,” *New Journal of Physics*, vol. 11, p. 113010, 2009.
- [35] J. Riedel, “Direct detection of classically undetectable dark matter through quantum decoherence,” *Physical Review D*, vol. 88, p. 116005, 2013.
- [36] A. Ashkin, “Optical Trapping and Manipulation of Neutral Particles Using Lasers,” *Proceedings of the National Academy of Sciences USA*, vol. 94, pp. 4853–4860, 1997.
- [37] A. Ashkin, “Acceleration and Trapping of Particles by Radiation Pressure,” *Physical Review Letters*, vol. 24, p. 156, 1970.
- [38] A. Ashkin and J. M. Dziedzic, “Optical Levitation by Radiation Pressure,” *Applied Physics Letters*, vol. 19, no. 8, pp. 283–285, 1971.
- [39] E. Reiger, L. Hackermüller, M. Berninger, and M. Arndt, “Exploration of gold nanoparticle beams for matter wave interferometry,” *Optics Communications*, vol. 264, pp. 326–332, 2006.
- [40] S. Nimmrichter, P. Haslinger, K. Hornberger, and M. Arndt, “Concept of an ionizing time-domain matter-wave interferometer,” *New Journal of Physics*, vol. 13, no. 7, p. 075002, 2011.
- [41] M. Arndt, O. Nairz, J. Voss-Andreae, C. Keller, G. van der Zouw, and A. Zeilinger, “Wave-particle duality of C60 molecules,” *Nature*, vol. 401, no. 6754, pp. 680–682, 1999.
- [42] T. Juffmann, A. Milic, M. Müllneritsch, P. Asenbaum, A. Tsukernik, J. Tüxen, M. Mayor, O. Cheshnovsky, and M. Arndt, “Real-time single-molecule imaging of quantum interference,” *Nature Nanotechnology*, vol. 7, pp. 297 – 300, 2012.

- [43] B. Brezger, L. Hackermüller, S. Uttenthaler, J. Petschinka, M. Arndt, and A. Zeilinger, “Matter-Wave Interferometer for Large Molecules,” *Physical Review Letters*, vol. 88, p. 100404, 2002.
- [44] S. Gerlich, L. Hackermüller, K. Hornberger, A. Stibor, H. Ulbricht, M. Gring, F. Goldfarb, T. Savas, M. Müri, M. Mayor, and M. Arndt, “A Kapitza-Dirac-Talbot-Lau interferometer for highly polarizable molecules,” *Nature Physics*, vol. 3, no. 10, pp. 711–715, 2007.
- [45] R. Feynman, R. B. Leighton, and M. L. Sands, *The Feynman Lectures on Physics, Vol III, Quantum Mechanics*. Addison Wesley, Reading (Mass), 1965.
- [46] M. Sclafani, T. Juffmann, C. Knobloch, and M. Arndt, “Quantum coherent propagation of complex molecules through the frustule of the alga *amphipleura pellucida*,” *New Journal of Physics*, vol. 15, p. 083004, 2013.
- [47] J. F. Clauser and S. Li, “Talbot-von Lau atom interferometry with cold slow potassium,” *Physical Review A*, vol. 49, p. R2213, 1994.
- [48] J. Clauser, *Boston Studies in the Philosophy of Science*, book section De Broglie-wave interference of small rocks and live viruses, pp. 1–11. Kluwer Academic, 1997.
- [49] L. Hackermüller, S. Uttenthaler, K. Hornberger, E. Reiger, B. Brezger, A. Zeilinger, and M. Arndt, “Wave nature of biomolecules and fluorofullerenes,” *Physical Review Letters*, vol. 91, p. 90408, 2003.
- [50] T. Juffmann, S. Truppe, P. Geyer, A. Mayor, S. Deachapunya, H. Ulbricht, and M. Arndt, “Wave and particle in molecular interference lithography,” *Physical Review Letters*, vol. 103, p. 263601, 2009.
- [51] A. Stibor, A. Stefanov, F. Goldfarb, E. Reiger, and M. Arndt, “A scalable optical detection scheme for matter wave interferometry,” *New Journal of Physics*, vol. 7, pp. 1–10, 2005.
- [52] O. Nairz, M. Arndt, and A. Zeilinger, “Quantum interference experiments with large molecules,” *American Journal of Physics*, vol. 71, no. 4, pp. 319–325, 2003.
- [53] P. L. Kapitza and P. A. M. Dirac, “The reflection of electrons from standing light waves,” *Mathematical Proceedings of the Cambridge Philosophical Society*, vol. 29, pp. 297 – 300, 1933.
- [54] L. Hackermüller, K. Hornberger, S. Gerlich, M. Gring, H. Ulbricht, and M. Arndt, “Optical polarizabilities of large molecules measured in near-field interferometry,” *Applied Physics B*, vol. 89, no. 4, pp. 469–473, 2007.
- [55] S. Gerlich, M. Gring, H. Ulbricht, K. Hornberger, J. Tuxen, M. Mayor, and M. Arndt, “Matter-wave metrology as a complementary tool for mass spectrometry,” *Angewandte Chemie-International Edition*, vol. 47, no. 33, pp. 6195–6198, 2008.

- [56] M. Gring, S. Gerlich, S. Eibenberger, S. Nimmrichter, T. Berrada, M. Arndt, H. Ulbricht, K. Hornberger, M. Mürri, M. Mayor, M. Böckmann, and N. Doltsinis, “Influence of conformational molecular dynamics on matter wave interferometry,” *Physical Review A*, vol. 81, p. 031604, 2010.
- [57] S. Gerlich, S. Eibenberger, M. Tomandl, S. Nimmrichter, K. Hornberger, P. Fagan, J. Tüxen, M. Mayor, and M. Arndt, “Quantum interference of large organic molecules,” *Nature Communications*, vol. 2, p. 263, 2011.
- [58] S. Eibenberger, X. Cheng, J. P. Cotter, and M. Arndt, “Absolute absorption cross sections from photon recoil in a matter-wave interferometer,” *Physical Review Letters*, vol. 112, p. 250402, Jun 2014.
- [59] S. Eibenberger, S. Gerlich, M. Arndt, M. Mayor, and J. Tüxen, “Matter-wave interference with particles selected from a molecular library with masses exceeding 10'000 amu,” *Physical Chemistry Chemical Physics*, vol. 15, pp. 14696–14700, 2013.
- [60] S. B. Cahn, A. Kumarakrishnan, U. Shim, T. Sleator, P. R. Berman, and B. Dubetsky, “Time-Domain de Broglie Wave Interferometry,” *Physical Review Letters*, vol. 79, pp. 784–787, 1997.
- [61] A. Turlapov, A. Tonyushkin, and T. Sleator, “Talbot-Lau effect for atomic de Broglie waves manipulated with light,” *Physical Review A*, vol. 71, no. 4, p. 43612, 2005.
- [62] A. V. Turlapov, D. V. Strekalov, A. Kumarakrishnan, S. B. Cahn, and T. Sleator, “Atom interference in pulsed standing-wave fields,” in *SPIE Proceedings: ICONO'98: Quantum Optics, Interference Phenomena in Atomic Systems, and High-Precision Measurements*, 1998.
- [63] L. Deng, E. W. Hagley, J. Denschlag, J. Simsarian, M. Edwards, C. Clark, K. Helmerson, S. Rolston, and W. Phillips, “Temporal, matter-wave-dispersion Talbot effect,” *Physical Review Letters*, vol. 83, pp. 5407– 5411, 1999.
- [64] M. Born and E. Wolf, *Principles of Optics*. Pergamon Press, 1993.
- [65] K. Hornberger and J. E. Sipe, “Collisional Decoherence Reexamined,” *Physical Review A*, vol. 68, p. 12105, 2003.
- [66] M. T. Bell, A. D. Gingell, J. M. Oldham, T. P. Softley, and S. Willitsch, “Ion-molecule chemistry at very low temperatures: cold chemical reactions between Coulomb-crystallized ions and velocity-selected neutral molecules,” *Faraday Discussions*, vol. 142, pp. 73–91, 2009.
- [67] K. M. Jones, E. Tiesinga, P. D. Lett, and P. S. Julienne, “Ultracold photoassociation spectroscopy: Long-range molecules and atomic scattering,” *Reviews of Modern Physics*, vol. 78, pp. 483–535, May 2006.
- [68] J. Ulmanis, J. Deiglmayr, M. Repp, R. Wester, and M. Weidemüller, “Ultracold molecules formed by photoassociation: Heteronuclear dimers, inelastic collisions, and interactions with ultrashort laser pulses,” *Chemical Reviews*, vol. 112, no. 9, pp. 4890–4927, 2012.

- [69] T. E. Wall, S. Armitage, J. J. Hudson, B. E. Sauer, J. M. Dyne, E. A. Hinds, and M. R. Tarbutt, "Transport of polar molecules by an alternating-gradient guide," *Physical Review A*, vol. 80, p. 043407, Oct 2009.
- [70] G. Meijer, "Cold molecules: Cooling and trapping of molecules is not straight forward - recent experiments have succeeded in slowing down and storing molecules with time-varying electrical fields," *Physik Journal*, vol. 1, pp. 41 – 46, 2002.
- [71] R. Fulton, A. Bishop, M. Shneider, and P. Barker, "Controlling the motion of cold molecules with deep periodic optical potentials," *Nature Physics*, vol. 2, p. 465, 2006.
- [72] W. D. Hall and J. C. Zorn, "Measurement of alkali-metal polarizabilities by deflection of a velocity-selected atomic beam," *Physical Review A*, vol. 10, no. 4, pp. 1141–1144, 1974.
- [73] I. Compagnon, R. Antoine, M. Broyer, P. Dugourd, J. Lermé, and D. Rayane, "Electric polarizability of isolated  $c_{70}$  molecules," *Physical Review A*, vol. 64, p. 025201, Jul 2001.
- [74] R. Antoine, I. Compagnon, D. Rayane, M. Broyer, P. Dugourd, G. Breaux, F. C. Hagemeister, D. Pippen, R. R. Hudgins, and M. F. Jarrold, "Electric Susceptibility of Unsolvated Glycine-based Peptides," *Journal of the American Chemical Society*, vol. 124, pp. 6737 – 6741, 2002.
- [75] F. Filsinger, J. Kupper, G. Meijer, L. Holmegaard, J. H. Nielsen, I. Nevo, J. L. Hansen, and H. Stapelfeldt, "Quantum-state selection, alignment, and orientation of large molecules using static electric and laser fields," *Journal of Chemical Physics*, vol. 131, no. 6, p. 064309, 2009.
- [76] S. Y. T. van de Meerakker, H. L. Bethlem, N. Vanhaecke, and G. Meijer, "Manipulation and Control of Molecular Beams," *Chemical Reviews*, vol. 112, no. 9, pp. 4828–4878, 2012.
- [77] M. Berninger, A. Stéfanov, S. Deachapunya, and M. Arndt, "Polarizability measurements in a molecule near-field interferometer," *Physical Review A*, vol. 76, p. 013607, 2007.
- [78] S. Eibenberger, S. Gerlich, M. Arndt, J. Tüxen, and M. Mayor, "Electric moments in molecule interferometry," *New Journal of Physics*, vol. 13, p. 43033, 2011.
- [79] J. B. Fenn, M. Mann, C. K. Meng, S. F. Wong, and C. M. Whitehouse, "Electrospray Ionization for mass spectrometry of large biomolecules," *Science*, vol. 246, pp. 64–71, 1989.
- [80] K. Tanaka, H. Waki, Y. Ido, S. Akita, Y. Yoshida, and T. Yoshida, "Protein and polymer analyses up to  $m/z$  100 000 by laser ionization time-of-flight mass spectrometry," *Rapid Communications in Mass Spectrometry*, vol. 2, no. 8, pp. 151–153, 1988.
- [81] B. B. Schneider, V. I. Baranov, H. Javaheri, and T. R. Covey, "Particle discriminator interface for nanoflow ESI-MS," *Journal of the American Society for Mass Spectrometry*, vol. 14, no. 11, pp. 1236 – 1246, 2003.

- [82] A. A. Puretzky, D. B. Geohegan, G. B. Hurst, M. V. Buchanan, and B. S. Lukyanchuk, "Imaging of Vapor Plumes Produced by Matrix Assisted Laser Desorption: A Plume Sharpening Effect," *Physical Review Letters*, vol. 83, pp. 444 – 447, 1999.
- [83] W.-P. Peng, Y. Cai, Y. Lee, and H.-C. Chang, "Laser-Induced Fluorescence/Ion Trap as a Detector for Mass Spectrometric Analysis of Nanoparticles," *International Journal of Mass Spectrometry*, vol. 229, pp. 67 – 76, 2003.
- [84] R. B. Cole, *Electrospray and MALDI Mass Spectrometry - Fundamentals, Instrumentation, Practical, and Biological Applications*. John Wiley & Sons, 2010.
- [85] F. Hillenkamp and J. Peter-Katalinic, *MALDI MS - A practical guide to instrumentation, methods and application*. WILEY-VCH Verlag GmbH & Co. KGaA, Weinheim, 2007.
- [86] F. Hillenkamp, "Laser induced ion formation from organic solids," *Springer Series in Chemical Physics*, vol. 25, pp. 190–205, 1983.
- [87] M. Karas and F. Hillenkamp, "Laser Desorption Ionization of Proteins with Molecular Mass Exceeding 10,000 Daltons," *Analytical Chemistry*, vol. 60, pp. 2299–2301, 1988.
- [88] M. Karas, D. Bachmann, and F. Hillenkamp, "Influence of the Wavelength in High-Irradiance Ultraviolet Laser Desorption Mass Spectrometry of Organic Molecules," *Analytical Chemistry*, vol. 57, pp. 2935–2939, 1985.
- [89] R. C. Beavis, B. T. Chait, and K. G. Standing, "Matrix-assisted laser-desorption mass spectrometry using 355 nm radiation," *Rapid Communications in Mass Spectrometry*, vol. 3, no. 12, pp. 436–439, 1989.
- [90] C. B. Lietz, A. L. Richards, Y. Ren, and S. Trimpin, "Inlet ionization: protein analyses from the solid state without the use of a voltage or a laser producing up to 67 charges on the 66 kDa BSA protein," *Rapid Communications in Mass Spectrometry*, vol. 25, no. 22, pp. 3453 – 3456, 2011.
- [91] M. Karas and R. Krüger, "Ion Formation in MALDI: The Cluster Ionization Mechanism," *Chemical Reviews*, vol. 103, no. 2, pp. 427–440, 2003.
- [92] R. Knochenmuss and R. Zenobi, "Maldi Ionization: The Role of In-Plume Processes," *Chemical Reviews*, vol. 103, pp. 441–452, 2003.
- [93] K. Dreisewerd, "The desorption process in MALDI," *Chemical Reviews*, vol. 103, pp. 395 – 425, 2003.
- [94] O. Kostko, L. K. Takahashi, and M. Ahmed, "Desorption dynamics, internal energies and imaging of organic molecules from surfaces with laser desorption and vacuum ultraviolet (VUV) photoionization," *Chemistry – An Asian Journal*, vol. 6, pp. 3066 – 3076, 2011.
- [95] M. Karas, M. Glückmann, and J. Schäfer, "Ionization in Matrix-Assisted Laser Desorption/Ionization: Singly Charged Molecular Ions are the Lucky Survivors," *Journal of Mass Spectrometry*, vol. 35, pp. 1 – 12, 2000.

- [96] C. D. Mowry and M. V. Johnston, "Simultaneous Detection of Ions and Neutrals Produced by Matrix-Assisted Laser Desorption," *Rapid Communication in Mass Spectrometry*, vol. 7, pp. 569–575, 1993.
- [97] K. Dreisewerd, M. Schürenberg, M. Karas, and F. Hillenkamp, "Influence of the laser intensity and spot size on the desorption of molecules and ions in matrix-assisted laser desorption/ionization with a uniform beam profile," *International Journal of Mass Spectrometry and Ion Processes*, vol. 141, no. 2, pp. 127 – 148, 1995.
- [98] A. Ingendoh, M. Karas, F. Hillenkamp, and U. Giessmann, "Factors affecting the resolution in matrix-assisted laser desorption–ionization mass spectrometry," *International Journal of Mass Spectrometry and Ion Processes*, vol. 131, pp. 345 – 354, 1994.
- [99] K. A. Dave, M. J. Headlam, T. P. Wallis, and J. J. Gorman, *Preparation and Analysis of Proteins and Peptides Using MALDI TOF/TOF Mass Spectrometry*, ch. 16.13, p. 1–16. John Wiley & Sons, Inc., 2001.
- [100] A. M. Schaiberger and J. A. Moss, "Optimized Sample Preparation for MALDI Mass Spectrometry Analysis of Protected Synthetic Peptides," *Journal of the American Society for Mass Spectrometry*, vol. 19, no. 4, pp. 614 – 619, 2008.
- [101] Bruker Daltonik GmbH, *Bruker Guide to MALDI Sample Preparation*, 2012.
- [102] T. Yalcin, Y. Dai, and L. Li, "Matrix-assisted laser desorption/ionization time-of-flight mass spectrometry for polymer analysis: solvent effect in sample preparation," *Journal of the American Society for Mass Spectrometry*, vol. 9, no. 12, pp. 1303 – 1310, 1998.
- [103] E. Nordhoff, A. Ingendoh, R. Cramer, A. Overberg, B. Stahl, M. Karas, F. Hillenkamp, P. F. Crain, and B. Chait, "Matrix-assisted laser desorption/ionization mass spectrometry of nucleic acids with wavelengths in the ultraviolet and infrared," *Rapid Communications in Mass Spectrometry*, vol. 6, pp. 771–776, 1992.
- [104] A. Bajuk, G. Krzysztof, and L. Michalak, "Effect of impurities on the matrix-assisted laser desorption/ionization mass spectra of insulin," *Rapid Communications in Mass Spectrometry*, vol. 15, no. 24, pp. 2383–2386, 2001.
- [105] S. D. Hanton and D. M. Parees, "Extending the solvent-free MALDI sample preparation method," *Journal of the American Society for Mass Spectrometry*, vol. 16, no. 1, pp. 90 – 93, 2005.
- [106] M. Kussmann, E. Nordhoff, H. Rahbek-Nielsen, S. Haebel, M. Rossel-Larsen, L. Jakobsen, J. Gobom, E. Mirgorodskaya, A. Kroll-Kristensen, L. Palm, and P. Roepstorff, "Matrix-assisted Laser Desorption/Ionization Mass Spectrometry Sample Preparation Techniques Designed for Various Peptide and Protein Analytes," *Journal of Mass Spectrometry*, vol. 32, pp. 593–601, 1997.
- [107] K. Owens, "Maldi matrix information." <http://maldimatrixinfo.wikispaces.com/>, July 2014.

- [108] V. Vidova, P. Novak, M. Strohal, J. Pol, V. Havlicek, and M. Volny, “Laser Desorption-Ionization of Lipid Transfers: Tissue Mass Spectrometry Imaging without MALDI Matrix,” *Analytical Chemistry*, vol. 82, no. 12, pp. 4994–4997, 2010.
- [109] P. Schmid, F. Stohr, M. Arndt, J. Tuxen, and M. Mayor, “Single-Photon Ionization of Organic Molecules Beyond 10 kDa,” *Journal of the American Society for Mass Spectrometry*, vol. 24, no. 4, pp. 602–8, 2013.
- [110] U. Sezer, P. Schmid, L. Felix, M. Mayor, and M. Arndt, “Slow beams and VUV post-ionization of macromolecular libraries,” *Journal of Mass Spectrometry*, vol. submitted, 2014.
- [111] S. Berkenkamp, M. Karas, and F. Hillenkamp, “Ice as a matrix for IR-Matrix-Assisted Laser Desorption/Ionization: Mass spectra from a Protein Single Crystal,” *Proceedings of the National Academy of Sciences USA*, vol. 93, pp. 7003–7007, 1996.
- [112] M. L. Vestal, P. Juhasz, and S. A. Martin, “Delayed extraction matrix-assisted laser desorption time-of-flight mass spectrometry,” *Rapid Communications in Mass Spectrometry*, vol. 9, no. 11, pp. 1044 – 1050, 1995.
- [113] B. Spengler and V. Bökelmann, “Angular and time resolved intensity distributions of laser-desorbed matrix ions,” *Nuclear Instruments and Methods in Physics Research Section B: Beam Interactions with Materials and Atoms*, vol. 82, pp. 379–385, 1993.
- [114] M. Glückmann and M. Karas, “The initial ion velocity and its dependence on matrix, analyte and preparation method in ultraviolet matrix-assisted laser desorption/ionization,” *Journal of Mass Spectrometry*, vol. 34, no. 5, pp. 467–477, 1999.
- [115] L. Zhigilei and B. Garrison, “Velocity distributions of analyte molecules in matrix-assisted laser desorption from computer simulations,” *Rapid Communications in Mass Spectrometry*, vol. 12, pp. 1273–1277, 1998.
- [116] S. Berkenkamp, C. Menzel, F. Hillenkamp, and K. Dreisewerd, “Measurements of mean initial velocities of analyte and matrix ions in infrared matrix-assisted laser desorption ionization mass spectrometry,” *Journal of the American Society for Mass Spectrometry*, vol. 13, no. 3, pp. 209–220, 2002.
- [117] I. Tomalová, V. Frankevich, and R. Zenobi, “On initial ion velocities in MALDI: A novel ft-icr {MS} approach,” *International Journal of Mass Spectrometry*, vol. 372, no. 0, pp. 51 – 53, 2014.
- [118] P. Horak, G. Hechenblaikner, K. M. Gheri, H. Stecher, and H. Ritsch, “Cavity-Induced Atom Cooling in the Strong Coupling Regime,” *Physical Review Letters*, vol. 79, pp. 4974 – 4977, 1997.
- [119] P. Domokos and H. Ritsch, “Collective Cooling and Self-Organization of Atoms in a Cavity,” *Physical Review Letters*, vol. 89, no. 25, p. 253003, 2002.
- [120] R. Fulton, A. I. Bishop, and P. F. Barker, “Optical Stark Decelerator for Molecules,” *Physical Review Letters*, vol. 93, pp. 243004–4, 2004.

- [121] H. B. G. Meijer, S. van der Meerakker, "Taming molecular beams," *Nature Physics*, vol. 4, p. 595, 2008.
- [122] B. Lev, A. Vukics, E. Hudson, B. Sawyer, P. Domokos, H. Ritsch, and J. Ye, "Prospects for the cavity-assisted laser cooling of molecules," *Physical Review A*, vol. 77, no. 2, p. 23402, 2008.
- [123] N. Kiesel, F. Blaser, U. Delic, D. Grass, R. Kaltenbaek, and M. Aspelmeyer, "Cavity cooling of an optically levitated submicron particle," *Proceedings of the National Academy of Sciences USA*, vol. 110, no. 35, pp. 14180–14185, 2013.
- [124] D. E. Chang, C. A. Regal, S. B. Papp, D. J. Wilson, J. Ye, O. Painter, H. J. Kimble, and P. Zoller, "Cavity opto-mechanics using an optically levitated nanosphere," *Proceedings of the National Academy of Sciences USA*, vol. 107, no. 3, pp. 1005–1010, 2010.
- [125] W. R. Leo, *Techniques for Nuclear and Particle Physics Experiments: A How-to Approach*. Springer, 2012.
- [126] D. Ding, J. Huang, R. Compton, C. Klots, and R. Haufler, "CW laser ionization of C60 and C70," *Physical Review Letters*, vol. 73, no. 8, pp. 1084–1087, 1994.
- [127] G. von Helden, I. Holleman, A. J. A. van Roij, G. M. H. Knippels, A. F. G. van der Meer, and G. Meijer, "Shedding New Light on Thermionic Electron Emission of Fullerenes," *Physical Review Letters*, vol. 81, pp. 1825 – 1828, Aug 1998.
- [128] A. Amirav and M. J. Cardillo, "Ion emission due to the scattering of hyperthermal Xe atoms from single crystal surfaces," *Surface Science*, vol. 198, no. 1-2, pp. 192 – 206, 1988.
- [129] C. Weickhardt, L. Draak, and J. Grotemeyer, "Hyperthermal Surface Ionization in a Time-of-Flight Mass Spectrometer," *European Journal of Mass Spectrometry*, vol. 6, pp. 319–323, 2000.
- [130] A. P. Tinke, W. M. A. Niessen, U. R. Tjaden, and J. van der Greef, "Hyperthermal Surface Ionization as a New Interfacing Approach in Liquid Chromatography/Mass Spectrometry," *Analytical Chemistry*, vol. 66, no. 19, pp. 3005–3012, 1994.
- [131] A. Amirav, "Electron impact and hyperthermal surface ionization mass spectrometry in supersonic molecular beams," *Organic Mass Spectrometry*, vol. 26, pp. 1–17, 1991.
- [132] M. S. B. Munson and F. H. Field, "Chemical Ionization Mass Spectrometry. I. General Introduction," *Journal of the American Chemical Society*, vol. 88, p. 2621–2630, 1966.
- [133] A. Harrison, *Chemical ionization mass spectrometry*. CRC Press, 1992.
- [134] F. Field and M. Munson, "Reactions of Gaseous Ions XIV: Mass Spectrometric Studies of Methan at pressure to 2 Torr," *Journal of the American Chemical Society*, vol. 87, pp. 3289–3294, 1965.

- [135] J. Gross, *Mass spectrometry: a textbook*. Heidelberg: Springer Verlag, 2011.
- [136] M. Marksteiner, *Production and detection of neutral molecular beams: From single amino acids to biomolecular complexes*. Dissertation, University of Vienna, 2010.
- [137] S. Lias, "Ionization Energy Evaluation," in *NIST Chemistry WebBook, NIST Standard Reference Database Number 69* (E. P. Linstrom and W. Mallard, eds.), ch. Ionization Energy Evaluation, National Institute of Standards and Technology, Gaithersburg MD, 20899, 2014.
- [138] K. R. Wilson, M. Jimenez-Cruz, C. Nicolas, L. Belau, S. R. Leone, and M. Ahmed, "Thermal vaporization of biological nanoparticles: fragment-free vacuum ultraviolet photoionization mass spectra of tryptophan, phenylalanine-glycine-glycine, and beta-carotene," *Journal of Physical Chemistry A*, vol. 110, pp. 2106–2113, 2005.
- [139] K. R. Wilson, D. S. Peterka, M. Jimenez-Cruz, S. R. Leone, and M. Ahmed, "VUV photoelectron imaging of biological nanoparticles: Ionization energy determination of nanophase glycine and phenylalanine-glycine-glycine," *Physical Chemistry Chemical Physics*, vol. 8, no. 16, pp. 1884–1890, 2006.
- [140] J. Berkowitz, *Atomic and Molecular Photoabsorption: Absolute Total Cross Sections*. London: Academic Press, 2002.
- [141] C. H. Becker and K. J. Wu, "On the photoionization of large molecules," *Journal of the American Society for Mass Spectrometry*, vol. 6, pp. 883 – 888, 1995.
- [142] J. Berkowitz, "The Quantum Yield of Ionization," *Physics Essays*, vol. 13, pp. 248 – 255, 2000.
- [143] A. Jones, M. Dale, G. Keenan, and P. Langridge-Smith, "Photoionisation and photodissociation of laser-vaporised metallotetraphenylporphyrins," *Chemical Physics Letters*, vol. 219, no. 3-4, pp. 174–180, 1994.
- [144] M. Marksteiner, P. Haslinger, M. Sclafani, H. Ulbricht, and M. Arndt, "UV and VUV Ionization of Organic Molecules, Clusters, and Complexes," *Journal of Physical Chemistry A*, vol. 113, no. 37, pp. 9952–9957, 2009.
- [145] P. D. Edirisinghe, J. F. Moore, K. A. Skinner-Nemec, C. Lindberg, C. S. Giometti, I. V. Veryovkin, J. E. Hunt, M. J. Pellin, and L. Hanley, "Detection of In Situ Derivatized Peptides in Microbial Biofilms by Laser Desorption 7.87 eV Postionizatton Mass Spectrometry," *Analytical Chemistry*, vol. 79, no. 2, pp. 508–514, 2006.
- [146] L. Hanley, P. D. Edirisinghe, W. F. Calaway, I. V. Veryovkin, M. J. Pellin, and J. F. Moore, "7.87 eV postionization of peptides containing tryptophan or derivatized with fluorescein," *Applied Surface Science*, vol. 252, pp. 6723–6726, 2006.
- [147] F. Mühlberger, J. Wieser, A. Morozov, A. Ulrich, and R. Zimmermann, "Single-Photon Ionization Quadrupole Mass Spectrometry with an Electron Beam Pumped Excimer Light Source," *Analytical Chemistry*, vol. 77, pp. 2218–2226, 2005.

- [148] R. Hilbig and R. Wallenstein, "Enhanced production of tunable VUV radiation by phase-matched frequency tripling in Krypton and Xenon," *IEEE Journal of Quantum Electronics*, vol. 17, pp. 1566–1573, 1981.
- [149] A. H. Kung, "Third-harmonic generation in a pulsed supersonic jet of xenon," *Optics Letters*, vol. 8, no. 1, pp. 24–26, 1983.
- [150] S. Heinbuch, M. Grisham, D. Martz, and J. J. Rocca, "Demonstration of a desk-top size high repetition rate soft x-ray laser," *Optics Express*, vol. 13, no. 11, pp. 4050–4055, 2005.
- [151] S. Heinbuch, F. Dong, J. J. Rocca, and E. R. Bernstein, "Single photon ionization of hydrogen bonded clusters with a soft x-ray laser:  $(\text{HCOOH})_x$  and  $(\text{HCOOH})_y(\text{H}_2\text{O})_z$ ," *The Journal of Chemical Physics*, vol. 126, p. 244301, 2007.
- [152] A. de Castro, C. Bostedt, E. Eremina, M. Hoener, H. Thomas, T. Laarmann, T. Fennel, K. Meiwes-Broer, E. Plönjes, M. Kuhlmann, H. Wabnitz, and T. Möller, "Spectroscopy of rare gas clusters using VUV light from a free-electron-laser," *Journal of Electron Spectroscopy and Related Phenomena*, vol. 156-158, pp. 25–29, 2007.
- [153] V. Ayvazyan, N. Baboi, I. Bohnet, R. Brinkmann, M. Castellano, P. Castro, L. Catani, S. Choroba, A. Cianchi, M. Dohlus, H. Edwards, B. Faatz, A. Fateev, J. Feldhaus, K. Flöttmann, A. Gamp, T. Garvey, H. Genz, C. Gerth, V. Gretchko, B. Grigoryan, U. Hahn, C. Hessler, K. Honkavaara, M. Hüning, R. Ischebeck, M. Jablonka, T. Kamps, M. Körfer, M. Krassilnikov, J. Krzywinski, M. Liepe, A. Liero, T. Limberg, H. Loos, M. Luong, C. Magne, J. Menzel, P. Michelato, M. Minty, U.-C. Müller, D. Nölle, A. Novokhatski, C. Pagani, F. Peters, J. Pflüger, P. Piot, L. Plucinski, K. Rehlich, I. Reyzl, A. Richter, J. Rossbach, E. Saldin, W. Sandner, H. Schlarb, G. Schmidt, P. Schmüser, J. Schneider, E. Schneidmiller, H.-J. Schreiber, S. Schreiber, D. Sertore, S. Setzer, S. Simrock, R. Sobierajski, B. Sonntag, B. Steeg, F. Stephan, K. Sytchev, K. Tiedtke, M. Tonutti, R. Treusch, D. Trines, D. Türke, V. Verzhilov, R. Wanzenberg, T. Weiland, H. Weise, M. Wendt, T. Wilhein, I. Will, K. Wittenburg, S. Wolff, M. Yurkov, and K. Zapfe, "A new powerful source for coherent VUV radiation: Demonstration of exponential growth and saturation at the TTF free-electron laser," *The European Physical Journal D - Atomic, Molecular, Optical and Plasma Physics*, vol. 20, no. 1, pp. 149–156, 2002.
- [154] L. Hanley, O. Kornienko, E. T. Ada, E. Fuoco, and J. L. Trevor, "Surface mass spectrometry of molecular species," *Journal of Mass Spectrometry*, vol. 34, pp. 705–723, 1999.
- [155] L. Hanley and R. Zimmermann, "Light and Molecular Ions: The Emergence of Vacuum UV Single-Photon Ionization in MS," *Analytical Chemistry*, vol. 81, pp. 4174–4182, 2009.
- [156] D. S. Anex, M. S. d. Vries, A. Knebelkamp, J. Bargon, H. R. Wendt, and H. E. Hunziker, "Resonance-enhanced two-photon ionization time-of-flight

- spectroscopy of cold perfluorinated polyethers and their external and internal van der Waals dimers,” *International Journal of Mass Spectrometry and Ion Processes*, vol. 131, pp. 319–334, 1994.
- [157] J. M. Dixon, M. Taniguchi, and J. S. Lindsey, “Photochemcad 2: A Refined Program with Accompanying Spectral Databases for Photochemical Calculations,” *Photochemistry and Photobiology*, vol. 81, no. 1, pp. 212–213, 2005.
  - [158] S. Eibenberger, “Transmission losses in the KDTLI.” Private communication, 2014.
  - [159] D. Fenyo, B. T. Chait, T. E. Johnson, and J. S. Lindsey, “Laser Desorption Mass Spectrometry of Synthetic Multiporphyrin Arrays,” *Journal of Porphyrins and Phthalocyanines*, vol. 1, pp. 93–99, 1997.
  - [160] S. Feil, M. Winkler, P. Sulzer, S. Ptasinska, S. Denifl, F. Zappa, B. Kräutler, T. Märk, and P. Scheier, “Single, double and triple ionization of tetraphenyl iron(iii) porphyrin chloride,” *International Journal of Mass Spectrometry*, vol. 255, pp. 232 – 238, 2006.
  - [161] S. C. Khandelwal and J. L. Roebber, “The Photoelectron Spectra of Tetraphenylporphine and some Metallotetraphenylporphyrins,” *Chemical Physics Letters*, vol. 34, no. 2, pp. 355–359, 1975.
  - [162] J. Morris and M. Johnston, “Multiphoton ionization of transition-metal tetraphenylporphines. Metal complexes which display molecular ionization,” *International Journal of Mass Spectrometry and Ion Processes*, vol. 73, pp. 175 – 180, 1986.
  - [163] J. Tüxen, S. Eibenberger, S. Gerlich, M. Arndt, and M. Mayor, “Highly Fluorous Porphyrins as Model Compounds for Molecule Interferometry,” *European Journal of Organic Chemistry*, vol. 25, no. 25, pp. 4823–4833, 2011.
  - [164] J. Tüxen, *Highly Fluorinated Model Compounds for Matter-Wave Interferometry*. PhD thesis, University of Basel, 2012.
  - [165] L. Felix, U. Sezer, M. Arndt, and M. Mayor, “Photoionizable Highly Fluorinated Porphyrin-Systems for Quantum Interference Experiments.” submitted, 2014.
  - [166] O. Dolgounitcheva, V. Zakrzewski, and J. Ortiz, “Ab Initio Electron Propagator Calculations on the Ionization Energies of Free Base Porphine, Magnesium Porphyrin, and Zinc Porphyrin,” *Journal of Physical Chemistry A*, vol. 109, pp. 11596–11601, 2005.
  - [167] J. Tüxen, “MALDI of different perfluoroalkyl-functionalized TPP compounds.” Private communication, 2014.
  - [168] W. A. D. Heer and V. V. Kresin, “Electric and magnetic dipole moments of free nanoclusters,” in *Handbook of Nanophysics* (K. D. Sattler, ed.), ch. Electric and magnetic dipole moments of free nanoclusters, pp. 1–13, Taylor & Francis, CRC Press, 2010.
  - [169] W. De Heer and V. Kresin, “Electric and magnetic dipole moments of free nanoclusters,” *Handbook of Nanophysics*, 2010.

- [170] K. Bonin and V. Kresin, *Electric-Dipole Polarizabilities of Atoms, Molecules and Clusters*. World Scientific, Singapore, 1997.
- [171] S. Nimmrichter, P. Haslinger, K. Hornberger, and M. Arndt, “Concept of an ionizing time-domain matter-wave interferometer,” *New Journal of Physics*, vol. 13, p. 075002, 2011.
- [172] M. Wahl and A. Wucher, “VUV photoionization of sputtered neutral silver clusters,” *Nuclear Instruments and Methods in Physics Research Section B*, vol. 94, pp. 36–46, 1994.
- [173] Wucher, “ToF-sims: Materials analysis by mass spectrometry,” in *ToF-SIMS: Surface Analysis by Mass Spectrometry*, book section Laser Post-Ionisation: Fundamentals, IM Publications LLP and SurfaceSpectra Limited, 2013.
- [174] S. Gerlich, *Interferometry and metrology with macromolecules*. PhD thesis, University of Vienna, 2011.
- [175] N. Dörre, J. Rodewald, P. Geyer, B. von Issendorff, P. Haslinger, and M. Arndt, “Photofragmentation beam splitters for matter-wave interferometry,” *arXiv*, vol. arXiv:1407.0919, pp. 1–4, 2014.
- [176] K. Hornberger, L. Hackermüller, and M. Arndt, “Influence of molecular temperature on the coherence of fullerenes in a near-field interferometer,” *Physical Review A*, vol. 71, no. 2, p. 023601, 2005.
- [177] R. Otto, A. von Zastrow, T. Best, and R. Wester, “Internal state thermometry of cold trapped molecular anions,” *Physical Chemistry Chemical Physics*, vol. 15, pp. 612–618, 2013.
- [178] G. Gabrielse, X. Fei, L. A. Orozco, R. L. Tjoelker, J. Haas, H. Kalinowsky, T. A. Trainor, and W. Kells, “Thousandfold improvement in the Measured Antiproton Mass,” *Physical Review Letters*, vol. 65, p. 1317, 1990.
- [179] R. March and J. Todd, *Quadrupole ion trap mass spectrometry*. John Wiley & Sons, 2005.
- [180] K. Blaum, “High-accuracy mass spectrometry with stored ions,” *Physics Reports*, vol. 425, no. 1, pp. 1 – 78, 2006.
- [181] W. M. Itano, J. C. Bergquist, J. J. Bollinger, and D. J. Wineland, “Cooling methods in ion traps,” *Physica Scripta*, vol. T59, p. 106, 1995.
- [182] J. Eschner, G. Morigi, F. Schmidt-Kaler, and R. Blatt, “Laser cooling of trapped ions,” *Journal of the Optical Society of America B: Optical Physics*, vol. 20, pp. 1003–1015, May 2003.
- [183] A. K. Hansen, O. O. Versolato, L. Klosowski, S. B. Kristensen, A. Gिंगell, M. Schwarz, A. Windberger, J. Ullrich, J. R. C. Lopez-Urrutia, and M. Drewsen, “Efficient rotational cooling of Coulomb-crystallized molecular ions by a helium buffer gas,” *Nature*, vol. 508, pp. 76–79, 2014.
- [184] D. Leibfried, R. Blatt, C. Monroe, and D. Wineland, “Quantum dynamics of single trapped ions,” *Reviews of Modern Physics*, vol. 75, p. 281, 2003.

- [185] Y. Wan, F. Gebert, J. B. Wübbena, N. Scharnhorst, S. Amairi, I. D. Leroux, B. Hemmerling, N. Lörch, K. Hammerer, and P. O. Schmidt, “Precision spectroscopy by photon-recoil signal amplification,” *Nature Communications*, vol. 5, p. 3096, 2014.
- [186] C. Chou, D. B. Hume, J. C. J. Koelemeij, D. J. Wineland, and T. Rosenband, “Frequency Comparison of Two High-Accuracy Al Optical Clocks,” *Physical Review Letters*, vol. 104, p. 070802, 2010.
- [187] K. Blaum, Y. N. Novikov, and G. Werth, “Penning traps as a versatile tool for precise experiments in fundamental physics,” *Contemporary Physics*, vol. 51, no. 2, pp. 149–175, 2010.
- [188] G. B. Andresen and A. collaboration, “Trapped antihydrogen,” *Nature*, vol. 468, pp. 673–676, 2010.
- [189] H. Dehmelt, “Experiments with an isolated subatomic particle at rest,” *Reviews of Modern Physics*, vol. 62, pp. 525–530, Jul 1990.
- [190] L. S. Brown and G. Gabrielse, “Geonium theory: Physics of a single electron or ion in a Penning trap,” *Reviews of Modern Physics*, vol. 58, p. 233, 1986.
- [191] W. Paul, H. Reinhard, and U. Von Zahn, “Das elektrische Massenfilter als Massenspektrometer und Isotopentrenner,” *Zeitschrift für Physik A Hadrons and Nuclei*, vol. 152, no. 2, pp. 143–182, 1958.
- [192] W. Paul, “Electromagnetic traps for charged and neutral particles,” *Reviews of Modern Physics*, vol. 62, p. 531, 1990.
- [193] D. Gerlich, *Inhomogeneous RF fields: a versatile tool for the study of processes with slow ions*, ch. 1, p. 1. John Wiley & Sons, Inc., 1992.
- [194] D. Denison, “Operating Parameters of a Quadrupole in a Grounded Cylindrical Housing,” *The Journal of Vacuum Science and Technology*, vol. 8, p. 266, 1971.
- [195] P. Sta anum, K. Hojbjerre, and M. Drewsen, “Sympathetically-cooled single ion mass spectrometry,” in *Practical Aspects of Trapped Ion Mass Spectrometry, Vol V* (R. March and J. Todd, eds.), pp. 291 – 327, CRC Press, 2010.
- [196] F. Arscott, *Periodic differential equations: An introduction to Mathieu, Lamel, and allied functions*. International series of monographs in pure and applied mathematics, 1964.
- [197] F. Major, V. Gheorghe, and G. Werth, *Charged Particle Traps*. Springer Series on Atomic, Optical, and Plasma Physics, Springer, 2005.
- [198] M. Drewsen and A. Broner, “Harmonic linear Paul trap: Stability diagram and effective potentials,” *Physical Review A*, vol. 62, p. 045401, 2000.
- [199] P. H. Dawson, *Quadrupole Mass Spectrometry and its Applications*. Elsevier Scientific Publishing Company, Amsterdam, 1976.
- [200] D. Manura, *SIMION (R) 8.0*. Scietific Instrument Services, Inc., Ringoes, NJ, January 2008.

- [201] E. Fischer, “Die dreidimensionale Stabilisierung von Ladungsträgern in einem Vierpolfeld,” *Zeitschrift für Physik*, vol. 156, no. 1, pp. 1–26, 1959.
- [202] J. E. Fulford, D. Nhu-Hoa, R. J. Hughes, R. E. March, R. F. Bonner, and G. J. Wong, “Radiofrequency mass selective excitation and resonant ejection of ions in a three dimensional quadrupole ion trap,” *Journal of Vacuum Science & Technology*, vol. 17, p. 829, 1980.
- [203] M. H. Soni and R. G. Cooks, “Selective Injection and Isolation of Ions in Quadrupole Ion Trap Mass Spectrometry Using Notched Waveforms Created Using the Inverse Fourier Transform,” *Analytical Chemistry*, vol. 66, no. 15, pp. 2488–2496, 1994.
- [204] D. Goeringer, W. Whitten, J. Ramsey, S. McLuckey, and G. Glush, “Theory of high-resolution mass spectrometry achieved via resonance ejection in the quadrupole ion trap,” *Analytical Chemistry*, vol. 64, pp. 1434–1439, 1992.
- [205] C. Champenois, “About the dynamics and thermodynamics of trapped ions,” *Journal of Physics B: Atomic, Molecular and Optical Physics*, vol. 42, p. 154002, 2009.
- [206] D. Gerlich, “Ion-neutral collisions in a 22-pole trap at very low energies,” *Physica Scripta*, vol. 95, p. 256, 1995.
- [207] A. V. Tolmachev, H. R. Udseth, and R. D. Smith, “Radial stratification of ions as a function of mass to charge ratio in collisional cooling radio frequency multipoles used as ion guides of ion traps,” *Rapid Communications in Mass Spectrometry*, vol. 14, pp. 1907–1913, 2000.
- [208] F. Talbot, S. Sciuto, and R. Jockusch, “Fluorescence Imaging for Visualization of the Ion Cloud in a Quadrupole Ion Trap Mass Spectrometer,” *Journal of the American Society for Mass Spectrometry*, vol. 24, no. 12, pp. 1823–1832, 2013.
- [209] K. Zimmermann, M. V. Okhapkin, and O. A. H.-S. und E. Peik, “Laser ablation loading of a radiofrequency ion trap,” *Applied Physics B: Lasers and Optics*, vol. 107, p. 883, 2012.
- [210] S. Guan and A. Marshall, “Equilibrium space charge distribution in a quadrupole ion trap,” *Journal of the American Society for Mass Spectrometry*, vol. 5, p. 64, 1994.
- [211] K. Avinash, A. K. Agarwal, M. R. Jana, A. Sen, and P. K. Kaw, “Space charge effects in the Paul trap,” *Physics of Plasmas*, vol. 2, pp. 3569–3572, 1995.
- [212] S. Sevugarajan and A. Menon, “Frequency perturbation in nonlinear Paul traps: a simulation study of the effect of geometric aberration, space charge, dipolar excitation, and damping on ion axial secular frequency,” *International Journal of Mass Spectrometry*, vol. 197, pp. 263–278, 2000.
- [213] D. Guo, Y. Wang, X. Xiong, H. Zhang, X. Zhang, T. Yuan, X. Fang, and W. Xu, “Space Charge Induced Nonlinear Effects in Quadrupole Ion Traps,” *Journal of the American Society for Mass Spectrometry*, vol. 25, no. 3, pp. 498–508, 2014.

- [214] C. Meis, M. Desaintfuscien, and M. Jardino, “Analytical calculation of the space charge potential and the temperature of stored ions in an rf quadrupole trap,” *Applied Physics B*, vol. 45, no. 2, pp. 59–64, 1988.
- [215] N. Kjærgaard, K. Molhave, and M. Drewsen, “Stability of Coulomb crystals in a linear Paul trap with storage-ring-like confinement,” *Physical Review E*, vol. 66, p. 015401(R), 2002.
- [216] C.-S. O and H. A. Schuessler, “Confinement of ions created externally in a radio frequency ion trap,” *Journal of Applied Physics*, vol. 52, no. 3, p. 1157, 1981.
- [217] F. Herfurth, J. Dilling, G. Bollen, and H.-J. Kluge, “A linear radiofrequency ion trap for accumulation, bunching, and emittance improvement of radioactive ion beams,” *Nuclear Instruments and Methods in Physics Research A*, vol. 469, p. 254, 2001.
- [218] D. Papanastasiou, O. Belgacem, M. Sudakov, and E. Raptakis, “Ion thermalization using pressure transients in a quadrupole ion trap coupled to a vacuum matrix-assisted laser desorption ionization source and a reflectron time-of-flight mass analyzer,” *Review of Scientific Instruments*, vol. 79, no. 5, p. 055103, 2008.
- [219] M. Cetina, A. T. Grier, and V. Vuletić, “Micromotion-Induced Limit to Atom-Ion Sympathetic Cooling in Paul Traps,” *Physical Review Letters*, vol. 109, p. 253201, Dec 2012.
- [220] P. K. Ghosh, *Ion traps*. International Series of Monographs on Physics, Oxford University Press, 1995.
- [221] F. Vedel, A. Alili, and J. Andre, “Buffer gas cooling of ion stored in an RF trap: computed properties of the ionic cloud,” *Physica Scripta*, vol. T22, p. 325, 1988.
- [222] Y. Moriwaki, M. Tachikawa, Y. Maeno, and T. Shimizu, “Collisional Cooling of Ions Stored in a Quadrupole Radio-Frequency Trap,” *Japanese Journal of Applied Physics*, vol. 31, pp. 1640–1643, 1992.
- [223] T. Kim, *Buffer gas cooling of ions in a radio frequency quadrupole ion guide: A study of the cooling process and cooled beam parameters*. Thesis, McGill University, 1997.
- [224] S. Schwarz, “Simulations for ion traps buffer gas cooling,” in *Trapped charged particles and fundamental Interactions - Lecture Notes in Physics*, Springer-Link, 2008.
- [225] D. Gerlich and G. Borodi, “Buffer gas cooling of polyatomic ions in RF multi-electrode traps,” *Faraday Discussions*, vol. 142, pp. 57–72, 2009.
- [226] T. Baba and I. Waki, “Sympathetic cooling rate of gas-phase ions in a radio-frequency-quadrupole ion trap,” *Applied Physics B: Lasers and Optics*, vol. 74, p. 375, 2002.

- [227] S. Schiller, A. Ostendorf, C. Zhang, M. Wilson, D. Offenberger, and B. Roth, “Sympathetic cooling of complex molecular ions to millikelvin temperatures,” *Physical Review Letters*, vol. 97, p. 243005, 2006.
- [228] H. Schaaf, U. Schmeling, and G. Werth, “Trapped ion density distribution in the presence of He-Buffer gas,” *Applied Physics*, vol. 25, pp. 249–251, 1981.
- [229] T. Hasegawa and K. Uehara, “Dynamics of a single particle in a Paul trap in the presence of the damping force,” *Applied Physics B*, vol. 61, no. 2, pp. 159–163, 1995.
- [230] M. Nasse and C. Foot, “Influence of background pressure on the stability region of a Paul trap,” *European Journal of Physics*, vol. 22, no. 6, p. 563, 2001.
- [231] A. Ostendorf, C. B. Zhang, M. A. Wilson, D. Offenberger, B. Roth, and S. Schiller, “Sympathetic Cooling of Complex Molecular Ions to Millikelvin Temperatures,” *Physical Review Letters*, vol. 97, p. 243005, 2006.
- [232] I. Gilmore and M. Seah, “Ion detection efficiency in SIMS: Dependencies on energy, mass and composition for microchannel plates used in mass spectrometry,” *International Journal of Mass Spectrometry*, vol. 202, p. 217, 2000.
- [233] R. Liu, Q. Li, and L. Smith, “Detection of Large Ions in Time-of-Flight Mass Spectrometry: Effects of Ion Mass and Acceleration Voltage on Microchannel Plate Detector Response,” *Journal of the American Society for Mass Spectrometry*, vol. 25, no. 8, pp. 1374–1383, 2014.
- [234] R. Haugland, *Handbook of Fluorescent Probes and Research Products*. Molecular Probes, 2002.
- [235] J. Lakowicz, *Principles of fluorescence spectroscopy*. Springer, 3 ed., 2006.
- [236] B. Valeur and M. N. Berberan-Santos, *Molecular Fluorescence - Principles and Applications*. Wiley-VCH, 2013.
- [237] A. Jabonski, “Efficiency of Anti-Stokes Fluorescence in Dyes,” *Nature*, vol. 131, pp. 839–840, 1933.
- [238] M. Sclafani, *Molecular beam methods for quantum optics experiments: sources, detection schemes and coherent manipulation*. PhD thesis, University of Vienna, 2013.
- [239] L. Andersen, A. Lapierre, S. Nielsen, I. Nielsen, S. Pedersen, U. Pedersen, and S. Tomita, “Chromophores of the green fluorescent protein studied in the gas phase,” *The European Physical Journal D - Atomic, Molecular, Optical and Plasma Physics*, vol. 20, no. 3, pp. 597–600, 2002.
- [240] M. W. Forbes, A. M. Nagy, and R. A. Jockusch, “Photofragmentation of and electron photodetachment from a GFP model chromophore in a quadrupole ion trap,” *International Journal of Mass Spectrometry*, vol. 308, no. 2–3, pp. 155–166, 2011.

- [241] V. Frankevich, K. Barylyuk, K. Chingin, R. Nieckarz, and R. Zenobi, "Native biomolecules in the gas phase? The case of Green Fluorescent Protein," *ChemPhysChem*, vol. 14, pp. 929–35, 2013.
- [242] J. Khoury, S. Rodriguez-Cruz, and J. Parks, "Pulsed fluorescence measurements of trapped molecular ions with zero background detection," *Journal of the American Society for Mass Spectrometry*, vol. 13, no. 6, pp. 696–708, 2002.
- [243] Y. Cai, W. P. Peng, S. J. Kuo, S. Sabu, C. C. Han, and H. C. Chang, "Optical Detection and Charge-State Analysis of MALDI-Generated Particles with Molecular Masses Larger Than 5 MDa," *Analytical Chemistry*, vol. 74, no. 17, pp. 4434–4440, 2002.
- [244] N. Sassin, S. Everhart, B. Dangi, K. Ervin, and J. Cline, "Fluorescence and photodissociation of rhodamine 575 cations in a quadrupole ion trap," *Journal of the American Society for Mass Spectrometry*, vol. 20, no. 1, pp. 96–104, 2009.
- [245] F. Talbot, A. Rullo, H. Yao, and R. Jockusch, "Fluorescence Resonance Energy Transfer in Gaseous, Mass-Selected Polyproline Peptides," *Journal of the American Chemical Society*, vol. 132, pp. 16156 – 16164, 2010.
- [246] P. D. McQueen, S. Sagoo, H. Yao, and R. A. Jockusch, "On the Intrinsic Photophysics of Fluorescein," *Angewandte Chemie*, vol. 122, no. 48, pp. 9379–9382, 2010.
- [247] Q. Bian, M. W. Forbes, F. O. Talbot, and R. A. Jockusch, "Gas-phase fluorescence excitation and emission spectroscopy of mass-selected trapped molecular ions," *Physical Chemistry Chemical Physics*, vol. 12, no. 11, pp. 2590–2598, 2010.
- [248] S. K. Sagoo and R. A. Jockusch, "The fluorescence properties of cationic rhodamine B in the gas phase," *Journal of Photochemistry and Photobiology A: Chemistry*, vol. 220, no. 2–3, pp. 173–178, 2011.
- [249] M. Forbes and R. Jockusch, "Gas-Phase Fluorescence Excitation and Emission Spectroscopy of Three Xanthene Dyes (Rhodamine 575, Rhodamine 590 and Rhodamine 6g) in a Quadrupole Ion Trap Mass Spectrometer," *Journal of the American Society for Mass Spectrometry*, vol. 22, no. 1, pp. 93–109, 2011.
- [250] M. Dashtiev, V. Azov, V. Frankevich, L. Scharfenberg, and R. Zenobi, "Clear Evidence of Fluorescence Resonance Energy Transfer in Gas-Phase Ions," *Journal of the American Society for Mass Spectrometry*, vol. 16, pp. 1481–1487, 2005.
- [251] M. Dashtiev, *Fluorescence Spectroscopy of Trapped Molecular Ions Produced with Matrix-Assisted Laser Desorption/Ionization*. PhD thesis, ETH Zürich, 2006.
- [252] K. Chingin, H. Chen, G. Gamez, and R. Zenobi, "Exploring fluorescence and fragmentation of ions produced by electrospray ionization in ultrahigh vacuum," *Journal of the American Society for Mass Spectrometry*, vol. 20, no. 9, pp. 1731–1738, 2009.

- [253] J. He, W. Zhong, A. Tang, X. Yan, C. Lewis, V. Majidi, and W. Hang, “A fluorescence detection scheme for ultra large molecules after gas phase separation,” *Talanta*, vol. 71, pp. 2126–8, 2007.
- [254] Y. Cai, W. P. Peng, and H. C. Chang, “Ion Trap Mass Spectrometry of Fluorescently Labeled Nanoparticles,” *Analytical Chemistry*, vol. 75, no. 8, pp. 1805–1811, 2003.
- [255] M. Dashtiev and R. Zenobi, “Effect of buffer gas on the fluorescence yield of trapped gas-phase ions,” *Journal of the American Society for Mass Spectrometry*, vol. 17, no. 6, pp. 855–858, 2006.
- [256] J. Prestage, G. Dick, and L. Maleki, “New Ion Trap for Atomic Frequency Standard Applications,” *TDA Progress Report*, vol. 97, p. 58, 1989.
- [257] R. Brown and C. Wilkins, “Laser-desorption Fourier transform mass spectrometry of synthetic porphyrins,” *Analytical Chemistry*, vol. 58, p. 3196, 1986.
- [258] H. B. Pedersen, D. Strasser, O. Heber, M. L. Rappaport, and D. Zajfman, “Stability and loss in an ion trap resonator,” *Physical Review A*, vol. 65, p. 042703, Mar 2002.
- [259] J. Rocher, M. Vedel, and F. Vedel, “Well defined chopping of the paul trap rf potential up to a 1.5 {MHz} frequency combined with a time-of-flight method,” *International Journal of Mass Spectrometry*, vol. 181, no. 1–3, pp. 173 – 180, 1998.
- [260] P. Marmillod, S. Antonioni, and U. J. Lorenz, “A radio frequency/high voltage pulse generator for the operation of a planar multipole ion trap/time-of-flight mass spectrometer,” *Review of Scientific Instruments*, vol. 84, no. 4, p. 044707, 2013.
- [261] J. Hager, “A new linear ion trap mass spectrometer,” *Rapid Communications in Mass Spectrometry*, vol. 16, p. 512, 2002.
- [262] K. Hornberger, S. Uttenthaler, B. Brezger, L. Hackermüller, M. Arndt, and A. Zeilinger, “Collisional decoherence observed in matter wave interferometry,” *Physical Review Letters*, vol. 90, p. 160401, 2003.
- [263] R. Wester, “Radiofrequency multipole traps: tools for spectroscopy and dynamics of cold molecular ions,” *Journal of Physics B: Atomic, Molecular and Optical Physics*, vol. 42, no. 15, p. 154001, 2009.
- [264] D. J. Douglas, A. J. Frank, and D. Mao, “Linear Ion Traps in Mass Spectrometry,” *Mass Spectrometry Reviews*, vol. 24, pp. 1–29, 2005.
- [265] D. Berkeland, J. Miller, J. Bergquist, W. Itano, and D. Wineland, “Minimization of ion micromotion in a Paul trap,” *Journal of Applied Physics*, vol. 83, p. 5025, 1998.
- [266] X. Yi, W. Wei, Z. Fei, C. Liang, L. Chao-Hong, and F. Mang, “Linear ion trap imperfection and the compensation of excess micromotion,” *Chinese Physics B*, vol. 21, no. 6, p. 063201, 2012.

- [267] L. Turner, “Collective effects on equilibria of trapped charged plasmas,” *Physics of Fluids*, vol. 30, p. 3196, 1987.
- [268] M. E. Poitzsch, J. C. Bergquist, W. M. Itano, and D. J. Wineland, “Cryogenic linear ion trap for accurate spectroscopy,” *Review of Scientific Instruments*, vol. 67, no. 1, pp. 129–134, 1996.
- [269] J. Pedregosa, C. Champenois, M. Houssin, and M. Knoop, “Anharmonic contributions in real {RF} linear quadrupole traps,” *International Journal of Mass Spectrometry*, vol. 290, no. 2–3, pp. 100 – 105, 2010.
- [270] E. Hecht, *Optics*. Addison-Wesley, 4th edition ed., 2001.
- [271] G. Lamouche, P. Lavallard, and T. Gacoin, “Optical properties of dye molecules as a function of the surrounding dielectric medium,” *Physical Review A*, vol. 59, p. 4668, 1999.
- [272] D. W. Piston, “Choosing Objective Lenses: The importance of Numerical Aperture and Magnification in Digital Optical Microscopy,” *The Biological Bulletin*, vol. 195, pp. 1–4, 1998.
- [273] M. Drewsen, I. Jensen, J. Lindballe, N. Nissen, R. Martinussen, A. Mortensen, P. Staantum, and D. Voigt, “Ion Coulomb crystals: a tool for studying ion processes,” *International Journal of Mass Spectrometry*, vol. 229, p. 83, 2003.
- [274] S. Willitsch, M. Bell, A. Gingell, and T. Softley, “Chemical applications of laser- and sympathetically-cooled ions in ion traps,” *Physical Chemistry Chemical Physics*, vol. 10, p. 7189, 2008.
- [275] W. Demtröder, *Experimentalphysik 2 - Elektrizität und Optik*. Springer-Verlag, 2013.
- [276] M. Arndt, “Absorption and emission in LIF processes.” Private communication, 2013.
- [277] T. Basché, W. P. Ambrose, and W. E. Moerner, “Optical spectra and kinetics of single impurity molecules in a polymer: spectral diffusion and persistent spectral hole burning,” *Journal of the Optical Society of America B: Optical Physics*, vol. 9, pp. 829–836, May 1992.
- [278] U. Brackmann, *Lambdachrome Laser Dyes*. Lambda Physik, 2000.
- [279] G. van Soest, *Experiments on random lasers*. PhD thesis, University of Amsterdam, 2001.
- [280] K. Cheung, *Chip-Scale Quadrupole Mass Filters for a Micro-Gas Analyzer*. PhD thesis, Massachusetts Institute of Technology, 2005.
- [281] J. Siverns, L. Simkins, S. Weidt, and W. Hensinger, “On the application of radio frequency voltages to ion traps via helical resonators,” *Applied Physics B*, vol. 107, pp. 921–934, 2012.
- [282] M. Kumph, M. Brownnutt, and R. Blatt, “Two-dimensional arrays of radio-frequency ion traps with addressable interactions,” *New Journal of Physics*, vol. 136, p. 073043, 2011.

- [283] R. M. Jones, D. Gerlich, and S. L. Anderson, "Simple radio-frequency power source for ion guides and ion traps," *Review of Scientific Instruments*, vol. 68, no. 9, pp. 3357–3362, 1997.
- [284] S. Willitsch, "Design of an RF tank circuit." private communication, 2013.
- [285] D. M. Bell, C. R. Howder, R. C. Johnson, and S. L. Anderson, "Single CdSe/ZnS Nanocrystals in an Ion Trap: Charge and Mass Determination and Photophysics Evolution with Changing Mass, Charge, and Temperature," *ACS Nano*, vol. 8, no. 3, pp. 2387–2398, 2014.
- [286] H. Koizumi, X. Wang, W. B. Whitten, and P. T. Reilly, "Controlling the expansion into vacuum-the enabling technology for trapping atmosphere-sampled particulate ions," *Journal of the American Society for Mass Spectrometry*, vol. 21, no. 2, pp. 242–8, 2010.
- [287] M. Dashtiev, V. Frankevich, and R. Zenobi, "Kinetic Energy of Free Electrons Affects MALDI Positive Ion Yield via Capture Cross-Section," *The Journal of Physical Chemistry A*, vol. 110, no. 3, pp. 926–930, 2005.
- [288] I. of Analytical Chemistry Technical University of Graz, "Fluorophores.org - database of fluorescent dyes, properties and applications." <http://www.fluorophores.tugraz.at/>, May 2014.
- [289] P. Greenspan and S. Fowler, "Spectrofluorometric studies of the lipid probe, Nile red," *Journal of Lipid Research*, vol. 26, p. 781, 1985.
- [290] T. L. Pugh and W. Heller, "Density of polystyrene and polyvinyltoluene latex particles," *Journal of Colloid Science*, vol. 12, no. 2, pp. 173 – 180, 1957.
- [291] B. Daltonik, "Bruker guide to maldi sample preparation - maldi preparation protocols," tech. rep., Bruker Daltonik GmbH, 2012.
- [292] P. Dawson, "The acceptance of the quadrupole mass filter," *International Journal of Mass Spectrometry and Ion Physics*, vol. 17, no. 4, pp. 423 – 445, 1975.
- [293] Y. Lu and A. Penzkofer, "Absorption behaviour of methanolic Rhodamine 6G solutions at high concentrations," *Chemical Physics*, vol. 107, p. 175, 1986.
- [294] Y. Y. Kievsky, B. Carey, S. Naik, N. Mangan, D. ben Avraham, and I. Sokolov, "Dynamics of molecular diffusion of rhodamine 6G in silica nanochannels," *The Journal of Chemical Physics*, vol. 128, p. 151102, 2008.
- [295] D. R. Lide, *CRC Handbook of Chemistry and Physics*. New York: CRC Press, 1999.
- [296] I. V. Chernushevich and B. A. Thomson, "Collisional Cooling of Large Ions in Electrospray Mass Spectrometry," *Analytical Chemistry*, vol. 76, pp. 1754–1760, 2004.
- [297] R. Moore, M. Lunney, and F. Buchinger, "The temperature of buffer-gas cooled ions in a Paul trap," *Journal of Modern Optics*, vol. 39, p. 349, 1992.

- [298] W. M. Haynes, ed., *CRC Handbook of Chemistry and Physics, 94th Edition: a Ready-reference Book of Chemical and Physical Data*. Taylor & Francis Ltd., 2013.
- [299] V. Frankevich, X. Guan, M. Dashtiev, and R. Zenobi, “Laser-induced fluorescence of trapped gas-phase molecular ions generated by internal-source matrix-assisted laser desorption/ionization in a Fourier transform ion cyclotron resonance mass spectrometer,” *European Journal of Mass Spectrometry*, vol. 11, no. 5, p. 475, 2005.
- [300] A. E. Siegman, *Lasers*. University Science Books, 1986.
- [301] I. Siemers, R. Blatt, T. Sauter, and W. Neuhauser, “Dynamics of ion clouds in Paul traps,” *Physical Review A*, vol. 38, p. 5121, 1988.
- [302] M. Chung, E. P. Gilson, R. C. Davidson, P. Efthimion, and R. Majeski, “Initial density profile measurement using a Laser-Induced Fluorescence diagnostic in the Paul Trap Simulator Experiment,” in *Proceedings of PAC07, Albuquerque, New Mexico, USA*, 2007.
- [303] M. Karas, U. Bahr, I. Fournier, M. Glückmann, and A. Pfenninger, “The initial-ion velocity as a marker for different desorption-ionization mechanisms in MALDI,” *International Journal of Mass Spectrometry*, vol. 226, pp. 239–248, 2003.
- [304] P. Juhasz, M. L. Vestal, and S. A. Martin, “On the initial velocity of ions generated by matrix-assisted laser desorption ionization and its effect on the calibration of delayed extraction time-of-flight mass spectra,” *Journal of the American Society for Mass Spectrometry*, vol. 8, pp. 209 – 217, 1997.
- [305] M. Drewsen and A. Brøner, “Harmonic linear paul trap: Stability diagram and effective potentials,” *Phys. Rev. A*, vol. 62, p. 045401, Sep 2000.
- [306] R. E. March and J. F. J. Todd, *Cylindrical Ion Trap Mass Spectrometer*, vol. 165 of *Chemical Analysis-A Series of Monographs on Analytical Chemistry and Its Applications*, pp. 188–210. Oxford: Blackwell Science Publ, 2005.
- [307] J. M. Campbell, B. A. Collings, and D. J. Douglas, “A new linear ion trap time-of-flight system with tandem mass spectrometry capabilities,” *Rapid Communications in Mass Spectrometry*, vol. 12, pp. 1463–1474, 1998.
- [308] D. J. Douglas and N. V. Kononkov, “Ion cloud model for a linear quadrupole ion trap,” *European Journal of Mass Spectrometry*, vol. 18, pp. 419–429, 2012.
- [309] V. Enders, P. Courteille, W. Neuhauser, and R. Blatt, “Motional Sidebands in the Microwave Spectra of Ions in an RF Trap,” *Journal of Modern Optics*, vol. 39, pp. 325–334, 1992.
- [310] S. Hanton, “Mass Spectrometry of Polymers and Polymer Surfaces,” *Chemical Reviews*, vol. 101, pp. 527–569, 2001.
- [311] E. S. Shuman, J. F. Barry, and D. DeMille, “Laser cooling of a diatomic molecule,” *Nature*, vol. 467, p. 820, 2010.

- [312] C. Chin, R. Grimm, P. Julienne, and E. Tiesinga, “Feshbach resonances in ultracold gases,” *Reviews of Modern Physics*, vol. 82, pp. 1225 – 1286, Apr 2010.
- [313] A. Frisch, M. Mark, K. Aikawa, F. Ferlaino, J. L. Bohn, C. Makrides, A. Petrov, and S. Kotochigova, “Quantum chaos in ultracold collisions of gas-phase erbium atoms,” *Nature*, vol. 507, pp. 475–479, 2014.
- [314] J. Doyle, B. Friedrich, R. V. Krems, and F. Masnou-Seeuws, “Ultracold Polar Molecules: Formation and Collisions,” *The European Physical Journal D, special issue*, vol. 31, no. 2, 2004.
- [315] R. V. Krems, “Cold controlled chemistry,” *Physical Chemistry Chemical Physics*, vol. 10, pp. 4079–4092, 2008.
- [316] L. D. Carr, D. DeMille, R. V. Krems, and J. Ye, “Cold and ultracold molecules: science, technology and applications,” *New Journal of Physics*, vol. 11, no. 5, p. 055049, 2009.
- [317] A. Chotia, B. Neyenhuis, S. A. Moses, B. Yan, J. P. Covey, M. Foss-Feig, A. M. Rey, D. S. Jin, and J. Ye, “Long-Lived Dipolar Molecules and Feshbach Molecules in a 3D Optical Lattice,” *Physical Review Letters*, vol. 108, p. 080405, Feb 2012.
- [318] G. Poulsen and M. Drewsen, “Adiabatic cooling of a single trapped ion,” *arXiv*, vol. 1210.4309v1, p. 1, 2012.
- [319] B. Roth and S. Schiller, “Sympathetically Cooled Molecular Ions: From Principles to First Applications,” in *Cold Molecules: Theory, Experiment, Applications*, CRC Press, 2009.
- [320] T. J. Harmon, N. Moazzan-Ahmadi, and R. I. Thompson, “Instability heating of sympathetically cooled ions in a linear paul trap,” *Physical Review A*, vol. 67, p. 013415, Jan 2003.
- [321] P. Blythe, B. Roth, U. Fröhlich, H. Wenz, and S. Schiller, “Production of ultracold trapped molecular hydrogen ions,” *Physical Review Letters*, vol. 95, p. 183002, Oct 2005.
- [322] D. Offenberg, C. B. Zhang, C. Wellers, B. Roth, and S. Schiller, “Translational cooling and storage of protonated proteins in an ion trap at subkelvin temperatures,” *Physical Review A*, vol. 78, p. 061401(R), 2008.
- [323] R. Hayano and ASACUSA collaboration, “Atomic Spectroscopy and Collisions Using Slow Antiprotons,” tech. rep., CERN, 2005.
- [324] D. Trypogeorgos and C. Foot, “A two-frequency ion trap confining ions with widely different charge-to-mass ratios,” *arXiv*, vol. 1, p. 1, 2013.
- [325] M. Sclafani, M. Marksteiner, F. Keir, A. Divochiy, A. Korneev, A. Semenov, G. Gol’tsman, and M. Arndt, “Sensitivity of a superconducting nanowire detector for single ions at low energy,” *Nanotechnology*, vol. 23, p. 065501, 2012.

- [326] K. Suzuki, M. Ohkubo, M. Ukibe, S. Shiki, S. Miki, and Z. Wang, “Charge-state-derivation ion detection using a superconducting nanostructure device for mass spectrometry,” *Rapid Communications in Mass Spectrometry*, vol. 24, pp. 3290–3296, 2010.
- [327] M. Ohkubo, S. Shiki, M. Ukibe, S. Tomita, and S. Hayakawa, “Direct mass analysis of neutral molecules by superconductivity,” *International Journal of Mass Spectrometry*, vol. 299, p. 71, 2011.
- [328] M. Marksteiner, A. Divochiy, M. Sclafani, P. Haslinger, H. Ulbricht, A. Korneev, A. Semenov, G. Gol’tsman, and M. Arndt, “A superconducting NbN detector for neutral nanoparticles,” *Nanotechnology*, vol. 20, p. 455501, 2009.
- [329] O. Hadjar, G. Johnson, J. Laskin, G. Kibelka, S. Shill, K. Kuhn, C. Cameron, and S. Kassan, “IonCCD for direct position-sensitive charged-particle detection: from electrons and keV ions to hyperthermal biomolecular ions,” *Journal of the American Society for Mass Spectrometry*, vol. 22, p. 612, 2011.
- [330] J. C. Schwartz, J. E. Syka, and I. Jardine, “High resolution on a quadrupole ion trap mass spectrometer,” *Journal of the American Society for Mass Spectrometry*, vol. 2, no. 3, pp. 198 – 204, 1991.

# Philipp Schmid

## Personal data

Date and place of birth: August 4th 1982 in Vienna, Austria

## Education

- 1992 - 2000 Gymnasium BG18, Vienna
- 2000 - 2007 University of Vienna, major study in physics
- 2005 - 2006 Master thesis at the Stefan Meyer Institute  
under the supervision of Prof. Widmann
- 2006 - 2007 Mandatory civil service at Verein Wiener Sozialprojekte
- 2007 - 2008 Research year at Max-Planck Institute for Nuclear Physics  
topic: accelerator physics and ion optics research
- 2009 - 2014 PhD student under supervision of Prof. Arndt at the  
University of Vienna

November 4, 2014